Fate of Topological States of Matter in the Presence of External Magnetic Fields

Dissertation zur Erlangung des
Naturwissenschaftlichen Doktorgrades
der Julius-Maximilians-Universität Würzburg

vorgelegt von

Jan Frederic Böttcher

aus Bad Soden am Taunus

Würzburg, 2020

Eingereicht am: .....
bei der Fakultät für Physik und Astronomie

1. Gutachter: Prof. Dr. Ewelina M. Hankiewicz
2. Gutachter: .....
3. Gutachter: .....
der Dissertation

Vorsitzende(r): .....
1. Prüfer: Prof. Dr. Ewelina M. Hankiewicz
2. Prüfer: .....
3. Prüfer: .....
im Promotionskolloquium

Tag des Promotionskolloquiums: .....

Doktorurkunde ausgehändigt am: .....

Abstract

The quantum Hall (QH) effect, which can be induced in a two-dimensional (2D) electron gas by an external magnetic field, paved the way for topological concepts in condensed matter physics. While the QH effect can for that reason not exist without Landau levels, there is a plethora of topological phases of matter that can exist even in the absence of a magnetic field. For instance, the quantum spin Hall (QSH), the quantum anomalous Hall (QAH), and the three-dimensional (3D) topological insulator (TI) phase are insulating phases of matter that owe their nontrivial topology to an inverted band structure. The latter results from a strong spin-orbit interaction or, generally, from strong relativistic corrections. The main objective of this thesis is to explore the fate of these preexisting topological states of matter, when they are subjected to an external magnetic field, and analyze their connection to quantum anomalies. In particular, the realization of the parity anomaly in solid state systems is discussed. Furthermore, band structure engineering, i.e., changing the quantum well thickness, the strain, and the material composition, is employed to manipulate and investigate various topological properties of the prototype TI HgTe.

Like the QH phase, the QAH phase exhibits unidirectionally propagating metallic edge channels. But in contrast to the QH phase, it can exist without Landau levels. As such, the QAH phase is a condensed matter analog of the parity anomaly. We demonstrate that this connection facilitates a distinction between QH and QAH states in the presence of a magnetic field. We debunk therefore the widespread belief that these two topological phases of matter cannot be distinguished, since they are both described by a $\mathbb{Z}$ topological invariant. To be more precise, we demonstrate that the QAH topology remains encoded in a peculiar topological quantity, the spectral asymmetry, which quantifies the differences in the number of states between the conduction and valence band. Deriving the effective action of QAH insulators in magnetic fields, we show that the spectral asymmetry is thereby linked to a unique Chern-Simons term which contains the information about the QAH edge states. As a consequence, we reveal that counterpropagating QH and QAH edge states can emerge when a QAH insulator is

subjected to an external magnetic field. These helical-like states exhibit exotic properties which make it possible to disentangle QH and QAH phases. Our findings are of particular importance for paramagnetic TIs in which an external magnetic field is required to induce the QAH phase.

A byproduct of the band inversion is the formation of additional extrema in the valence band dispersion at large momenta (the 'camelback'). We develop a numerical implementation of the 8×8 Kane model to investigate signatures of the camelback in (Hg,Mn)Te quantum wells. Varying the quantum well thickness, as well as the Mn-concentration, we show that the class of topologically nontrivial quantum wells can be subdivided into direct gap and indirect gap TIs. In direct gap TIs, we show that, in the bulk p-regime, pinning of the chemical potential to the camelback can cause an onset to QH plateaus at exceptionally low magnetic fields (tens of mT). In contrast, in indirect gap TIs, the camelback prevents the observation of QH plateaus in the bulk p-regime up to large magnetic fields (a few tesla). These findings allowed us to attribute recent experimental observations in (Hg,Mn)Te quantum wells to the camelback. Although our discussion focuses on (Hg,Mn)Te, our model should likewise apply to other topological materials which exhibit a camelback feature in their valence band dispersion.

Furthermore, we employ the numerical implementation of the 8×8 Kane model to explore the crossover from a 2D QSH to a 3D TI phase in strained HgTe quantum wells. The latter exhibit 2D topological surface states at their interfaces which, as we demonstrate, are very sensitive to the local symmetry of the crystal lattice and electrostatic gating. We determine the classical cyclotron frequency of surface electrons and compare our findings with experiments on strained HgTe.

Zusammenfassung

Der Quanten-Hall (QH) Effekt, welcher in einem zwei-dimensionalen (2D) Elektronengas durch ein externes Magnetfeld erzeugt werden kann, ebnete den Weg für topologische Konzepte in der Physik der kondensierten Materie. Während der QH Effekt aus diesem Grund nicht ohne Landau Level existieren kann, gibt es eine Vielzahl von neuartigen topologischen Phasen, die auch in der Abwesenheit von Magnetfeldern existieren können. Zum Beispiel stellen die Quanten-Spin-Hall (QSH), die Quanten-Anomale-Hall (QAH) und die drei-dimensionale (3D) topologische Isolator-Phase isolierende, topologische Phasen dar, die Ihre nicht-triviale Topologie einer invertierten Bandstruktur verdanken. Letztere wird durch eine starke Spin-Bahn Wechselwirkung, oder im Allgemeinen durch starke relativistische Korrekturen, erzeugt. Das Hauptziel dieser Thesis ist es dabei das Schicksal dieser bereits bestehenden topologischen Zustände in Magnetfeldern zu erforschen und deren Verbindungen zu Quantenanomalien aufzuzeigen. In diesem Zusammenhang werden wir insbesondere die Realisierung der Paritätsanomalie in Festkörpersystemen diskutieren. Weitergehend wenden wir Bandstruktur-Engineering an, d.h. die Veränderung der Quantentrogdicke, der Verspannung und der Materialkomposition, um die vielfältigen topologischen Eigenschaften des topologischen Isolators (TIs) HgTe zu manipulieren und zu untersuchen.

Wie die QH Phase, zeichnet sich die QAH Phase durch unidirektional propagierende, metallische Randkanäle aus. Aber im Vergleich zur QH Phase, kann sie auch ohne Landau Level existieren. Die QAH Phase stellt daher ein Kondensierte-Materie-Analogon zur Paritätsanomalie dar. Wir zeigen, dass diese Verbindung es uns ermöglicht in der Gegenwart eines Magnetfelds zwischen QH und QAH Zuständen zu unterscheiden. Damit widerlegen wir den weitverbreiten Glauben, dass diese zwei topologischen Phasen nicht unterschieden werden können, da beide durch eine $\mathbb{Z}$ topologische Invariante beschrieben sind. Etwas genauer gesagt, zeigen wir, dass die QAH Topologie in einer besonderen topologischen Invarianten kodiert bleibt, der spektralen Asymmetrie. Diese quantifiziert die Differenz in der Anzahl von Zuständen in Leitungs- und Valenzbändern. Indem wir die effektive Wirkung eines QAH Isolators im Magnetfeld herleiten, zeigen wir, dass die spektrale Asymmetrie dabei mit einem einzigartigen Chern-Simons Term verbunden ist, welcher die Information über die QAH Randkanäle beinhaltet. Wenn ein QAH Isolator einem externen Magnetfeld ausgesetzt wird, kann dies zur Bildung von gegenläufigen QH und QAH Randkanälen führen. Diese helikalartigen Randzustände besitzen exo-

tische Eigenschaften, die es uns ermöglichen QH und QAH Phasen zu unterscheiden. Unsere Ergebnisse sind insbesondere für paramagnetische TIs von Bedeutung, da für diese ein externes Magnetfeld von Nöten ist, um die QAH Phase zu induzieren.

Ein Nebenprodukt der Bandinversion ist die Bildung von zusätzlichen Extrema in der Dispersion des Valenzbands bei großen Impulsen (oft auch als 'Kamelrücken' bezeichnet). Wir entwickeln eine numerische Implementierung des 8×8 Kane Modells um die Signaturen des Kamelrückens in (Hg,Mn)Te Quantentrögen zu untersuchen. Indem die Quantentrogdicke und die Mn-Konzentration variiert wird, zeigen wir, dass die Klasse von topologisch nicht-trivialen Materialien weiter in direkte und indirekte TIs unterteilt werden kann. Für direkte TIs mit p-Ladungsträgerdichten, zeigen wir, dass die Anheftung des chemischen Potentials an den Kamelrücken zu einem Beginn von QH-Plateaus bei ungewöhnlich kleinen Magnetfeldern (zweistelliger mT-Bereich) führen kann. Im Gegensatz dazu verhindert der Kamelrücken bei indirekten TIs die Beobachtung von QH Plateaus im p-Bereich bis zu großen Magnetfeldern (einige Tesla). Diese Ergebnisse erlauben es uns jüngste experimentelle Beobachtungen in (Hg,Mn)Te Quantentrögen der Existenz des Kamelrückens zuzuschreiben. Obwohl sich unsere Diskussion dabei auf (Hg,Mn)Te beschränkt, sollte sich unser Modell leicht auch auf andere topologische Materialien mit einer kamelartigen Struktur im Valenzband übertragen lassen.

Zusätzlich haben wir die numerische Implementierung des 8×8 Kane Modells verwendet, um den Übergang von einer 2D QSH zu einer 3D TI Phase in verspannten HgTe Quantentrögen zu untersuchen. Diese Halbleitermaterialien zeichnen sich durch 2D topologische Oberflächenzustände an Grenzflächen aus, welche, wie wir zeigen, sehr sensitiv für die lokale Kristallsymmetrie des Gitters und elektrostatische Ladung sind. Wir bestimmen die klassische Zyklotronfrequenz der Oberflächenelektronen und vergleichen diese mit experimentellen Messungen an verspannten HgTe Qunatentrögen.

Contents

Acronyms iii

Introduction 1

1. Introduction to Topological Matter and Topological Field Theories 5
1.1. Topological matter . . . 6
1.1.1. Topological Classification and Bulk-Boundary Correspondence . 7
1.1.2. Discrete symmetries . . . 9
1.1.3. Chern insulator . . . 11
1.1.4. Symmetries in the presence of an external magnetic field . . . 18
1.2. Landauer-Büttiker formalism . . . 19
1.3. The quantum Hall family . . . 21
1.3.1. Quantum Hall insulator . . . 21
1.3.2. Quantum spin Hall insulator . . . 25
1.3.3. Quantum anomalous Hall insulator . . . 31
1.4. Chiral anomaly and fermion number fractionalization in (1+1)D . . . 33
1.4.1. Dirac equation in (1+1)D . . . 34
1.4.2. Chiral (axial) anomaly . . . 35
1.4.3. Fermion number fractionalization . . . 38
1.5. Topological field theory . . . 41
1.5.1. Chern-Simons theory . . . 41
1.5.2. Anomaly inflow and bulk-boundary correspondence . . . 43
1.6. Parity anomaly . . . 46
1.6.1. Dirac equation in (2+1)D . . . 46
1.6.2. Violation of parity symmetry in (2+1)D . . . 47

2. Fate of QAH Effect in Magnetic Fields: The Parity Anomaly 51
2.1. Introduction and model . . . 53
2.1.1. Chern insulator on the lattice - numerical approach: . . . 57
2.2. Bulk particle number and spectral asymmetry in magnetic fields . . . 59
2.2.1. With particle-hole symmetry . . . 59
2.2.2. Without particle-hole symmetry . . . 64
2.3. Magnetotransport - signatures of parity anomaly . . . 67
2.4. Effective field theory . . . 71
2.5. Charge pumping . . . 73
2.5.1. Numerical approach . . . 73
2.5.2. Transport signature at constant density . . . 77
2.6. Coexistent QH and QAH edge states . . . 78
2.6.1. Transport in the Dirac mass gap - edge perspective . . . 79
2.6.2. Role of broken particle-hole symmetry . . . 82
2.6.3. Transport of coexistent QH and QAH edge states . . . 86
2.7. Signatures of parity anomaly in para- and ferromagnetic TIs . . . 90

2.8. Summary 95

3. Emergent QH Effect in 2D Topological Insulators 97
3.1. Narrow gap or inverted gap semiconductors - The Kane model 100
3.1.1. The 8-band Kane model 100
3.1.2. Bulk inversion asymmetry 103
3.1.3. Pikus-Bir-Hamiltonian 103
3.2. Finite-difference-method 104
3.2.1. BenDaniel–Duke boundary condition 108
3.3. External magnetic field and magnetization in the Kane model 109
3.3.1. Orbital effect of out-of-plane magnetic field 110
3.3.2. Zeeman interaction 111
3.3.3. Exchange interaction 113
3.3.4. Bulk inversion asymmetry 115
3.4. Band structure of (Hg,Mn)Te 116
3.4.1. Experimental characterization of (Hg,Mn)Te quantum wells . . . 118
3.5. Emergent QH effect in the bulk p-regime 121
3.5.1. Toy model 121
3.5.2. Direct gap topological insulators 122
3.5.3. Indirect gap topological insulators 128
3.6. Emergent QH effect in QSH regime 129
3.7. Summary and Discussion 131

4. Manipulating surface states of 3D topological insulators 133
4.1. 2D to 3D crossover 135
4.2. Manipulating topological surface states 138
4.2.1. HH–LH coupling at interfaces 138
4.2.2. Gating of topological surface states 140
4.3. Summary 142

5. Conclusion and Outlook 143

Appendices 147

A. Kane parameters for various compound semiconductors 149
A.1. Kane parameters for (Hg,Cd)Te 149
A.2. Kane parameters for (Hg,Mn)Te 150
A.3. Strain parameters 151

B. Limitations and extensions of Bernevig-Hughes-Zhang model 152

Bibliography 155

Publications 166

Acknowledgements 167

Acronyms

QH quantum Hall

QAH quantum anomalous Hall

QSH quantum spin Hall

TI topological insulator

LL Landau level

BHZ Bernevig-Hughes-Zhang

2D two-dimensional

3D three-dimensional

PH particle-hole

TR time-reversal

QED quantum electrodynamics

FDM finite-difference-method

BIA bulk inversion asymmetry

DOS density of states

TSS topological surface states

ARPES angle-resolved photoemission spectroscopy

Introduction

The technological progress of the last century was closely linked to advances in solid state physics. Especially, the last 50 years have been characterized by an almost exponential technological progress. This is best illustrated by Moore's law. It shows that the number of transistor on a microprocessor chip doubles every two years [1]. From today's perspective, it is therefore sometimes hard to imagine that the light bulb was only invented 150 years ago. As miniaturization of electric circuits has become increasingly difficult, technological progress is now close to reach a limit. Nevertheless, recent developments in condensed matter physics, such as spintronics, quantum computing, or graphene-based electronics [2, 3], give hope of finding new avenues for technological progress.

The hunt for novel materials plays, due to their variety of possible applications, a decisive role in condensed matter physics. For that reason, in 2016, David J. Thouless, F. Duncan M. Haldane, and J. Michael Kosterlitz have been awarded the Nobel Prize in physics. Way ahead of their time in the 1970s and 1980s, they explored the role of topological concepts in understanding the behavior of electrons in exotic states of matter [4–8]. Topology itself is a branch of mathematics. It deals with classifying geometrical objects in terms of their properties which do not change under continuous deformations (stretching, bending, etc.). Such properties are referred to as topological invariants. For instance, an orange is equivalent to a banana from a topological point of view as both objects possess the same number of holes. But what has this abstract concept to do with condensed matter physics?

It was Klaus von Klitzing who discovered in 1980 that the Hall conductivity of a two-dimensional (2D) electron gas is quantized in units of e^2/h when it is subjected to an external magnetic field [9]. The observed quantization was thereby so precise and basically independent of the material details, that it had to be based on a fundamental concept. Indeed, D. J. Thouless realized that the so-called quantum Hall (QH) effect owes its remarkable precision to topological effects [5]. While the bulk band structure forms Landau levels (LLs) and becomes insulating by applying an external magnetic field, the current is governed by metallic unidirectionally propagating (chiral) edge channels at the material's boundary. Similar to geometrical objects that can only possess an integer number of holes, the number of chiral edge channels in the QH

phase can only change in integer steps. It is a topological invariant. This discovery constituted in the 1980s a new paradigm in condensed matter physics, as it paved the way to classify quantum states based on topological concepts [10–12].

However, despite this seminal breakthrough, it took another three decades before topology finally became one of the central topics in condensed matter physics. In 2007, HgTe/(Hg,Cd)Te quantum wells became the first-ever 2D topological insulator (TI) [a] which was experimentally realized [15–17]. This 2D TI is characterized by a novel topological state, the quantum spin Hall (QSH) state, in which time-reversal (TR) symmetry protects the topological invariant[10, 14]. The nontrivial topology is thereby connected to an intrinsically inverted band structure [b] and comes along with a pair of counterpropagating (helical) edge states which traverse the otherwise insulating bulk gap. These helical edge states are of great interest for potential spintronic applications as they are spin polarized and protected from backscattering due to TR symmetry. In contrast to the QH effect, topological edge states can therefore exist in the QSH phase even in the absence of a magnetic field.

While at that time it was common belief that topological states of matter are rather exotic, we now know that more than a quarter of all materials in nature are topological [18]. This includes TIs in two and three dimensions [12, 19–29], topological semimetals like Dirac and Weyl semimetals [30–35], and topological superconductors [12, 36]. Some materials, like HgTe or Bi-compounds, can be even tuned into various topological phases by band structure engineering. This means changing the quantum well thickness, applying strain to the crystal structure, or changing the material composition by alloying it with magnetic or non-magnetic atoms. Just to name some possibilities, thin layers of HgTe with a quantum well thickness $d_{QW} > 6.3\,\mathrm{nm}$ are 2D TIs [15, 16], while applying tensile or compressive strain to bulk HgTe ($d_{QW} \gtrsim 40\,\mathrm{nm}$) leads to a three-dimensional (3D) TI [19, 28], or to a Dirac/Weyl semimetal [c] [35]. Furthermore and most relevant for this thesis is the diluted semiconductor (Hg,Mn)Te which was the first-ever predicted material to show the quantum anomalous Hall (QAH) effect [21]. This topological phase is characterized by chiral edge channels that can contrary to the QH phase exist even in the absence of an external magnetic field. This makes the QAH phase extremely interesting for potential low-energy applications.

The huge interest in topological materials is on the one hand fueled by the prospect of novel spintronic devices. On the other hand, from a more theoretical point of view, it

[a] Actually, the first theoretical prediction of a 2D TI goes back to C. L. Kane and E. J. Mele in 2005 [13, 14]. They showed that graphene in the presence of spin-orbit interaction becomes a 2D TI. However, the required bulk band gap was to small to allow experimental verification.

[b] The band ordering of an inverted band structure is in reverse compared to the atomic limit. This means the typical conduction band is energetically below the valence band.

[c] If bulk inversion asymmetry (BIA) is neglected, compressively strained HgTe is a Dirac semimetal. Including the effect of BIA leads then to a transition to a Weyl semimetal phase. However, this effect is so small in HgTe that it is hard to be experimentally verified.

is most remarkable that the effective low-energy theories of topological states resemble at a formal level the Dirac equation. Weyl semimetals, for instance, owe their name to Weyl fermions, which are solutions of the Dirac equation at zero mass. This implies that predictions, originally made in the context of particle physics, can be tested in conventional solid state laboratories. Moreover, these formal similarities allow us to analyze solid state systems using some of the tools that were originally developed in high energy physics. For that reason, much effort has been spent in recent years to identify condensed matter analogs of quantum anomalies [8, 37–41]. Roughly speaking, a quantum anomaly describes the fact that certain classical symmetries cannot be elevated onto the level of a quantum theory [a]. In condensed matter physics, such anomalies are of interest because they are tied to distinct, experimental signatures. A negative magnetoresistance arises, for instance, because of the axial-anomaly in Weyl semimetals [30]. Quantum anomalies are also a powerful tool to test effective theories for consistency. For instance, this concept can be used to prove that chiral edge channels must accompany the QH effect [42], or that Weyl fermions always come in pairs (Nielsen-Ninomiya theorem) [43, 44].

About this thesis: Exposing a topological material to an external magnetic field causes on top of the preexisting topological state [b] the formation of LLs. One of the main topics in this thesis is to trace and to identify hallmarks of these preexisting topological states even in the presence of LLs. In this context, we are mainly concerned with characteristic transport signatures of 2D topological phases which we describe by effective Hamiltonians or topological field theories. In particular, we clarify their relation to quantum anomalies. Furthermore, we investigate various HgTe quantum wells using band structure engineering, i.e., we analyze their topological properties varying the quantum well thickness, the material composition, as well as the strain.

We start in Ch. 1 by introducing a few theoretical concepts that are mandatory to follow the remainder of this thesis. The scientific results are then presented in the subsequent Chs. 2–4. In this regard, Ch. 2 deals with magnetically doped 2D TIs, like (Hg,Mn)Te quantum wells [c], that exhibit the QAH effect. We clarify that QAH insulators are condensed matter analogs of the so-called parity anomaly. The latter is usually known to characterize quantum electrodynamics (QED) in $d = 2 + 1$ spacetime dimensions [d]. The relation to the parity anomaly allows us to show that QAH and QH phases can coexist and can be experimentally distinguished in magnetic fields, even though they are both described by the same topological invariant. In Ch. 3, we use the

[a] Quantum anomalies arise in Dirac-like theories due to their infinite degrees of freedom (Dirac sea). A more detailed discussion on this subject is presented in Section 1.5.

[b] Preexisting topology refers to topological effects which are already present without a magnetic field.

[c] Actually, (Hg,Mn)Te is a paramagnetic TI so that a magnetic field is needed to drive the system from the QSH to the QAH phase. We comment on this in detail in Chapter 2.

[d] The notation, 2D and 3D, refers always to spatial dimensions. Spacetime dimensions (spatial dimensions plus one time dimension) are always denoted by, e.g., (2+1)D.

8×8 Kane model [45] to show that virtually all 2D TIs and, in particular, (Hg,Mn)Te quantum wells possess additional maxima at large momenta. These maxima, which are a byproduct of the inverted band structure, are not captured by low-energy effective models, which are typically used to describe topological effects that occur in the vicinity of high symmetry points in the Brillouin zone. We demonstrate that these additional maxima pin the chemical potential and can as result cause QH plateaus at ultra-low magnetic fields (tens of mT). While Ch. 3 focuses on thin HgTe quantum wells which exhibit the QSH or the QAH phase, we study in Ch. 4 the crossover to the 3D TI phase by increasing the thickness of the quantum well. Various ways to manipulate the topological 2D surface states are discussed and their properties are compared with the experiment. In Ch. 5, we summarize the scientific results and present some novel ideas for future research projects.

All results presented in Chs. 2–4 are largely based on Refs. [P3, P4, P5, P6, P7] which have been restructured and reorganized for this thesis. However, as we will make clear throughout this work, we partially adapt some of their content word by word.

Remarks on mathematical notation: We mainly utilize standard time-independent Hamiltonian approaches, with which the majority of condensed matter physicists seem to be rather familiar. Nevertheless, whenever it is necessary, we make use of the relativistic notation. Therein, we use the metric tensor in the west-coast convention, which in (2+1)D (two space + one time dimension) means, for instance, that the metric reads $g^{\mu\nu} = \mathrm{Diag}\,(1\,,\,-1\,,\,-1)$. Greek indices run over both the time and the spatial components [a]. For instance, an arbitrary relativistic three vector in (2+1)D is denoted by a^μ with $\mu = 0, 1, 2$. In contrast, Latin letters run only over the spatial components, e.g., $j = 1, 2$ for a given 2D space (2D refers only to spatial components). Bold symbols mark spatial vectors, for instance, $\mathbf{x} = (x, y)^T$. It is assumed that the reader is familiar with the Einstein summation convention, meaning that the occurrence of repeated indices indicate summation:

$$a^\mu b_\mu = \sum_{\mu=0}^{2} a^\mu b_\mu. \tag{0.1}$$

[a] In Minkowski space, the 0th component is intended exclusively for the time.

1.

Introduction to Topological Matter and Topological Field Theories

Contents

1.1. Topological matter **6**
1.1.1. Topological Classification and Bulk-Boundary Correspondence 7
1.1.2. Discrete symmetries 9
1.1.3. Chern insulator 11
1.1.4. Symmetries in the presence of an external magnetic field . . 18
1.2. Landauer-Büttiker formalism **19**
1.3. The quantum Hall family **21**
1.3.1. Quantum Hall insulator 21
1.3.2. Quantum spin Hall insulator 25
1.3.3. Quantum anomalous Hall insulator 31
1.4. Chiral anomaly and fermion number fractionalization in (1+1)D **33**
1.4.1. Dirac equation in (1+1)D 34
1.4.2. Chiral (axial) anomaly 35
1.4.3. Fermion number fractionalization 38
1.5. Topological field theory **41**
1.5.1. Chern-Simons theory 41
1.5.2. Anomaly inflow and bulk-boundary correspondence 43
1.6. Parity anomaly **46**
1.6.1. Dirac equation in (2+1)D 46
1.6.2. Violation of parity symmetry in (2+1)D 47

We establish in this chapter the broader mathematical scope on which this thesis is based on. Our journey starts in Sec. 1.1 by reviewing the topological classification of non-interacting, single-particle Hamiltonians in $d = 0, 1, 2$, and 3 dimensions. A 2D Chern insulator serves thereby as an exemplary system to familiarize the reader with the key concepts. Subsequently in Sec. 1.2, we discuss the Landauer-Büttiker formalism which describes edge dominated transport in the phase coherent regime. Section 1.3 discusses various topological states in 2D more in detail including the QH, the QSH, and the QAH effect, which are at the center of this thesis. We outline their key ingredients, discuss their experimental realization, and integrate them into the topological classification scheme. Following, in Sec. 1.4, we turn our attention to (1+1)D Dirac theories which govern the properties of chiral edge channels at low energies. We explain the effect of fermion number fractionalization and discuss the first example of a quantum anomaly. Starting with Sec. 1.5, we show how 2D topological states, such as the QH phase, can be described by effective topological field theories, or to be more precise by a Chern-Simons field theory. This sheds further light on the topological interpretation of the QH family. Finally, Sec. 1.6 reviews the properties of the Dirac equation in (2+1)D. In particular, it is shown that an odd number of Dirac fermions must violate parity symmetry in a quantum theory. This unique property, known as parity anomaly, is characteristic for odd dimensional spacetimes. Its understanding will be essential to follow the discussion in Ch. 2.

While the underlying idea of this chapter is to outline the most important theoretical concepts that are necessary for this thesis, I cannot cover here the enormous field of topological matter and topological field theories completely. For this purpose, I would like to refer the interested reader to existing reviews on topological insulators and topological classification [11, 12, 30, 46–48]. For a more in-depth discussion on topological field theories, we suggest Refs. [49–53].

1.1. Topological matter

This section reviews the topological classification of insulators [a] in the ten symmetry classes introduced by Altland and Zirnbauer [54, 55]. The connection between topological invariants and experimental signatures is explained. In Sec. 1.1.1, we discuss the periodic table of noninteracting topological states of matter. This classification is based on discrete symmetries whose physical meaning is explained in Sec. 1.1.2. Symmetry conditions for arbitrary single particle Hamiltonians are derived. This introduction follows thereby closely along the lines of Refs. [10] and [11]. In Sec. 1.1.3, a Chern insulator serves as an example to explain the important role of topology. Finally, in Sec. 1.1.4,

[a] The discussed classification is also applicable for topological superconductors. However, since this thesis deals exclusively with TIs, we do not comment explicitly about them.

the symmetry considerations are generalized to include also external fields.

1.1.1. Topological Classification and Bulk-Boundary Correspondence

We have already mentioned some examples of topological states in the introduction. It would be however desirable to have a universal classification scheme for topological states of matter, basically, some kind of 'periodic table' [56]. In the following, we review the classification of noninteracting systems which are characterized by an insulating bulk [10]. Further information on classifying interacting topological insulators or topological semimetals can be found, for instance, in Ref. [11].

The periodic table of topological states of matter can be developed in two steps. In the first step, arbitrary Hamiltonians are classified into ten different symmetry classes based on the three generic (discrete) symmetries, namely, TR, particle-hole (PH), and chiral symmetry. We denote the associated single-particle symmetry operators by T, C, and S, respectively. An overview is presented in Tab. 1.1. The subdivision into different symmetry classes arises as follows. First of all, each discrete symmetry may or may not be present. The absence of a symmetry is indicated in Tab. 1.1 by 0. Secondly, if a discrete symmetry is present, the square of its corresponding single-particle operator can take the following values

$$T^2 = \pm 1\,, \qquad C^2 = \pm 1\,, \quad \text{and} \quad S^2 = +1\,. \tag{1.1}$$

In total, there are ten different combinations and, hence, ten different symmetry classes [54, 55].

In the second step, a topological invariant can be assigned to a noninteracting Hamiltonian in each symmetry class for every dimension. A topological invariant is a quantity which is invariant under continuous deformations (homeomorphisms) of its associated Hamiltonian, which do not close its bulk gap and which preserve all its discrete symmetries. Two Hamiltonians are topologically equivalent if they are described by the same topological invariant. Based on this concept, Schnyder et al. [10] showed that noninteracting quantum states can be classified by $\mathbb{Z}$, $2\mathbb{Z}$, or $\mathbb{Z}_2$ topological invariants, as shown in Tab. 1.1. Here, $\mathbb{Z}$ refers to all integers, $2\mathbb{Z}$ to all even integers, and $\mathbb{Z}_2$ can take two values, 0 or 1. Note however that topological invariants cannot be defined for each symmetry class in every dimension.

An important signature of topological materials is the one-to-one correspondence between their nontrivial bulk topology and gapless, metallic states which can be located at their interfaces. To understand this concept, suppose that two insulators which are characterized by a different bulk topology are stacked next to each other. The

class	T	C	S	0	1	2	3
A	0	0	0	$\mathbb{Z}$	0	$\mathbb{Z}$	0
AIII	0	0	+	0	$\mathbb{Z}$	0	$\mathbb{Z}$
AI	+	0	0	$\mathbb{Z}$	0	0	0
BDI	+	+	+	$\mathbb{Z}_2$	$\mathbb{Z}$	0	0
D	0	+	0	$\mathbb{Z}_2$	$\mathbb{Z}_2$	$\mathbb{Z}$	0
DIII	-	+	+	0	$\mathbb{Z}_2$	$\mathbb{Z}_2$	$\mathbb{Z}$
AII	-	0	0	2 $\mathbb{Z}$	0	$\mathbb{Z}_2$	$\mathbb{Z}_2$
CII	-	-	+	0	$2\mathbb{Z}$	0	$\mathbb{Z}_2$
C	0	-	0	0	0	$2\mathbb{Z}$	0
CI	+	-	+	0	0	0	2 $\mathbb{Z}$

Table 1.1.: Periodic table of topological insulators in $d = 0, 1, 2$ and 3 space dimensions. There are ten different symmetry classes for gapped single-particle Hamiltonians which can be distinguished based on the three discrete symmetries: time-reversal (T), particle-hole (C) and chiral (S) symmetry. A '0' denotes the absence of a symmetry, while '±' imply whether the single-particle symmetry operator squares to ±1. The topological classes which are highlighted by color are subject of this thesis. From Ref. [10]. Adapted with permission from APS.

topological invariant changes therefore across their common interface. However, as a topological invariant can only change if the bulk band gap closes, metallic states must arise in the bulk gap which are located at this interface [a]. The relation between these metallic edge (or surface) states and the bulk topology is commonly referred to as the bulk-boundary correspondence [12].

At the center of this thesis are the symmetry classes A, D, AII, and DIII in 2D, as well as the symmetry class AII in 3D. We highlighted these cases in Tab. 1.1. The symmetry classes A and D in 2D are both linked to a $\mathbb{Z}$ topological invariant, the so-called Chern number, which is characterized by chiral edge channels at the boundary to a topologically trivial insulator. Typical examples are QH and QAH insulators which are described in more detail in Sec. 1.3. The symmetry classes DIII and AII are both connected to a $\mathbb{Z}_2$ topological invariant and describe QSH insulators, which are discussed in Sec. 1.3. Their hallmark is a pair of counterpropagating (helical) edge channels which are protected from backscattering by TR symmetry. The symmetry class AII in 3D describes 3D TIs and is characterized by metallic surface states which exhibit spin-momentum locking.

Before, we shed more light on the topological properties of these materials, we want to briefly discuss the physical meaning of TR, PH, and chiral symmetry. This list is

[a] We give a more sophisticated proof of the bulk-boundary correspondence in Section 1.5.

complemented by parity symmetry which is not mandatory for the topological classification, but which will play an important role in the context of Dirac-like systems in two spatial dimension (cf. Sec. 1.6).

1.1.2. Discrete symmetries

Our considerations start with a general noninteracting, manyparticle Hamiltonian in second quantization, which is denoted by

$$\mathcal{H} = \int d\mathbf{x}\, \Psi^\dagger(\mathbf{x}) H(\mathbf{k})\, \Psi(\mathbf{x})\,, \tag{1.2}$$

where $\Psi(\mathbf{x})$ is a fermionic field operator which fulfills the conventional anticommutation relation $\{\psi(\mathbf{x}), \psi^\dagger(\mathbf{x}')\} = \delta(\mathbf{x} - \mathbf{x}')$, and $H(\mathbf{k})$ is the corresponding single-particle Hamiltonian. External fields will not be considered until Sec. 1.1.4.

There are two types of symmetry transformations. Those which are described by a linear and unitary operator, and those which are described by an antilinear and antiunitary operator [57] [a]. In contrast to unitary operators, antiunitary operators switch the sign of complex numbers. Regardless of whether a second quantized operator $\mathcal{O}$ is unitary or antiunitary, a system obeys a certain symmetry only if

$$[\mathcal{H}, \mathcal{O}] = 0\,, \tag{1.3}$$

where $\mathcal{H}$ denotes a general second quantized Hamiltonian as given by Eq. (1.2).

Time-Reversal Symmetry: A system exhibits TR symmetry, if it is invariant under reversing the arrow of time. As a result, TR symmetry changes the propagation direction of particles:

$$\mathcal{T} : (t, \mathbf{x}) \to (-t, \mathbf{x})\,, \quad \text{and} \qquad \mathcal{T} : \mathbf{k} \to -\mathbf{k}\,, \tag{1.4}$$

where $\mathcal{T}$ denotes the TR symmetry transformation. Time-reversal is an antiunitary operator and acts on a fermionic field operator as

$$\mathcal{T}\Psi(\mathbf{x})\mathcal{T}^{-1} = U_T \Psi(\mathbf{x})\,, \quad \text{and} \qquad \mathcal{T}\mathrm{i}\mathcal{T}^{-1} = -\mathrm{i}\,, \tag{1.5}$$

where U_T is a unitary matrix. Inserting this into Eq. (1.3) with $\mathcal{O} = \mathcal{T}$, we get

$$\begin{aligned} \mathcal{H} \overset{!}{=} \mathcal{T}\mathcal{H}\mathcal{T}^{-1} &= \int d\mathbf{x}\, \mathcal{T}\Psi^\dagger(\mathbf{x})\mathcal{T}^{-1}\mathcal{T} H(\mathbf{k})\, \mathcal{T}^{-1}\mathcal{T}\Psi(\mathbf{x})\mathcal{T}^{-1} \\ &= \int d\mathbf{x}\, \Psi^\dagger(\mathbf{x}) U_T^\dagger H^\star(-\mathbf{k})\, U_T \Psi(\mathbf{x})\,, \end{aligned} \tag{1.6}$$

[a] Suppose that a symmetry transformation sends a quantum state $|a\rangle \to |\tilde{a}\rangle$ and another state $|b\rangle \to |\tilde{b}\rangle$. Such a transformation is a symmetry if it conserves the norm $|\langle a|b\rangle| = \left|\langle \tilde{a}|\tilde{b}\rangle\right|$. This condition is fulfilled by the aforementioned two types of operators.

where the complex conjugation follows from the antiunitarity of the TR operator. Equation (1.6) is only fulfilled if the single-particle Hamiltonian $H(\mathbf{k})$ fulfills that

$$T^\dagger H(\mathbf{k}) T = H(-\mathbf{k}) \,, \tag{1.7}$$

where $T = U_T K$ is the single-particle operator and K is the operator of complex conjugation. Note that every eigenstate of a TR symmetric Hamiltonian is at least, double degenerated. This is known as Kramers theorem [48].

Particle-Hole Symmetry: A system exhibits PH symmetry, if it is invariant under exchanging all fermionic creation and annihilation operators. This means we exchange electrons and holes. In second quantization, a PH transformation $\mathcal{C}$ is a unitary transformation. It acts on a fermionic field operator in the following way:

$$\mathcal{C}\Psi(\mathbf{x})\mathcal{C}^{-1} = U_C^* \Psi^\dagger(\mathbf{x}) \,, \quad \text{and} \quad \mathcal{C}\mathrm{i}\mathcal{C}^{-1} = \mathrm{i} \,, \tag{1.8}$$

where U_C is a unitary matrix. Note that the right-hand side contains the adjoint spinor which is the defining property of the PH transformation. Inserting Eq. (1.8) into Eq. (1.3), we end up with the following condition for the single-particle Hamiltonian:

$$C^\dagger H(\mathbf{k}) C = -H(-\mathbf{k}) \,, \tag{1.9}$$

where $C = U_C K$. On single-particle level, a PH symmetry operator is therefore an antiunitary operator. This is in contrast from its definition in second quantizaton where it acts as a unitary operator [a]. We highlight this difference as it can sometimes cause confusion. Physically, we see that a PH transformation switches the sign of energy, and momentum. For every states with positive energy there must be one corresponding state with negative energy and opposite momentum.

Chiral Symmetry: A chiral symmetry transformation is defined as the combination of TR and PH symmetry, $\mathcal{S} = \mathcal{T} \cdot \mathcal{C}$. As such, it is an antiunitary operator in second quantization and acts on fermionic field operators as

$$\mathcal{S}\Psi(\mathbf{x})\mathcal{S}^{-1} = U_S \Psi^\dagger(\mathbf{x}) \,, \quad \text{and} \quad \mathcal{S}\mathrm{i}\mathcal{S}^{-1} = -\mathrm{i} \,, \tag{1.10}$$

where U_S is a unitary matrix. Based on this, we can derive a symmetry condition in first quantization

$$S^\dagger H(\mathbf{k}) S = -H(\mathbf{k}) \,, \tag{1.11}$$

[a] This difference arises because, during the derivation of Eq. (1.9), we have to anticommute once the fermionic spinor $\Psi(\mathbf{x})$ with its corresponding adjoint spinor $\Psi^\dagger(\mathbf{x})$

where $S = U_S$. A chiral symmetry operator is unitary (antiunitarity) on the level of first (second) quantization. In contrast, to a PH transformation, a chiral symmetry transformation reverses only the sign of energy.

Parity Symmetry: The last discrete symmetry, which we want to consider, is parity symmetry. A parity transformation creates basically a spatial mirror image of an object. This is equivalent to stating that a parity transformation flips the chirality. In contrast to a rotation, the determinant of its representation yields -1. In 3D, a parity transformation refers therefore to a transformation which flips all spatial components:

$$\mathbf{P} : (t, x, y, z) \to (t, -x, -y, -z)\,. \tag{1.12}$$

In 2D, the situation is different since flipping all components would be equivalent to a rotation (determinant +1). Hence, in a flat world, parity symmetry is defined by flipping only the x- or the y-component.

$$\mathcal{P}_x : (t, x, y) \to (t, -x, y) \qquad \text{or} \qquad \mathcal{P}_y : (t, x, y) \to (t, x, -y)\,. \tag{1.13}$$

For the sake of simplicity, let us focus now on $\mathcal{P}_x$ in 2D. A fermionic field operator transforms then under parity as

$$\mathcal{P}_x \Psi(x, y) \mathcal{P}_x^{-1} = U_P \Psi(-x, y)\,, \tag{1.14}$$

where U_P is a unitary matrix. A single-particle Hamiltonian obeys parity symmetry if it holds that:

$$P^\dagger H\left(k_x, k_y\right) P = H\left(-k_x, k_y\right)\,, \tag{1.15}$$

where $P = U_P$. We will see later on that for an odd number of Dirac fermions living in a flat, 2D quantum world, parity symmetry is under no circumstance an appropriate symmetry. This is known as parity anomaly. We study this is in detail in Section 1.6.

1.1.3. Chern insulator

We use a Chern insulator as an example to review topological effects in 2D. This example is picked since a Chern insulator is a fundamental building block of the low-energy Hamiltonians of QSH and QAH insulators [cf. Section 1.3]. As such, we employ many of the following concepts frequently again during the course of this thesis. The

corresponding Hamiltonian reads

$$h(\mathbf{k}) = \begin{pmatrix} M - (B+D)\,k^2 & Ak_+ \\ Ak_- & -M + (B-D)\,k^2 \end{pmatrix}, \tag{1.16}$$

where $k^2 = k_x^2 + k_y^2$, $k_\pm = k_x \pm \mathrm{i}k_y$, $k_x \to -\mathrm{i}\partial_x$, and $k_y \to -\mathrm{i}\partial_y$. Furthermore, M, B, D, and A are system parameters [a]. The spectrum is given by

$$E_\pm(\mathbf{k}) = -Dk^2 \pm \sqrt{A^2k^2 + (M - Bk^2)^2}, \tag{1.17}$$

where $\pm$ denotes solutions of the valence and conduction band, respectively. And the corresponding solutions of the Schrödinger equation are given by:

$$\begin{aligned} E_+(\mathbf{k}) \quad &: \quad u_\mathbf{k}(\mathbf{x}) = \begin{pmatrix} M - Bk^2 + \epsilon(\mathbf{k}) \\ Ak_- \end{pmatrix} \mathrm{e}^{\mathbf{ikx}}, \\ E_-(\mathbf{k}) \quad &: \quad v_\mathbf{k}(\mathbf{x}) = \begin{pmatrix} M - Bk^2 - \epsilon(\mathbf{k}) \\ Ak_- \end{pmatrix} \mathrm{e}^{\mathbf{ikx}}. \end{aligned} \tag{1.18}$$

For $B = D = 0$, a Chern insulator matches the 2D Dirac Hamiltonian [b], for which the speed of light is renormalized by the parameter A. Due to this formal similarity, we refer to the parameter M as the Dirac mass. For $M \neq 0$, the system is a bulk insulator with an energy gap of $2M$ at $(k_x, k_y) = (0, 0)$ (the Γ point). The parameter B acts as an additional, momentum dependent mass term and the parameter D introduces an asymmetry between the effective masses of conduction and valence band.

Let us now classify the Hamiltonian of a Chern insulator in relation to the periodic table, Tab. 1.1. The single particle Hamiltonian, Eq. (1.16), obeys TR, PH, chiral, and parity symmetry only if $M = B = D = 0$. In this case, we find that the unitary part of the single-particle symmetry operators are determined by [cf. Eqs. (1.7), (1.9),(1.11), and (1.15)]

$$U_T = -\mathrm{i}\sigma_y \quad , \quad U_C = \sigma_x \quad , \quad U_S = \sigma_z \quad , \text{and} \quad U_P = \sigma_y\,. \tag{1.19}$$

Introducing either the Dirac mass M or the non-relativistic mass B breaks TR, parity, and chiral symmetry. A non-zero D parameter breaks PH and chiral symmetry. In the generic case, where all parameters are nonzero, a Chern insulator falls therefore into the symmetry class A and is described by a $\mathbb{Z}$ topological invariant.

We will now explicitly show that the $\mathbb{Z}$ topological invariant is related to the Hall conductivity σ_{xy} and is hence experimentally accessible. To this end, we follow Ref. [58]

[a] We require that $|D| < |B|$. This ensures that the system is an insulator for $M \neq 0$.

[b] The similarities between a 2D Dirac Hamiltonian and a Chern insulator are discussed more in detail in Sec 1.6.1.

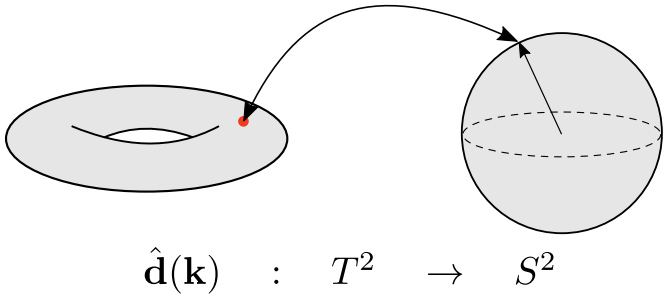

Figure 1.1.: The vector $\hat{\mathbf{d}}(\mathbf{k})$ describes a mapping from the compact Brillouin zone T^2 to the unit sphere S^2. The (integer) number of times, that the image of $\hat{\mathbf{d}}(\mathbf{k})$ covers the surface of the unit sphere, defines the winding number.

and assume that the chemical potential is placed in the bulk gap so that only the valence band is filled in the ground state. Although the system is a bulk insulator, it turns out that σ_{xy} can be nonzero due to topological effects. To show this, we impose periodic boundary conditions in the x- and y-direction:

$$\psi(x + L_x, y) = \psi(x, y) \quad \text{and} \quad \psi(x, y + L_y) = \psi(x, y)\,. \tag{1.20}$$

This compactifies the Brillouin zone by turning it into a torus, as seen in Fig. 1.1. The Hall conductivity can be now computed using the Kubo formula [48]:

$$\sigma_{xy} = -\frac{e^2}{\hbar} \int\limits_{BZ} \frac{d\mathbf{k}}{(2\pi)^2}\, \Omega_z^-(\mathbf{k})\,, \tag{1.21}$$

where $\Omega_z^-(\mathbf{k}) = \mathrm{i}\left(\boldsymbol{\nabla}_\mathbf{k} \times \langle v(\mathbf{k})|\boldsymbol{\nabla}_\mathbf{k}|v(\mathbf{k})\rangle\right)_z$ is the z-component of the Berry curvature. The minus sign in the superscript indicates that only the filled valence band can contribute to the total Hall conductivity. Qi et al. [58] showed that in the case of a Chern insulator Eq. (1.21) can be recast in the following way,

$$\sigma_{xy} = -\frac{e^2}{h} \frac{1}{4\pi} \int\limits_{BZ} d\mathbf{k}\, \hat{\mathbf{d}}(\mathbf{k}) \cdot \left(\partial_x \hat{\mathbf{d}}(\mathbf{k}) \times \partial_y \hat{\mathbf{d}}(\mathbf{k})\right)\,, \tag{1.22}$$

where $\hat{\mathbf{d}}(\mathbf{k}) = \mathbf{d}(\mathbf{k})/\left|\mathbf{d}(\mathbf{k})\right|$ is the normalized $\mathbf{d}$ vector. In this form, the topological nature of the Hall conductivity is most apparent. The vector $\hat{\mathbf{d}}(\mathbf{k})$ acts as a mapping from the compact Brillouin zone T^2 to the unit sphere S^2, as illustrated in Fig. 1.1 [a]. The integrand in Eq. (1.22) is the Jacobian of this mapping so that the integral yields $4\pi\nu$, where 4π is the surface area of the unit sphere and ν counts the number of times the $\hat{\mathbf{d}}(\mathbf{k})$ vector covers the surface of the sphere [58]. Since the base space (the torus) is compact, the surface of the sphere can only be covered an integer number of times

[a] The Brillouin zone forms a torus due to the periodic boundary conditions in x- and y-direction. The mapping $\hat{\mathbf{d}}(\mathbf{k}) : T^2 \rightarrow S^2$ is described by the homotopy class $\pi_2(S^2) = \mathbb{Z}$, i.e., by a $\mathbb{Z}$ topological invariant.

resulting in $\nu \in \mathbb{Z}$. The Hall conductivity yields therefore $\sigma_{xy} = \nu e^2/h$. The quantity ν is a so-called winding or Chern number. It is a $\mathbb{Z}$ topological invariant as it can only change in integer steps. This result clearly agrees with our symmetry considerations and demonstrates that the $\mathbb{Z}$ classification is experimentally accessible.

Let us now calculate the winding number of a Chern insulator explicitly by inserting the wave function, given by Eq. (1.18) into the Kubo formula [Eq. (1.21)]. It follows that [59]:

$$\begin{aligned}\sigma_{xy} = \frac{e^2}{2h}\int_0^\infty d(k^2)\,\frac{A^2\left(M+Bk^2\right)}{2\left[A^2k^2+\left(M-Bk^2\right)^2\right]^{\frac{3}{2}}} \\ = \frac{e^2}{2h}\left[\mathrm{sgn}\left(M\right)+\mathrm{sgn}\left(B\right)\right]\,,\end{aligned} \tag{1.23}$$

where we used that $d(k^2) = 2kdk$. We have hence found an explicit expression for the winding (Chern) number:

$$\nu = \frac{1}{2}\left[\mathrm{sgn}\left(M\right)+\mathrm{sgn}\left(B\right)\right]\,. \tag{1.24}$$

If $M/B < 0$, the Hall conductivity vanishes as $\nu = 0$. The system is topologically trivial and the associated band ordering is called normal. If the Dirac mass M is continuously varied, the band gap closes for $M = 0$ at the Γ point. This marks a topological phase transition since $\sigma_{xy} = \pm e^2/h$ for $M/B > 0$. Since the band ordering gets reversed during the topological transition, one speaks then of an inverted band structure.

Lattice approach: Within the scope of this thesis, we will frequently map continuum Hamiltonians on a finite lattice (numerical grid) with the size L_x in the x-direction and L_y in the y-direction. This allows us to study the properties of the associated edge states. The mapping procedure is performed by replacing the partial derivatives in Eq. (1.16) by the discrete (central) finite-difference-method (FDM) [a] , i.e.,

$$-\mathrm{i}\partial_x\psi(x,y) = -\mathrm{i}\frac{\psi(x+a,y)-\psi(x-a,y)}{2a}\,, \tag{1.26}$$

$$-\partial_x^2\psi(x,y) = -\frac{\psi(x+a,y)+\psi(x-a,y)-2\psi(x,y)}{a^2}\,, \tag{1.27}$$

where a is the lattice constant (grid spacing). The replacement for the y-direction is performed analogously. The resulting lattice Hamiltonian looks very similar to a

[a] We choose the central FDM as it is superior compared to the forward FDM, which is given by

$$-\mathrm{i}\partial_x\psi(x,y) = -\mathrm{i}\frac{\psi(x+a,y)-\psi(x,y)}{a}\,. \tag{1.25}$$

The forward FDM has two disadvantages. First of all, the truncation error is $\mathcal{O}(a)$, while it is only $\mathcal{O}(a^2)$ in the central method. Secondly, the central FDM yields a Hermitian matrix and, therefore, real eigenvalues. The truncation error in the forward FDM can also become imaginary which is unphysical.

tight-binding Hamiltonian, which is why this method is sometimes also known as tight-binding method. However, note that the similarities between these two approaches are only of formal nature, as the underlying lattice in Eqs. (1.26) and (1.27) is not related to the real crystal lattice.

To understand the implications of this approach, let us first study the bulk properties by imposing periodic boundary conditions in the x- and y-direction. The discrete translational symmetry of the cubic lattice implies in addition that $\psi(x+a,y) = \exp(\mathrm{i}k_x a)\psi(x,y)$ and $\psi(x,y+a) = \exp(\mathrm{i}k_y a)\psi(x,y)$. These identities can be used to simplify Eqs. (1.26) and (1.27) considerably:

$$-\mathrm{i}\partial_x\psi(x,y) = \frac{\sin(k_x a)}{a}\psi(x,y)\,, \tag{1.28}$$

$$-\partial_x^2\psi(x,y) = \frac{2-2\cos(k_x a)}{a^2}\psi(x,y)\,, \tag{1.29}$$

The same procedure must be repeated for the derivatives in the y-direction. The lattice version of a Chern insulator with periodic boundary conditions is therefore given by

$$h(\mathbf{k}) = \sigma_0\epsilon(\mathbf{k}) + \boldsymbol{\sigma}\cdot\mathbf{d}(\mathbf{k}) \quad , \quad \mathbf{d}(\mathbf{k}) = \begin{pmatrix} A\sin(k_x) \\ -A\sin(k_y) \\ M - B\left[4-2\cos(k_x)-2\cos(k_y)\right] \end{pmatrix}, \tag{1.30}$$

where $\epsilon(\mathbf{k}) = -D\left[4-2\cos(k_x)-2\cos(k_y)\right]$, and we set $a=1$. The corresponding Schrödinger equation has two solutions $h(\mathbf{k})\left|u_\pm(\mathbf{k})\right\rangle = E_\pm(\mathbf{k})\left|u_\pm(\mathbf{k})\right\rangle$, where

$$\begin{aligned} E_\pm = &-D\left(4-2\cos(k_x)-2\cos(k_y)\right) \\ &\pm\sqrt{A\left(\sin(k_x)^2+\sin(k_y)^2\right)+\left[M-B\left(4-2\cos(k_x)-2\cos(k_y)\right)\right]^2}\,. \end{aligned} \tag{1.31}$$

This shows that, regardless of the system parameters, the Hamiltonian, (1.30), is gapped in the full Brillouin zone except for the four high symmetry points meaning at $(k_x,k_y) = (0,0)$, $(\pi,0)$, $(0,\pi)$, and (π,π) for which $d_x = d_y = 0$. At these points, the bulk energy gap closes if

$$d_z = M - B\left[4-2\cos(k_x)-2\cos(k_y)\right] \stackrel{!}{=} 0\,. \tag{1.32}$$

The gap closing depends therefore on the exact values of M and B. Since a topological invariant can only change if a band gap closing occurs, the Hall conductivity of the full lattice model can be written as the sum of the individual contributions at each high

symmetry point [48]:

$$\sigma_{xy} = \sum_{i=0}^{3} \sigma_{xy}^{(i)} \,, \tag{1.33}$$

where $\sigma_{xy}^{(i)}$ denotes the contribution at the ith high symmetry point. The total expression of the Hall conductivity on a cubic lattice is hence given by

$$\begin{aligned} \sigma_{xy} = &\frac{e^2}{2h} \left[\mathrm{sgn}\,(M) + \mathrm{sgn}\,(B)\right] - 2\frac{e^2}{2h} \left[\mathrm{sgn}\,(M - 4B) + \mathrm{sgn}\,(B)\right] \\ &+ \frac{e^2}{2h} \left[\mathrm{sgn}\,(M - 8B) + \mathrm{sgn}\,(B)\right] \,, \end{aligned} \tag{1.34}$$

where the first term ($\sigma_{xy}^{(0)}$) is related to the Chern number at the Γ point and matches the result of our original, continuum model [cf. Eq. (1.16)]. The second and third term in Eq. (1.34) originate from the additional contributions from the other high symmetry points. They are as such a result of the numerical approach and have to be considered as artifacts. This issue is also known as fermion doubling [60]. To avoid any of these spurious solutions, we must restrict the scope of the FDM to the parameter regime

$$|M| < |4B| \,. \tag{1.35}$$

In the course of this thesis, we will often compare results for the continuum model with associated lattice models. This comparison is only valid if Eq. (1.35) is fulfilled.

Bulk-Boundary correspondence: So far, periodic boundary conditions have been imposed to analyze the bulk topological properties of a Chern insulator on the lattice. Now, we keep the periodic boundary conditions in the x-direction, but impose hard wall boundary conditions in the y-direction:

$$\psi(x, y = \pm L_y/2) = 0 \,. \tag{1.36}$$

We refer to this case as strip geometry. The ansatz for solving the Schrödinger equation with the FDM reads therefore $\psi(x, y) = \exp(\mathrm{i}k_x x)\psi_j$, where the abbreviation $\psi(y = ja) = \psi_j$ was introduced and $j \in \mathbb{Z}$ denotes the jth lattice point in the y-direction. Making use of Eqs. (1.26) and (1.27), the lattice Hamiltonian can be written as:

$$\sum_j H_{i,j}(k_x)\psi_j = E_i(k_x)\psi_i \,, \tag{1.37}$$

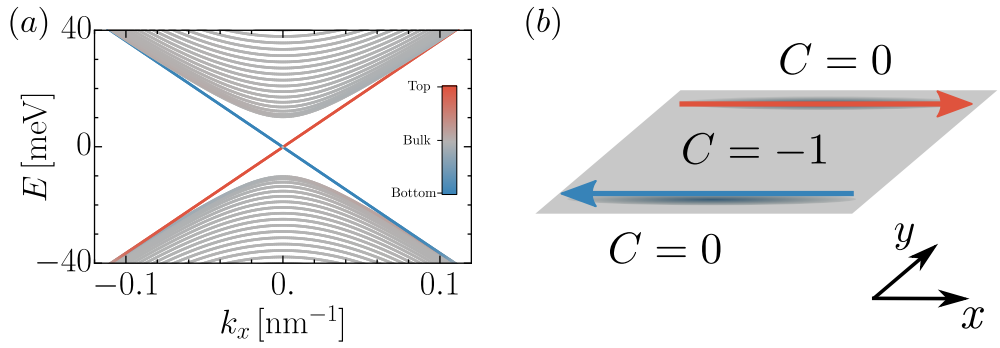

Figure 1.2.: (a) Spectrum of Eq. (1.37) with $M/B > 0$ for $D = 0$ is shown for a strip geometry. Bulk states are depicted in gray, while states close to the top and bottom edge are highlighted in red and blue, respectively. Edge states traverse the bulk gap due to the nontrivial bulk topology. (b) Corresponding strip geometry is schematically depicted. Arrows indicate the edge states propagating along the boundary.

where $H_{i,j}(k_x) = H_0(k_x)\delta_{i,j} + H_1\delta_{i,j-1} + H_1^\dagger\delta_{i-1,j}$ with

$$H_0(k_x) = \begin{pmatrix} M - \frac{2(B+D)}{a^2}\left[2 - \cos(k_x a)\right] & \frac{1}{a}A\sin(k_x a) \\ \frac{1}{a}A\sin(k_x a) & -M + \frac{2(B-D)}{a^2}\left[2 - \cos(k_x a)\right] \end{pmatrix}, \tag{1.38}$$

and

$$H_1 = \begin{pmatrix} \frac{1}{a^2}(B+D) & \frac{1}{2a}A \\ -\frac{1}{2a}A & -\frac{1}{a^2}(B-D) \end{pmatrix}. \tag{1.39}$$

In this approach, the hard wall boundary conditions are build in by truncating the matrix at $j = \pm L_y/(2a)$. Solving the Schrödinger equation boils therefore down to numerically diagonalizing at each k_x a $2N\times 2N$-dimensional matrix, where $N = L_y/a+1$ is the maximal number of lattice points.

For a topologically nontrivial case ($M/B > 0$) with $D = 0$, the resulting band structure is shown in Fig. 1.2(a). The color code depicts the expectation value $\langle y\rangle$, i.e, the localization of the wave function in the y-direction; red represents the top edge ($y = L_y/2$), blue the bottom edge ($y = -L_y/2$), and gray the bulk. Figure 1.2(a) demonstrates the existence of chiral edge states in the bulk gap [a]. These topological edge states arise as a consequence of the bulk-boundary correspondence. The number of edge states is thereby given by $|\nu|$, where ν is given by Eq. (1.24). Their chirality (propagation direction) is given by $\mathrm{sgn}\,(\nu)$. Note that the two edge states cross exactly at $E = 0$, called the Dirac point, due to the underlying PH symmetry. The situation is schematically depicted in Fig. 1.2(b). Similar results were, for example, obtained by König et al. [16] and Scharf et al. [61].

[a] Recall that the Fermi velocity $v_f = \hbar^{-1}\partial E/\partial k|_{k=k_f}$, where k_f is the Fermi momentum.

1.1.4. Symmetries in the presence of an external magnetic field

In the present discussion we have not yet included an external vector potential $\mathbf{A}(\mathbf{x})$. It can be incorporated in a Hamiltonian or in a field theoretical approach using the Peierls substitution,

$$\mathbf{k} \to \boldsymbol{\pi} = \mathbf{k} + \frac{e}{\hbar}\mathbf{A}(\mathbf{x})\,. \tag{1.40}$$

For instance, a magnetic field $\mathbf{B} = B_\perp \mathbf{e}_z$ which points in the z-direction can be incorporated in the Landau gauge choosing $\mathbf{A} = -yB_\perp \mathbf{e}_x$. As long as the source of this external field lies outside of the considered (closed) system, $\mathbf{A}$ remains unaffected by any symmetry operation [57]. In other words, it should not be treated as a quantum operator. This is the typical scenario in a solid state laboratory. For instance, suppose we consider a 2D system, the vector potential transforms as

$$\mathcal{O}\mathbf{A}(x,y)\mathcal{O}^{-1} = \mathbf{A}(x,y) \quad \text{with} \quad \mathcal{O} = \mathcal{T}, \mathcal{C}, \mathcal{S} \tag{1.41}$$

$$\mathcal{P}_x\mathbf{A}(x,y)\mathcal{P}_x^{-1} = \mathbf{A}(-x,y)\,, \tag{1.42}$$

where we assumed that $\mathbf{A}$ is time-independent. Only the spatial components transform under parity symmetry [a].

Making use of Eqs. (1.41) and (1.42), it is straightforward to include an external vector potential in Eqs. (1.7), (1.9), (1.11), and (1.15):

$$U_T^\dagger H^*\left[\mathbf{k};\mathbf{A}(\mathbf{x})\right] U_T = H\left[-\mathbf{k};\mathbf{A}(\mathbf{x})\right], \tag{1.43}$$

$$U_C^\dagger H^*\left[\mathbf{k};\mathbf{A}(\mathbf{x})\right] U_C = -H\left[-\mathbf{k};\mathbf{A}(\mathbf{x})\right], \tag{1.44}$$

$$U_S^\dagger H\left[\mathbf{k};\mathbf{A}(\mathbf{x})\right] U_S = -H\left[\mathbf{k};\mathbf{A}(\mathbf{x})\right], \tag{1.45}$$

$$U_P^\dagger H\left[k_x,k_y;\mathbf{A}(x,y)\right] U_P = H\left[-k_x,k_y;\mathbf{A}(-x,y)\right]\,. \tag{1.46}$$

These four equations demonstrate that the vector potential $\mathbf{A}$ transforms differently from the momentum $\mathbf{k}$ under TR, PH, and parity symmetry. This implies that an external magnetic field breaks all discrete symmetries except for the chiral symmetry.

The role of a magnetic field can be also understood within a classical picture. Consider an electron that propagates with velocity $\mathbf{v} = v_x\mathbf{e}_x$ in the x-direction in a 2D system. And the system is subjected to an external magnetic field that points in the out-of-plane direction (z-direction). Such an electron would feel a Lorentz force, $\mathbf{F} = -e\mathbf{v}\times\mathbf{B} =$

[a] The parity symmetry also clearly leaves the magnetic field invariant:

$$\mathbf{B} = \nabla_{x,y}\times\mathbf{A}(x,y) \quad \overset{\mathcal{P}_x}{\to} \quad \mathbf{B}' = \nabla_{-x,y}\times\mathbf{A}(-x,y) \overset{!}{=} \mathbf{B}\,.$$

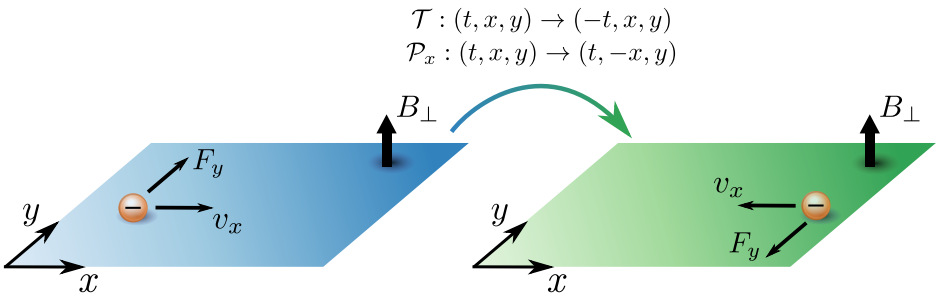

Figure 1.3.: Magnetic field breaks parity and TR symmetry in a 2D system. The symmetry operation is considered here as an active transformation, i.e., we transform the physical object but keep the coordinate system invariant. The violation of parity and TR symmetry is here illustrated in terms of the Lorentz force which is odd under both symmetry transformations.

$ev_x B_\perp \mathbf{e}_y$, pointing in the y-direction. This is schematically illustrated on the left-hand side of Fig. 1.3. Now, suppose a TR or a parity transformation is applied to the system. Both transformations clearly result in the reversal of the propagation direction of the electron ($v_x \to -v_x$), while they leave the magnetic field invariant. The Lorentz force changes therefore its sign under TR and parity symmetry, as indicated on the right-hand side of Fig. 1.3. The physical picture is not invariant which demonstrates that an external magnetic field breaks TR and parity symmetry.

Finally, let us emphasize that the scenario changes when the vector potential is considered as an integral part of the closed system. This is for instance the case in (2+1)D QED [62]. In this case, the vector potential must be considered as a quantum operator. For instance, $\mathbf{A}$ transforms then under parity symmetry via $\mathcal{P}_x A_x(x, y)\mathcal{P}_x^{-1} = -A_x(-x, y)$ and $\mathcal{P}_x A_y(x, y)\mathcal{P}_x^{-1} = A_y(-x, y)$. As a result parity symmetry flips the sign of the magnetic field [50, 62] [a]. It is a pseudo-scalar in (2+1)D QED.

1.2. Landauer-Büttiker formalism

If we would experimentally determine the Hall conductivity of a single Chern insulator, we would find that its quantization is basically independent on the impurity concentration and on the system dimensions [b]. This astonishing feature can be attributed to the existence of chiral edges channels [63]. An electron propagating along such a channel cannot be backscattered. The only possible process for this to happen would involve chiral edge channels at the opposite side of the sample. Edge dominated transport is protected by the system size. This is in stark contrast to bulk transport, where impurities cause scattering which ultimately leads to localization and, therefore, to a decrease

[a] This is a special property of a 2D space. In 3D, all three components of $\mathbf{A}$ are flipped. Hence, the magnetic field is invariant even if the vector potential is treated as a quantum operator.
[b] We assume that the chemical potential is placed in the bulk gap.

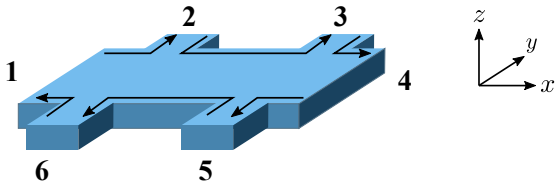

Figure 1.4.: Schematics of six-terminal Hall bar. A single chiral edge channel is indicated propagating in clockwise direction.

in conductivity.

The crucial role of edge channels was first revealed by Halperin [64] and Büttiker [63]. In particular, Büttiker developed a very simple and elegant formalism to study coherent transport of edge channels within multi-terminal setups. This approach is known as the Landauer-Büttiker-formalism [63]. For a six terminal Hall bar, the setup is schematically depicted in Fig. 1.4. To drive a current through the system, a voltage difference $\Delta V = -e(\mu_1 - \mu_4)$ can be applied between contact 1 and 4, where μ_i is the local chemical potential in the ith contact. The two contacts serve as source and drain of the electric current. All other contacts are used as voltage probes. This means $I_2 = I_3 = I_5 = I_6 = 0$ and $I_1 = -I_4$. The total current is conserved $\sum_{j=1}^{6} I_j = 0$.

Under these assumptions, Büttiker showed that the current in the ith contact is given by [63]

$$I_i = -\frac{e}{h} \sum_{j=1}^{N} \left[T_{ij}\mu_j - T_{ji}\mu_i \right] , \tag{1.47}$$

where T_{ij} is the transmission probability from the jth to the ith contact and N is the total number of contacts (here, $N = 6$). The Hall resistance is defined by $R_{\mathrm{H}} = -e(\mu_2 - \mu_6)/I_1$; the longitudinal resistance is given by $R_{\mathrm{L}} = -e(\mu_2 - \mu_3)/I_1$. In the following, we assume that transport is only carried between adjacent contacts and that the system obeys translational invariance in the sense that $T_{i,j} = T_{i+1,j+1}$. The transmission probabilities in clockwise and anticlockwise direction are then determined by $T_{i+1,i} = T_{\mathrm{c}}$ and $T_{i,i+1} = T_{\mathrm{a}}$, respectively. Solving the linear system, given by Eq. (1.47), leads to the following analytic expressions for the Hall and the longitudinal resistance [65]:

$$R_H = \frac{h}{e^2} \frac{T_c - T_a}{T_c^2 - T_a T_c + T_a^2} , \tag{1.48}$$

$$R_L = \frac{h}{e^2} \frac{T_c T_a}{T_c^3 + T_a^3} . \tag{1.49}$$

In the case of a Chern insulator with $C = -1$ [cf. Fig. 1.2], there is only one edge channel which propagates in clockwise direction. This implies that $T_c = 1$ and $T_a = 0$. A typical measurement yields therefore $R_H = h/e^2$, while $R_L = 0$. There is no longitudinal

resistance as backscattering is absent.

The Landauer-Büttiker formalism is a coherent transport formalism. Inelastic scattering events can be only treated in a simplistic fashion by including so called virtual voltage probes within the calculation. A voltage probe serves as an infinite reservoir. This means when an electron enters a voltage probe from a perfect edge channel, it equilibrates to the local chemical potential and loses its phase information. This means a voltage probe acts similar to an inelastic scattering event [63, 66]. If the channel length is larger than the inelastic mean free path, we can therefore add virtual voltage probes in Eq. (1.47) to account for inelastic scattering. However, as long as, only chiral edge channels exist, inelastic scattering cannot induce any resistance. A perfect quantization which is independent on the exact material properties is therefore a signature of chiral edge transport.

1.3. The quantum Hall family

We present an overview of topological states of matter in 2D solid state systems including the QH, QSH, and QAH phase. Thereby, we work exclusively within a Hamiltonian approach and discuss in each case characteristic band structure, as well as transport signatures. The field theoretical description, which complements the understanding of these topological states, will be developed later on, starting in Sec. 1.5. Here, we start by reviewing the QH effect in Sec. 1.3.1. Based on our results for a single Chern insulator, we introduce QSH and QAH insulators in Secs. 1.3.2 and 1.3.3, respectively.

1.3.1. Quantum Hall insulator

Probably the best understood topological state of matter is the QH phase. To understand its properties, let us start with a quadratic Hamiltonian in 2D which is subjected to an external magnetic field:

$$\begin{aligned} H &= \frac{\hbar^2}{2m}\left[\left(k_x + \frac{e}{\hbar}A_x(\mathbf{x})\right)^2 + \left(k_y + \frac{e}{\hbar}A_y(\mathbf{x})\right)^2\right] \\ &= \frac{\hbar^2}{2m}\left(\pi_x^2 + \pi_y^2\right), \end{aligned} \tag{1.50}$$

where π_i with $i = \{x, y\}$ is defined in Eq. (1.40). Analogously to the discussion in Sec. 1.1.4, we account for the magnetic field in the Landau gauge, $\mathbf{A}(\mathbf{x}) = -yB_\perp \mathbf{e}_x$. This breaks translational invariance in the y-direction and maintains the translational

invariance in the x-direction [a]. As a result, the momentum k_x remains a good quantum number.

The following calculation is similar to solving a simple quantum harmonic oscillator. It is hence convenient to introduce ladder operators to compute the bulk spectrum:

$$a = \frac{l_{B_\perp}}{\sqrt{2}\hbar}\left[\mathrm{sgn}\left(eB_\perp\right)\pi_x - \mathrm{i}\pi_y\right] \quad , \quad a^\dagger = \frac{l_{B_\perp}}{\sqrt{2}\hbar}\left[\mathrm{sgn}\left(eB_\perp\right)\pi_x + \mathrm{i}\pi_y\right] , \tag{1.51}$$

where $l_{B_\perp} = \sqrt{\hbar/|eB_\perp|}$ is the magnetic length. Ladder operators fulfill the following useful identities

$$\begin{aligned} a^\dagger a\,|n\rangle = n\,|n\rangle \quad , \quad a^\dagger\,|n\rangle = \sqrt{n+1}\,|n\rangle \quad , \\ a\,|n\rangle = \sqrt{n}\,|n-1\rangle \quad , \quad \text{and} \quad \left[a, a^\dagger\right] = 1\,, \end{aligned} \tag{1.52}$$

where $n = 0, 1, 2, \ldots$ denotes the nth harmonic oscillator function. Recasting Eq. (1.50) in terms of ladder operators yields

$$H = \hbar\omega_C\left(a^\dagger a + \frac{1}{2}\right) , \tag{1.53}$$

where the cyclotron frequency is denoted by $\omega_c = |eB_\perp|/m$. Making use of Eq. (1.52), we see that the eigenvalues of the Schrödinger equation are determined by

$$E_{n,k_x}(B_\perp) = \hbar\omega_c\left(n + \frac{1}{2}\right) . \tag{1.54}$$

Each of these so-called LLs (LL index n) is highly degenerate since the energy does not depend on k_x. In particular, one can show that the LL degeneracy (per area) equals to [68]

$$n_{B_\perp} = \frac{1}{2\pi l_{B_\perp}^2} . \tag{1.55}$$

The number of filled LLs as a function of the magnetic field is therefore given by the filling factor

$$\nu = \frac{n_{el}}{n_{B_\perp}} , \tag{1.56}$$

where n_{el} is the electron density in the associated 2D electron gas. Solving the differential equation, one can show that the corresponding wave function is a product state of a plane wave in the x-direction and harmonic oscillator states in the

[a] It is actually possible to reintroduce a set of magnetic translational operators. They allow the definition of a magnetic Brillouin zone which is restricted to a smaller area in momentum space, compared to the Brillouin zone in the absence of a magnetic field. The interested reader finds further information in Ref. [67].

y-direction [69]:

$$\psi_{n,k_x}(\mathbf{x}) = \mathrm{e}^{\mathrm{i}k_x x} H_n\left(\frac{y - y_{k_x}}{l_{B_\perp}}\right) \mathrm{e}^{-(y-y_{k_x})^2/\left(4l_{B_\perp}^2\right)}, \tag{1.57}$$

where $y_{k_x} = k_x l_{B_\perp}^2 \,\mathrm{sgn}\,(eB_\perp)$, and H_n stands for the nth Hermite polynomial. Note that there is a one-to-one correspondence between the momentum k_x and the localization of the wave function in the y-direction. The wave functions are centered around y_{k_x} and their width is related to the magnetic length $l_{B_\perp}$. One should keep these identities in mind as they are helpful to interpret band structures in magnetic fields.

So far, we have mainly considered a simple quantum mechanical problem. Let us now turn to the topological interpretation of the QH phase. In this regard, we have to mention four seminal papers which together yield a comprehensive picture of the QH effect as a topological state of matter. Thouless, Kohmoto, Nightingale, and den Nijs [5] showed for the first time using the Kubo formula that, while the longitudinal conductivity σ_{xx} vanishes in the QH phase, the Hall conductivity is quantized with $\sigma_{xy} = -\nu e^2/h$ [a]. The subsequent work by Avron, Seiler, and Simon [70], as well as the work by Kohmoto [67] shed for the first time light on the topological interpretation of the QH effect. Assuming a non-interacting electron system, they provided proof that the Hall conductivity is determined by a topological invariant representing the filling factor ν. The topological invariant is the first Chern number which, in the context of the QH phase, is often times referred to as the TKKN invariant. The name is a reference to the four authors of Ref. [5]. A generalization to interacting systems was later given by Niu, Thouless, and Wu [7]. They showed that the topological interpretation remains valid even in the presence of manybody interactions and disorder. As such, these references taken together are compelling evidence that the topological interpretation is robust and, hence, suitable to describe the experiment. Finally, note that this result can be also understood from the periodic table, Tab.1.1. The quadratic Hamiltonian breaks TR, PH, and chiral symmetry in the presence of a magnetic field. Hence, the 2D system falls into the symmetry class A and is described by a $\mathbb{Z}$ topological invariant.

To present a short, intuitive proof that σ_{xy} is indeed quantized, we follow Ref. [52]. Assuming that $\sigma_{xx} = 0$ in the bulk gap, we can write the ith component of the current as $j_i = \sigma_{xy}\epsilon_{ij}E_j$, where ϵ_{ij} is the two-dimensional Levi-Civita symbol and E_j is the jth component of an applied electric field. Since the continuity equation must be fulfilled, it follows that

$$\frac{\partial \rho}{\partial t} = -\nabla \mathbf{j} = -\sigma_{xy}\left(\partial_x E_y - \partial_y E_x\right) = \sigma_{xy}\frac{\partial B_\perp}{\partial t}, \tag{1.58}$$

[a] We assumed $T = 0\,\mathrm{K}$ and that the chemical potential is placed in the bulk gap between adjacent LLs.

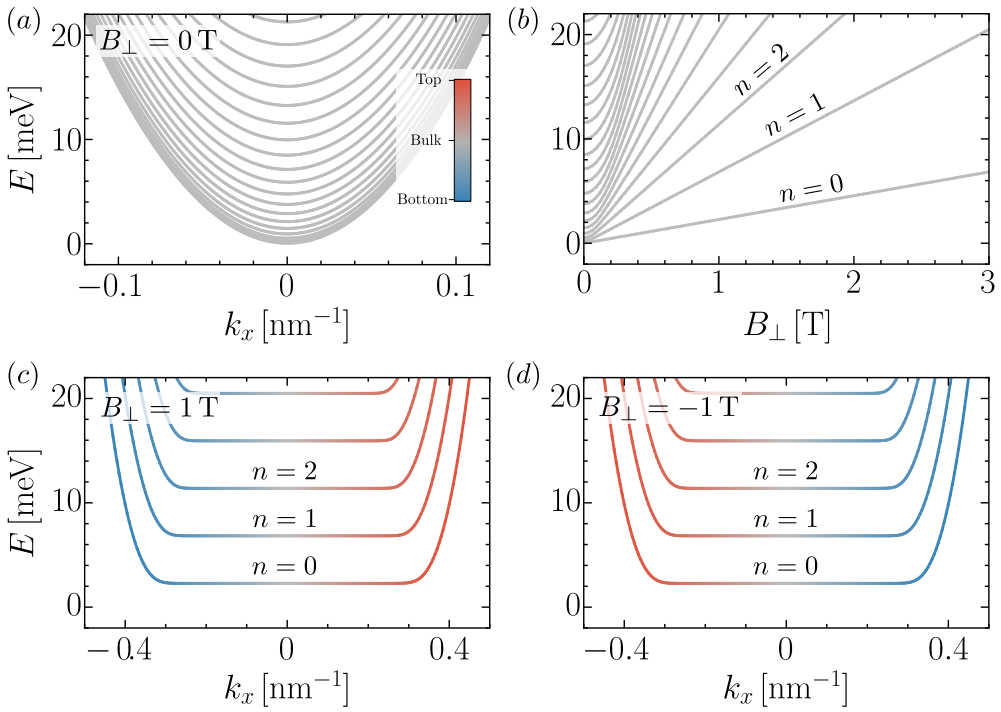

Figure 1.5.: Band structure and LL fan for quadratic Hamiltonian, Eq. (1.50), employing a strip geometry. Band structure is shown for $B_\perp =$ (a) $0\,\mathrm{T}$, (c) $+1\,\mathrm{T}$, and (d) $-1\,\mathrm{T}$. (b) LL fan: Evolution of bulk LL energies as function of magnetic field $B_\perp$. At small magnetic fields, deviations from ideal linear behavior [cf. Eq. (1.54)] is observed due to finite system size. Color code highlights edge versus bulk localization.

where $\rho = -en_{el}$ is the charge carrier density. We arrive therefore at a very simple equation for the Hall conductivity, also known as Streda's relation [71]:

$$\sigma_{xy} = \frac{\partial \rho}{\partial B_\perp}\,. \tag{1.59}$$

If ν electron-like LLs are filled, such that $\rho = -e\nu n_{B_\perp}$, Streda's relation yields $\sigma_{xy} = -\nu e^2/h$ which completes the proof.

The QH effect is from a topological point of view similar to a Chern insulator. Both are described by a $\mathbb{Z}$ topological invariant. This implies that bulk LLs should come along with chiral edge channels [a]. Using Eq. (1.27), we can employ the finite-difference-method to calculate the band structure of Eq. (1.50) for a strip geometry. The results are shown in Fig. 1.5. The color code highlights analogously to Fig. 1.2 the wave function localization. The strip geometry breaks translational invariance in the y-direction which results in the formation of quantum well subbands as observed in Fig. 1.5(a) for $B_\perp = 0$. Switching on the magnetic field, we trace in Fig. 1.5(b) the evolution of the band edge energies at $k_x = 0$ as a function of $B_\perp$. The quantum well confinement

[a] The main difference between QH and Chern insulators is that the topology in Chern insulators is linked to an inverted band structure without LLs.

induces deviations from a perfectly linear behavior for small $B_\perp$, i.e., if $l_{B_\perp} > L_y$. In the opposite limit when $l_{B_\perp} < L_y$, the LL fan recovers a perfectly linear behavior as expected from Eq. (1.54)[61]. The full band structure for $B_\perp = +1\,\mathrm{T}$ and $-1\,\mathrm{T}$ as a function of k_x is shown in Fig. 1.5(c) and (d), respectively. While flat LLs are observed for small k_x, the band structure starts to cross the band gaps for large k_x. These deviations from Eq. (1.54) are a consequence of the finite system size of the strip geometry [a]. As the color shows, bands which cross the gaps are strongly localized at the edges of the strip. They form chiral edge channels [64].

So far, we have discussed transport properties of a QH insulator based on a pure bulk picture. Let us now analyze these transport properties within the associated edge picture. To this end, we follow along the lines of Sec. 1.2 and assume that associated transport measurements would be performed on a six-terminal Hall bar. Furthermore, we place, as an example, the chemical potential between the $n = 1$ and the $n = 2$ LL in Fig. 1.5(c) ($B_\perp = 1\,\mathrm{T}$). In this case, there are two chiral edge channels with positive (negative) Fermi velocity which are localized at the top (bottom) edge of the strip geometry (cf. Fig. 1.4) [b]. The chiral edge channels propagate therefore in clockwise direction. In comparison in Fig. 1.4, flipping the magnetic field direction results in flipping the sign of the Fermi velocity for all edge channels. This means they propagate in anticlockwise direction for negative magnetic fields. Making use of the Landauer-Büttiker formalism, it should be hence apparent that the transmission probabilities change for these two examples from $T_c = 2$ and $T_a = 0$ at $B_\perp = 1\,\mathrm{T}$, to $T_c = 0$ and $T_a = 2$ at $B_\perp = -1\,\mathrm{T}$. Inserting this into Eqs. (1.48) and (1.49), it turns out that the Hall resistance is quantized to $\mathrm{sgn}\,(B_\perp)\,h/2e^2$, while $R_L = 0$ [c]. We can therefore comprehensively understand transport in the QH phase by chiral edge channels [63]. Furthermore, we notice that the Hall resistance is an odd function of the magnetic field in the QH phase. Since in 2D it holds that $\sigma_{xy} = R_H^{-1}$ given that $R_L = 0$, this implies that

$$\sigma_{xy}(-B_\perp) = -\sigma_{xy}(B_\perp)\,, \tag{1.60}$$

which is commonly known as the Onsager relation [72, 73].

1.3.2. Quantum spin Hall insulator

In Sec. 1.1.3, we studied in detail the properties of a Chern insulator defined in two spatial dimensions. We saw that in such models parity and TR symmetry are generically

[a] In deriving Eq. (1.57), we implicitly assumed an infinite space. Wave functions are therefore only required to be square-integrable. Deviations from bulk results are therefore expected when the finite system size starts to play a role for potential wave functions.

[b] By top and bottom edge, we refer to $y = L_y/2$ and $y = -L_y/2$, respectively.

[c] In 2D, resistance and resistivity have the same units. It holds that $\rho_{xy} = R_{xy}$ and $\rho_{xx} = R_{xx}W/L$, where L is the length and W is the width of the Hall bar.

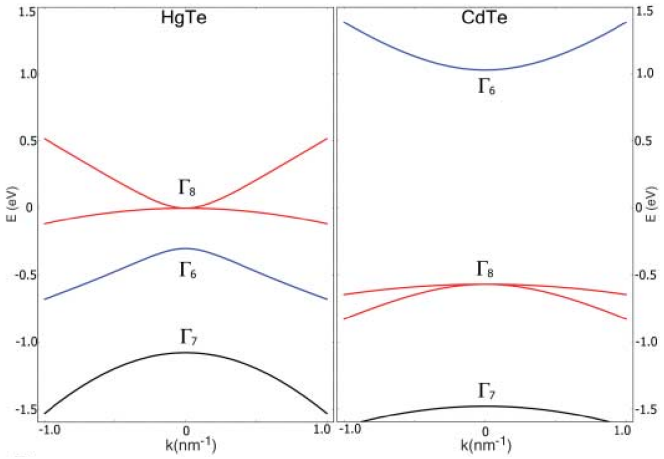

Figure 1.6.: Bulk band structure of HgTe (left) and CdTe (right). Band character is highlighted. Band ordering between Γ_6 and Γ_8 bands is in reverse in HgTe compared to the trivial insulator CdTe. From Ref. [15]. Reprinted with permission from AAAS.

violated. This is because of the mass operators $M\sigma_z$ and $Bk^2\sigma_z$ which are odd under parity and TR symmetry. A Chern insulator is therefore described by a $\mathbb{Z}$ topological invariant.

From the periodic table, Tab. 1.1, we know that there are other symmetry classes in 2D which are associated to $\mathbb{Z}_2$ topological invariants. The two existing classes DIII and AII rely both on the presence of TR symmetry. A topological material which falls into one of these classes is known as quantum spin Hall (QSH) insulator. Its first theoretical proposal goes back to Kane and Mele [13, 14]. They suggested that, in graphene, spin-orbit interaction induces the QSH phase by opening a band gap at the two high symmetry point, K and K', of the honeycomb lattice. Unfortunately, this gap is very small so that temperatures below 10 mK [74] would be required to actually observe this effect. The first successful proposal of a QSH insulator was made by B. A. Bernevig, T. L. Hughes, and S.-C. Zhang [15]. They proposed that thin layers of HgTe/(Hg,Cd)Te quantum wells are characterized by the QSH phase. Their proposal was verified by König et al. using magneto transport experiments [16, 17]. Nowadays, there is still only a handful of materials which have been identified as QSH insulators. Most notably are in this regard InAs/GaSb quantum wells [75], WTe_2 [76], and bismuthene on SiC substrate [77]. In particular, the latter material offers the prospect for realizing a QSH insulator that operates at room temperatures.

As a prototype example, we focus here on HgTe/(Hg,Cd)Te quantum wells. The bulk band structures of HgTe and CdTe are shown in the vicinity of the Γ-point in Fig. 1.6. Bulk HgTe is a semimetal which exhibits an inverted band structure. The two p-type Γ_8 bands lie $\sim 300\,\text{meV}$ above the s-type Γ_6 band, which conventionally represents the conduction band. The band inversion in HgTe is driven by a large relativistic mass-

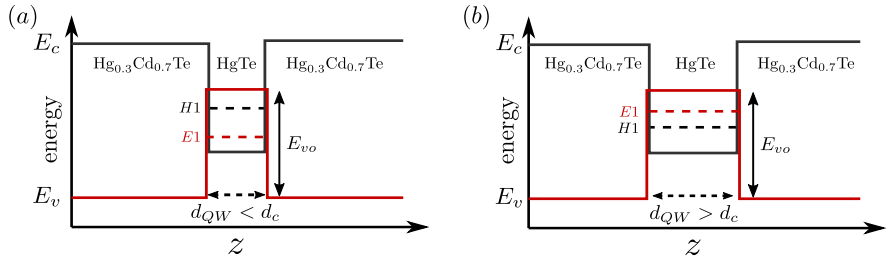

Figure 1.7.: Evolution of bulk band edge energies of conduction (E_c) and valence (E_v) band for HgTe/$Hg_{0.3}Cd_{0.7}Te$ quantum wells with (a) $d_{QW} < d_c$ and (b) $d_{QW} > d_c$. E_{vo} stands for the valence band offset between HgTe and (Hg,Cd)Te. Dashed lines indicate subband levels. From Ref. [15]. Adapted with permission from AAAS.

velocity correction [a] and spin-orbit interaction [78, 79]. In comparison, bulk CdTe shows a normal band ordering, in which the Γ_6 band is above the two Γ_8 bands. A typical experimental setup consists, for instance, of a HgTe/$Hg_{0.3}Cd_{0.7}Te$ quantum well with [001] growth direction (z axis) which is grown on a $Cd_{0.96}Zn_{0.04}Te$ substrate [17]. In this specific configuration, the lattice constants of the adjacent layers roughly match. The corrections due to strain are therefore almost negligible (for further details see App. A). Other substrates, like superlattice virtual substrates [80], can be used to manipulate the band structure further.

The band diagram for the quantum well geometry is schematically shown for two different thicknesses in Fig. 1.7(a) and (b). For very thin quantum wells, the band ordering of the quantum well subbands is in the normal regime, i.e., topologically trivial. This means the s derived E1 subbands [b], are above the p derived heavy-hole H1 subbands (both are double degenerated because of the spin degree of freedom). If the thickness exceeds the critical thickness $d_c = 6.3\,\mathrm{nm}$, the subband order changes and the band structure enters the inverted regime [16, 17]. Since in HgTe the charge neutrality point lies between the E1 and H1 subbands, this implies that the system enters the QSH phase. The explicit evolution of the band edge energies as a function of the quantum well thickness d_{QW} is shown in Fig. 1.8. Higher order HH subbands, indicated by H(n) increase in energy (with d_{QW}) due to their negative effective mass. In comparison, higher order E(n) subbands decrease in energy due to their positive effective mass.

To derive now a low energy Hamiltonian, it is sufficient to take only the two E1

[a] This term originates from a higher order relativistic correction in the Schrödinger-Pauli equation:

$$\sqrt{|\mathbf{p}|^2 c^2 + m_0^2 c^4} - m_0 c^2 \approx \frac{|\mathbf{p}|^2}{2m} - \frac{|\mathbf{p}|^4}{8m^3 c^2} + \dots ,$$

where the first term is the conventional kinetic term and the second terms denotes the mass-velocity correction, which is large in HgTe.

[b] To be precise, the E1 subband consists of a mixture of $|\Gamma_6, 1/2\rangle$ and $|\Gamma_8, 1/2\rangle$. Further details are discussed in Ch. 3.

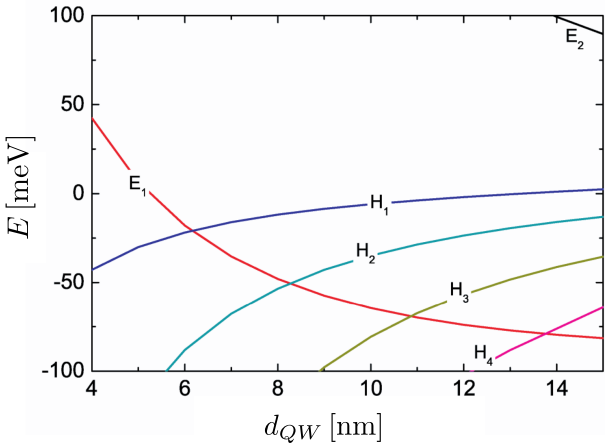

Figure 1.8.: Evolution of band edge energies of quantum well subbands as function of quantum well thickness d_{QW}. The corresponding layer structure is shown in Fig. 1.7. From Ref. [17]. Reprinted with permission from the Physical Society of Japan.

and the two H1 subbands into account, provided the discussion is limited to thicknesses $d_{QW} < 8.3\,\text{nm}$. Above this critical thickness, it would be necessary to include more bands within the model, as other heavy-hole subbands start to additionally cross the E1 subbands [81]. This low energy model is commonly known as the Bernevig-Hughes-Zhang (BHZ) model [15]. The Hamiltonian, written in the subband basis $\{|E1\uparrow\rangle, |H1\uparrow\rangle, |E1\downarrow\rangle, |H1\downarrow\rangle\}$, reads

$$H(\mathbf{k}) = \begin{pmatrix} h(\mathbf{k}) & 0 \\ 0 & h^*(-\mathbf{k}) \end{pmatrix}, \tag{1.61}$$

where $h(\mathbf{k})$ denotes a single Chern insulator, defined by Eq. (1.16). In contrast to a single Chern insulator, the BHZ model obeys TR and parity symmetry even if the Dirac mass M and the nonrelativistic mass Bk^2 are nonzero. This is possible because both spin blocks are involved in the symmetry transformations [a]. The corresponding single-particle symmetry operators read [cf. Eqs. (1.7), (1.9), (1.11), and (1.15)]

$$T = U_T K \quad , \quad U_T = -\mathrm{i}\tau_y \otimes \sigma_0 \quad , \quad T^2 = -1\,; \tag{1.62}$$

$$P_x = U_P \quad , \quad U_P = \tau_y \otimes \sigma_0 \quad , \quad P_x^2 = 1\,. \tag{1.63}$$

This means a QSH insulator can be simplistically understood as two copies of Chern insulators which are connected by TR symmetry. The symmetry operators for PH and

[a] By spin degree of freedom, we actually refer to the total angular momentum. The two basis states of the spin up block have both a positive angular momentum quantum number m_j, while the two basis states of of the spin down block have a negative m_j. To be precise, the $|E1, (\uparrow, \downarrow)\rangle$ subbands have $m_j = \pm 1/2$, respectively, and the $|H1, (\uparrow, \downarrow)\rangle$ subbands have $m_j = \pm 3/2$, respectively.

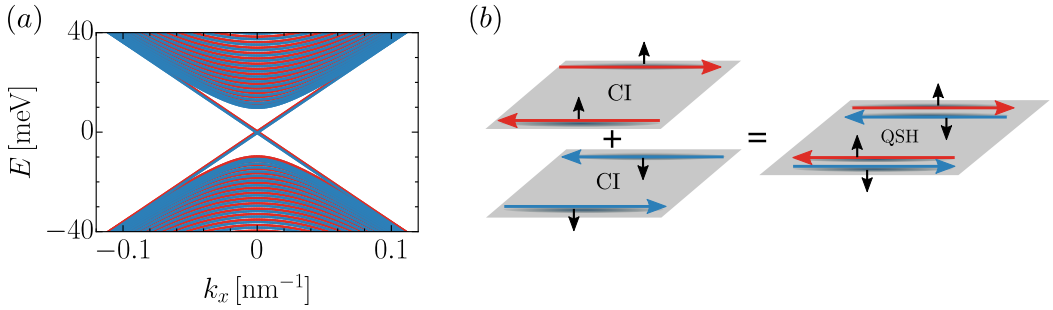

Figure 1.9.: (a) Band structure of QSH insulator described by BHZ model, Eq. (1.61). The two spin blocks are indicated by color. Spin up (down) is highlighted in red (blue). A small offset was introduced between the two spin blocks, which are usually double degenerated due to TR and inversions symmetry. (b) QSH insulator can be schematically understood as two copies of Chern insulators (CIs) which are connected by TR symmetry. The two Chern insulators have opposite spin polarizations and chiralities. The spin is indicated by arrows.

chiral symmetry are given by

$$C = U_C K \quad , \quad U_C = \tau_0 \otimes \sigma_x \quad , \quad C^2 = 1\,; \tag{1.64}$$

$$S = U_S \quad , \quad U_S = \tau_x \otimes \sigma_x \quad , \quad S^2 = 1\,. \tag{1.65}$$

Introducing the D-parameter respects TR and parity symmetry, but breaks PH and chiral symmetry. A QSH insulator falls therefore into the symmetry class DIII if $D = 0$, or into the symmetry class AII if $D \neq 0$ (cf. Tab. 1.1). In either case, the topological invariant is $\mathbb{Z}_2$. Note that although Eq. (1.61) was motivated as the low energy model of HgTe quantum wells, it applies similarly to other QSH insulators [13, 75].

To analyze the characteristic edge properties of a QSH insulator, let us follow the recipe introduced in Sec. 1.1.3 to map the Hamiltonian onto a strip geometry. The corresponding band structure is shown in Fig. 1.9(a). A more detailed analysis can be found in Ref. [61]. Since the system consists of two Chern insulators which are connected by TR symmetry, we observe that a pair of counterpropagating, spin polarized edge channels traverse the bulk band gap [15]. These helical edge channels are schematically illustrated in Fig. 1.9(b). Remarkably, they are protected against elastic backscattering if the perturbation preserves TR symmetry. This means electrons cannot change their propagation direction if $TV(\mathbf{x})T^{-1} = V(\mathbf{x})$, where $V(\mathbf{x})$ describes an arbitrary time-independent perturbation [82]. They are the key signature of a nontrivial $\mathbb{Z}_2$ classification in 2D.

Let us now turn our attention to transport properties of QSH insulators. To this end, Eq. (1.23) can be employed to show that the total Hall conductivity σ_{xy} vanishes in

the bulk gap:

$$\sigma_{xy} = \sigma_{xy}^{\uparrow} + \sigma_{xy}^{\downarrow} = 0\,, \tag{1.66}$$

where σ_{xy}^{s} with $s = \{\uparrow, \downarrow\}$ denotes the Hall conductivity of the spin up $[h(\mathbf{k})]$ or the spin down block $[h^{\star}(-\mathbf{k})]$ of Eq. (1.61), respectively. That $\sigma_{xy} = 0$ is a consequence of TR symmetry [a] [48]. Hence, a QSH insulator shares the same Hall conductivity as a trivial insulator. But it can be distinguished from a trivial insulator by its nontrivial spin Hall conductivity σ_{xy}^{S} in the bulk gap, where [58]

$$\sigma_{xy}^{S} = \sigma_{xy}^{\uparrow} - \sigma_{xy}^{\downarrow}\,. \tag{1.67}$$

The spin Hall conductivity yields $\pm 2e^2/h$ in the case of a QSH insulator, while it vanishes in the case of a trivial insulator.

While Eq. (1.67) is a beautiful theoretical result, it is actually not easy to measure a spin Hall conductivity experimentally [b]. But how do we then verify the existence of QSH insulators? So far, we have focused on the pure bulk conductivity of QSH insulators. However, in actual experiments, one has to also account for the crucial role of contacts [84]. In fact, it turns out that QSH insulators have a very clear hallmark when multiterminal Hall bars are employed. To this end, let us apply the Landauer-Büttiker formalism for a six terminal set-up, as discussed in Sec. 1.2, to determine the longitudinal and Hall resistance. Assuming that the transport between contacts is ballistic and preserves TR symmetry, the transmission probabilities between adjacent contacts of the helical edge states is given by $T_{i,i+1} = T_{i+1,i} = 1$ [16, 17]. All other transmission probabilities vanish. Inserting this into Eqs. (1.48) and (1.49), we find that while the Hall resistance is zero, the longitudinal resistance R_L is quantized to $h/2e^2$ [c]. This quantization is characteristic for QSH insulators and has been verified by König et al. for HgTe quantum wells in the inverted regime [16, 17]. Further evidence that transport is indeed carried by helical edge channels has been obtained using nonlocal transport experiments [66]. Note however that this quantization is only reached for small Hall bars with a few μm length [16, 85, 86]. This limitation is a consequence of inelastic scattering and TR symmetry breaking perturbations which can cause deviations from a perfect quantization in large samples. In this regard, charge puddles were identified as the major source of backscattering [86–88].

[a] TR symmetry implies that the Berry curvature is an odd function of $\mathbf{k}$. The Hall conductivity, which is determined by the integral of the Berry curvature over the Brillouin zone must therefore vanish.
[b] The spin polarization of the helical edge channels was verified in Ref. [83] using a split gate technique.
[c] That $R_L \neq 0$ results from the contact resistance of the voltage probes. A voltage probe populates edge channels incoherently with equal probability which causes the nonzero resistance [66].

1.3.3. Quantum anomalous Hall insulator

The conceptual idea of a QAH insulator is to realize a quantized Hall conductivity similar to the QH phase, but without the necessity of an external magnetic field. This means in the absence of LLs. The realization of such a topological state would allow dissipationless chiral edge transport without requiring any symmetry constrains or a magnetic field [a]. Its physical realization is therefore of great interest for possible low-energy electronics.

Because TR symmetry demands that $\sigma_{xy} = 0$, the key ingredient to realize the QAH phase is to break TR symmetry. The proof of principal, that such a topological state exists, dates back to the seminal work by Haldane in 1988 [8]. He showed that a staggered magnetic flux in graphene can be utilized to break TR symmetry and, to that end, generate a quantized σ_{xy} [b]. Even though he believed at that time, that his model was unlikely to be 'physically realizable' [8], his idea inspired later work by Liu et al. [21]. Their proposal was the origin for the intense research into QAH insulators in condensed matter systems [c] [90].

Liu et al.'s profound idea was to realize the QAH phase by incorporating magnetic atoms in the crystal structure of topological insulators. In particular, HgTe alloyed with a few percent of manganese was proposed as the first solid state realization of the QAH phase. The low energy physics of this material compound, similarly to HgTe, is still described by the BHZ model [cf. (1.61)], except for an additional Hamiltonian which accounts for the magnetization of the Mn atoms [d]. This Hamiltonian reads

$$H_S = \begin{pmatrix} G_E & 0 & 0 & 0 \\ 0 & G_H & 0 & 0 \\ 0 & 0 & -G_E & 0 \\ 0 & 0 & 0 & -G_H \end{pmatrix}, \tag{1.68}$$

where G_E and G_H represent the out-of-plane magnetization. If G_E and G_H are nonzero, this Hamiltonian clearly breaks TR symmetry since $T^\dagger H_S T = -H_S$, where T is given by Eq. (1.62). The magnetization removes the relation between the two spin blocks in the BHZ model and therefore allows a finite σ_{xy}.

More specifically, introducing Eq. (1.68) renormalizes the bulk band gaps of the two

[a] As we have pointed out in Sec. 1.3.2, symmetry protected topological phases are fragile. Any perturbation that breaks the underlying symmetry introduces a resistance and, therefore, prevents dissipationless transport. A strong magnetic field is not compatible with typical electronic devices.

[b] The staggered potential is constructed such that the net magnetic flux in each unit cell is zero.

[c] In 2014, researchers working in the field of quantum optics realized an actual Haldane model with ultracold fermions using an optical honeycomb lattice [89].

[d] The Mn atoms only alter the BHZ parameters. This is discussed in Ch. 3.

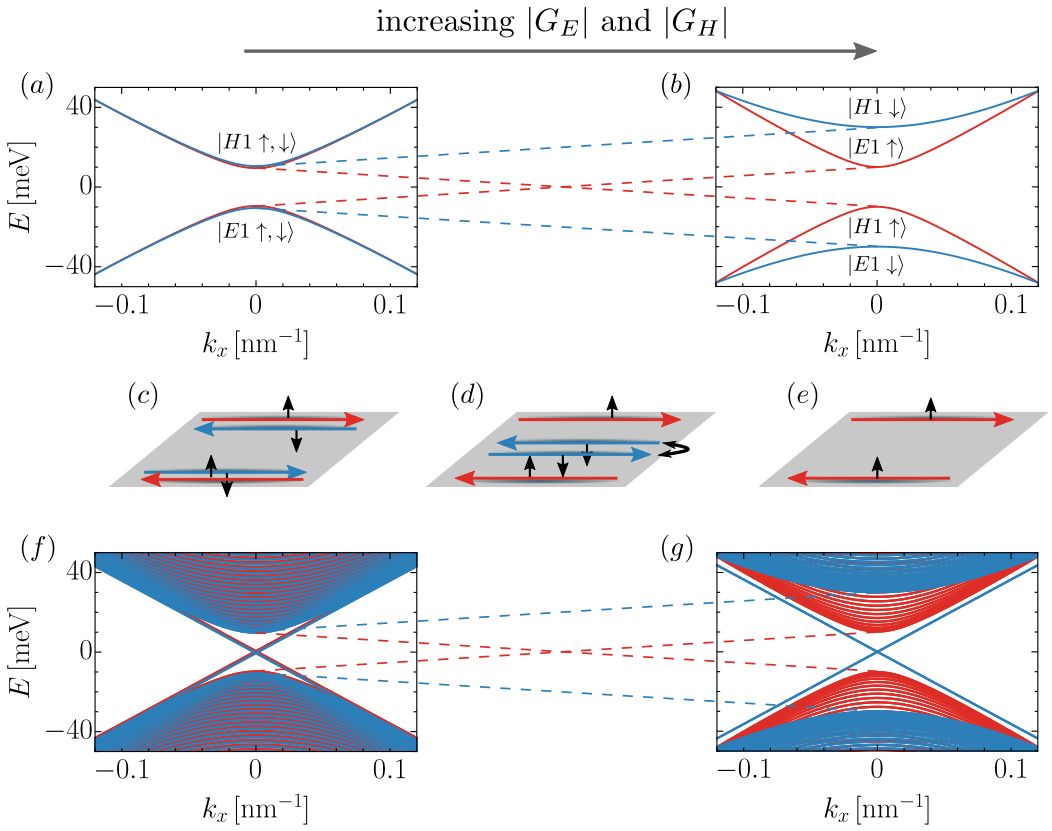

Figure 1.10.: (a) and (b) show transition from QSH to QAH insulator via increasing the exchange coupling $|G_E|$ and $|G_H|$. If $G_E G_H < 0$, it is possible to invert the band structure of only a single spin block. (a) Schematic evolution of band structure. (b) One pair of the QSH edge states is destroyed during the process. One pair of chiral edge states characterizes QAH phase. From Ref. [21]. Adapted with permission from APS.

spin blocks separately:

$$E_g^{\uparrow,\downarrow} = 2M \pm G_E \mp G_H \,, \tag{1.69}$$

where $\pm$ belongs to the spin-up and down block, respectively. As indicated in Fig. 1.10(a) and (b), the QSH phase merges into the QAH phase when one of the two spin blocks is driven into the trivial regime. The condition to realize the QAH phase therefore reads $E_g^{\uparrow} E_g^{\downarrow} < 0$ [a]. If this condition is fulfilled, only one of the two Chern insulators contributes to the total Hall conductivity resulting in $\sigma_{xy} = \pm e^2/h$. As indicated in Fig. 1.10(c)-(g), this process goes hand in hand with the destruction of the helical edge channels which merge at the transition point into purely chiral edge channels. Note that these chiral edge channels originate from the intrinsically inverted band structure and, thus, exist in the absence of LLs.

[a] There is actually a second condition. We have to ensure during the transition that the system remains a bulk insulator. This amounts to $G_E G_H < 0$ [21].

In the case of (Hg,Mn)Te, there is however a problem with Liu's argumentation which we did not mention so far. The magnetization, which is induced by the *sp-d* exchange interaction between s and p band electrons with the localized d electrons of Mn, is in fact paramagnetic [45, 91]. The topological transition, shown in Fig. 1.10, requires therefore an external magnetic field [a]. Nonetheless, Liu's idea applies also to other topological insulators alloyed with magnetic atoms. But to realize a QAH insulator without an external magnetic field, a specific material has to be found which exhibits a ferromagnetic insulating groundstate. This goal was finally achieved by Yu et al. who predicted that thin films of Bi_2Te_3, Bi_2Se_3, or Sb_2Te_3 doped with Cr or Fe are in fact QAH insulators in the absence of a magnetic field [22] [b]. Based on Yu's proposal, there were numerous experimental realizations of the QAH effect in $(Bi, Sb)_2Te_3$ doped with chromium [23, 25, 93] or vanadium [24]. In these material compounds, transport experiments [c] show a quantization of the QAH plateau with a precision of almost 10 parts-per-million [94, 95]. Finally, let us note that while the mechanism behind the ferromagnetic ground state was originally explained by the van Vleck mechanism [22], there has been an intense debate in the literature about its exact mechanism. The interested reader can find further information on this subject in Refs. [96, 97]. Further information on the QAH effect can be found in Refs. [90, 92].

1.4. Chiral anomaly and fermion number fractionalization in (1+1)D

In Sec. 1.4.1, we review some important properties and symmetries of the Dirac equation in (1+1)D which can be interpreted as the associated low-energy theory of a chiral edge state. Subsequently in Sec. 1.4.2, we show that the global symmetry of the classical Dirac theory, which guarantees that the difference in the number of right and left movers is conserved, cannot be elevated to the associated quantum theory. This will be our first example of a quantum anomaly. The presented calculations are thereby strongly based on Refs. [98, 99]. Finally, in Sec. 1.4.3, we discuss fermion number fractionalization which can result from a spatial dependence of the Dirac mass in (1+1)D. Further information on this subject can be found in one of the extensive reviews [100–102].

[a] We therefore have to disentangle the QAH from the QH effect which is induced additionally by the magnetic field. This issue will be the starting point for the discussion in Ch. 2.

[b] The bulk materials Bi_2Te_3, Bi_2Se_3, and Sb_2Te_3 are all 3D TIs. The low energy physics of their surface states is described by a Dirac Hamiltonian at each surface. In the thin film limit, the surface states hybridize which effectively gives rise to a BHZ-like model [22, 92]. The basis states of the associated low-energy Hamiltonian are therefore, in contrast to (Hg,Mn)Te determined by a combination of top and bottom surface states.

[c] That the transport is indeed carrier by edge channels, as in the QH phase, has been verified by nonlocal measurements [93].

1.4.1. Dirac equation in (1+1)D

The Lagrangian of a Dirac system in (1+1)D coupled to a $U(1)$ electromagnetic vector potential A_μ reads

$$\mathcal{L} = \bar{\psi}\left(\mathrm{i}\not{D} - m\right)\psi\,, \tag{1.70}$$

where $\not{D} = \not{\partial} - \mathrm{i}e\not{A}$, the adjoint spinor $\bar{\psi} = \psi^\dagger\gamma^0$, and $\{\gamma^\mu, \gamma^\nu\} = 2g^{\mu\nu}$ with $g^{\mu\nu} = g_{\mu\nu} = \mathrm{Diag}\left[1\,, -1\right]$ [a]. In the following, we use $\gamma^0 = \sigma_y$ and $\gamma^1 = \mathrm{i}\sigma_x$, implying that $\gamma^5 = \gamma^0\gamma^1 = \sigma_z$. We focus at first on the case $m = 0$, before we consider the effects of a nonzero Dirac mass in Sec. 1.4.3. The massless Dirac Lagrangian is invariant under the two global $U(1)$ symmetries, $\psi \to e^{\mathrm{i}\phi}\psi$ and $\psi \to e^{\mathrm{i}\phi\gamma_5}\psi$, where ϕ denotes a constant phase. According to Noether's theorem, these continuous global symmetries imply two locally conserved currents:

$$\partial_\mu j^\mu = \partial_t\rho + \partial_x j_x = 0 \qquad \text{with} \qquad j^\mu = -e\bar{\psi}\gamma^\mu\psi\,, \tag{1.71}$$

$$\partial_\mu j_5^\mu = \partial_t\rho_5 + \partial_x j_{5,x} = 0 \qquad \text{with} \qquad j_5^\mu = -e\bar{\psi}\gamma^\mu\gamma^5\psi\,. \tag{1.72}$$

Equations (1.71) and (1.72) imply the conservation of charge $Q = \int dx\, j^0$ and axial charge $Q_5 = \int dx\, j_5^0$, respectively. While the concept of charge should be clear, let us recast Eq. (1.70) slightly to shed light on the concept of axial charge. In the massless limit, we can insert

$$\psi = \begin{pmatrix}\psi_R \\ \psi_L\end{pmatrix} \tag{1.73}$$

into Eq. (1.70) to see that the Lagrangian decomposes into chiral left and right movers

$$\mathcal{L} = \psi_R^\dagger \mathrm{i}\left(D_0 + D_1\right)\psi_R + \psi_L^\dagger \mathrm{i}\left(D_0 - D_1\right)\psi_L\,. \tag{1.74}$$

In the same way, we can recast the two conserved currents to see that

$$j^\mu = j_R^\mu + j_L^\mu \qquad \text{with} \qquad j_i^\mu = -e\bar{\psi}_i^\dagger\gamma^\mu\psi_i\,, \tag{1.75}$$

$$j_5^\mu = j_R^\mu - j_L^\mu \qquad \text{with} \qquad j_{5,i}^\mu = -e\bar{\psi}_i^\dagger\gamma^\mu\gamma^5\psi_i\,, \tag{1.76}$$

where $i = \{R, L\}$. Hence, the conservation of Q means that the total number of left and right movers is fixed, while the conservation of Q_5 means that the difference in the number of left and right movers remains constant. This seems to be a natural result as left and right movers are decoupled for $m = 0$. However, we will see now that life becomes much more complicated when we try to quantize the classical theory.

[a] We work in (1+1)D which has one time and one space component. Greek indices run over 0 and 1.

1.4.2. Chiral (axial) anomaly

We will now elevate the classical Lagrangian to a quantum theory. To this end, we cross over to the second quantized Hamiltonian that is associated to Eq. (1.74):

$$\mathcal{H} = \int dx \, \left[\psi_R^\dagger \left(-\mathrm{i}\partial_x + eA_x \right) \psi_R - \psi_L^\dagger \left(-\mathrm{i}\partial_x + eA_x \right) \psi_L \right] , \tag{1.77}$$

where ψ_i with $i = \{R, L\}$ denote second quantized field operators and we set $A_0 = 0$ [a]. To solve the corresponding Schrödinger equation, we impose antiperiodic boundary conditions on the fermionic wave functions ψ_i and periodic boundary conditions on the vector potential A_x:

$$\psi_i(x = 0) = -\psi_i(x = L) \qquad \text{and} \qquad A_x(x = 0) = A_x(x = L) \, . \tag{1.78}$$

Choosing antiperiodic boundary conditions for ψ_i has the advantage that we eliminate zero energy solutions. This guarantees a unique definition of the ground state [b]. Choosing periodic boundary conditions for A_x implies that we can pick the vector potential to be constant in space [c]. Note however that we still allow A_x to be a slowly varying function of time (adiabatic).

Given these requirements, it is straightforward to calculate the spectrum:

$$E_{\pm,n} = \pm \left(k_n + eA_x \right) , \tag{1.79}$$

where $\pm$ corresponds to right and left chiral movers, respectively, and

$$k_n = \frac{2\pi(n + \frac{1}{2})}{L} \quad \text{with} \quad n \in \mathbb{Z} \, . \tag{1.80}$$

The additional factor $1/2$ originates from the antiperiodic boundary conditions. The spectrum for $A_x = 0$ is shown in Fig. 1.11(a). All states which are filled in the vacuum are highlighted by blue (right mover) or red (left mover). Let us now trace the evolution of the spectrum (keeping the occupation of states fixed), while we increase the vector potential adiabatically from $A_x = 0$ to $A_x = 2\pi/Le$. This specific transformation does not alter the spectrum, since $E_{+,n} \to E_{+,n+1}$ and $E_{-,n} \to E_{-,n-1}$. During this large gauge transformation [d], each state is exactly mapped onto another adjacent state as indicated in Fig. (1.11)(b) [e]. However, since we did not change the occupation of each

[a] We use $\hbar = 1$.

[b] The ground state (vacuum) is defined by occupying all states below $E = 0$. Zero energy states pose a problem as they can be either filled or empty.

[c] Any space dependent function which is in accordance with the boundary conditions can be gauged away. A constant potential is therefore the only nontrivial choice for A_x.

[d] Transformations, that connect two gauge equivalent Hamiltonians and cannot be reduced to the identity, are called large gauge transformations. Gauge invariance requires invariance under small and large gauge transformations.

[e] The permutation of states which occurs during a large gauge transformation is called spectral flow.

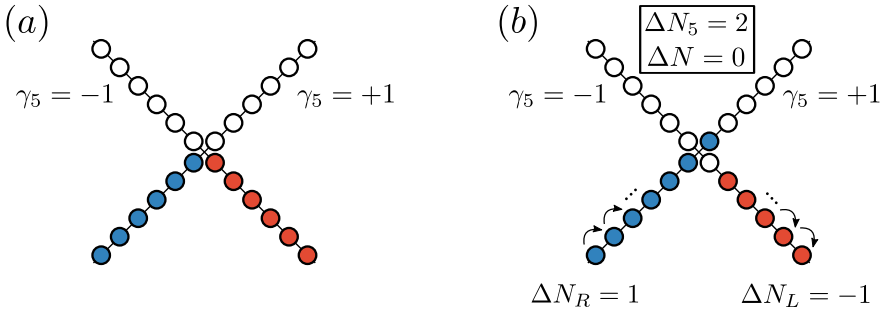

Figure 1.11.: Schematics of chiral anomaly in (1+1)D QED. Spectrum $[E(k)]$ for two types of chiral movers with opposite chirality, $\gamma_5 = \pm 1$, is shown. Filled right (left) movers are depicted in blue (red). Empty states are depicted in white. Ground state is defined in (a) in the absence of any external field and with the same number of filled right ($\gamma_5 = +1$) and left ($\gamma_5 = -1$) movers. (b) Subjecting the system to a vector potential A_x causes a permutation of states as indicated by arrows. This effectively reduces the number of left movers while the number of right movers increases, $\Delta N_5 = 2$. The total number of chiral movers is conserved $\Delta N = 0$.

state during this process, we find that there are actually two more right than left movers (cf. Fig. 1.11). To be precise, this amounts to

$$\Delta N_5 = \Delta N_R - \Delta N_L = -\frac{1}{e}\int dt\, dx\, \partial_\mu j_5^\mu = 2\,, \tag{1.81}$$

$$\Delta N = \Delta N_R + \Delta N_L = -\frac{1}{e}\int dt\, dx\, \partial_\mu j_5^\mu = 0\,, \tag{1.82}$$

where $\Delta N_5 = -\Delta Q_5/e$ is the change in the axial particle number and $\Delta N = -\Delta Q/e$ is the change in the particle number. More generally, we can write the change of the axial charge under a large gauge transformation with an arbitrary winding number as

$$\Delta N_5 = \int dt\, dx\, \frac{e}{2\pi}\epsilon^{\mu\nu}F_{\mu\nu}\ , \tag{1.83}$$

which implies that

$$\partial_\mu j_5^\mu = -\frac{e^2}{2\pi}\epsilon^{\mu\nu}F_{\mu\nu} \tag{1.84}$$

$$= -\frac{e^2}{h}\epsilon^{\mu\nu}F_{\mu\nu}\,. \tag{1.85}$$

where we reintroduced h in the second line. This highlights a violation of the classical conservation law for axial charge, Eq. (1.72). Equation (1.84) is also surprising from a naive physical point of view as the two chiral movers in Eq. (1.77) seem to be decoupled.

Equation (1.84) describes a so-called chiral (or axial) anomaly. It means that the underlying $U_A(1)$ symmetry of our classical theory has been violated on the quantum level. Quantum anomalies essentially originate from the infinite degrees of freedom of a

Dirac (or Dirac-like) theory [a] (there are no anomalies in theories with a finite number of degrees of freedom [103]). Their origin can essentially be traced back to the unboundedness of the Dirac spectrum which causes (unphysical) divergences in many physical observables, without careful treatment. By this, we mean that divergences must be removed by the procedure of regularization and renormalization during quantization to ensure finite results [98] [b]. There are however cases where such a procedure cannot be performed without violating any of the underlying classical symmetries. If this is the case, we speak of a quantum anomaly [c]. Note that if the classical symmetry is a continuous symmetry, Noether's theorem implies that a classical conservation law must be violated.

In deriving Eq. (1.84), we actually performed a laymen version of renormalization by computing the change in the (axial) particle number. Doing so, we subtracted the infinite Dirac sea at $A_x = 0$ from the final system at $A_x = 2\pi/Le$. For our purpose, this procedure is more than sufficient to focus on the physical essence of the chiral anomaly. The presented calculation followed thereby along the lines of Refs. [98, 99]. For a more detailed discussion, we would like to refer the interested reader to standard literature on regularization [49, 98, 99] and, in particular, to the seminal work by Fujikawa [104, 105].

Finally, let us note that chiral anomalies can only occur in even spacetime dimensions, such as (1+1)D or (3+1)D, in which the concept of chirality is well-defined [d]. For example, the corresponding chiral anomaly in (3+1)D reads [98]

$$\partial_\mu j_5^\mu = \frac{e^3}{16\pi^2}\epsilon^{\kappa\lambda\mu\nu}F_{\kappa\lambda}F_{\mu\nu} \propto \mathbf{E}\cdot\mathbf{B}\,, \tag{1.86}$$

where $\mathbf{E}$ and $\mathbf{B}$ denote the electric and magnetic field, respectively. In recent years, this became a hot topic in condensed matter physics as it was realized that 3D Weyl semimetals exhibit the chiral anomaly[30]. In this thesis, we mostly concentrate however on another anomaly, the parity anomaly, which will be discussed in Sec. 1.6. Nonetheless, the chiral anomaly in (1+1)D will turn out to be crucial to verify the existence of chiral edge states within a field theoretical approach, see Sec. 1.5.2.

Anomaly cancellation: Quantum anomalies are a vital tool in testing effective field theories for consistency. For instance, let us assume that we would write down the

[a] The concept is very much related to the unique properties of infinite series. A helpful conceptual understanding can be gained studying the thought experiment known as 'Hilbert's Hotel'.

[b] Roughly speaking, regularization and renormalization allows us to subtract the divergent contributions from the infinite Dirac sea and, thereby, allow us to define a proper ground state.

[c] In fact, which symmetries are violated by regularization can depend on the specific regularization scheme. However, any regularization scheme should ensure small and large gauge invariance. This is because a gauge symmetry is more than a symmetry. It actually describes a redundancy in the theory. If we violate gauge symmetries, particle can be created or destroyed out of nowhere.

[d] γ_5 does not exist in odd spacetime dimensions [50].

Lagrangian of a single chiral mover in (1+1)D. Following our previous discussion, it should be apparent that, in this case, the total particle number is not conserved under large gauge transformation (chiral anomaly). Instead, we would find that

$$\partial_\mu j^\mu = -\frac{e^2}{2h}\epsilon^{\mu\nu}F_{\mu\nu}\,. \tag{1.87}$$

If a single chiral mover could actually exist, particles could be created and destroyed out of nowhere. The resolution of this paradox lies in realizing that in any consistent theory (in even spacetime dimensions), there has to be the same number of chiral left and right movers [106]. This allows the anomaly to cancel in total, as the sign in Eq. (1.87) depends on the chirality of the associated edge channel. In condensed matter physics, this rule is also known as Nielsen-Ninomiya theorem [43, 44]. In fact, there is one exception to this rule which we got to know already as bulk-boundary correspondence: An odd number of chiral movers can exist if their (1+1)D world is only the boundary of a higher dimensional space. The chiral anomaly is then canceled by an associated anomaly of the bulk theory. We explain this mechanism in more detail in Sec. 1.5.2.

1.4.3. Fermion number fractionalization

We start again with the second quantized Hamiltonian of (1+1)D Dirac system. Only this time, we consider the case $A_\mu = 0$ and $m \neq 0$:

$$\mathcal{H} = \int dx \begin{pmatrix}\psi_R\\ \psi_L\end{pmatrix}^\dagger \begin{pmatrix}-\mathrm{i}\partial_x & \mathrm{i}m\\ -\mathrm{i}m & \mathrm{i}\partial_x\end{pmatrix}\begin{pmatrix}\psi_R\\ \psi_L\end{pmatrix}\,. \tag{1.88}$$

In the following, our goal is to compute the particle number in the ground state. To this end, we notice that Eq. (1.88) exhibits a chiral symmetry, as the associated single particle Hamiltonian anticommutes with σ_x. This means for every solution with positive energy, there is exactly one corresponding solution with negative energy (cf. Sec. 1.1.2). To be precise, the spectrum reads $E_\pm(k) = \pm\sqrt{m^2+k^2}$. We can expand the field operators in terms of the corresponding solutions:

$$\psi(x) = \sum_k \left[b_k u_k(x) + d_k^\dagger v_k(x)\right]\,, \tag{1.89}$$

where $u_k(x)$ and $v_k(x)$ denote the (two-component) solutions of the Schrödinger equation for positive and negative energies, respectively. The fermionic operator b_k destroys an electron with momentum k in the conduction band (E_+), while d_k destroys a hole with momentum k in the valence band (E_-) [a]. The fermionic operators fulfill the

[a] As it is standard procedure, we employed a particle-hole transformation for all states with negative energy [98].

conventional anticommutator relations:

$$\left\{b_k^\dagger, b_q\right\} = \left\{d_k^\dagger, d_q\right\} = \delta_{kq}\,. \tag{1.90}$$

The ground state is defined by filling all negative energy solutions (empty all holes):

$$|\text{vac}\rangle = \prod_k d_k\,|0\rangle\ . \tag{1.91}$$

If we naively try to compute the particle number in this ground state via the familiar expression for the particle number operator, $N = \int dx\,\psi^\dagger(x)\psi(x)$, we would end up with an infinite result. This is not acceptable and shows that a careful renormalization is necessary (as discussed previously). A simple way to renormalize the number operator is normal ordering [107]. In the case of a Dirac operator, it turns out that normal ordering is equivalent to antisymmetrization of the particle number operator [100]:

$$\begin{aligned} :N: &= \frac{1}{2}\int dx \sum_\alpha \left[\psi_\alpha^\dagger(x), \psi_\alpha(x)\right] \\ &= \frac{1}{2}\sum_k \left(\left[b_k^\dagger, b_k\right] + \left[d_k, d_k^\dagger\right]\right) \\ &= \sum_k \left[\left(b_k^\dagger b_k - \frac{1}{2}\right) - \left(d_k^\dagger d_k - \frac{1}{2}\right)\right] \\ &= \sum_k \left(b_k^\dagger b_k - d_k^\dagger d_k\right)\ . \end{aligned} \tag{1.92}$$

Here, we used in the first step the orthonormality of the basis states u_k and v_k. In the third line, it is important to notice that the presence of chiral symmetry implies that the two infinite (separately divergent) sums ($\sum_k 1/2$) cancel each other. For every factor $1/2$ in the first sum, there is exactly one corresponding term with opposite sign in the second sum [a]. Since $b_k\,|\text{vac}\rangle = d_k\,|\text{vac}\rangle = 0$, Eq. (1.92) clearly fulfills that $:N:\,|\text{vac}\rangle = 0$.

Fermion number fractionalization: Let us now replace the constant mass in Eq. (1.88) by a soliton profile, $m(x) = m\tanh x$, where m is a constant. A soliton is a time-independent domain wall that interpolates between $\pm m$ at $x \to \pm\infty$. Since the Hamiltonian still anticommutes in this case with σ_x, there are continuum solutions with $E_\pm(k)$ [109, 110]. As before, we label their wave functions by u_k and v_k [b]. However, in contrast to the previous case with $m(x) = const$, there is now one additional

[a] If there is neither chiral nor PH symmetry, this is no longer the case and calculating the difference of the two infinite sums becomes more complicated [51, 108].

[b] We do not need to determine their exact analytical solution. It is only important that they appear in pairs. For the exact wave functions, we refer the reader to Ref. [110].

normalizable solution at $E = 0$ [a]. Its wave function reads [102]

$$\phi_0(x) = \frac{1}{\sqrt{2}} \begin{pmatrix} 1 \\ -\mathrm{sgn}\,(m) \end{pmatrix} \exp\left[-\mathrm{sgn}\,(m) \int_0^x dx' m(x') \right] . \tag{1.93}$$

This solution is self charge conjugate, i.e., $\sigma_x \phi_0 = -\mathrm{sgn}\,(m)\, \phi_0$. In the literature, this type of zero energy solution is often dubbed Jackiw-Rebbi solution.

Taking this new solution into account, the field operator becomes

$$\psi(x) = \sum_k \left[b_k u_k(x) + d_k^\dagger v_k(x) \right] + a \phi_0(x) \,, \tag{1.94}$$

where a is a fermionic destruction operator for the zero energy solution. With this expression, we can again compute the particle number operator [cf. Eq. (1.92)]

$$\begin{aligned} N &= \frac{1}{2} \int dx \, \left[\psi^\dagger(x), \psi(x) \right] \\ &= \frac{1}{2} \sum_k \left(\left[b_k^\dagger, b_k \right] + \left[d_k, d_k^\dagger \right] \right) + \frac{1}{2} \left[a^\dagger, a \right] \\ &= \sum_k \left(b_k^\dagger b_k - d_k^\dagger d_k \right) + a^\dagger a - \frac{1}{2} \,. \end{aligned} \tag{1.95}$$

Remarkably, a single factor $1/2$ is left over in the final expression. This happens because the zero energy mode has no partner. As a consequence, the total particle number turns out to be fractional.

This surprising result was first described in the work by Jackiw and Rebbi [109]. It triggered a series of important follow-up works due to its counterintuitive nature [111–114]. In particular, it was shown that a single soliton cannot exist in a finite system [102, 112]. This is because solitons must come in pairs due to the finite system size, resulting in an even number of zero energy modes [b]. As a result, the total number of fermions is always integral in finite systems.

Finally, let us make a remark concerning the connection between Jackiw-Rebbi solutions and the edge states of a Chern insulator. Provided that $k_x = 0$, we can easily verify that the Hamiltonian of a Chern insulator is equivalent to Eq. (1.88), except for the Bk^2 term. In this sense, the zero energy modes which we found in Sec. 1.1.3 are conceptually very similar to Jackiw-Rebbi bound states.

[a] For $E = 0$, the Schrödinger equation becomes $\partial_x \phi_0(x) = m(x) \sigma_x \phi_0(x)$.

[b] These pairs can be locally separated which means that fractional fermion numbers can be at least realized locally [102, 112].

1.5. Topological field theory

In this section, we will introduce the effective topological field theory of the QH effect, the Chern-Simons theory. It captures the essential topological features of the QH effect without relying on its microscopic details. This means it describes the quantization of the Hall conductivity and the existence of chiral edge states without relying on the microscopic Schrödinger equation. In contrast to the previous sections, we will therefore leave the Hamiltonian formalism and work within an effective field theoretical approach. This section is a corner stone in understanding the effective topological field theory of topological insulators [52]. In Sec. 1.5.1, the Chern-Simons action is introduced on a compact domain (no boundaries). Its fundamental connection to the QH effect is revealed. Thereby, we follow in particular along the lines of Refs. [53] and [50]. In Sec. 1.5.2, we go one step further and discuss a Chern-Simons theory on a finite domain with boundaries. It is shown that in order to end up with a consistent theory edge channels must exist at the boundary. This is the field-theoretical analog of the bulk-boundary correspondence which we have encountered previously using a Hamiltonian approach. The line of reasoning in this section is similar to that of Ref. [115]. The interested reader can find further details and generalization to the fractional QH effect for instance in Ref. [42, 116–120].

1.5.1. Chern-Simons theory

In (2+1)D, there is a unique type of action which is known as Chern-Simons term:

$$S_{CS} = k\frac{e^2}{2h}\int d^3x\, \epsilon^{\mu\nu\rho} a_\mu(x)\partial_\nu a_\rho(x)\,, \tag{1.96}$$

where k is called the Chern-Simons level, $\epsilon^{\mu\nu\rho}$ is the Levi-Civita symbol, and $a_\mu(x)$ is a $U(1)$ Abelian electromagnetic vector potential. In the following, we will show that the Chern-Simons theory captures the topological response of the QH effect which we have described in Sec. 1.3.1.

In the context of the QH effect, a_μ is considered as a small perturbing vector potential, that comes on top of the underlying external vector potential A_μ. The latter, which gives rise to the QH effect in the first place, is not explicitly considered within Eq. (1.96). The small perturbing vector potential a_μ transforms under parity symmetry as $a_0(t,\mathbf{x}) \to a_0(t,\mathbf{x}')$, $a_1(t,\mathbf{x}) \to -a_1(t,\mathbf{x}')$, and $a_2(t,\mathbf{x}) \to a_2(t,\mathbf{x}')$ with $\mathbf{x}' = (t,-x,y)$ [a] [62]. A Chern-Simons term is hence odd under parity symmetry, $\epsilon^{\mu\nu\rho}a_\mu\partial_\nu a_\rho \to -\epsilon^{\mu\nu\rho}a_\mu\partial_\nu a_\rho$. In the same fashion, it can be proven that a CS term also breaks TR symmetry. Hence, Eq. (1.96) breaks analogously to the QH effect parity

[a] The small perturbing vector potential a_μ, opposed to the background vector potential A_μ, is considered as a quantum operator. As such, it transform under parity (cf. Sec. 1.1.4).

and TR symmetry.

To determine the corresponding charge carrier density and the current density, we can take the functional derivative of the effective action with respect to $a_\lambda(x)$

$$\begin{aligned} j^\lambda(x) &= \frac{\delta S_{CS}}{\delta a_\lambda(x)} \\ &= k\frac{e^2}{2h}\left[\int d^3y\, \epsilon^{\mu\nu\rho}\delta(x-y)\delta_\mu^{\ \lambda}\partial_\nu a_\rho(y) - \int d^3y\, \epsilon^{\mu\nu\rho}\partial_\nu a_\mu(y)\delta(x-y)\delta_\rho^{\ \lambda}\right] \\ &= k\frac{e^2}{h}\epsilon^{\lambda\nu\rho}\partial_\nu a_\rho\,. \end{aligned} \tag{1.97}$$

Here, we applied the product rule in the first step and made use of the properties of the antisymmetric Levi-Civita symbol in the second step. Let us recast the result in nonrelativistic notation. The $0th$ component of the three current determines the charge carrier density:

$$j^0 = \rho = k\frac{e^2}{h}\left(\epsilon^{012}\partial_1 a_2 + \epsilon^{021}\partial_2 a_1\right) = -k\frac{e^2}{h}B_\perp\,. \tag{1.98}$$

The remaining two components stand for the current density in $x.$ and y-direction:

$$j^i = -k\frac{e^2}{h}\epsilon^{ij}E_j \quad \text{with} \quad i,j = \{x,y\}\,. \tag{1.99}$$

This looks like the typical, quantized Hall response. But so far, we have not yet shown that k is actually an integer number.

To complete the proof that a Chern-Simons term serves as the effective field theory of the QH effect, we have to discuss another important property of a CS term. Its properties under gauge transformation, $a_\mu \to a_\mu + \partial_\mu\omega$:

$$\begin{aligned} S_{CS} &\to S_{CS} + k\frac{e^2}{2h}\int d^3x\, \epsilon^{\mu\nu\rho}\left(a_\mu\partial_\nu\partial_\rho\omega + \partial_\mu\omega\partial_\nu a_\rho + \partial_\mu\omega\partial_\nu\partial_\rho\omega\right) \\ &= S_{CS} + k\frac{e^2}{2h}\int d^3x\, \partial_\mu\left(\omega\epsilon^{\mu\nu\rho}\partial_\nu A_\rho\right)\,. \end{aligned} \tag{1.100}$$

The CS term is only gauge invariant up to a total derivative [62]. In many circumstances, such boundary terms can be ignored as the variation vanishes at spatial infinity. However, there are actually exceptions to this rule and Eq. (1.100) is an example of this. In particular, let us impose a compact S^2 manifold for the two spatial components and a compact S^1 manifold for the time [a]. The Chern-Simons action transforms then under a large gauge transformation to [53]

$$S_{CS} \to S_{CS} + 2\pi\hbar k\,, \tag{1.101}$$

[a] To be precise, we have to insert a single flux in the unit sphere which is given by $\frac{1}{2\pi}\int_{S^2} F_{12} = \frac{\hbar}{e}$. Further details can be for instance found in Ref. [53].

which shows that the boundary term is nonzero. This result looks dangerous because any physically meaningful theory should be invariant under small and large gauge transformations. However, to be precise, it is the partition function $Z = \exp(\mathrm{i}S_{CS}/\hbar)$ for which gauge invariance must hold. This means an effective action has to be only gauge invariant up to integer multiples of $2\pi\hbar$, restricting k to integer numbers. This allows us to identify the Chern-Simons level k as the QH filling factor ν, defined in Eq. (1.56).

1.5.2. Anomaly inflow and bulk-boundary correspondence

So far, we have considered a Chern-Simons action on a sphere, i.e., on a domain without boundaries. Suppose we restrict now the Chern-Simons action onto a half-space with $x < x_{edge}$. More precisely, let us assume a single LL ($\nu = 1$) is occupied for $x < x_{edge}$ and the other half of the 2D plane describes a vacuum where no current can flow ($\nu = 0$). This case is schematically illustrated in Fig. 1.12. Looking at Eq. (1.97), let us assert that the current of the entire system is given by

$$j^{\mu}_{bulk} = \Theta(-x + x_{edge})\frac{e^2}{h}\epsilon^{\mu\nu\rho}\partial_\nu a_\rho \,, \tag{1.102}$$

where we replaced the constant filling factor ν by a soliton-like profile, $\nu(x) = \theta(-x + x_{edge})$. We can easily see that this assertion must be incorrect. Equation (1.102) cannot describe the entire system, since this would imply that the current conservation is violated at the edge (the system is not gauge invariant):

$$\begin{aligned}
\partial_\mu j^{\mu}_{bulk} &= \frac{e^2}{h}\left[\Theta(-x + x_{edge})\epsilon^{\mu\nu\rho}\partial_\mu\partial_\nu a_\rho + (\partial_x\Theta(-x + x_{edge}))\,\epsilon^{1\nu\rho}\partial_\nu a_\rho\right] \\
&= -\delta(-x + x_{edge})\frac{e^2}{h}\epsilon^{1\nu\rho}\partial_\nu a_\rho \\
&= \delta(x - x_{edge})\frac{e^2}{2h}\epsilon^{\alpha\beta}F_{\alpha\beta} \qquad (1.103) \\
&= \delta(x - x_{edge})\frac{e^2}{2h}E_y \,, \qquad (1.104)
\end{aligned}$$

where $\alpha, \beta = \{0, 2\}$, $\epsilon^{02} = -\epsilon^{20} = 1$, and E_y stands for a small electric field in the y-direction. How does this violation of charge conservation at the edge of the domain appears? As a response to an electric field in the y-direction, a current is induced in the x-direction in the half-space $x < x_{edge}$ (cf. Fig. 1.12). However, since we have assumed that current cannot flow for $x > x_{edge}$, electrons must disappear at the boundary, which is the result of Eq. (1.104). This is unphysical [a]. It seems that we must have missed

[a] Recall that a Chern-Simons action is only gauge invariant up to a boundary term. On a domain without boundaries, we fixed this issue by restricting the filling factor to integer values. On a domain with boundaries, we see that equivalently we must add a local degree of freedom to the effective theory.

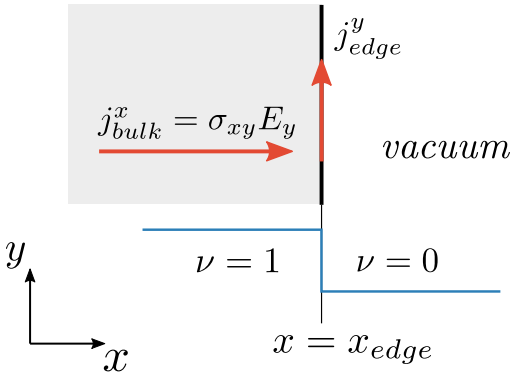

Figure 1.12.: Anomaly cancellation between bulk and edge theories at $x = x_{edge}$ is schematically depicted. Single LL with $\nu = 1$ occupies half-space with $x < x_{edge}$. No current can flow for $x > x_{edge}$ (vacuum). To ensure charge conservation, a chiral edge channel must exist at the boundary between these domain.

an important degree of freedom.

To resolve this issue, let us carefully look at Eqs. (1.104) and (1.87). We notice that the non-conservation of the bulk current matches exactly the chiral anomaly of a single chiral mover in (1+1)D (living along the line at $x = x_{edge}$), i.e.:

$$\partial_\mu j^\mu_{bulk} = -\partial_\mu j^\mu_{edge} \,. \tag{1.105}$$

We can therefore define a physical meaningful theory by extending the effective Chern-Simons action by the effective action of a (1+1)D Dirac system [42, 120]. The latter must exist at the boundary of the domain. The current of the full system is then again conserved:

$$j^\mu_{tot} = j^\mu_{bulk} + j^\mu_{edge} \tag{1.106}$$

$$\partial_\mu j^\mu_{tot} = \partial_\mu \left(j^\mu_{bulk} + j^\mu_{edge} \right) = 0 \,. \tag{1.107}$$

The bulk current which is lost at the boundary does not spontaneously disappear. It just flows from the bulk onto the edge of the system. This process is schematically depicted in Fig. 1.12.

We have so far considered a semi-infinite space with a single boundary at $x = x_{edge}$. Based on this it is now straightforward to generalize the discussion to a finite domain with boundaries at $x = x_L$ and $x = x_R$ [a]:

$$\nu \to \nu(x) = \frac{1}{2} \left[\theta(x - x_L) - \theta(x - x_R) \right] \,. \tag{1.108}$$

Due to the required anomaly cancellation, one can immediately infer the existence

[a] The interested reader can find further information in Ref. [120].

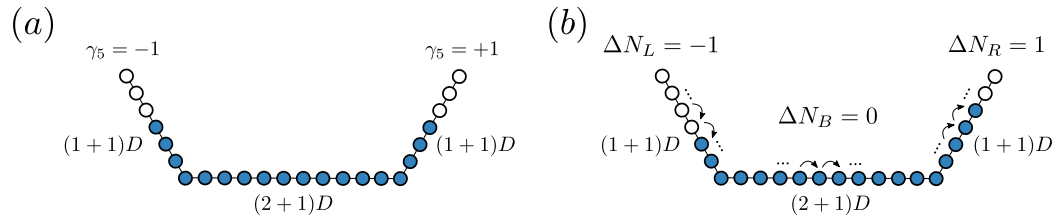

Figure 1.13.: Anomaly cancellation between bulk and edge theory for single LL. (1+1)D chiral movers are embedded in higher dimensional space, i.e., (2+1)D bulk. (a) Ground state is defined by same number of left and right movers and a completely filled bulk LL. Filled states are depicted in blue, empty states in white. (b) Anomaly cancellation occurs not directly between (1+1)D chiral movers but, at each edge, between the respective edge and and bulk theory. Constant electric field pumps carriers from left to right edge through bulk.

of chiral edge channels at the two edges. The non-conservation of bulk current at $x = \{x_L, x_R\}$ must be locally compensated by the existence of chiral edge channels. Hence, we can now understand the presence of edge states in the QH effect, which we encountered previously in Fig. 1.5, in terms of anomaly cancellation.

To shed more light on the conceptual idea, let us study the effect of an electric field on a single LL. As shown in Fig. 1.13(a), suppose thereby that the system is at first in equilibrium. The local chemical potential is the same at both edges. We apply now, analogously to Sec. 1.4.2, an electric field along the x-direction. This causes the momentum to shift from $k_x \to k_x + 2\pi/L$. Making use of the explicit form of the $n = 0$ LL wave function ψ_{0,k_x}, given by Eq. (1.57), we notice that a shift in k_x is accompanied by a change of the spatial localization of all wave functions in the y-direction [a]. More concretely, each wave function is exactly mapped onto its neighboring state with momentum $k_x + 2\pi/L$ [b]. This process is highlighted by arrows in Fig. 1.13(b). While apparently the number of filled bulk states did not change during the process, a single electron was effectively transferred from the left to the right edge. This is in essence Laughlin's gauge argument [121] and highlight the crucial role of edge channels in the QH effect.

In a nutshell, we have found that it is possible to locally circumvent the Nielsen-Ninomiya theorem (Sec. 1.4.2) by embedding a chiral edge channel within a higher dimensional space [c]. This is also known as Callan-Harvey mechanism [106], which can be interpreted as the field-theoretical analog of the bulk-boundary correspondence.

[a] Recall that the wave functions are centered at y_{k_x}. Applying an electric field alters k_x such that $y_{k_x} \to y_{k_x + 2\pi/L}$. Hence, all wave functions are shifted.

[b] Recall that we assumed periodic boundary conditions in the x-direction resulting in $k_x = 2\pi n/L$ with $n = \ldots -2, -1, 0, 1, 2, \ldots$.

[c] There is an odd number of chiral movers at the boundary of a Chern-Simons action.

1.6. Parity anomaly

We have shown so far that Dirac theories in even spacetime dimensions exhibit the chiral anomaly. In this section, we will now focus instead on Dirac theories which are defined in odd spacetime dimensions. To be more specific, we consider a single Dirac fermion in (2+1)D. If the Dirac fermion is massless, such a theory obeys parity symmetry on the classical level. But, as it was pointed out by Redlich [122, 123], the parity symmetry cannot be maintained on the quantum level as it is in conflict with gauge invariance. Since a Dirac system in (2+1)D is equivalent to a Chern insulator, except for the Bk^2 term, the parity anomaly implies that a single, massless Chern insulator cannot exist in (2+1)D. Further consequences of this statement will be the main topic of Ch. 2. In Sec. 1.6.1, the Dirac Lagrangian is introduced and the analogy to a Chern insulator is explicitly shown. Following, the parity anomaly is explained based on the work by Redlich [122].

1.6.1. Dirac equation in (2+1)D

The Lagrangian of a Dirac system in (2+1)D QED coupled to an abelian $U(1)$ electromagnetic vector potential A_μ reads

$$\mathcal{L} = \bar{\psi}\left(\mathrm{i}\not{D} - m\right)\psi\,, \tag{1.109}$$

where $\not{D} = \not{\partial} - \mathrm{i}e\not{A}$, the adjoint spinor $\bar{\psi} = \psi^\dagger\gamma^0$, and $\{\gamma^\mu, \gamma^\nu\} = 2g^{\mu\nu}$ with $g^{\mu\nu} = g_{\mu\nu} = \mathrm{Diag}\left[1\,, -1\,, -1\right]$ [a]. In the following, we use $\gamma^0 = \sigma_z$, $\gamma^1 = \mathrm{i}\sigma_y$, and $\gamma^2 = \mathrm{i}\sigma_x$. Note that we cannot define γ^5 for a single Dirac fermion in (2+1)D, since all basis elements of 2D Hermitian matrices were already employed (all Pauli matrices). The concept of chirality, which is based on γ^5 does not exist in (2+1)D for a single Dirac fermion.

To see the connection between QED and a Chern insulator, let us derive the second quantized Hamiltonian associated to Eq. (1.109) [b]:

$$H_{QED} = \int dx^2\, \psi^\dagger \left[-\mathrm{i}\psi^\dagger\gamma^0\gamma^i D_i + m\gamma^0\right]\psi \tag{1.110}$$

$$= \int dx^2\, \psi^\dagger \begin{pmatrix} m & \pi_x + \mathrm{i}\pi_y \\ \pi_x - \mathrm{i}\pi_y & -m \end{pmatrix}\psi\,, \tag{1.111}$$

where π_i with $i = \{x, y\}$ is given by Eq. (1.40), and $\psi(x)$ denotes a second quantized (two-component) field operator. The QED Hamiltonian is equivalent to a Chern insulator [Eq. (1.16)] except for the Bk^2 term.

[a] All Greek indices run over $0, 1$ and 2.
[b] Note that the Hamiltonian is not yet renormalized properly.

1.6.2. Violation of parity symmetry in (2+1)D

Let us start with a single, massless Dirac fermion which is described by the classical Lagrangian given by Eq. (1.109) with $m = 0$. This theory obeys parity and TR symmetry [cf. symmetry considerations in Sec. 1.1.3.]. The presented discussion follows along the lines of Refs. [122] and [123]. To quantize the theory, we use the fermionic path integral in Minkowski spacetime which for $m = 0$ reads

$$Z[A] = \int d\bar{\psi} d\psi \, \exp\left[\mathrm{i} \int d^3x \, \bar{\psi} \, \mathrm{i} \not{D} \psi \right] , \tag{1.112}$$

where the integral is taken over the independent Grassman fields $\bar{\psi}$ and ψ, which fulfill that $\{\bar{\psi}, \psi\} = 0$. It is now convenient to apply a Wick rotation (analytic continuation in time) to work in Euclidean spacetime [49]:

$$\begin{aligned} x^0 &= -\mathrm{i} x^3 \qquad , \qquad \partial_0 = \frac{\partial}{\partial x^0} = \mathrm{i} \frac{\partial}{\partial x^3} \\ \gamma^0 &= -\mathrm{i} \gamma^3 \qquad , \qquad A_0 = \mathrm{i} A_3 \, , \end{aligned} \tag{1.113}$$

so that the metric becomes $g^{\mu\nu} = -\delta^{\mu\nu}$ with $\mu = 1, 2, 3$, and all γ-matrices are anti-Hermitian, i.e., $(\gamma^\mu)^\dagger = -\gamma^\mu$. The Dirac operator is form invariant under this transformation:

$$\mathrm{i} \not{D}_M \to \mathrm{i} \not{D}_E \, , \tag{1.114}$$

where we added the indices to distinguish between Minkowski (M) and Euclidean spacetime (E). In the following, we drop however the index E to keep the notation as simple as possible. The main reason, that the Wick rotation was employed, is that the Dirac operator $\not{D}$ is now Hermitian and has therefore real eigenvalues λ_i:

$$\not{D} \psi_i = \lambda_i \psi_i \, . \tag{1.115}$$

The fermionic path integral in Euclidean spacetime is given by

$$Z[A] = \int d\bar{\psi} d\psi \, \exp\left[- \int d^3x \, \bar{\psi} \, \mathrm{i} \not{D} \psi \right] = \det\left(\mathrm{i} \not{D} \right) , \tag{1.116}$$

where we made use of the coordinate transformation $\psi' = \mathrm{i} \not{D} \psi$ to transform the integral into a Gaussian integral. The latter is then easy to evaluate [51]. The determinant of the matrix $\mathrm{i} \not{D}$ is given by the product of its eigenvalues

$$Z[A] = \det\left(\mathrm{i} \not{D} \right) = \prod_i \mathrm{i} \lambda_i \, . \tag{1.117}$$

As we have not yet regularized the theory, there are still an infinite number of eigen-

values λ_i which can be either positive or negative. It is hence impossible to decide whether $Z[A]$ has a positive or a negative sign [103].

The problematic nature of this ambiguity becomes apparent when we try to define the fermion determinant to be positive. It turns out that this definition is in conflict with gauge invariance. As it was shown in Ref. [122, 123], the fermion determinant changes its sign under large gauge transformations that are characterized by an odd winding number n

$$\det\left(\mathrm{i}\not{D}\right) \to (-1)^{|n|}\det\left(\mathrm{i}\not{D}\right) \ . \tag{1.118}$$

This is because an odd number of eigenvalues cross zero if n is an odd integer number [a]. Note that this effect resembles the origin of the chiral anomaly.

In order to restore gauge invariance, a proper regularization scheme has to be chosen. For instance, we can employ a Pauli-Villars regulator which comes however at the cost of breaking parity symmetry [62, 122]. In the case of this regularization scheme, we introduce an additional massive Lagrangian

$$\mathcal{L}_{PV} = \bar{\chi}\left(\mathrm{i}\not{D} - M\right)\chi \tag{1.119}$$

to our system, where M is the Pauli-Villars mass and χ fulfills a bosonic statistics. It can be shown that a Pauli-Villars regulator induces a Chern-Simons term in the effective action $Z[A] = \exp(\mathrm{i}S_{eff}/\hbar)$, where [122, 123]

$$S_{eff} = \mathrm{sgn}\left(M\right)\frac{e^2}{4h}\int d^3x\, \epsilon^{\mu\nu\rho}A_\mu\partial_\nu A_\rho + S_{NA} \tag{1.120}$$

and S_{NA} is a nonanalytic term. The latter is associated with infrared divergences originating from the massless Dirac fermion [122]. The total effective action, including the effect of the Pauli-Villars regulator, is gauge invariant [124] but breaks parity symmetry.

In fact, this statement is universal. There is no regularization method that preserves both parity symmetry and gauge invariance for an odd number of Dirac fermions in (2+1)D. Hence, parity symmetry cannot be maintained on the quantum level for an odd number of Dirac fermions [b]. This is the essence of the parity anomaly [c]. More

[a] The detailed proof of Eq. (1.118) is based on the Atiyah-Patodi-Singer index theorem [51] and can be found in Ref. [122].

[b] Recall that large gauge invariance cannot be violated in a consistent theory.

[c] TR symmetry is also violated by the Pauli-Villar regulator. In fact, in (2+1)D, TR and parity symmetry behave always in the same way. It is therefore also valid to refer to the parity anomaly as TR anomaly [103].

generally, it can be shown that large gauge invariance requires that [125]

$$\frac{N_f}{2} + k \in \mathbb{Z}\,, \tag{1.121}$$

where N_f is the number of Dirac fermions and k is the Chern-Simons level which must be introduced during regularization (for example by Pauli-Villars method). In our case, $N_f = 1$ and a Chern-Simons term with $k = 1/2$ is induced by the Pauli-Villar regulator.

The parity anomaly goes hand in hand with a nonzero vacuum (ground state) current which arises from the Chern-Simons term. To show this, we can take the functional derivative of Eq. (1.120) with respect to A_μ to arrive at [cf. Sec. 1.5.1]

$$j^\mu = \frac{\delta S_{eff}}{\delta A_\mu} = \mathrm{sgn}\,(M)\,\frac{e^2}{2h}\epsilon^{\mu\nu\rho}\partial_\nu A_\rho\,. \tag{1.122}$$

The same result was first obtained by Niemi and Semenoff using a different approach [126]. Hence, the parity anomaly implies the requirement of a nonzero Hall conductivity σ_{xy} even in the absence of a magnetic field. In this sense, the QAH effect can be understood as the condensed matter analog of the parity anomaly [8].

2.

Fate of QAH Effect in Magnetic Fields: The Parity Anomaly

Contents

2.1. Introduction and model **53**
2.1.1. Chern insulator on the lattice - numerical approach: 57
2.2. Bulk particle number and spectral asymmetry in magnetic fields **59**
2.2.1. With particle-hole symmetry 59
2.2.2. Without particle-hole symmetry 64
2.3. Magnetotransport - signatures of parity anomaly **67**
2.4. Effective field theory **71**
2.5. Charge pumping **73**
2.5.1. Numerical approach 73
2.5.2. Transport signature at constant density 77
2.6. Coexistent QH and QAH edge states **78**
2.6.1. Transport in the Dirac mass gap - edge perspective 79
2.6.2. Role of broken particle-hole symmetry 82
2.6.3. Transport of coexistent QH and QAH edge states 86
2.7. Signatures of parity anomaly in para- and ferromagnetic TIs **90**
2.8. Summary **95**

In the course of this thesis, we have come across two 2D topological states of matter, which are both described by a quantized σ_{xy} due to a broken parity and TR symmetry: The QH and the QAH phase. In the QH phase, we clarified that parity and TR symmetry are broken by an external out-of-plane magnetic field. As such, the QH phase relies on the formation of LLs. In comparison, these symmetries are violated in the QAH phase by the band structure itself [21, 90]. As such, the QAH phase is a condensed matter analog of the parity anomaly. This means the quantization of σ_{xy} arises even in the absence of LLs [8], as explained in Sec. 1.6 [a]. Although QH and QAH phases have therefore different physical origins, they fall into the same symmetry class [b] and are both described by a $\mathbb{Z}$-topological invariant [10, 11]. When a QAH insulator is subjected to an external magnetic field, it is hence natural to ask whether unique signatures of the QAH phase and, hence, of the parity anomaly persist in the presence of LLs.

Let us clarify this question: In an analytic calculation, the bulk spectrum of a QAH insulator consists solely of LLs in the presence of a magnetic field [cf. Eqs. (2.9) and (2.10)]. As it was pointed out in Sec. 1.5, the bulk-boundary correspondence demands that each of these LLs is uniquely related to a single, chiral edge state (per edge) because of the requirement of anomaly cancellation. It is hence a priori not obvious whether the information of the QAH phase, i.e., the inverted band structure, can remain encoded in the presence of LLs. Moreover, assuming signatures of the QAH phase survive in magnetic fields, the question arises whether it can be experimentally distinguished from the QH phase, which is also characterized by chiral edge channels and a quantized σ_{xy}. These questions are of particular importance for paramagnetic TIs, such as (Hg,Mn)Te, as a finite magnetic field is required in these materials to induce the QAH phase [21, 90].

In this chapter, we answer these questions by revealing that the QAH topology remains encoded in the bulk LL spectrum by means of a particular topological quantity, the spectral asymmetry η [51, 127]. This quantity, which is a signature of the parity anomaly [108, 128], represents the difference in the number of states between valence and conduction band. While a QAH insulator is characterized by a nonzero spectral asymmetry in magnetic fields, a conventional insulator is in contrast always characterized by a vanishing η. This connection allows us to differentiate QAH from QH phases in magnetic fields. In addition, we show that the spectral asymmetry is connected to unique, experimentally accessible signatures. In that regard, we show that, similar to the QSH phase, a pair of counterpropagating QH and QAH edge states can emerge in a QAH insulator in magnetic fields. However, in contrast to the helical edge states of

[a] To be precise, the statement of the parity anomaly goes one step further. An odd number of Dirac-like fermions in (2+1)D can only exist if parity and TR symmetry are broken.

[b] This statement is only correct in the absence of PH symmetry.

QSH insulators, these counterpropagating edge states are not protected by symmetry. They form a pair of quasi-helical edge states [129]. We analyze the evolution of these quasi-helical edge states in magnetic field and discuss their transport signatures.

The chapter is structured as follows: We recap in Sec. 2.1 properties of Chern insulators and the BHZ model and clarify their connection to the parity anomaly. Focusing at first on a Chern insulator, we reveal in Sec. 2.2 a connection between the particle number operator of a Chern (QAH) insulator and the spectral asymmetry in magnetic fields. This allows us in Sec. 2.3 to derive a general expression for σ_{xy} as a function of μ and $B_\perp$ via Streda's formula. In Sec. 2.4, the effective field theory of a QAH insulator is derived. Using anomaly cancellation, it is shown that the QAH edge states survive in magnetic fields and can coexist with counterpropagating QH edge states at certain chemical potentials. The subsequent sections shed further light on the specific properties of quasi-helical edge states. In Sec. 2.5, it is shown that a unique type of charge pumping is linked, in increasing magnetic fields, to the survival of the QAH edge states. In Sec. 2.6, hybridization between the quasi-helical edge states is examined [a] and a scenario is proposed, in which transport measurements allow their unambiguous identification. Finally in Sec. 2.7, the role of the parity anomaly and the spectral asymmetry is discussed for the BHZ model. Differences between ferro- and paramagnetic TIs are explained, and experimental consequences are derived. We conclude this chapter in Sec. 2.8 by providing a summary of our main results.

The results of this chapter have been published in Refs. [P5] and [P6]. Reference [P5] is copyrighted by the American Physical Society [b]. This chapter contains revised versions of these publications, including the associated supplementary materials.

2.1. Introduction and model

Our starting point is the BHZ model [15] (see also Eq. (1.61))

$$H(\mathbf{k}) = \begin{pmatrix} h(\mathbf{k}) & 0 \\ 0 & h^\star(-\mathbf{k}) \end{pmatrix}, \tag{2.1}$$

[a] Recall that they are not protected by symmetry and can therefore hybridize.

[b] Christian Tutschku and I contributed equally to Ref. [P5]. I performed all calculations regarding the spectral asymmetry which allowed us to calculate the effective action. Christian Tutschku derived the effective edge theories, presented in Eqs. (2.71a)–(2.71c). The numerical code in Sec. 2.5 was developed in close collaboration. Recently, C. Tutschku extended his work on the effective field theoretical description of QAH insulators. His work has been published in Ref. [P8] (I am a co-author of this manuscript).

where both spin blocks are connected by TR and parity symmetry, and each spin block is determined by a single Chern insulator (see also Eq. 1.16):

$$h(\mathbf{k}) = \begin{pmatrix} M - (B+D)k^2 & Ak_+ \\ Ak_- & -M + (B-D)k^2 \end{pmatrix} . \tag{2.2}$$

Using a unitary transformation, it is useful to recast Eq. (2.1) into the following form:

$$UH(\mathbf{k})U^\dagger = \mathrm{Diag}\left[h(\mathbf{k}, M, B)\,,\, h(\mathbf{k}, -M, -B)\right] , \tag{2.3}$$

where $U = \mathrm{Diag}\left[\sigma_0\,,\,\sigma_y\right]$ and the dependence on the parameters M and B was written out explicitly. Equation (2.3) shows that it is sufficient to obtain analytical results for a single spin block of the BHZ model. That is because results for the second spin block can be obtained by replacing

$$M \to -M \qquad \text{and} \qquad B \to -B \tag{2.4}$$

at the end of the calculation. In the following, we focus therefore at first on a single Chern insulator. Results for the full BHZ model are discussed in Sec. 2.7.

Parity anomaly: A Chern insulator describes a Dirac-like system. This means its Hamiltonian matches the one of a Dirac fermion in (2+1)D, except for the additional, non-relativistic mass term B. A Chern insulator is characterized by a broken TR and parity symmetry by virtue of the Dirac mass M and the non-relativistic mass B. This comes along with an integer quantized Hall response in the bulk gap, even in the absence of a magnetic field [cf. Eq. (1.23)] [59]

$$\sigma_{xy} = \frac{e^2}{2h}\left[\mathrm{sgn}\,(M) + \mathrm{sgn}\,(B)\right] . \tag{2.5}$$

In the case that $M/B > 0$, a Chern insulator is a QAH insulator. And as such, it is a condensed matter analog of the parity anomaly.

There are several consequences of this connection, which we would like to point out. The Hall conductivity does not vanish in the limit of $M, B \to 0^{\pm}$. Instead, it depends on whether the limit is approached from above or below. This is because parity symmetry must be violated for an odd number of Dirac fermions in (2+1)D. A single, parity-invariant Chern insulator cannot exist in two (spatial) dimensions. This is the essence of the parity anomaly, as explained in Sec. 1.6. It means that even if we had started with a parity symmetric theory ($M = B = 0$), we would have had to still break parity symmetry during the computation of σ_{xy} [122, 126, 130]. The quantized Hall conductivity of a Chern insulator can be therefore interpreted as a mandatory

consequence of the parity anomaly [a]. There are only two ways to re-establish parity symmetry and, thereby, cancel the parity anomaly in (2+1)D. We have to either embed the Chern insulator within a higher dimensional space [in this case, (3+1)D], or we have to add a second Chern insulator to our effective model [122, 125].

These two mechanisms are very similar to anomaly cancellation for a single chiral fermion in (1+1)D. Recall that in this case, the anomaly can be either canceled by another chiral fermion with the opposite chirality (cf. Sec. 1.4.2), or by embedding the theory in a (2+1)D space (cf. Sec. 1.5.2). However, there is one important difference between the two cases. While the chiral anomaly must be canceled in a consistent theory [106], there is no problem in having an effective theory that does not obey parity symmetry. In other words, the parity anomaly does not need to be canceled which is why a QAH insulator can exist in nature.

Magnetic field: Similar to the discussion in Sec. 1.3.1, we are now going to consider the effect of an external, out-of-plane magnetic field $B_\perp$ that is incorporated via the Peierls substitution in the Landau gauge $\boldsymbol{\pi} = \mathbf{k} + e\mathbf{A}/\hbar$ with $\mathbf{A} = -yB_\perp \mathbf{e}_x$. We impose periodic boundary conditions in the x-direction and require the wave functions to be square-integrable in the y-direction. Analytic results for the corresponding bulk LL energies are then obtained by replacing the canonical momentum operators of Eq. (2.2) by ladder operators, according to Eq. (1.51). This yields for $\operatorname{sgn}(eB_\perp) > 0$ [17]:

$$h = \begin{pmatrix} M - 2l_{B_\perp}^{-2}(B+D)\left(a^\dagger a + 1/2\right) & \sqrt{2} l_{B_\perp}^{-1} A a^\dagger \\ \sqrt{2} l_{B_\perp}^{-1} A a & -M + 2l_{B_\perp}^{-2}(B-D)\left(a^\dagger a + 1/2\right) \end{pmatrix} . \tag{2.6}$$

This allows us to make the following ansatz to solve the corresponding Schrödinger equation:

$$|\psi^\pm_{n\neq 0,k_x}\rangle = \begin{pmatrix} f_\pm(n, B_\perp)\,|n, k_x\rangle \\ g_\pm(n, B_\perp)\,|n-1, k_x\rangle \end{pmatrix} \quad \text{and} \quad |\psi^\pm_{n=0,k_x}\rangle = \begin{pmatrix} |0, k_x\rangle \\ 0 \end{pmatrix} , \tag{2.7}$$

where n is the LL index and $\psi_{n,k_x}(\mathbf{x}) = \langle \mathbf{x}|n, k_x\rangle$ is explicitly given by Eq. (1.57); $f_\pm(n, B_\perp)$ and $g_\pm(n, Bz)$ depend on the model parameters, and $\pm$ denotes solutions of the conduction $(+)$ or the valence band $(-)$, respectively. We can proceed analogously for $\operatorname{sgn}(eB_\perp) < 0$ to determine the following ansatz:

$$|\psi^\pm_{n\neq 0,k_x}\rangle = \begin{pmatrix} f_\pm(n, B_\perp)\,|n-1, k_x\rangle \\ g_\pm(n, B_\perp)\,|n, k_x\rangle \end{pmatrix} \quad \text{and} \quad |\psi^\pm_{n=0,k_x}\rangle = \begin{pmatrix} 0 \\ |0, k_x\rangle \end{pmatrix} . \tag{2.8}$$

Using the appropriate ansatz and employing the properties of the ladder operators,

[a] Recall that an integer quantized conductivity ensures large gauge invariance of the effective action.

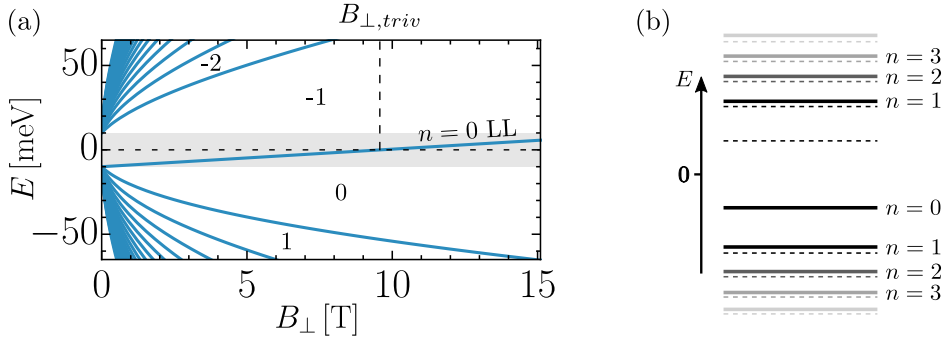

Figure 2.1.: (a) Evolution of LL energies, Eq. (2.9) and (2.10), as function of $B_\perp$ with $M = -10\,\mathrm{meV}$, $B = -685\,\mathrm{meVnm}^2$, $D = 0$, and $A = 365\,\mathrm{meVnm}$. The gray area highlights the bulk gap at $B_\perp = 0$. $B_{\perp,triv}$ is defined by Eq. (2.33) and marks the point at which the $n = 0$ LL crosses $E = 0$. (b) Solid lines show sketch of LL spectrum at constant $B_\perp$. All LLs except for the $n = 0$ LL come in pairs. Mirroring the spectrum at $E = 0$, depicted by dashed lines, highlights the asymmetry of the spectrum (introduced by $B_\perp$). Reprinted from Ref. [P6].

given by Eq. (1.52), we arrive at a general expression for the LL spectrum [17]:

$$E_{\mathrm{n=0}} = \mathrm{sgn}\,(eB_\perp)\left(M - B/l_{B_\perp}^2\right) - \frac{D}{l_{B_\perp}^2}\,, \tag{2.9}$$

$$E_{n\neq 0}^{\pm} = -\frac{\mathrm{sgn}\,(eB_\perp)\,B + 2nD}{l_{B_\perp}^2} \pm \sqrt{\frac{2A^2 n}{l_{B_\perp}^2} + \left(M - \frac{2nB + \mathrm{sgn}\,(eB_\perp)\,D}{l_{B_\perp}^2}\right)^2}\,. \tag{2.10}$$

For an exemplary set of parameters, the LL fan is shown in Fig. 2.1(a).

While $D \neq 0$ breaks the PH symmetry already at $B_\perp = 0$, it is evident that switching on the magnetic field breaks the PH symmetry even if $D = 0$ [a]. This is on the one hand reflected by the formation of a single, unpaired $n = 0$ LL [see Fig. 2.1]. This specific LL is a hallmark of a Dirac-like Hamiltonian and is located either in the valence ($E < 0$) or in the conduction band ($E > 0$) depending on $\mathrm{sgn}\,(eB_\perp)\,\mathrm{sgn}\left(M - B/l_{B_\perp}^2\right)$. On the other hand, although all LLs with $n \geq 1$ come in pairs, they are not symmetric with respect to zero energy. This is because of the non-relativistic mass parameter B. To be precise, this additional contribution to the asymmetry is proportional to $\mathrm{sgn}\,(eB_\perp)\,\mathrm{sgn}\,(B)$ [cf. Eq. (2.10)]. This is visualized by a sketch of the bulk LL energies in Fig. 2.1(b). The asymmetry, which is induced by the magnetic field, has profound consequences as we will see in the following section.

Zeroth LL: The existence of a single, (pseudo)spin polarized $n = 0$ LL is characteristic for Dirac-like systems in (2+1)D [8]. We can better understand its peculiar nature by

[a] We presented a detailed symmetry analysis in Sec. 1.1.4.

recasting Eq. (2.2) in the following form [a]:

$$H = -\mathrm{i}\not{D} + \left\{ M + B\left[(\partial_x + \mathrm{i}eA_x/\hbar)^2 + \partial_y^2 \right] \right\} \sigma_z \,, \tag{2.11}$$

where $-\mathrm{i}\not{D} = -\mathrm{i}[(\partial_x + \mathrm{i}eA_x/\hbar)\sigma_x - \partial_y \sigma_y]$. The first term, $-\mathrm{i}\not{D}$, can be interpreted as a 2D euclidean Dirac operator [128] [b]. In the presence of an external vector potential, such an operator possesses zero modes, i.e., eigenstates ϕ_0 for which $-\mathrm{i}\not{D}\phi_0 = 0$. To be precise, the number of zero modes is given by the Atiyah-Singer index theorem, [51, 108, 131]

$$\mathrm{ind}\,(-\mathrm{i}\not{D}) = \int F = \frac{e}{h} \int_S B_\perp dS \,, \tag{2.12}$$

This means the number of zero modes of the 2D euclidean Dirac operator is given by the magnetic flux (divided by a unit flux quantum $\phi_0 = h/e$). These solutions are chiral since $\{-\mathrm{i}\not{D}, \sigma_z\} = 0$. Moreover, they are also eigenstates of the full Hamiltonian [126, 128, 132], Eq. (2.11), with energy $E = E_0$, given by Eq. (2.9). This explains why a single, (pseudo)spin polarized LL exist for a (2+1)D Dirac-like system, even though chirality cannot be defined in (2+1)D, cf. Sec. 1.6.1. We have made this short detour to emphasize the particular role of the $n = 0$ LL in a QAH insulator. Its physics is much richer compared to any conventional LL.

2.1.1. Chern insulator on the lattice - numerical approach:

So far, we have discussed the bulk properties of a QAH insulator in magnetic fields. To conclude this section, we study the corresponding spectrum for a finite system (strip geometry). To this end, we impose periodic boundary conditions in the x-direction, and hard wall boundary conditions in the y-direction. Making use of the numerical approach, which was developed in Sec. 1.1.3, we focus in the following on an exemplary QAH insulator with $M, B < 0$ and $D \neq 0$. The resulting band structures for $B_\perp = 0$, 1.5, and 2.5 T are shown in Figs. 2.2(a)–(c), respectively. The color code depicts the localization of the wave functions.

As a signature of the nontrivial Chern number at $B_\perp = 0$, chiral edge states traverse the bulk band gap in Fig. 2.2(a). In comparison to the PH symmetric case (shown in Fig. 1.2), the Dirac point is shifted away from zero energy and lies at [133]

$$E_D = -\frac{MD}{B} \,. \tag{2.13}$$

[a] For simplicity, we consider the case $D = 0$.

[b] The operator matches exactly the one of a (1+1)D Dirac system, cf. Sec. 1.4.1, except that in the present case, there are two spatial and no time components. Roughly speaking, the momentum k_x plays the same role as the time in a conventional Dirac system.

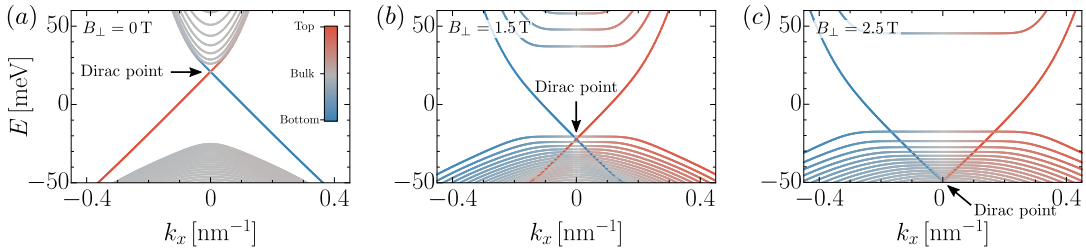

Figure 2.2.: We show the band structure of a QAH insulator with $M = -25\,\mathrm{meV}$, $B = -1075\,\mathrm{meVnm}^2$, $D = -900\,\mathrm{meVnm}^2$, and $A = 365\,\mathrm{meVnm}$ for magnetic fields of (a) $B_\perp = 0\,\mathrm{T}$, (b) $1.5\,\mathrm{T}$, and (c) $2.5\,\mathrm{T}$. The color code indicates the localization of the wave functions. The Dirac point shifts down in energy with increasing magnetic fields, until it becomes buried in the valence band.

Gradually increasing the magnetic field pushes the QAH edge states into the valence band, shown in Figs. 2.2(b) and (c). At the same time, flat bulk LLs and associated QH edge states emerge. Comparing this result to Fig. 1.5, it is apparent that the spectrum of a conventional QH insulator looks clearly distinct from the one of a QAH insulator. Above a critical magnetic field, the surviving QAH edge states can coexist in the valence band with other QH edge states of opposite chirality [a], as shown in Fig. 2.2(c). In particular, below the $n = 0$ LL a pair of counterpropagating edge states emerges in the valence band. In contrast to helical edge states, which characterize the QSH phase, these quasi-helical edge states [129] are not protected by symmetry.

Puzzle: These observations show that although a QAH insulator is described by a $\mathbb{Z}$-topological invariant in magnetic fields, the spectrum at the edge of the system can differ significantly from the one of a conventional QH insulator. This finding is particularly surprising with respect to our discussion in Sec. 1.5. The bulk calculation shows that the spectrum consists only of LLs which should each be described by a single Chern-Simons term. As such, each LL should come along with a single chiral edge channel (per edge). But how is the information about the QAH edge states then encoded in the LL spectrum? Throughout the remainder of this chapter, we will try to answer the following questions:

1. How is it possible that the information of the QAH edge states is still encoded in the spectrum, if it consist only of bulk LLs? In other words, how is the inverted band structure of a QAH insulator encoded in the bulk LL spectrum?
2. Up to which critical magnetic field can signatures of the QAH topology survive?
3. How can quasi-helical edge states be detected in potential transport experiments?

[a] QH and QAH edge states at the same edge have opposite group velocities in the valence band.

2.2. Bulk particle number and spectral asymmetry in magnetic fields

As a Dirac-like Hamiltonian, a Chern insulator possesses an infinite number of degrees of freedom. This gives rise to infinities in many physical observables if one naively tries to calculate expectation values. For instance, the bulk particle number of a Chern insulator would diverge if the familiar number operator,

$$N = \int d\mathbf{x}\, \Psi^\dagger(\mathbf{x})\Psi(\mathbf{x})\,, \tag{2.14}$$

is employed. To remove these infinities, proper renormalization schemes must be employed [see also discussion in Sec. 1.4.3] [a].

In Sec. 2.2.1, we derive analytically the renormalized particle number operator for a Chern insulator which obeys PH symmetry ($D = 0$) at $B_\perp = 0$. In the subsequent Sec. 2.2.2, this derivation is generalized to Chern insulators which exhibit a broken PH symmetry.

2.2.1. With particle-hole symmetry

In Sec. 1.4.3, we have seen that antisymmetrization is equivalent to normal-ordering and, as such, an appropriate way to renormalize the number operator of a (1+1)D Dirac system [107, 134]. In fact, we will show now that antisymmetrization is a proper renormalization scheme for all Dirac-like systems which obey PH or chiral symmetry. This means it ensures a vanishing particle number in the bulk gap. To verify this statement, let us consider the antisymmetrized number operator explicitly [b]:

$$N = \frac{1}{2}\int d\mathbf{x} \sum_\alpha \left[\Psi_\alpha^\dagger(\mathbf{x}), \Psi_\alpha(\mathbf{x})\right]\,, \tag{2.15}$$

where $\Psi(\mathbf{x})$ is the time-independent field operator (two component spinor) of a Dirac-like system. If this system obeys PH symmetry, the ground state, which is defined by filling all states (emptying all holes) in the valence band ($E < 0$), is invariant under a PH transformation:

$$\mathcal{C}\,|\text{vac}\rangle = |\text{vac}\rangle\,, \tag{2.16}$$

[a] The finite-difference-method, which we employ in our numerics, can be also interpreted as a regularization scheme. This is explained in more detail in Sec. 2.6.1.

[b] We prove this statement only for PH symmetry. The proof for chiral symmetry follows analogously.

where $\mathcal{C}$ is the PH operator. Recall that a PH transformation acts on fermionic field operators as [cf. Eq. (1.8)],

$$\mathcal{C}\Psi(\mathbf{x})\mathcal{C}^{-1} = U_C^* \Psi^\dagger(\mathbf{x})\,. \tag{2.17}$$

This allows us to recast Eq. (2.15) in the following way:

$$\begin{aligned}
\langle \mathrm{vac}|N|\mathrm{vac}\rangle &= \langle \mathrm{vac}|\mathcal{C}^{-1}\mathcal{C}N\mathcal{C}^{-1}\mathcal{C}|\mathrm{vac}\rangle \\
&= \langle \mathrm{vac}|\frac{1}{2}\int d\mathbf{x}\,\mathcal{C}\sum_\alpha \left[\Psi_\alpha^\dagger(\mathbf{x}), \Psi_\alpha(\mathbf{x})\right]\mathcal{C}^{-1}\mathrm{vac}\rangle \\
&= \langle \mathrm{vac}|\frac{1}{2}\int d\mathbf{x}\sum_\alpha \left[\Psi_\alpha(\mathbf{x}), \Psi_\alpha^\dagger(\mathbf{x})\right]\mathrm{vac}\rangle \\
&= -\langle \mathrm{vac}|N|\mathrm{vac}\rangle \overset{!}{=} 0\,.
\end{aligned} \tag{2.18}$$

The last step follows as the equality $\langle \mathrm{vac}|N|\mathrm{vac}\rangle = -\langle \mathrm{vac}|N|\mathrm{vac}\rangle$ can only be fulfilled if the ground state charge is zero. This concludes the proof: Assuming the system obeys either PH or chiral symmetry, antisymmetrization is a proper renormalization scheme for the particle number operator. In particular, antisymmetrization can be therefore used to renormalize the number operator of a Chern insulator with $D = 0$.

Bulk particle number operator in finite magnetic fields: We calculate now the renormalized bulk particle number operator in the presence of LLs. To this end, we use Eq. (2.15) and expand the associated fermionic field operator in terms of the normalized LL spinors:

$$\Psi(\mathbf{x}) = \sum_{k_x,n} b_{n,k_x} u_{n,k_x}(\mathbf{x}) + \sum_{k_x,n} d_{n,k_x}^\dagger v_{n,k_x}(\mathbf{x})\,, \tag{2.19}$$

where all operators are normal-ordered with respect to the ground state $|\mathrm{vac}\rangle$ defined by $\mu = 0$, i.e.,

$$b_{n,k_x}\,|\mathrm{vac}\rangle = d_{n,k_x}\,|\mathrm{vac}\rangle = 0\,. \tag{2.20}$$

Moreover, $u_{n,k_x}(\mathbf{x}) = \langle \mathbf{x}|\psi^+_{n,k_x}\rangle$, $v_{n,k_x}(\mathbf{x}) = \langle \mathbf{x}|\psi^-_{n,k_x}\rangle$, and $|\psi^\pm_{n,k_x}\rangle$ is given by Eq. (2.7) or (2.8), depending on the magnetic field direction. Note that b_{n,k_x} destroys an electron in the nth conduction band LL, and $d^\dagger_{n,k_x}$ creates a hole in the nth valence band LL with momentum k_x. Moreover, all fermionic operators fulfill conventional anti-commutation relations

$$\left\{b_{n,k_x}, b^\dagger_{m,q_x}\right\} = \delta_{n,m}\delta_{k_x,q_x} \qquad \text{and} \qquad \left\{d_{n,k_x}, d^\dagger_{m,q_x}\right\} = \delta_{n,m}\delta_{k_x,q_x}\,. \tag{2.21}$$

The $n = 0$ LL plays a special role. Since it is either part of the valence band or the conduction band, it contributes either to the first or to the second sum in Eq. (2.19).

To be more specific, if the $n = 0$ LL belongs to the valence band ($E_0 < 0$), the first sum in Eq. (2.19) runs from $n = 1$ to ∞ and the second sum from $n = 0$ to ∞. The situation is vice versa if the $n = 0$ LL is part of the conduction band.

To determine now the particle number operator explicitly, the field operator Eq. (2.19) is inserted into Eq. (2.15). This yields

$$\begin{aligned} N &= \frac{1}{2}\left(\sum_{k_x,n}\left[b^\dagger_{n,k_x}, b_{n,k_x}\right] + \sum_{k_x,n}\left[d_{n,k_x}, d^\dagger_{n,k_x}\right]\right) \\ &= \sum_{k_x,n}\left(b^\dagger_{n,k_x} b_{n,k_x} - \frac{1}{2}\right) - \sum_{k_x,n}\left(d^\dagger_{n,k_x} d_{n,k_x} - \frac{1}{2}\right) \\ &= N_0 - \frac{\eta(B_\perp)}{2}\,, \end{aligned} \tag{2.22}$$

where we made use of Eq. (2.21) and

$$N_0 = \sum_{k_x,n} b^\dagger_{n,k_x} b_{n,k_x} - \sum_{k_x,n} d^\dagger_{n,k_x} d_{n,k_x}\,, \tag{2.23}$$

$$\eta(B_\perp) = \sum_{E>0} 1 - \sum_{E<0} 1 = \sum_E \mathrm{sgn}\,(E)\ . \tag{2.24}$$

This shows that the renormalized particle number operator consists of two contributions: The first term N_0 denotes the 'conventional' (fermionic) number operator [a]. It counts the number of filled and empty states with respect to $\mu = 0$. The second term $\eta(B_\perp)$ is the so-called spectral asymmetry [127, 128, 134]. It quantifies the difference in the number of states between valence and conduction band [b]. For that reason, the spectral asymmetry vanishes in the presence of PH or chiral symmetry [c]. However, if we violate these symmetries by introducing a finite magnetic field, as discussed in Secs. 1.1.4 and 2.1, $\eta(B_\perp)$ can be nonzero.

To calculate $\eta(B_\perp)$ explicitly, two separately divergent sums must be subtracted from each other which requires the introduction of a regulator [51]. Here, we make use of a heat-kernel regulator. This means we replace all summands in Eq. (2.24) according to [51]:

$$\begin{aligned} n \neq 0 \quad &: \quad 1 \to \mathrm{e}^{-\kappa|E^\pm_n|}\,, \\ n = 0 \quad &: \quad 1 \to \mathrm{e}^{-\kappa|E_0|}\,, \end{aligned} \tag{2.25}$$

where $\kappa > 0$ ensures the absolute convergence of both sums. The LL energies E_0 and

[a] We mean by 'conventional' that N_0 consists only of fermionic operators.

[b] The spectral asymmetry is a topological quantity as it is invariant under small, local perturbations [134].

[c] Suppose the system obeys PH symmetry. Then there is for each positive, a corresponding negative energy solution, resulting in $\eta(B_\perp) = 0$. We have proven this statement in general in Eq. (2.18).

E_n are given by Eq. (2.9) and Eq. (2.10) with $D = 0$, respectively. At the end of the calculation, we will regain $\eta(B_\perp)$ by taking the limit $\kappa \to 0^+$. Employing now Eq. (2.25) to rewrite Eq. (2.24), we obtain the regularized spectral asymmetry:

$$\begin{aligned}\eta_\kappa(B_\perp) =& s\,\mathrm{sgn}\left(M - B/l_{B_\perp}^2\right)\sum_{k_x} \mathrm{e}^{-\kappa|E_0|} + \sum_{k_x,n=1} \mathrm{e}^{-\kappa E_n^+} - \sum_{k_x,n=1} \mathrm{e}^{\kappa E_n^-} \\ =& n_0\left[s\,\mathrm{sgn}\left(M - B/l_{B_\perp}^2\right)\,\mathrm{e}^{-\kappa|E_0|} + \sum_{n=1} \mathrm{e}^{-\kappa E_n^+} - \sum_{n=1} \mathrm{e}^{\kappa E_n^-}\right], \end{aligned} \tag{2.26}$$

where the abbreviation $s = \mathrm{sgn}\,(eB_\perp)$ was introduced. The first term marks the contribution of the $n = 0$ LL. Its prefactor determines whether it is part of the valence ($E_0 < 0$) or the conduction ($E_0 > 0$) band. The second and third term mark the contribution of all LLs with $n \geq 1$. In the second equality, we made use of the momentum independence of the eigenvalues to extract the LL degeneracy, given by $n_0 = \sum_{k_x} 1 = S/(2\pi l_{B_\perp}^2)$ [cf. Eq. (1.55)]. Here, S is the area of the system. To simplify Eq. (2.26), we Taylor expand the LL energies in the exponents for large n:

$$\begin{aligned} E_n^\pm =& -sB/l_{B_\perp}^2 \pm \frac{2n\,|B|}{l_{B_\perp}^2}\sqrt{1 + \frac{M^2 + 2nl_{B_\perp}^{-2}\,(A^2 - 2MB)}{4n^2B^2l_{B_\perp}^{-4}}} \\ =& -sB/l_{B_\perp}^2 \pm \left[\frac{2n\,|B|}{l_{B_\perp}^2} + \mathrm{sgn}\,(B)\left(\frac{A^2}{2B} - M\right)\right] + \mathcal{O}\left(n^{-1}\right). \end{aligned} \tag{2.27}$$

Since the heat-kernel regulator affects only large energy (large n) solutions, this approximation becomes exact for $\kappa \to 0^+$. Inserting Eq. (2.27) into (2.26) yields [a]

$$\begin{aligned}\frac{\eta_\kappa(B_\perp)}{n_0} =& s\,\mathrm{sgn}\left(M - B/l_{B_\perp}^2\right)\mathrm{e}^{-\kappa|E_0|} + \mathrm{e}^{\kappa\,\mathrm{sgn}(B)\left(M - A^2/2B\right)} \\ &\times \sum_{n=1}^{\infty} \mathrm{e}^{-2n\kappa|B|/l_{B_\perp}^2}\left[\mathrm{e}^{\kappa sB/l_{B_\perp}^2} - \mathrm{e}^{-\kappa sB/l_{B_\perp}^2}\right]. \end{aligned} \tag{2.29}$$

As the infinite sum represents a geometric series,

$$\sum_{n=1}^{\infty} \mathrm{e}^{-2n\kappa|B|/l_{B_\perp}^2} = \sum_{n=0}^{\infty}\left(\mathrm{e}^{-2\kappa|B|/l_{B_\perp}^2}\right)^n - 1 = \frac{1}{1 - \mathrm{e}^{-2\kappa|B|/l_{B_\perp}^2}} - 1\,, \tag{2.30}$$

we can further simplify Eq. (2.29). Proceeding with a Taylor expansion of $\eta_\kappa(B_\perp)$ for

[a] In writing Eq. (2.29), we omitted higher order terms in the exponent which are $\mathcal{O}(n^{-1})$. This step is justified since these terms are at least $\mathcal{O}(\kappa)$ and, therefore, vanish in the limit $\kappa \to 0^+$ at the end of the calculation. This statement can be explicitly proven making use of the polygarithm. For instance, one has to use that

$$\sum_{n=1}^{\infty} \frac{\kappa}{n}\mathrm{e}^{-\kappa cn} = -\kappa \log\left(1 - \mathrm{e}^{-c\kappa}\right) = \mathcal{O}(\kappa)\,. \tag{2.28}$$

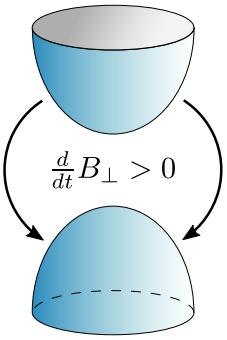

Figure 2.3.: Sketch illustrates schematically evolution of spectral asymmetry $\eta(B_\perp)$, provided that $M, B < 0$ and $\mathrm{sgn}\,(eB_\perp) > 0$. With increasing magnetic fields more and more states are removed from the conduction band and accumulate in the valence band. This process happens exclusively for nontrivial Chern insulators. Reprinted from Ref. [P6].

small κ, we finally arrive at

$$\begin{aligned}\eta(B_\perp) &= \lim_{\kappa\to 0^+} \eta_\kappa(B_\perp) \\ &= n_0\,\mathrm{sgn}\,(eB_\perp)\left[\mathrm{sgn}\left(M - B/l_{B_\perp}^2\right) + \mathrm{sgn}\,(B)\right] . \end{aligned} \tag{2.31}$$

Since all operators are normal-ordered with respect to $\mu = 0$, this shows that the ground state (bulk) particle number is solely related to the spectral asymmetry:

$$\langle \mathrm{vac}|N|\mathrm{vac}\rangle = \underbrace{\langle \mathrm{vac}|N_0|\mathrm{vac}\rangle}_{=0} - \frac{\eta(B_\perp)}{2} = -\frac{\eta(B_\perp)}{2} . \tag{2.32}$$

Discussion: The spectral asymmetry, given by Eq. (2.31), contains two distinct contributions: Firstly, the asymmetry which arises from the existence of the unpaired $n = 0$ LL, reflected by $\mathrm{sgn}\,(eB_\perp)\,\mathrm{sgn}\left(M - B/l_{B_\perp}^2\right)$, and, secondly, from the asymmetry of all other LLs with $n \geq 1$, reflected by $\mathrm{sgn}\,(eB_\perp)\,\mathrm{sgn}\,(B)$. Comparing the Eqs. (2.5) and (2.31), it is apparent that the spectral asymmetry is a direct consequence of the intrinsic Chern number and is as such a signature of the parity anomaly. Moreover, Eq. (2.31) shows that, for a QAH insulator with $M, B < 0$ and $\mathrm{sgn}\,(eB_\perp) > 0$, increasing the magnetic field is accompanied by an increase in the spectral asymmetry. This means the magnetic field pushes successively more and more states from the conduction into the valence band, as schematically illustrated in Fig. 2.3. The spectral asymmetry acts as if there is effectively one more LL in the valence band [a]. This process continues until the $n = 0$ LL, which traverses the bulk gap for $B \neq 0$, crosses over into the conduction band ($E_0 > 0$) at

$$M - B/l_{B_{\perp,triv}}^2 \stackrel{!}{=} 0$$

[a] Note that the extra charge in the valence band is not only related to the $n = 0$ LL.

$$\rightarrow B_{\perp,triv} = \mathrm{sgn}\,(eB_\perp)\,\frac{\hbar M}{eB}\,. \tag{2.33}$$

This point is marked for clarity in Fig. 2.1(a). Above this critical field, the two distinct contributions of $\eta(B_\perp)$ cancel each other, resulting in $\eta(B_\perp) = 0$. For $B_\perp > B_{\perp,triv}$, valence and conduction band contain the same number of states. In contrast, a trivial Chern insulator ($M/B < 0$) exhibits $\eta(B_\perp) = 0$ independent of the magnetic field. This distinguishes a trivial Chern insulator from a QAH insulator in magnetic fields. Note however, that we have not yet shown whether the spectral asymmetry is connected to any experimentally accessible quantity. We answer this question starting with Sec. 2.3.

Relation to QED in (2+1)D: Let us briefly comment on the connection between these findings and QED in $d = 2 + 1$ spacetime dimensions. If the same calculation is repeated for a conventional Dirac system (cf. Sec. 1.6.1), only the unpaired $n = 0$ LL would contribute to the spectral asymmetry, resulting in $\eta(B_\perp) = n_0\,\mathrm{sgn}\,(eB_\perp)\,\mathrm{sgn}\,(M)$ [108, 122, 126, 128, 132, 135]. In particular, the spectral asymmetry would be in this case purely linked to the Atiyah-Singer index-theorem [108]. This leaves us with a fractional ground state charge. In contrast, a QAH insulator, as described by Eq. (2.50) exhibits an integer-valued ground state charge. The momentum-dependent mass term B contributes additionally to the spectral asymmetry and acts as if there is an effective partner of the otherwise unpaired $n = 0$ LL. The field theoretical aspect of this point is discussed in detail in Ref. [P8] [a].

2.2.2. Without particle-hole symmetry

In the following, we want to include the D-parameter in our model, which breaks PH symmetry already at $B_\perp = 0$. One might naively expect that this should alter the spectral asymmetry, Eq. (2.31), as $\eta(B_\perp)$ measures the asymmetry of the underlying spectrum. However, this would be in conflict with our statement that $\eta(B_\perp)$ is a signature of the parity anomaly. The D-parameter breaks neither parity nor TR symmetry and is from this point of view not expected to appear in the spectral asymmetry. To resolve this issue, we have to calculate the particle number operator explicitly.

But before we are able to proceed with the calculation in magnetic fields, it is necessary to properly renormalize the particle number operator. This means the renormalization procedure must ensure a vanishing ground state charge at $B_\perp = 0$. From the previous discussion, it is expected that antisymmetrization should no longer be an appropriate method since PH symmetry is broken already at $B_\perp = 0$. Let us check this assertion by using Eq. (2.15) for the case $D \neq 0$ at $B_\perp = 0$. Thereby, we normal-order all fermion operators with respect to $E_D = -MD/B$, implying that $\langle \mathrm{vac}|N_0|\mathrm{vac}\rangle = 0$, where N_0

[a] The author of this thesis is a co-author of this manuscript.

is understood analogously to Eq. (2.23). This specific value is chosen because E_D corresponds to the Dirac point and, hence, to the charge neutrality point of our system [cf. Eq. (2.13)]. To determine the ground state charge, we are left with computing the spectral asymmetry:

$$\eta(0) = \sum_{E>E_D} 1 - \sum_{E<E_D} 1\,. \tag{2.34}$$

The following derivation is very similar to the previous calculation for $D = 0$. First, we employ a heat-kernel regulator to subtract the two divergent sums from each other. This means we replace the summands in Eq. (2.34) according to:

$$1 \to \mathrm{e}^{-\kappa|E_\pm(\mathbf{k})-E_D|}\,, \tag{2.35}$$

where $E_\pm(\mathbf{k})$ is the spectrum of the Chern insulator at $B_\perp = 0$, given by Eq. (1.17). After we substituted the summands in Eq. (2.34), the regularized spectral asymmetry takes the form:

$$\eta_\kappa(0) = \sum_{\mathbf{k}} \mathrm{e}^{-\kappa[E_+(\mathbf{k})-E_D]} - \sum_{\mathbf{k}} \mathrm{e}^{\kappa[E_-(\mathbf{k})-E_D]}\,. \tag{2.36}$$

It is convenient to replace both sums by integrals in the continuum limit, $\sum_{\mathbf{k}} \to S/(2\pi)^2 \int d\mathbf{k}$. Additionally, we Taylor expand the eigenenergies in Eq. (2.36) for large momenta to simplify the expression further:

$$\begin{aligned} E^\pm(\mathbf{k}) &= -Dk^2 \pm |B|\, k^2 \sqrt{1 + \frac{A^2k^2 - 2BMk^2 + M^2}{B^2k^4}} \\ &= \pm \mathrm{sgn}\,(B) \left(\frac{A^2}{2B} - M\right) - (D \mp |B|)\, k^2 + \mathcal{O}(k^{-2})\,. \end{aligned} \tag{2.37}$$

This allows us to recast Eq. (2.36) into conventional Gaussian integrals [a],

$$\eta_\kappa(0) = \frac{S}{(2\pi)^2} \mathrm{e}^{-\kappa\,\mathrm{sgn}(B)\left(\frac{A^2}{2B} - M\right)} \left[\mathrm{e}^{\kappa E_D} \int\limits_{\mathbb{R}^2} d\mathbf{k}\, \mathrm{e}^{-\kappa B_- k^2} - \mathrm{e}^{-\kappa E_D} \int\limits_{\mathbb{R}^2} d\mathbf{k}\, \mathrm{e}^{-\kappa B_+ k^2}\right]\,, \tag{2.38}$$

where $B_\pm = |B| \pm D$. After the Gaussian integrals have been evaluated, we perform a Taylor expansion of the resulting expression for small κ. This yields

$$\eta_\kappa(0) = \frac{S}{2\pi} \frac{D}{B^2 - D^2} \left(\frac{1}{\kappa} - \frac{A^2}{2\,|B|}\right) + \mathcal{O}(\kappa)\,. \tag{2.39}$$

[a] Recall that the heat-kernel regulator in Eq. (2.36) affects only large energy solutions. In writing Eq. (2.38), we dropped terms in the exponent which are $\mathcal{O}(k^{-2})$ since they vanish in the limit $\kappa \to 0^+$ at the end of the calculation.

The corresponding vacuum charge would be hence given by [a]

$$N_{vac} = \langle \mathrm{vac}|N|\mathrm{vac}\rangle = -\frac{1}{2}\lim_{\kappa\to 0^+}\eta_\kappa(0) \neq 0\,. \tag{2.40}$$

From this result, it is apparent that antisymmetrization is no longer equivalent to normal-ordering. It does not to ensure a vanishing particle number in the bulk gap for $\kappa \to 0^+$. This issue can be traced back to the PH asymmetry, which breaks the one-to-one correspondence between terms in the first and the second sum of Eq. (2.34). As a result, even in the absence of a magnetic field, the two divergent sums do not longer cancel each other.

Renormalization: However based on Eq. (2.40), we can now define a new, properly renormalized number operator $\tilde{N}$. To this end, we subtract the vacuum charge at $B_\perp = 0$, Eq. (2.39), from the antisymmetrized number operator:

$$\tilde{N} = N - N_{vac} = N_0 - \lim_{\kappa\to 0^+}\left[\frac{\eta_\kappa(B_\perp) - \eta_\kappa(0)}{2}\right], \tag{2.41}$$

where $\eta_\kappa(B_\perp = 0) = \eta_\kappa(0)$. By definition, Eq. (2.41) fulfills the requirement that $\langle \mathrm{vac}|\tilde{N}|\mathrm{vac}\rangle = 0$ for $B_\perp = 0$.

Spectral asymmetry in magnetic fields: To be able to make use of Eq. (2.41), we still have to evaluate $\eta(B_\perp)$ in the presence of LLs. The calculation is very similar to Sec. 2.2.1, except for the terms that arise from the nonzero D-parameter. The spectral asymmetry, $\eta(B_\perp) = \sum_{E>E_D} 1 - \sum_{E<E_D} 1$, can be regularized by introducing the following heat-kernel regulator:

$$\begin{aligned} n \neq 0 \quad &: \quad 1 \to \mathrm{e}^{-\kappa|E_n^\pm - E_D|}\,, \\ n = 0 \quad &: \quad 1 \to \mathrm{e}^{-\kappa|E_0 - E_D|}\,, \end{aligned} \tag{2.42}$$

where E_0 and E_n are the LL energies and $\kappa > 0$. The regulated spectral asymmetry reads

$$\frac{\eta_\kappa(B_\perp)}{n_0} = s\,\mathrm{sgn}\left(M - B/l_{B_\perp}^2\right)\mathrm{e}^{-\kappa|E_0 - E_D|} + \sum_{n=1}^{\infty}\mathrm{e}^{-\kappa\left(E_n^+ - E_D\right)} - \sum_{n=1}^{\infty}\mathrm{e}^{\kappa\left(E_n^- - E_D\right)}\,, \tag{2.43}$$

where $s = \mathrm{sgn}\,(eB_\perp)$ and the sum over all momenta was already replaced by the LL degeneracy $\sum_{k_x} = n_0$. The first term represents the contribution of the $n = 0$ LL. Its prefactor matches exactly the one of the PH symmetric system [cf. Eq. (2.26)]. This is because the critical magnetic field at which the $n = 0$ LL crosses over from the conduction into the valence band, i.e., $E_0(B_\perp) \stackrel{!}{=} E_D$, is independent on the D-parameter.

[a] The vacuum state is defined by filling at states up to $\mu = E_D$.

It is still given by Eq. (2.33). Analogously to the approximation used in Eq. (2.37), we Taylor expand the exponents in the latter equation for large n. Equation (2.43) takes then the form:

$$\frac{\eta_\kappa(B_\perp)}{n_0} = s\,\mathrm{sgn}\left(M - B/l_{B_\perp}^2\right) \mathrm{e}^{-\kappa|E_0-E_D|} + \mathrm{e}^{\kappa\,\mathrm{sgn}(B)\left(M-A^2/2B-sD/l_{B_\perp}^2\right)} \cdot \left[\mathrm{e}^{\kappa\left(sB/l_{B_\perp}^2+E_D\right)} \sum_{n=1}^{\infty} \mathrm{e}^{-2n\kappa B_-/l_{B_\perp}^2} - \mathrm{e}^{-\kappa\left(sB/l_{B_\perp}^2+E_D\right)} \sum_{n=1}^{\infty} \mathrm{e}^{-2n\kappa B_+/l_{B_\perp}^2}\right], \quad (2.44)$$

where $B_\pm = |B| \pm D$. This result can be recast noting that both sums form geometric series. After additionally Taylor expanding this result for small κ, we find that Eq. (2.44) reduces to

$$\eta_\kappa(B_\perp) = \eta(B_\perp) + \eta_\kappa(0) + \mathcal{O}(\kappa)\,, \quad (2.45)$$

where $\eta(B_\perp)$ and $\eta_\kappa(0)$ are given by Eq. (2.31) and Eq. (2.39), respectively. Inserting now Eq. (2.45) into Eq. (2.41) and performing the limit $\kappa \to 0^+$, we obtain the final result for the renormalized bulk particle number in magnetic fields:

$$\tilde{N} = N_0 - \frac{\eta(B_\perp)}{2}\,, \quad (2.46)$$

which matches exactly the result of a PH symmetric Chern insulator, cf. Eq. (2.31). The naive expectation that the D-parameter should contribute to the spectral asymmetry is therefore wrong. Equation (2.46) shows that $\eta(B_\perp)$ depends only on the parity breaking mass terms M and B. Physically, this underlines once more that the spectral asymmetry is a consequence of the parity anomaly and is therefore exclusively related to parity breaking mass terms.

2.3. Magnetotransport - signatures of parity anomaly

In the previous section, we have derived a general expression for the particle number operator in magnetic fields. This enables us now to determine the charge carrier density for an arbitrary chemical potential μ via

$$\rho(\mu, B_\perp) = -\frac{e}{S} \langle \mu, B_\perp | \tilde{N} | \mu, B_\perp \rangle\,, \quad (2.47)$$

where $|\mu, B_\perp\rangle$ defines a many-particle state, for which all states are filled up to the chemical potential μ, and the particle number operator $\tilde{N}$ is given by Eq. (2.46). Using Streda's formula [cf. Eq. (1.59)], this allows us to derive the corresponding expression

for the Hall conductivity via [71]

$$\sigma_{xy}(\mu, B_\perp) = \frac{\partial \rho(\mu, B_\perp)}{\partial B_\perp} \,. \tag{2.48}$$

Based on the special form of the number operator, the Hall conductivity can be divided into two distinct contributions,

$$\sigma_{xy}(\mu, B_\perp) = \sigma_{xy}^{I}(B_\perp) + \sigma_{xy}^{II}(\mu, B_\perp) \,. \tag{2.49}$$

We define the first term by its exclusive relation to the spectral asymmetry:

$$\sigma_{xy}^{I} = \frac{e}{2S}\frac{\partial \eta(B_\perp)}{\partial B_\perp} = \frac{e^2}{2h}\left[\operatorname{sgn}\left(M - B/l_{B_\perp}^2\right) + \operatorname{sgn}(B)\right] \,. \tag{2.50}$$

This quantity is independent of μ as it is a property of the entire spectrum. In comparison, σ_{xy}^{II} depends on μ since it comprises all contributions associated to the conventional number operator N_0:

$$\sigma_{xy}^{II} = -\frac{e}{S}\frac{\partial}{\partial B_\perp}\langle \mu, B_\perp | N_0 | \mu, B_\perp \rangle \,. \tag{2.51}$$

Recall that it is zero in the ground state, since all fermionic operators are normal-ordered with respect to E_D, meaning:

$$N_0 \left|\text{vac}\right\rangle = N_0 \left(\prod_{n=\{0,1\}}^{\infty} \prod_{k_x=-\infty}^{\infty} d_{n,k_x} \left|0\right\rangle \right) = 0 \,, \tag{2.52}$$

where $n = \{0, 1\}$ means that the product starts either at $n = 0$ or 1, depending on whether the $n = 0$ LL is part of the valence or the conduction band, respectively. Consequently, Eq. (2.51) can be only nonzero for $\mu \neq E_D$, and is directly related to the number of filled, or empty, LLs with respect to E_D.

To find a general expression for $\sigma_{xy}^{II}(\mu, B_\perp)$, we have to distinguish several cases due to the special properties of the $n = 0$ LL. Let us start with $M, B < 0$ and $|B_\perp| < B_{\perp,triv}$, implying that the $n = 0$ LL is filled in the ground state. In that case, the many-particle state $|\mu, B_\perp\rangle$ with $\mu < E_D$ and $B_\perp > 0$ reads

$$\left|\mu, B_\perp\right\rangle = \prod_{n=0}^{N_{max}(\mu)} \prod_{k_x=-\infty}^{\infty} d_{n,k_x}^{\dagger} \left|\text{vac}\right\rangle \,, \tag{2.53}$$

where $N_{max}(\mu)$ gives the number of empty valence band LLs. Inserting this state into Eq. (2.51), we arrive at

$$\sigma_{xy}^{II} = \frac{e^2}{h}\left[\theta(-\mu + E_0) + \sum_{n=1}^{\infty} \theta(-\mu + E_n^-)\right] \,, \tag{2.54}$$

where for the given magnetic field direction $E_0 = M - (B + D)/l_{B_\perp}^2$. Taking the same parameters but choosing $\mu > E_D$, the corresponding many-particle state reads

$$|\mu, B_\perp\rangle = \prod_{n=1}^{N_{max}(\mu)} \prod_{k_x=-\infty}^{\infty} b_{n,k_x}^\dagger \, |\text{vac}\rangle \ , \tag{2.55}$$

where $N_{max}(\mu)$ is the number of filled conduction band LLs. The associated Hall conductivity is given by

$$\sigma_{xy}^{II} = -\frac{e^2}{h} \sum_{n=1}^{\infty} \theta\left(\mu - E_n^+\right) \ . \tag{2.56}$$

The latter equation does not include the $n = 0$ LL, since it is already filled in the ground state for the given set of parameters.

In the next step, we keep the same parameters but flip the sign of the magnetic field, $B_\perp < 0$. Most importantly and in contrast to the case $B_\perp > 0$, the $n = 0$ LL is now unoccupied in the ground state. The arbitrary many-particle states with $\mu \neq E_D$ are therefore given by

$$|\mu < E_D, B_\perp\rangle = \prod_{n=1}^{N_{max}(\mu)} \prod_{k_x=-\infty}^{\infty} d_{n,k_x}^\dagger \, |\text{vac}\rangle \ , \tag{2.57}$$

$$|\mu > E_D, B_\perp\rangle = \prod_{n=0}^{N_{max}(\mu)} \prod_{k_x=-\infty}^{\infty} b_{n,k_x}^\dagger \, |\text{vac}\rangle \ , \tag{2.58}$$

where one should pay attention to the role of the $n = 0$ LL. Again, we insert these equations into Eq. (2.51) and arrive for $\mu < E_D$ at

$$\sigma_{xy}^{II} = -\frac{e^2}{h} \sum_{n=1}^{\infty} \theta\left(-\mu + E_n^-\right) \ , \tag{2.59}$$

and for $\mu > E_D$ at

$$\sigma_{xy}^{II} = \frac{e^2}{h} \left[\theta\left(\mu - E_0\right) + \sum_{n=1}^{\infty} \theta\left(\mu - E_n^+\right)\right] \ , \tag{2.60}$$

where $E_0 = -M + (B - D)/l_{B_\perp}^2$. These steps must be repeated for all possible signs of M, B and D, as well as one has to consider the additional cases for which $|B_\perp| > B_{\perp,triv}$. After a lengthy but straightforward calculation, a general expression for σ_{xy}^{II} can be finally determined:

$$\sigma_{xy}^{II} = \sigma_0^{II} \, \theta\left(|\bar{\mu}| - \left|M - B/l_{B_\perp}^2\right|\right) + \sigma_n^{II} \sum_{n=1}^{\infty} \left[\theta\left(\mu - E_n^+\right) - \theta\left(-\mu + E_n^-\right)\right] \ , \tag{2.61}$$

where $\bar{\mu} \equiv \mu + D/l_{B_\perp}^2$ and

$$\sigma_0^{II} = -\frac{e^2}{2h}\left[\mathrm{sgn}\left(M - B/l_{B_\perp}^2\right) + \mathrm{sgn}\left(eB_\perp\right)\mathrm{sgn}\left(\bar{\mu}\right)\right], \tag{2.62a}$$

$$\sigma_n^{II} = -\frac{e^2}{h}\mathrm{sgn}\left(eB_\perp\right). \tag{2.62b}$$

Discussion: Let us summarize the physical implications which we can derive from Eqs. (2.50) and (2.61). The first term, σ_{xy}^I, is connected solely to the spectral asymmetry and is as such a signature of the parity anomaly. It is only nonzero if the system is a QAH insulator for $B_\perp = 0$, i.e., $M/B > 0$. We probe exclusively σ_{xy}^I, the 'QAH regime', if the chemical potential is placed within

$$\left|\mu + D/l_{B_\perp}^2\right| \leq \left|M - B/l_{B_\perp}^2\right|. \tag{2.63}$$

We refer to this regime as the Dirac mass gap because of its relation to the intrinsic bulk band gap of a Chern insulator. Given that μ is placed within the Dirac mass gap, the Hall conductivity is an even function of the magnetic field, i.e., $\sigma_{xy}^I(-B_\perp) = \sigma_{xy}^I(B_\perp)$. This constitutes a violation of the Onsager relation [a]. Moreover, Eqs. (2.50) and (2.63) highlight a competition between the bare Dirac mass M and the non-relativistic mass B. The B-parameter causes a decrease of the Dirac mass gap until it is eventually closed at $B_\perp = B_{\perp,triv}$, given by Eq. (2.33), above which $\sigma_{xy}^I = 0$. In comparison, the D-parameter comes at the same level as the chemical potential and, hence, shifts the center of the Dirac mass gap in magnetic fields. The difference between the parameters arises because only M and B break parity symmetry at $B_\perp = 0$.

The second term in Eq. (2.49), σ_{xy}^{II}, contributes additionally to the total Hall conductivity only if the chemical potential is placed outside of the Dirac mass gap, so that extra LLs are filled/emptied with respect to the ground state. In contrast to Eq. (2.50), each of these contributions is related to a single LL. Their origin is reflected by their $\mathrm{sgn}\left(eB_\perp\right)$-dependence, seen in Eq. (2.61). More precisely, for $\mathrm{sgn}\left(eB_\perp\right) > 0$ every conduction band LL contributes $-e^2/h$ and every valence band LL $+e^2/h$. The signs come vice versa when we flip the direction of the magnetic field. Hence, Eq. (2.61) describes conventional QH physics, generated by the external magnetic field.

[a] In a conventional QH phase, the Onsager relation [68] imply that $\sigma_{xy}(B_\perp) = -\sigma_{xy}(-B_\perp)$, cf. Eq. (1.60). When we refer to a violation of the Onsager relation, we want to highlight that, in contrast to a conventional QH phase, the Hall conductivity of a QAH insulator is an even function of the magnetic field if the chemical potential is placed in the Dirac mass gap, i.e., $\sigma_{xy}(B_\perp) = \sigma_{xy}(-B_\perp)$. The Hall conductivity only switches its sign if we flip both the sign of the intrinsic Chern number, $(M, B) \to (-M, -B)$, as well as the sign of the external magnetic field. A QAH insulator is therefore characterized by

$$\sigma_{xy}(M, B, B_\perp) = -\sigma_{xy}(-M, -B, -B_\perp). \tag{2.64}$$

2.4. Effective field theory

In the previous sections, it was found that a QAH insulator, subjected to an external magnetic field, is related to a peculiar topological quantity, the spectral asymmetry $\eta(B_\perp)$. The presented calculations were thereby performed for a domain without boundaries. Our next goal is to connect these bulk results to the special edge properties of our system [cf. Sec. 2.1.1]. To this end, we will derive the effective action of a QAH insulator in magnetic fields and make use of anomaly cancellation to determine the associated edge states. In the following, we switch to relativistic notation.

Effective action - bulk: If a perturbing external vector potential a_μ is applied on top of the underlying magnetic field $B_\perp = \nabla \times \mathbf{A}$, the induced current is given by [cf. Sec. 1.5]:

$$j^\mu_{ind} = \sigma_{xy}(\mu, B_\perp)\epsilon^{\mu\nu\rho}\partial_\nu a_\rho \,, \tag{2.65}$$

where σ_{xy} is defined by Eq. (2.49). Recall that j^0_{ind} is the bulk charge density, and $j^{1,2}_{ind}$ is the bulk current density in x- and y-direction, respectively. Since $j^\mu_{ind} = \delta S^{bulk}_{eff}/\delta a_\mu$ with $S^{bulk}_{eff} = \int d^3x\, \mathcal{L}^{bulk}_{eff}$, we can deduce the corresponding effective bulk Lagrangian:

$$\mathcal{L}^{bulk}_{eff}(\mu, B_\perp) = \frac{\sigma_{xy}(\mu, B_\perp)}{2}\, \epsilon^{\mu\nu\rho} a_\mu \partial_\nu a_\rho \,, \tag{2.66}$$

where $\epsilon^{\mu\nu\rho}$ is the Levi-Civita symbol. The effective field theory is a Chern-Simons theory, which arises in (2+1)D due to a broken TR and parity symmetry [50, 62, 122]. There are two physically different mechanisms in our model that break parity and TR symmetry and, therefore, give rise to Chern-Simons terms. On the one hand, the mass terms M and B, and, on other hand, the external magnetic field $B_\perp$. This allows us to distinguish two types of Chern-Simons terms: The first type, related to Eq. (2.50), is defined by its exclusive relation to M and B. It is solely related to the spectral asymmetry $\eta(B_\perp)$ and, hence, to the parity anomaly. This type of Chern-Simons term is not related to a single LL, but reflects the asymmetry of the entire spectrum. As such, it does not come along with a Heaviside step function. The second type of Chern-Simons terms, related to Eq. (2.61), describes conventional QH physics. Each of these terms is related to a single LL, which is reflected by the Heaviside step functions in Eq. (2.61).

Effective action - edge: Each Chern-Simons term in Eq. (2.66) must be accompanied by an associated edge state at the boundary $\partial\Omega$ of our system. This field theoretical analog of the bulk-boundary correspondence can be verified noting, that Chern-Simons terms, which are defined on a finite domain, are not gauge invariant, cf. Eqs. (1.100) and (1.101). If our system is only described by $\mathcal{L}^{bulk}_{eff}$, this non-invariance would mean

that the induced bulk current, Eq. (2.65), is not conserved at $\partial\Omega$,

$$\partial_\mu j^\mu_{ind}\big|_{\partial\Omega} \neq 0\,. \tag{2.67}$$

The latter describes a chiral anomaly which must be canceled via the Callan-Harvey mechanism [cf. Sec. 1.5.2] to ensure a consistent theory [106]. To be precise, we must cancel the anomaly by enlarging the effective theory by an additional edge degree of freedom, which we denote by $\mathcal{L}^{\partial\Omega}_{eff}$ [a]. Gauge invariance can be then restored via anomaly cancellation between edge and bulk[42, 115]:

$$\begin{aligned} &\partial_\mu j^\mu_{tot} = \partial_\mu \left(j^\mu_{ind} + j^\mu_{L} + j^\mu_{R}\right) = 0 \\ \rightarrow \quad &\partial_\mu j^\mu_{ind} = -\partial_\mu j^\mu_{L/R} = \sigma_{xy}(\mu, B_\perp)\,\delta\left(y - y_{L/R}\right)\epsilon^{2\nu\lambda}\partial_\nu a_\lambda\,, \end{aligned} \tag{2.68}$$

where $j^\mu_{L/R}$ symbolizes currents at the left (y_L) and right (y_R) edge of the strip geometry, respectively, which are associated to $\mathcal{L}^{\partial\Omega}_{eff}$. Equation (2.68) implies that the non-conservation of bulk charge at $\partial\Omega$, as a response to a_μ, is compensated by a non-conservation of charge in the corresponding edge theories. An increase of the magnetic field by $\nabla\times\mathbf{a}$ causes charge accumulation in the bulk, with

$$j^0_{ind} = \sigma_{xy}(\mu, B_\perp)\nabla\times\mathbf{a}\,, \tag{2.69}$$

that is compensated by a charge depletion at the edges. Throughout this process, no particles are created or destroyed, so that the charge of the entire system (bulk+edge) remains constant [128].

The effective edge theories, associated to $j^\mu_{L/R}$, are given by

$$\mathcal{L}^{\partial\Omega}_{eff} = \mathcal{L}^{L}_{eff}\,\delta\left(y - y_L\right) + \mathcal{L}^{R}_{eff}\,\delta\left(y - y_R\right)\,, \tag{2.70}$$

where

$$\mathcal{L}^{L/R}_{eff} = \chi^\dagger\,\mathrm{i}\left(\partial_t \mp \frac{h}{e^2}\sigma^I_{xy}\,D_x\right)\chi \tag{2.71a}$$

$$+\,\xi_0^\dagger\,\mathrm{i}\left(\partial_t \mp \frac{h}{e^2}\sigma^{II}_0 D_x\right)\xi_0\,\Theta\left[|\bar{\mu}| - \left|M - B/l^2_{B_\perp}\right|\right] \tag{2.71b}$$

$$+\sum_{\substack{n=1\\ s=\pm}}^{\infty} s\,\xi_n^\dagger\,\mathrm{i}\left(\partial_t \mp \frac{h}{e^2}\sigma^{II}_n\,D_x\right)\xi_n\Theta\left[s(\mu - E^s_n)\right]\,. \tag{2.71c}$$

Here, L/R corresponds to $\mp$, respectively, σ^I_{xy} is given by Eq. (2.50), σ^{II}_0 by Eq. (2.62a), and σ^{II}_n by Eq. (2.62b); χ (ξ_n) defines QAH (QH) edge states and $D_x = \partial_x + \mathrm{i}ea_x/\hbar$. Equation (2.71a) is linked to the spectral asymmetry and characterizes QAH edge

[a] This theory is defined in (1+1)D and describes chiral fermions.

states, persisting in magnetic fields [a]. The QAH edge states are not bound to a specific LL (no Heaviside step function) but instead bridge the gap between valence and conduction band. This finding is in accordance with our band structure calculations, shown in Figs. 2.2 and 2.4, and explains how the information of the QAH edge states can persist in magnetic fields. Interestingly, since Eq. (2.71a) is connected to $\eta(B_\perp)$, charge pumping via anomaly cancellation can occur from the QAH edge states into any LL. As such, this peculiar type of charge pumping is a signature of the parity anomaly. It can exist in general until $\sigma_{xy}^I = 0$, i.e., until the Dirac mass gap is eventually closed at $B_\perp = B_{\perp,triv}$, given by Eq. (2.33). This is in stark contrast to Eqs. (2.71b) and (2.71c) which are related to the conventional fermion number operator N_0 and, therefore, describe QH edge states. Each of these edge states is bound to a single LL, so that charge flow can only appear between an edge state and its associated LL.

Moreover, Eqs. (2.71a)–(2.71c) shed light on the coexistence of QH and QAH edge states outside of the Dirac mass gap, that were observed in Fig. 2.2. The QAH edge states can coexist with QH edge states, as they are not bound by a Heaviside step function. However, to derive the effective edge theories, we did not include possible hybridization mechanisms between these coexisting states. Hybridization is in general not forbidden, since the quasi-helical edge states are not protected by symmetry. For that reason, QH and QAH edge states can in general hybridize if they exist at the same energy and momentum. To complete our understanding of the survival of the QAH edge states in magnetic fields, we will therefore numerically analyze in the next section charge pumping between the QAH edge states and the bulk LLs. Moreover, we analyze the survival and the protection of the quasi-helical edge states in detail in Sec. 2.6 using the finite-difference-method.

2.5. Charge pumping

The aim of this section is to analyze differences in charge pumping between QAH and QH edge states, discussed so far from a field theoretical perspective, using a numerical approach. In Sec. 2.5.1, we consider at first an impurity-free system and comment on elastic and inelastic scattering effects in Sec. 2.5.2.

2.5.1. Numerical approach

We simulate the evolution of the charge distribution as a function of $B_\perp$ by solving the time-dependent Schrödinger equation. Thereby, we keep the total charge (not the chemical potential) constant. In particular, we consider a time-dependent vector

[a] Their existence requires that $M/B > 0$. This term is zero for a trivial Chern insulator, for which $M/B < 0$.

potential

$$\mathbf{A}(t) = \mathbf{A}(t_i) + \mathbf{a}(t) \quad \text{with} \quad t \in [t_i = 0, t_f] \ , \tag{2.72}$$

where $\mathbf{A}(t_i)$ is a time-independent, constant vector potential and $\mathbf{a}(t) = -yB_\perp(t)\mathbf{e}_x$ is a time-dependent perturbation with $\mathbf{a}(t_i) = 0$.

At the initial time t_i, the system is described by the solutions of the initial Schrödinger equation [a]:

$$H(t_i)\,|\psi_{j,k_x}(t_i)\rangle = E_{j,k_x}(t_i)\,|\psi_{j,k_x}(t_i)\rangle \ , \tag{2.73}$$

where the subscript j labels the jth subband. For $t > t_i$, the perturbation is switched on and each initially occupied state, with $j \leq j_{max}$ and $k \leq k_{max}$, evolves under unitary time evolution to [b]

$$|\psi_{j,k_x}(t)\rangle = U(t, t_i)\,|\psi_{j,k_x}(t_i)\rangle \ , \tag{2.74}$$

where $U(t, t_i)$ is the time-evolution operator. The quantities j_{max} and k_{max} are determined by the initial chemical potential μ, which defines the ground state. To be precise, we compute the time-evolution of the eigenstates using an iterative procedure, numerically:

$$\begin{aligned} |\psi_{j,k_x}(t + \Delta t)\rangle &= \mathrm{e}^{-\mathrm{i}H(t)\Delta t/\hbar}\,|\psi_{j,k_x}(t)\rangle \\ &= U(t + \Delta t, t)\,|\psi_{j,k_x}(t)\rangle \ , \end{aligned} \tag{2.75}$$

where Δt has to be chosen sufficiently small to ensure convergence. Linearly increasing the magnetic field $B_\perp(t)$ with time, we can trace the occupation of states in each instantaneous spectrum, defined by the time-independent Schrödinger equation (t only parametrizes the Hamiltonian)

$$H(t)\,|\phi_{i,k_x}(t)\rangle = E_{i,k_x}(t)\,|\phi_{i,k_x}(t)\rangle \ . \tag{2.76}$$

The occupation probability of an instantaneous eigenstate $|\phi_{i,k_x}(t)\rangle$ is determined by

$$P_{i,k_x}(t) = \sum_{j=0}^{j_{max}} |\langle\psi_{j,k_x}(t)|\phi_{i,k_x}(t)\rangle|^2 \ . \tag{2.77}$$

To differentiate charge pumping in the QAH and in the QH phase, we compare two

[a] We assume a strip geometry and solve the Schrödinger equation numerically by employing the finite-difference-method.

[b] Due to translational symmetry in the x-direction, the Hamiltonian and its corresponding Hilbert space are given by a direct sum, $H(t) = \bigoplus_{k_x} H_{k_x}(t)$. The numerical simulations can be carried out separately on each Hilbert subspace H_{k_x}.

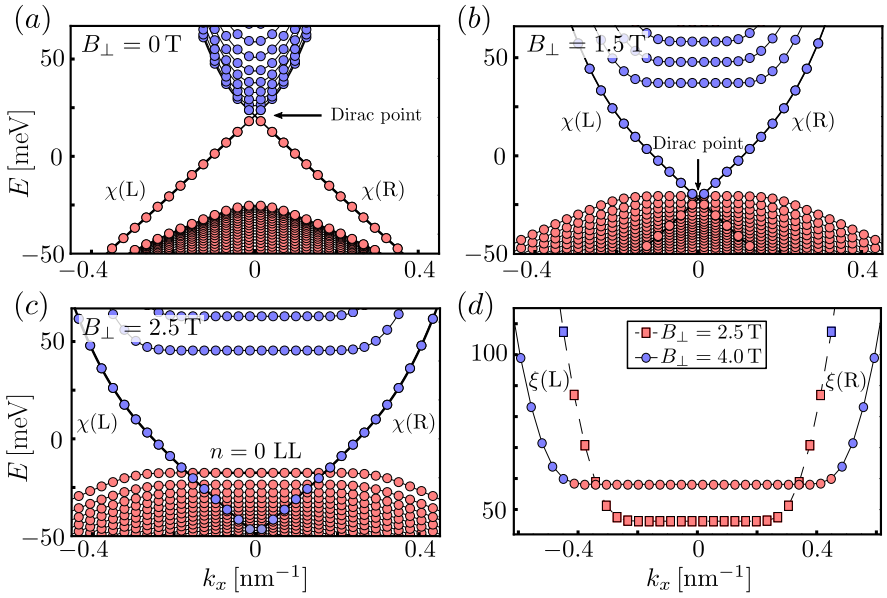

Figure 2.4.: Band structure of QAH insulator (solid black lines) with the same parameters as in Fig. 2.2 at (a) $B_\perp = 0\,\mathrm{T}$, (b) $1.5\,\mathrm{T}$, and (c) $2.5\,\mathrm{T}$. $\chi(L/R)$ and $\xi(L/R)$ depict QAH and QH edge states at the left and right boundary. (a) Spectrum at half filling with chiral QAH edge states traversing the bulk gap. (a)–(c) Evolution of the spectrum and its filling with increasing $B_\perp$, where empty/filled states are marked in blue/red. (d) Analogous analysis for an initially filled conduction band LL. From Ref. [P5]. Reprinted with permission from APS.

different initial cases ($t = t_i$):

(I) In the QAH phase, we take $\mathbf{A}(t_i) = 0$. The ground state is defined by filling all states up to the Dirac point, $\mu = E_D$.

(II) In the QH phase, a constant background vector potential $\mathbf{A}(t_i) = -yB_{\perp,0}\mathbf{e}_x$ must be applied to induce LLs. The ground state is defined by filling only a single LL.

These initial scenarios are depicted in Figs. 2.4(a) and (d), respectively.

Discussion: Let us now analyze the numerical results, starting with the QAH phase under initial condition (I). Increasing $B_\perp(t)$ linearly with time, the occupation of the eigenstates and the induced charge carrier density,

$$j^0_{ind}(\mathbf{x}, t) = -e\, n_{ind}(\mathbf{x}, t)\,, \tag{2.78}$$

evolve as shown in Figs. 2.4(a)–(c) and Fig. 2.5(a). Here,

$$n_{ind}(\mathbf{x}, t) = \sum_{i,k_x} P_{i,k_x}(t)\, |\phi_{i,k_x}(\mathbf{x}, t)|^2 - n_{back}\,, \tag{2.79}$$

where n_{back} is a constant background charge which is chosen such that $n_{ind}(\mathbf{x}, t_i) = 0$. Starting from a flat (zero) charge density distribution, an increase of $B_\perp(t)$ causes a

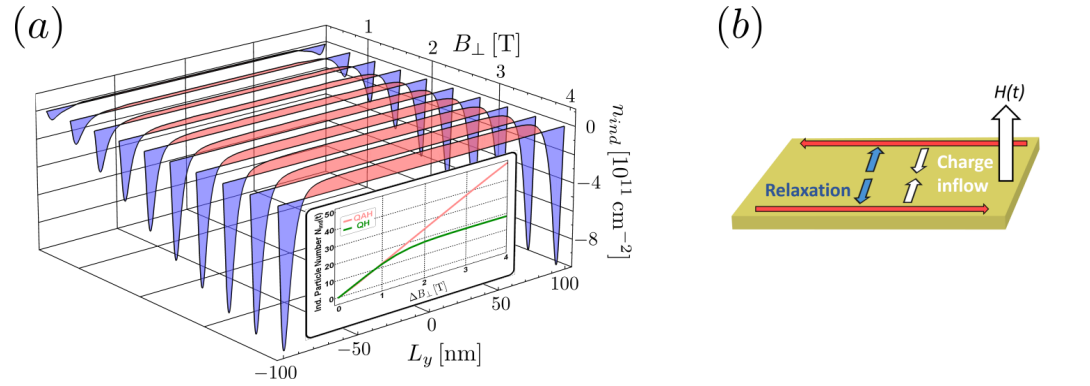

Figure 2.5.: (a) Induced particle density n_{ind} as a function of the magnetic field, corresponding to Figs. 2.4(a)–(c). An increase of $B_\perp$ causes charge depletion (blue) at the edges and charge accumulation (red) in the bulk. Inset compares the induced bulk particle number $N_{ind}(t) = \int d\mathbf{x}\, n_{ind}(\mathbf{x}, t)$ between the QAH (red) and the QH phase (green). (b) Schematic illustration of charge flow: Increasing magnetic field causes charge accumulation in the bulk. For $B_\perp > B_{\perp,scat}$, relaxation processes can take place causing charge flow in opposite direction, cf. Sec. 2.5.2. (a) From Ref. [P5]. Reprinted with permission from APS.

net charge flow from the QAH edge states (charge depletion) into all valence band LLs (charge accumulation), cf. Fig. 2.5(b) [a]. Since our system is a bulk insulator, this redistribution of charges is driven by polarization effects. This means all occupied wave functions shift as a function of the magnetic field their spectral weight, giving effectively rise to the charge redistribution shown in Fig. 2.5(a). During this process, all valence band LLs, including the $n = 0$ LL, remain filled. As illustrated in the inset of Fig. 2.5(a), this causes a linear increase of the bulk charge with $B_\perp$. The numerical result matches therefore exactly our analytical result, given by Eq.(2.69), which was derived based on anomaly cancellation. Since this type of pumping is bound to the existence of the QAH edge states, it can in general exist for $B_\perp < B_{\perp,triv}$, given by Eq. (2.33).

The described scenario resembles Laughlin's gauge argument with the exception that we have considered here a time-dependent magnetic field. In Laughlin's case, a constant electric field is applied along the x-direction, so that charge is effectively pumped from one edge to the other through the insulating bulk. In our case, the time-dependent magnetic field causes an azimuthal electric field [b] that causes charge inflow from the edges into the insulating bulk, as illustrated in Fig. 2.5(b).

In contrast, our results for the QH phase under initial condition (II) are shown in Fig. 2.4(d) and in the inset of Fig. 2.5(a). In agreement with our field-theoretical approach, we find that the bulk charge originates purely from the associated QH edge

[a] Assuming the system is topologically nontrivial, the direction of charge flow depends on the sign of σ^I_{xy} and on the magnetic field direction. Here, we focus on the case $M, B < 0$ and $\mathrm{sgn}\,(eB_\perp) > 0$.
[b] This follows from Maxwell's third equation, $\nabla \times \mathbf{E} = -\partial \mathbf{B}/\partial t$.

states, implying a saturation of the charge accumulation already for small magnetic fields [a]. As a consequence, our numerical results confirm that the QAH edge states are related to a distinct Chern-Simons term which is not only connected to a single LL but to the collection of all LLs.

Limitations: The numerical results presented in this section are independent of the time scale t_f in which $B_\perp(t)$ is ramped up, provided that $t_f^{min} \ll t_f \ll t_f^{max}$. The lower bound prevents excitations across bulk gaps E_g and is therefore determined by $t_f^{min} \equiv \hbar/E_g \sim 10^{-13}\,\mathrm{s}$. If the Dirac point is below the $n = 0$ LL, the upper bound comes from the requirement to overcome hybridization gaps Δ_{hyb} forming between the QAH edge states and bulk LLs. As long as these hybridization gaps are finite size gaps [b], as it is the case in Fig. 2.4(a)–(c), $t_f^{max} \propto \Delta_{hyb}^{-1}$ tends to infinity. A detailed discussion on the hybridization between the QAH edge states and the $n = 0$ LL is presented in Sec. 2.6.2.

2.5.2. Transport signature at constant density

So far, an ideal system without impurities has been considered, for which the total charge remains constant. We will now discuss the effect of disorder on charge pumping in the QAH phase. In the following, we distinguish two particular regimes: The Dirac point is above, or below the $n = 0$ LL. To gain an analytic expression for the corresponding, critical magnetic field, we can employ the analytic result by Zhou et al. [133]. They showed that the QAH edge states evolve in magnetic fields as:

$$E_{edge}(k_x, B_\perp) = E_D - \mu_B g_{eff} B_\perp \pm \hbar v_x k_x \,, \tag{2.80}$$

where $g_{eff} \approx m_0 v_x L_y/\hbar$ is an effective g-factor [c] and $v_x = A\sqrt{(B^2 - D^2)/B^2}/\hbar$ is the edge state velocity. The Dirac point enters the valence band therefore at the critical field $B_{\perp,scat}$ which is given by

$$\begin{aligned} E_{edge}(0, B_{\perp,scat}) &\stackrel{!}{=} E_0(B_{\perp,scat}) \\ \rightarrow B_{\perp,scat} &= \frac{M(B+D)}{B(B+D)\frac{e}{\hbar} - \frac{e}{2}Bv_x\hbar L_y} \propto \frac{1}{L_y} \,. \end{aligned} \tag{2.81}$$

For $B_\perp < B_{\perp,scat}$, when the Dirac point is above the $n = 0$ LL, the system is in its ground state. This means scattering cannot cause relaxation of the induced bulk charge and, hence, disorder cannot affect the results of Figs. 2.4(b) and 2.5(a). The hallmark of this regime is a quantized Hall plateau, given by σ_{xy}^I, whose length scales with

[a] The local chemical potential quickly drops towards the energy of the bulk LL. If it reaches the bulk LL, charge pumping breaks down.

[b] Finite size gaps are exponentially suppressed by the system size, i.e., $\Delta_{hyb} \propto e^{-\lambda L_y}$, where $\lambda > 0$.

[c] The approximation is valid for $L_y \gg \lambda_{1,2}$, where $\lambda_{1,2}$ are related to the decay length scales of the QAH edge states [133].

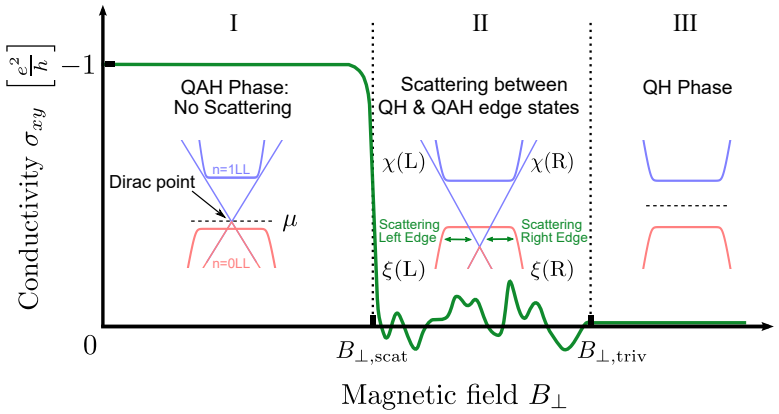

Figure 2.6.: Schematic evolution of σ_{xy} for a QAH insulator in magnetic fields in the presence of disorder at constant (zero) total charge. The insets illustrate schematically the underlying band structure according to Fig. 2.4(a)–(c) (same color code). In region II, scattering processes between counterpropagating QH $\xi(L/R)$ (red) and QAH $\chi(L/R)$ (blue) edge states allow for momentum and energy relaxation. From Ref. [P5]. Reprinted with permission from APS.

$B_{\perp,scat} \sim L_y^{-1}$, as depicted by region I in Fig. 2.6. For $B_\perp > B_{\perp,scat}$, when the Dirac point is below the $n = 0$ LL, the system is driven into a state with no common chemical potential. Its signature is a selective population of states (charge inversion), as shown in Fig. 2.4(c). This charge inversion is protected by momentum conservation, since direct relaxation processes, such as spontaneous emission, are exponentially suppressed by the spatial localization of the wave functions. However, since realistic systems are rather imperfect, in(elastic) scattering events between occupied QH and unoccupied QAH edge states facilitate momentum and energy relaxation, as indicated by region II in Fig. 2.6. As a result, the charge inversion relaxes due to the presence of disorder eventually, until a common chemical potential has set in. In this new ground state, coexisting, counterpropagating QAH and QH edge states dominate the magnetotransport. This means at constant carrier density, we expect a length-dependent transition from a quantized plateau with σ_{xy}^I to a regime, which is governed by quasi-helical edge states. In Sec. 2.6.3, we will show that in this peculiar regime deviations from a perfectly quantized Hall plateau can arise from scattering between QH and QAH edge states. This is indicated by the wiggly line in Fig. 2.6. Ultimately for $B_\perp > B_{\perp,triv}$, when the Dirac mass gap is closed by the magnetic field [cf. Eq. (2.63)], σ_{xy} vanishes exactly as indicated by region III in Fig. 2.6.

2.6. Coexistent QH and QAH edge states

In the course of this chapter, we have identified signatures of the QAH effect in the presence of LLs. In particular, it was demonstrated that the Hall conductivity in the Dirac mass gap is an even function of the magnetic field, $\sigma_{xy}(-B_\perp) = \sigma_{xy}(B_\perp)$

(violation of Onsager relation). Moreover, we explained why, outside of the Dirac mass gap, QAH edge states can coexist with counterpropagating QH edge states. While these quasi-helical edge states can in general exist until the Dirac mass gap is closed in magnetic fields [cf. Eq. (2.33)], we have not yet studied their parameter dependence nor their transport signatures in detail.

In this section, we complement our understanding of QAH insulators in magnetic fields by examining its edge properties in detail. First, the violation of the Onsager relation within the Dirac mass gap is explained in terms of the survival of the QAH edge state. Subsequently in Sec. 2.6.2, we analyze hybridization of the quasi-helical edge states outside of the Dirac mass gap. Finally in Sec. 2.6.3, we consider a toy model to demonstrate that quasi-helical edge states can entail unique transport signatures.

2.6.1. Transport in the Dirac mass gap - edge perspective

To analyze now the behavior of the topological edge states in magnetic fields in detail, we use once more the finite-difference-method to map the Hamiltonian of a Chern insulator [Eq. (2.2)] on a lattice. This procedure introduces a hard cut-off in momentum space with $k_{max} \sim a^{-1}$, where a is the lattice constant, i.e., the lattice acts as the necessary regulator [136]. In comparison to the continuum theory, this guarantees a finite number of degrees of freedom, so that no further regularization, like employing a heat-kernel, is needed to determine physical observables like the charge or the Hall conductivity. Note that physical observables should not depend on the chosen regularization/renormalization scheme. This means we should reproduce here the same results as in Sec. 2.2. The advantage of the numerical approach is that it is much simpler to determine the explicit edge spectrum. In comparison, the advantage of the (analytic) heat-kernel approach is that it allowed us to gain a much deeper inside into the regularization procedure. To this end, we were able to show how the information of the QAH effect remains encoded in the bulk LL spectrum. Together, both approaches complement each other and allow us to gain a comprehensive understanding of the QAH effect in magnetic fields.

Let us now focus on a QAH insulator with $M, B < 0$. In particular, we computed the spectra of a QAH insulator for $B_\perp = 0$, 1, and $-1\,\mathrm{T}$, shown in Figs. 2.7(a)–(c), respectively. The color code reflects the spatial wave function localization in the y-direction. Wave functions that are localized in the bulk (edge) are depicted in gray (red). As it was explained in Sec. 2.1.1, the Dirac point is located in the bulk gap for $B_\perp = 0$. An increase of the magnetic field pushes the QAH edge states and, associated, the Dirac point into the valence or into the conduction band, depending on whether $\mathrm{sgn}\,(eB_\perp)$ is greater or lesser than zero. It is apparent that for the given system parameters and independent of the magnetic field direction, edge states traverse

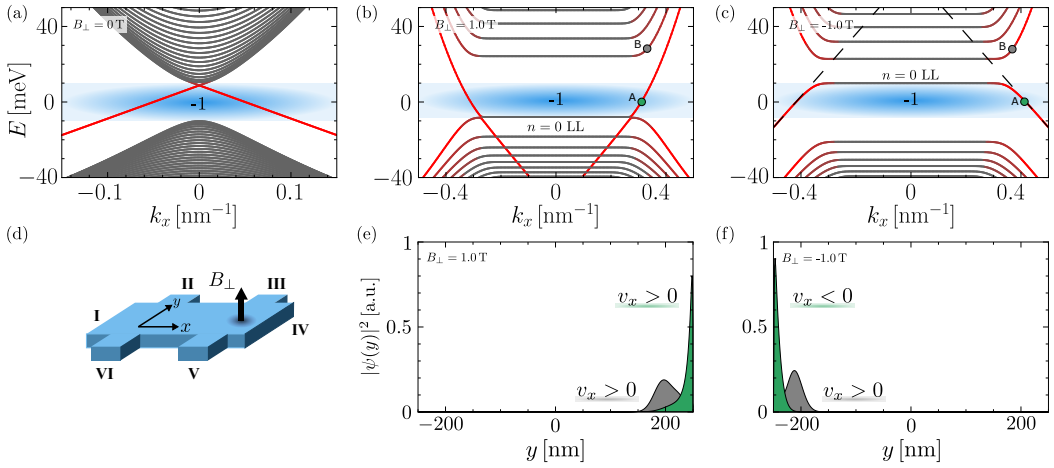

Figure 2.7.: LL spectrum of Chern insulator with $M = -10\,\mathrm{meV}$, $B = -685\,\mathrm{meV\,nm^2}$, $D = -600\,\mathrm{meV\,nm^2}$, and $A = 365\,\mathrm{meV\,nm}$ mapped on a lattice with $L_y = 500\,\mathrm{nm}$, and $a = 1\,\mathrm{nm}$ for a magnetic field of (a) $0\,\mathrm{T}$, (b) $1\,\mathrm{T}$, and (c) $-1\,\mathrm{T}$. Color code displays the wave function localization. Edge (bulk) states are depicted in red (gray). The blue shaded area marks the Dirac mass gap [Eq. (2.63)] characterized by $\sigma_{xy}(-B_\perp) = \sigma_{xy}(B_\perp)$, where Chern numbers are explicitly shown. In (c), dashed line indicates evolution of QAH edge states in the conduction band before hybridizing with bulk states. (d) Sketch of conventional six-terminal Hall bar. In (e) and (f), probability density of two wave functions is depicted corresponding to point A (green dot) and B (gray dot) in the spectrum shown in (b) and (c), respectively. Sign of Fermi velocity is highlighted. Reprinted from Ref. [P6].

the Dirac mass gap [cf. Eq. (2.63)], which is marked by the blue area in Figs. 2.7(a)–(c) [a]. As shown in Sec. 2.4, these edge states are uniquely related to σ^I_{xy}, Eq. (2.50), since this is the only term which can contribute within the Dirac mass gap. Ergo, these states are descendants of the QAH edge states and exist only if $M/B > 0$ and $B_\perp < B_{\perp,triv}$.

The QAH edge states can continue to exist outside of the Dirac mass gap, since they are not bound by a Heaviside step function [cf. discussion below Eq. (2.70)]. This is clearly observed for positive magnetic fields as shown in Fig. 2.7(b), where quasi-helical QH and QAH edge states coexist in the valence band. However, there is no clear signature of QAH edge states outside of the Dirac mass gap for negative magnetic fields, as shown in Fig. 2.7(c). In the latter case, this is because the QAH edge states are strongly hybridized with conduction band states. The reason for this will be explained in detail in the next section. To schematically illustrate the hybridization process, we indicated the QAH edge states before hybridizing with QH states by dashed lines in Fig. 2.7(c).

Let us now focus at first on the signatures of the QAH edge states within the Dirac

[a] Recall that the Dirac mass gap signifies the regime where the Hall conductivity is an even function of the magnetic field.

mass gap. In this regime, QH edge states cannot exist [see Eqs. (2.50) and (2.61)] so that the QAH edge states are protected from hybridization. In particular, we focus on how the violation of the Onsager relation, $\sigma_{xy}(-B_\perp) = \sigma_{xy}(B_\perp)$, is connected to the QAH edge states. To this end, the wave functions for two selected points are shown in Figs. 2.7(e) and (f), corresponding to the two marked points in Figs. 2.7(b) and (c), for the two magnetic field configurations. Point A marks a QAH edge state inside of the Dirac mas gap, while point B marks a conventional QH edge state outside of the Dirac mass gap. For $B_\perp > 0$, edge states with positive momenta are localized at the top edge ($y = L_y/2$) of our stripe geometry [Fig. 2.7(e)], while they localize at the bottom edge ($y = -L_y/2$) for $B_\perp < 0$ [Fig. 2.7(f)]. Flipping the magnetic field direction results therefore in changing the spatial localization of edge states at given k_x.

Transport in Dirac mass gap: The associated Hall resistance R_H can be now computed employing the Landauer-Büttiker formalism, as explained in Sec. 1.2. For a six terminal set-up, schematically depicted in Fig. 2.7(d), it follows that [see also Eq. (1.48)]:

$$R_H = \frac{h}{e^2} \frac{T_c - T_a}{T_c^2 - T_a T_c + T_a^2}\,, \tag{2.82}$$

where $T_c = T_{i+1\leftarrow i}$ is the transmission probability in clockwise direction, i.e., from the ith to the $(i+1)$th contact; $T_a = T_{i\leftarrow i+1}$ is the transmission probability in anticlockwise direction. We consider first the QAH case in which the chemical potential is placed at the point A in Fig. 2.7(b). Since the Fermi velocity $v_x = \hbar^{-1}\partial E/\partial k_x$ is positive for $k_x > 0$ and the wave function is located at the top edge of our stripe geometry, there is only one chiral edge channel propagating clockwise along the edges of the Hall bar. This amounts to $T_c = 1$ and $T_a = 0$ resulting in $R_H = h/e^2$.

In comparison, placing the chemical potential at the point A in Fig. 2.7(c), the wave function of the QAH edge state for $k_x > 0$ is located at the bottom edge and exhibits a negative Fermi velocity, i.e., both, the edge localization and the Fermi velocity flip sign for $B_\perp \to -B_\perp$. The two effects combined yield again a clockwise propagating edge state which exhibits the same transmission probabilities and, hence, the same Hall resistance $R_H = h/e^2$, as the QAH edge state in Fig. 2.7(b). This originates from the fact that, in both cases, the same QAH edge state is probed whose chirality is defined by the intrinsic Chern number, Eq. (2.5), and not by the magnetic field. As a result, the Hall conductivity in the Dirac mass gap is an even function of the magnetic field and, therefore, violates the Onsager relation (cf. to discussion in Sec. 2.3). This holds as long as QAH edge states are allowed to bridge this gap, i.e., for $B_\perp < B_{\perp,triv}$ and $M/B > 0$. We highlighted the connection to the QAH effect, since one might naively conclude, by looking at Fig. 2.7(c), that no signature of the QAH effect survived in magnetic fields.

This clearly differentiates QAH edge states from QH edge states, that are induced by the external magnetic field outside of the Dirac mass gap. While QH edge states also change their spatial localization, their Fermi velocity remains the same for $B_\perp \to -B_\perp$. As a result, the transmission probability of each QH edge state in the conduction band changes from $(T_c, T_a) = (1, 0)$ to $(0, 1)$ for $B_\perp \to -B_\perp$ and their contribution to the total Hall resistance [Eq. (2.82)] changes from $+h/e^2$ to $-h/e^2$. The signs are opposite for valence band LLs, where the Hall resistance changes from $-h/e^2$ to $+h/e^2$.

2.6.2. Role of broken particle-hole symmetry

We now turn the focus to properties of the QAH edge states outside of the Dirac mass gap. In particular, we clarify why, in this regime for the given set of parameters, QAH edge states are only clearly visible for $B_\perp > 0$ [Fig. 2.7(b)] and not for $B_\perp < 0$ [Fig. 2.7(c)]. Let us first start with the case of positive magnetic fields.

As we have stressed earlier, QAH edge states can hybridize with QH states outside of the Dirac mass gap, since they are not protected by symmetry. The crossing (up to finite size gaps) between the QAH edge states and the $n = 0$ LL, as it is observed in Fig. 2.8(a) at k_{cross}, is instead protected by differently localized wave functions [Fig. 2.8(c)]. This situation is however not generic as a comparison with a Chern insulator with smaller D-parameter shows [see avoided crossings in Fig. 2.8(b)]. To analyze this process quantitatively, we plot in Fig. 2.8(d) at $B_\perp = 1\,\mathrm{T}$ the hybridization gap Δ_{hyb} of the QAH edge states and the $n = 0$ LL as a function of D for various Dirac masses M. The numerical results show that increasing the absolute value of M and D increases the regime in which Δ_{hyb} drops to zero (numerical resolution: $\pm 0.1\,\mathrm{meV}$). This means that a strong PH asymmetry protects the edge states from hybridizing with bulk LLs. In the following, we label the critical magnetic field above which $\Delta_{hyb} \neq 0$, i.e., a hybridization gap starts to form, by $B_{\perp,hyb}$.

Physically, the behavior of $B_{\perp,hyb}$ in Fig. 2.8(d) can be understood noting that this critical field is basically determined by the parameter dependence of k_{cross}. This is because k_{cross} is intimately linked to the wave function overlap of QAH edge states and QH states. We can derive an analytic expression for k_{cross} based on the energetic position of the $n = 0$ LL and the dispersion of the QAH edge states in magnetic fields, given by given by Eq. (2.9) and (2.80), respectively:

$$\begin{aligned} E_0(B_\perp) &= E_{edge}(k_{cross}, B_\perp) \\ \to k_{cross} &= \pm \frac{1}{\hbar v_x} \left[E_0(B_\perp) + \mu_B g_{eff} B_\perp - E_D \right] . \end{aligned} \tag{2.83}$$

Hybridization is almost absent if $|k_{cross}| \ll k_{max}$ ($\Delta_{hyb} \approx 0$), where $2k_{max} = L_y \left| eB_\perp \right| / \hbar$ is the maximal width of a bulk LL. This is due to the fact that the QAH edge states

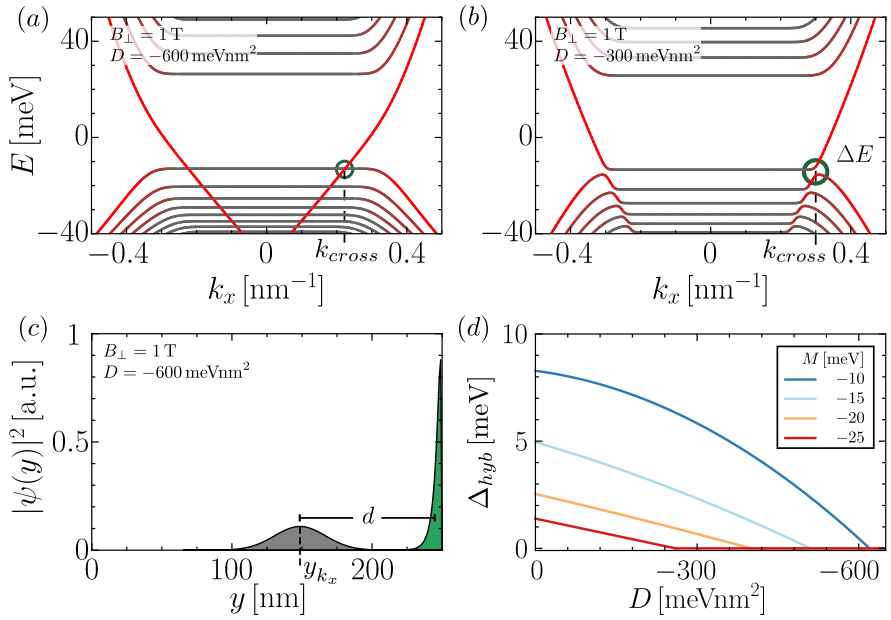

Figure 2.8.: Effect of D-parameter on band structure of Chern insulator for $M = -15\,\mathrm{meV}$, $A = 365\,\mathrm{meVnm}$, $B = -685\,\mathrm{meVnm}^2$, (a) $D = -600\,\mathrm{meVnm}^2$, and (b) $-300\,\mathrm{meVnm}^2$ at $B_\perp = 1\,\mathrm{T}$. (Anti)crossing at k_{cross} between QAH edge state and $n = 0$ LL is marked by green circle. (c) Probability density of wave functions at crossing point in (a) between QAH edge state (green) and Gaussian wave function of $n = 0$ LL (gray). The Gaussian wave function is centered at $y \approx 145\,\mathrm{nm}$. The distance between the centers of the wave functions is given by d. (d) Hybridization gap between QAH edge state and $n = 0$ LL as function of D-parameter for various Dirac masses M. The numerical resolution determining the gap is $\Delta E = \pm 0.1\,\mathrm{meV}$. Reprinted from Ref. [P6].

are exponentially localized at the edges, while the Gaussian wave functions of the QH states are each centered at $y_{k_x} = l_{B_\perp}^2 k_x$ and have a standard deviation of $\sigma = \sqrt{2} l_{B_\perp}$ [cf. Eq. (1.57)]. The wave functions are shown exemplary in Fig. 2.8(c) for the marked crossing point in Fig. 2.8(a).

A hybridization gap Δ_{hyb} starts to form only if the distance d between the wave function centers gets of the order of the standard deviation σ, i.e., if $d < d_{crit} = c\sigma$. Here, $c > 0$ is a fitting parameter which can be adjusted to gain good agreement with the numerical results (typically, $c \sim 1$). Assuming that the center of the QAH edge state lies approximately at the sample edge, the distance between the wave function centers is roughly given by $d = L/2 - y_{k_x}$. Hybridization takes therefore place for

$$k_{cross} > l_{B_\perp}^{-2}(L/2 - c\sigma) \equiv k_{hyb}\,. \tag{2.84}$$

An expression for the corresponding critical magnetic field is found by solving

$$E_0(B_{\perp,hyb}) = E_{edge}(k_{hyb}, B_{\perp,hyb}) \tag{2.85}$$

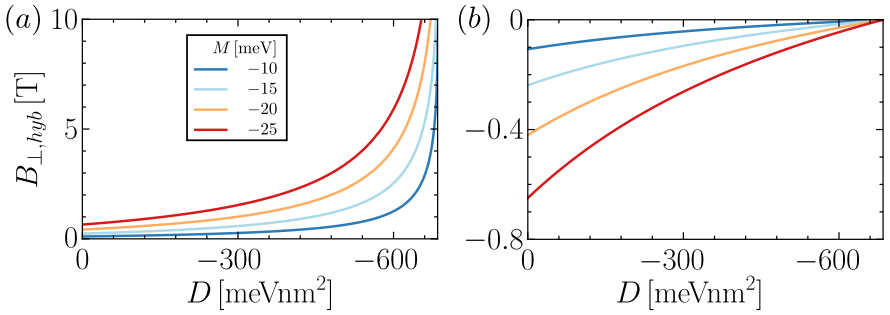

Figure 2.9.: Evolution of $B_{\perp,hyb}$ as function of D-parameter for (a) positive and (b) negative magnetic fields with $M = -10, -15, -20$, and -25 meV [see plot legend in (a)]. $B_{\perp,hyb}$ increases with increasing absolute value of M and D. The fitting parameter $c = 1.5$ (see text for further discussion). Reprinted from Ref. [P6].

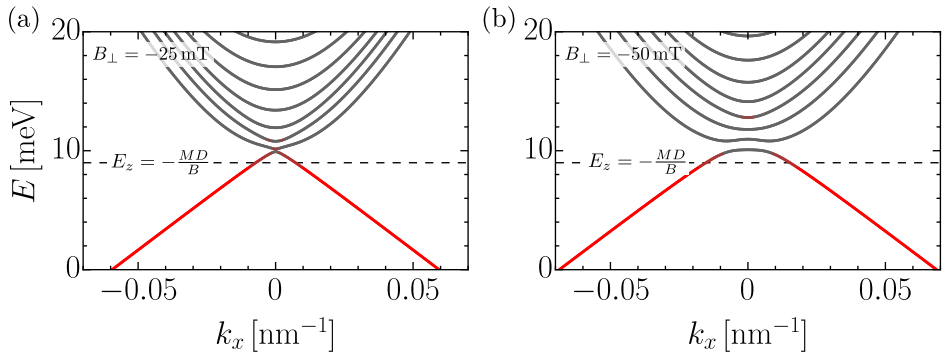

Figure 2.10.: Band structures of Chern insulator for small, negative magnetic fields of (a) -25 mT and (b) -50 mT are shown. QAH edge states are pushed into the conduction band, where they strongly hybridize with bulk bands. Dashed line marks energy of Dirac point for $B_\perp = 0$. For a better visibility, the energy range is limited from $E = 0$ to 20 meV. Reprinted from Ref. [P6].

for $B_{\perp,hyb}$, but we refrain here from showing the full analytic expression as it is very long and cumbersome. Instead to gain some insight in the parameter dependence of $B_{\perp,hyb}$, we Taylor expand the analytical expression up to first order in D, resulting in

$$B_{\perp,hyb} \approx B_0 \left(\mathrm{sgn}\,(eB_\perp) + \frac{2cA}{B\sqrt{2MB + c^2A^2}} D \right) , \tag{2.86}$$

where

$$B_0 = \frac{\hbar}{eB^2} \left[MB + cA \left(cA - \sqrt{c^2A^2 + 2MB} \right) \right] . \tag{2.87}$$

The exact analytic behavior of $B_{\perp,hyb}(D)$ for positive and negative magnetic fields is shown in Fig. 2.9(a) and (b), respectively.

Discussion: Taken together, Eq. (2.86) and Fig. 2.9 show that, for $B_\perp > 0$, the absolute value of $B_{\perp,hyb}$ increases when D approaches B, i.e., a strong PH asymme-

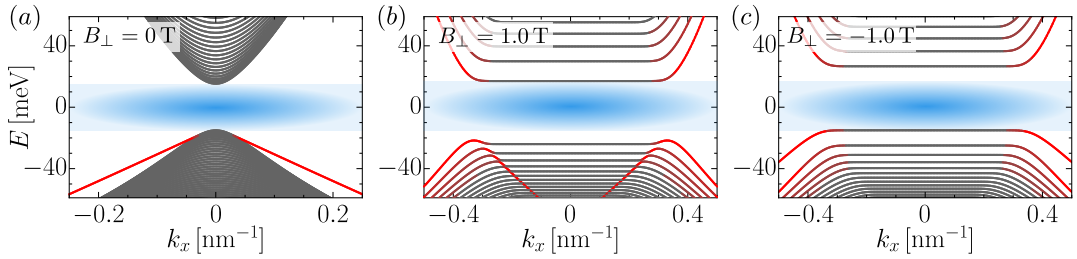

Figure 2.11.: Band structure of trivial Chern insulator for (a) $B_\perp = 0\,\mathrm{T}$, (b) $1\,\mathrm{T}$, and (c) $-1\,\mathrm{T}$. Same parameters as in Fig. 2.7 are used except for $M = +15\,\mathrm{meV}$. A trivial edge state is observed in (a) which does not traverse the Dirac mass gap. By virtue of the trivial topology, there are no edge states in the Dirac mass gap (blue regime) in magnetic fields. Reprinted from Ref. [P6].

try protects the edge channels from hybridization. This is in contrast to the case of negative magnetic fields, where a strong PH asymmetry causes already at very small magnetic fields ($\sim$ mT) a strong hybridization of QH and QAH edge states. This is in accordance with the band structure calculations presented in Fig. 2.10, which show that already magnetic fields of $B_\perp < -25\,\mathrm{mT}$ are sufficient to push the Dirac point into the conduction band and to cause large hybridization gaps. We can therefore attribute the difference in the appearance of the QAH edge states in Fig. 2.7(b) and (c) at $B_\perp = \pm 1\,\mathrm{T}$ to a strong PH asymmetry.

Let us finally reiterate that this does not affect any signatures of the QAH edge states within the Dirac mass gap, where they remain to be protected from hybridization. However, strong hybridization gaps between the QAH edge state and the $n = 0$ LL should make it more difficult to observe signatures of coexistent edge states in the experiment. This includes the charge pumping, discussed in Sec. 2.5, which will be limited to $B_\perp < B_{\perp,hyb}$, if hybridization gaps start to appear [a]. Note however that in real 2D TIs, which are described at low energies by the BHZ model, like (Hg,Mn)Te [15] or InAs/GaSb bilayers [20], numerical deviations from the predicted form of Δ_{hyb} might occur due to the natural limitations of the model. In particular, deviations can arise from employing the low-energy BHZ model and assuming an impurity-free system. Both assumptions can affect the explicit form of the wave functions, the position of the Dirac point [137] and, hence, alter the hybridization of QH and QAH edge states. It has been also argued that the use of hard wall boundary condition can cause additional spurious solutions which might affect the position of the Dirac point [138, 139]. The latter effect must be further studied in the future. Independent of the detailed microscopics, Eq. (2.50) shows that the critical magnetic field, above which a hybridization gap ultimately must start to form, is given by $B_{\perp,triv}$ [Eq. (2.33)]. This is due to the fact that QAH edge states are then no longer allowed to traverse the Dirac mass gap.

[a] This does not affect regime I in Fig. 2.6, where the Dirac point has not yet crossed any bulk LL.

We conclude this section by comparing our findings with a topologically trivial Chern insulator ($M/B < 0$) with $D \neq 0$. In this case, the Hall conductivity σ_{xy} is solely determined by σ_{xy}^{II}, since the two contributions to the spectral asymmetry cancel each other, resulting in $\sigma_{xy}^{I} = 0$ [see Eqs. given by Eq. (2.50) and (2.61)]. Even though the system is of trivial topology, edge states, depicted in red, can exist outside of the Dirac mass gap for $B_\perp = 0$, as shown in Fig. 2.11(a). This paradoxical extension of edge states to the topologically trivial regime can be explained by an emergent, approximate chiral symmetry, provided that the PH symmetry is broken at $B_\perp = 0$ [140]. But in stark contrast to QAH edge states, trivial edge states can never enter the Dirac mass gap, even for $B_\perp \neq 0$ [cf. Fig. 2.7 and 2.11].

2.6.3. Transport of coexistent QH and QAH edge states

The appearance of counterpropagating QH and QAH edge channels, that are not protected by symmetry (quasi-helical), is a unique feature of QAH insulators in magnetic fields. In particular, this feature differentiates a QAH insulator from a conventional QH phase. The latter is characterized by unidirectionally propagating edge channels. The goal of this section is to show in a proof of concept that transport, governed by quasi-helical edge states, can appear very similar to the one of helical-edge channels in a 'clean system', while they can have unique transport signatures in a 'dirty system'.

Let us start from the analytic expressions for the Hall and longitudinal resistance which were derived in Sec. 1.2 based on the Landauer-Büttiker approach [see also Eqs. (1.48) and (1.49)]:

$$R_H = \frac{h}{e^2} \frac{T_c - T_a}{T_c^2 - T_a T_c + T_a^2} \,, \tag{2.88}$$

$$R_L = \frac{h}{e^2} \frac{T_c T_a}{T_c^3 + T_a^3} \,, \tag{2.89}$$

where T_c (T_a) is the transmission probability between adjacent contacts on a typical Hall bar in clockwise (anti-clockwise) direction. In Fig. 2.12, we map out the full parameter space for Hall and longitudinal resistance for $T_c, T_a \leq 1$. In the case that $T_c = T_a = 1$, we reach the characteristic values of the QSH phase, where $R_H = 0$ and $R_L = h/2e^2$ [17]. In the case that $T_c = 1$ and $T_a = 0$ (or, $T_c = 0$ and $T_a = 1$), the transport signature is equivalent to the one of a single chiral mode in the QH phase. As our system contains two counterpropagating edge channels which are not protected by symmetry, realistic transmission probabilities can deviate from these limiting cases. Nevertheless, note that resistance values in the vicinity of the contour lines, depicted in Fig. 2.12, can be still close to quantized values for a large range of parameters. In addition, Fig. 2.12(b) demonstrates that small deviations from the symmetric case (i.e., from $T_c = T_a$) cause large deviations from $R_H = 0$, if $T_c, T_a \ll 1$.

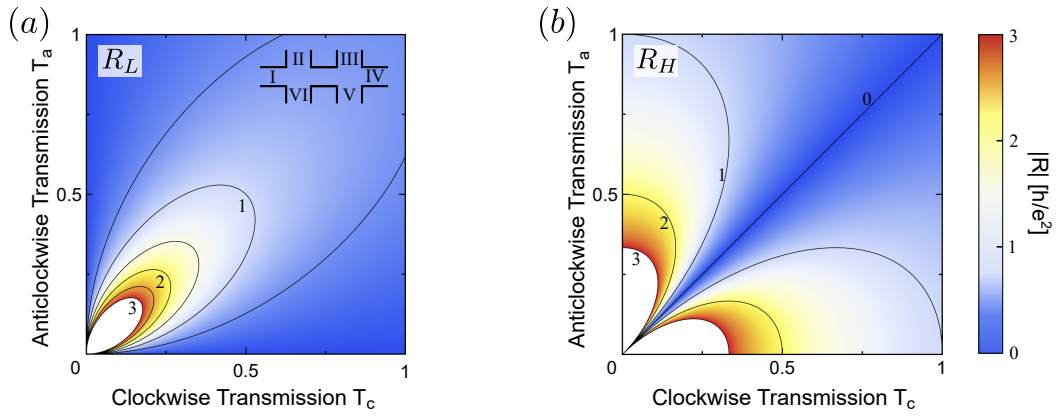

Figure 2.12.: We map out the full phase space for (a) longitudinal and (b) (transverse) Hall resistance with $T_{12}, T_{21} \leq 1$. The underlying six-terminal Hall bar is schematically depicted in the inset of (a). Current flows between contact 1 and 4. The color code highlights the absolute value of resistance with white indicating that the resistance is out of scale. Contour lines highlight in (a) $R_L = 0.5, 1, 1.5, 2, 2.5, 3$ and in (b) $R_H = 0, 1, 2, 3$ (given in units of h/e^2). From Ref. [P5]. Reprinted with permission from APS.

Let us now investigate QH and QAH edge states in more detail. We assume at first that the mean-free path l_m of the quasi-helical edge channels is long compared to the distance between adjacent contacts L ('clean system') [a] . The transmission probabilities are then roughly given by $T_c = T_a = 1$. This means quasi-helical edge states can have similar transport features as QSH edge states if $l_m \ll L$.

In the opposite limit when $L > l_m$, even point-like impurities contribute to backscattering since quasi-helical edge states are not protected by symmetry. Due to the required unitarity of the S-matrix, we find in this case that $T_c = T_a < 1$, which both tend to zero in the large system limit. However, any small difference between the two sides of the Hall bar can cause slight deviations from a perfect quantization, as indicated schematically by the noisy plateau Fig. 2.6.

Another very prominent source for backscattering are charge puddles [87] constituting a major, if not the dominant, source for backscattering in HgTe based 2D TIs [86] [b]. Here, we want to focus however on large samples, where $L > n_p^{-1/2}$ and n_p is the puddle density [87]. In this limit, Väyrynen et al. [87] showed that the bulk conductivity cannot be neglected if the system size exceeds the leakage length $L^\star = 1/\sigma_B \rho_e$. Here, σ_B is the bulk conductivity and ρ_e is the edge resistivity.

If $L > L^\star$, the top and bottom edge can be connected via puddle-to-puddle hopping.

[a] QH and QAH edge states possess different wave function localizations and (pseudo)spin polarizations. This might suppress scattering even if the system contains impurities. For a detailed understanding, a microscopic model is however required.

[b] The characteristic value of $R_L = h/2e^2$ in the QSH phase has been therefore only achieved in microstructured Hall bars.

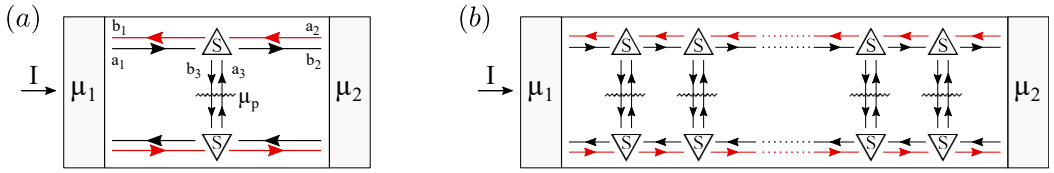

Figure 2.13.: Schematic two-terminal set-up, where counterpropagating QH and QAH edge states are depicted by red and black arrows, respectively. The triangle indicates a scatterer with scattering matrix S that partially transmits particles coherently and partially scatters particles into a fictitious contact (wiggly line) with chemical potential μ_p. The fictitious contact models an inelastisc scattering event connecting top and bottom edge. In (a), we consider a toy model with a single charge puddles whereas (b) generalizes the situation to the case of N charge puddles. In (a), incoming a_i and outgoing b_i scattering states are labeled for the top edge. From Ref. [P5]. Reprinted with permission from APS.

To gain a better understanding of this situation, we study a toy model using the Landauer-Büttiker approach. Here, the top and bottom edge are (for the sake of simplicity) connected via a single charge puddle [a]. This situation is schematically depicted in Fig. 2.13(a). The scattering from the edge states onto the charge puddle can be described by the following S-matrix:

$$S = \begin{pmatrix} r_{11} & t_{12} & t_{13} \\ t_{21} & r_{22} & t_{23} \\ t_{31} & t_{32} & r_{33} \end{pmatrix}, \tag{2.90}$$

where t_{ij} and r_{ij} denote transmission and reflection amplitudes from the jth incoming to the ith outgoing scattering state, respectively. For the top edge, scattering states are labeled according to Fig. 2.13(a). For the bottom edge, we assume the same type of scatterer but QH and QAH edge states switch their propagation direction. This model describes partially coherent transmission [141] of QH and QAH edge states (t_{12} and t_{21}), where only a fraction of the current is transmitted onto the charge puddle (t_{31} and t_{32}). Since charge puddles act like inelastic scatterers [cf. Sec. 1.2, they cause dephasing and can be therefore modeled as fictious voltage probes [63].

Since QH and QAH edge states have different spin character and wave function localization [b], the QH-to-puddle tunneling probability ($|t_{32}|^2$) can differ from the QAH-to-puddle tunneling probability ($|t_{31}|^2$). The latter should be related to the respective wave function overlaps. The exact values should depend on the band character and the spatial location of the specific charge puddle. We start with a toy model to prove the possibility of asymmetric transmission probabilities T_{ij}. Choosing $r_{11} = r_{22} = t_{32} = t_{13} = 0$,

[a] In a realistic model, an electron would need to hop multiple times between adjacent puddles to reach the other edge.

[b] This difference is connected to their different physical origin. QH edge states are induced by the magnetic field, while QAH edge states are related to the inverted band structure.

unitarity of the S-matrix requires that

$$T_{QH} = 1, \qquad T_{QAH} + T_p = 1, \qquad R_p + T_p = 1\,, \tag{2.91}$$

where $T_{QAH} = |t_{21}|^2$, $T_{QH} = |t_{12}|^2$, $T_p = |t_{31}|^2 = |t_{23}|^2$, and $R_p = |r_{33}|^2$. Importantly, T_p denotes the transmission probability from the chiral QH edge state to the charge puddle. Without loss of generality, we take $\mu_1 > \mu_2$ and $\mu_2 = 0$. The current into the puddle is therefore given by

$$I_p = -\frac{e}{h}\left[(2 - 2R_p)\,\mu_p - T_p\,\mu_1\right]\,. \tag{2.92}$$

With $I_p = 0$, it follows that $\mu_p = \mu_1/2$. The current which flows along the top edge into contact 2 is given by

$$I_2 = -\frac{e}{h}\left(T_{QAH}\,\mu_1 + T_p\,\mu_p\right) \tag{2.93}$$

$$= -\frac{e}{h}\left(1 - T_p/2\right)\mu_1\,. \tag{2.94}$$

We can identify $1 - T_p/2$ as an effective transmission coefficient between contact 1 and 2, i.e., T_{21}. Since $T_{12} = T_{QH} = 1$ and $T_{21} < 1$ for $T_p \neq 0$, we showed the possibility of having asymmetric transmission coefficients when top and bottom edge states are connected via puddle-to-puddle hopping.

As T_p is in general a small number, it is interesting to look at the case of many charge puddles. This situation is schematically illustrated in Fig. 2.13(b). Following an analogous calculation, it is straightforward to generalize Eq. (2.94) to the situation of N puddles:

$$I_2 = -\frac{e}{h}\frac{2 - T_p}{2 + (N-1)T_p}\mu_1\,. \tag{2.95}$$

In conclusion, this shows that, for $L > L^\star$, it is possible to find peculiar values for R_H and R_L in magnetotransport experiments, if transport is governed by quasi-helical edge states. Intriguingly, it is even possible to measure Hall resistance values that are close to quantized values. The presented toy model serves as a proof-of-principle. This means that the microscopic scaling behavior in realistic samples may deviate from the analytic form shown in Eq. (2.95). The presented model was motivated by recent experiments on (Hg,Mn)Te quantum wells in the group by Laurens W. Molenkamp. In these specific systems, (noisy) QH plateaus were observed in a regime in which quasi-helical edge states should determine the transport behavior. The latter results are going to be published in the future.

2.7. Signatures of parity anomaly in para- and ferromagnetic TIs

So far, we have focused on a single Chern insulator in magnetic fields. We now go back to a QSH insulator that is described by the full BHZ model. To this end, we reintroduce the spin index to distinguish the two spin blocks of Eq. (2.1). Employing Eq. (2.4), we see that $\eta_\downarrow(B_\perp) = -\eta_\uparrow(B_\perp)$, where $\eta_\uparrow(B_\perp) \equiv \eta(B_\perp)$ is given by Eq. (2.31). The spectral asymmetry in the QSH phase is therefore determined by

$$\eta_{BHZ}(B_\perp) = \eta_\uparrow(B_\perp) + \eta_\downarrow(B_\perp) = 0\,. \tag{2.96}$$

This is accompanied by a vanishing Hall conductivity σ_{xy} in the Dirac mass gap:

$$\sigma^I_{xy} = \sigma^I_{xy,\uparrow} + \sigma^I_{xy,\downarrow}\,, \tag{2.97}$$

where, according to Eq. (2.50),

$$\sigma^I_{xy,s} = \pm\frac{e^2}{2h}\left[\mathrm{sgn}\left(M - B/l^2_{B_\perp}\right) + \mathrm{sgn}\,(B)\right]\,. \tag{2.98}$$

Here, $s = \uparrow,\downarrow$ corresponds to $\pm$, respectively. The QSH phase is characterized by $\sigma^I_{xy} = 0$ due to the underlying parity and TR symmetry at $B_\perp = 0$. Nonetheless, we can consider the odd combination of both spin blocks

$$\eta^S_{BHZ}(B_\perp) = \eta_\uparrow(B_\perp) - \eta_\downarrow(B_\perp) \tag{2.99}$$

to distinguish this state from a trivial insulator. A similar idea was discussed in Ref. [37] for Dirac fermions which do not come with a Bk^2 term. Equation (2.99) is nonzero for $M/B > 0$ and $B_\perp < B_{\perp,triv}$, where $B_{\perp,triv}$ is given by Eq. (2.33). This concept is clearly related to the nontrivial spin Hall conductivity of a QSH insulator [58]:

$$\sigma^S_{xy} = \sigma^I_{xy,\uparrow} - \sigma^I_{xy,\downarrow}\,, \tag{2.100}$$

which we encountered in Sec. 1.3.2. The latter takes on quantized values in the ballistic regime if $M/B > 0$ [142]. This relation highlights the fact that the nontrivial spin Hall conductivity of a QSH insulator can be also interpreted in the language of the parity anomaly [37], since it is related to the topological quantity η^S_{BHZ}. For $B_\perp > B_{\perp,triv}$, Eq. (2.99) drops to zero corresponding to the point at which the spectral asymmetry of each spin block vanishes. Notably, $B_{\perp,triv}$ coincides exactly with the critical field, at which the two spin polarized $n = 0$ LLs cross [61]. This demonstrates that the information about the band inversion is not only contained in the full BHZ model, but in each individual Chern insulator.

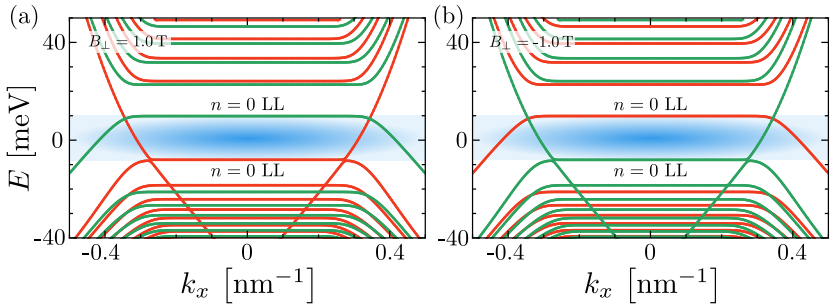

Figure 2.14.: Landau level spectrum of BHZ model without Zeeman or exchange interaction terms for (a) $B_\perp = 1\,\mathrm{T}$ and (b) $-1\,\mathrm{T}$. The color code distinguishes between the spin up (orange) and the spin down (green) block. Model parameters are the same as in Fig. 2.7. The Dirac mass gap (blue shaded area) is characterized by counterpropagating edge states. The spectrum is invariant under $B_\perp \to -B_\perp$ with the exception that the spin up and down block interchange their role. Reprinted from Ref. [P6].

For completeness, we show in Figs. 2.14(a) and (b) the spectra of a QSH insulator for magnetic fields of $1\,\mathrm{T}$ and $-1\,\mathrm{T}$, respectively. The spectra are calculated using the finite-difference-method to determine the eigenvalues of Eq. (2.1) in magnetic fields. The color code marks the two spin blocks. A pair (per edge) of counterpropagating edge states traverses the Dirac mass gap (blue area), which is a hallmark of the underlying QSH topology [17, 142] [a]. Comparing Figs. 2.14(a) and (b), we see that the spectrum remains unaltered for $B_\perp \to -B_\perp$, with the exception that the spin up and down block interchange their role. This effect can be understood noting that reversing the magnetic field direction is equivalent to a parity transformation, as both processes effectively flip the sign of M and B and, therefore, interchange the two spin blocks [cf. to Eqs. (2.9) and (2.10)]. This result also explains the salient asymmetry between the appearance of the QAH edge states for the two spin directions. In Fig. 2.14(a), the strong PH asymmetry protects the QAH edge states of the spin-up block from hybridization, while it causes hybridization gaps for the spin-down block already at very small, positive magnetic fields. As observed in Fig. 2.14(b), the situation is reversed, when we flip the magnetic field direction [cf. to discussion in Sec. 2.6.2].

Let us now introduce additionally a Zeeman or an exchange term of the following form $H_s = \sigma_0 \otimes \tau_z\, g(B_\perp)$, given in the basis of Eq. (2.3). This term can be easily incorporated by replacing in our results $M \to M \pm g(B_\perp)$ for the spin up $(+)$ and spin down block $(-)$, respectively. The two contributions to the total Hall conductivity, which are exclusively determined by the spectral asymmetry in the Dirac mass gap, are

[a] Note that in the QSH effect both edge states in the Dirac mass gap are related to the intrinsic topology. The counterpropagating ('helical') edge states possess the same wave functions except for a different spin polarization. This is different from quasi-helical QH and QAH edge states which arise from different physical mechanisms outside of the Dirac mass gap. Quasi-helical edge states share neither the same band character, nor the same spatial localization.

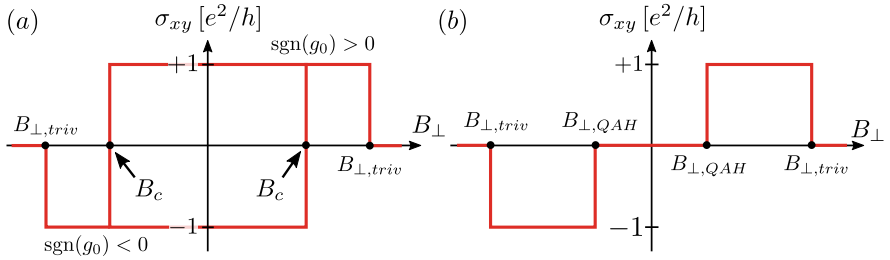

Figure 2.15.: Sketch of σ^I_{xy} is shown for (a) ferromagnetic, and (b) paramagnetic exchange interaction (Zeeman term) as function of external magnetic field $B_\perp$ at a constant chemical potential (placed within the Dirac mass gap). (a) Sign of σ^I_{xy} is determined by polarization direction of magnetic domains (g_0) of the ferromagnet which is here supposed to follow a hysteresis. Signs of g_0 are indicated. The Hall conductivity can switch its sign at the coercive field B_c. (b) In the case of a paramagnet, a finite magnetic field $B_{\perp,QAH}$ is needed to overcome the Dirac mass gap of one of the two spin blocks, resulting in a nonzero σ^I_{xy}. We assumed for this paramagnetic case that $g_0 > 0$. In both cases, the Hall conductivity vanishes at $B_\perp > B_{\perp,triv}$, where $\eta_{BHZ} = 0$. Reprinted from Ref. [P6].

therefore given by [cf. Eq. (2.98)]

$$\sigma^I_{xy,s} = \pm\frac{e^2}{2h}\left[\mathrm{sgn}\left(M \pm g(B_\perp) - B/l^2_{B_\perp}\right) + \mathrm{sgn}\,(B)\right] , \tag{2.101}$$

where $s = \uparrow,\downarrow$ corresponds to $\pm$, respectively. The particular importance of exchange and Zeeman terms arises from the fact, that they can both drive a 2D TI from the QSH to the QAH phase, as explained in Sec. 1.3.3. In the following, we are going to compare two cases: Firstly, H_s describes a ferromagnetic exchange interaction, and, secondly, H_s describes a paramagnetic exchange or, equivalently, a Zeeman interaction [a].

Ferromagnetic TI: Let us first consider the ferromagnetic case, where the magnetization $g(B_\perp)$ follows a hysteresis. For our model, we assume that $g(B_\perp) \equiv g_0$ remains constant for a given polarization direction of the magnetic domains. This holds until the external magnetic field exceeds the coercive field B_c of the ferromagnet. Above this threshold, the magnetic domains can flip their polarization direction to align with the external magnetic field. At $B_\perp = 0$, we assume that the system is in the QAH phase, i.e., $(M + g_0)(M - g_0) < 0$ [21]. This condition, which was explained in Sec. (1.3.3), guarantees that only one of the two spin blocks is topologically nontrivial. The conductivity in the Dirac mass gap is hence determined solely by the magnetization direction, $\sigma^I_{xy} = \mathrm{sgn}\,(g_0)\,e^2/h$. Applying an external magnetic field, Eqs. (2.97) and (2.101) show that the Hall conductivity at constant μ follows in quantized steps the magnetic hysteresis (g_0). This statement remains valid as long as the orbital contribution in Eq. (2.101), the $B/l^2_{B_\perp}$ term, is small compared to the magnetization. More precisely, σ^I_{xy} drops to

[a] In a realistic material, a Zeeman term will always come on top of the either paramagnetic or ferromagnetic exchange interaction.

zero, when the term $B/l_{B_\perp}^2$ exceeds the effective Dirac mass, $M \pm g_0$, at $B_\perp > B_{\perp,triv}$, where

$$\begin{aligned} M \pm g_0 - B/l_{B_{\perp,triv}}^2 &\stackrel{!}{=} 0 \\ \rightarrow B_{\perp,triv} &= \mathrm{sgn}\,(eB_\perp)\,\frac{\hbar}{e}\max\left(\frac{M \pm g_0}{B}\right) . \end{aligned} \tag{2.102}$$

Ultimately, the orbital contribution drives both spin blocks into the trivial regime. The behavior of σ_{xy}^I as a function of $B_\perp$ at constant μ is schematically shown in Fig. 2.15(a), where we assume that $B_c < B_{\perp,triv}$. Since σ_{xy}^I follows the magnetic hysteresis, the Hall conductivity is an even function of the magnetic field for $B_\perp < B_c$. This represents a violation of the Onsager relation (compare to discussion in Sec. 2.3). The peculiar behavior of σ_{xy}^I is encoded in a nonzero spectral asymmetry η_{BHZ}, which only drops to zero for $B_\perp > B_{\perp,triv}$. As we have stated previously, this is a signature of the QAH effect in magnetic field and is as such a consequence of the parity anomaly.

Finally, note that in this scenario, the Dirac mass gap is defined by [cf. Eq. (2.63)]

$$\left|\mu + D/l_{B_\perp}^2\right| \leq \min\left|M \pm g_0 - B/l_{B_\perp}^2\right| . \tag{2.103}$$

In comparison to the case of a single Chern insulator, the minimum is required to ensure that the chemical potential is placed within the Dirac mass gap of both spin blocks.

To analyze the role of the QAH edge states in the ferromagnetic case for $B_\perp < B_c$, we show exemplary the band structure of a QAH insulator with $g_0 > 0$ in Fig. 2.16(a) and (b) for $B_\perp = 1\,\mathrm{T}$ and $-1\,\mathrm{T}$, respectively. For the given system parameters and independent of the magnetic field direction, only the spin down (green) block is in the inverted regime. This is reflected by the existence of only spin down QAH edge states in the Dirac mass gap (blue area). It hence follows that $\sigma_{xy}(-B_\perp) = \sigma_{xy}(B_\perp)$. Due to the strong PH asymmetry, the appearance of the QAH edge states outside of the Dirac mass gap changes with the magnetic field direction.

Paramagnetic TI: Let us now turn to the (second) paramagnetic case. For simplicity, we assume that $g(B_\perp) = g_0 B_\perp$, although one should bare in mind that a paramagnetic exchange interaction is actually determined by a Brillouin function [21]. Since we are here interested in a qualitative discussion, this approximation allows us to write down analytic results. In comparison to the ferromagnetic case, the system is in the QSH phase, i.e., $\sigma_{xy}^I = 0$ at $B_\perp = 0$ [cf. Fig. 2.15(b)]. Applying now an external magnetic field breaks the symmetry between the two spin blocks. Their Dirac mass gaps close at two different critical magnetic fields, i.e., $B_{\perp,triv,\uparrow} \neq B_{\perp,triv,\downarrow}$. Ultimately, the QAH phase is induced when one of the two spin blocks becomes trivial. From Eq. (2.101),

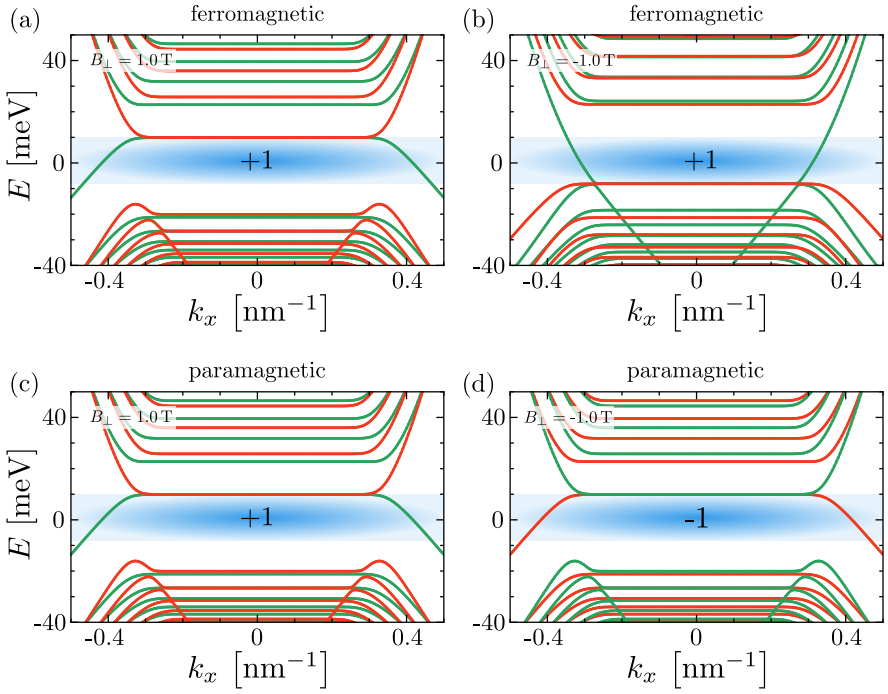

Figure 2.16.: Landau level spectrum of BHZ model in the presence of a (a)–(b) ferromagnetic, or (c)–(d) paramagnetic exchange interaction, where in (a) and (c) $B_\perp = 1\,\mathrm{T}$, and in (b) and (d) $B_\perp = -1\,\mathrm{T}$. The color codes marks the spin up (orange) and spin down (green) block. We employed the following set of parameters: $M = -1\,\mathrm{meV}$, $B = -685\,\mathrm{meV\,nm^2}$, $D = -600\,\mathrm{meV\,nm^2}$, and $A = 365\,\mathrm{meV\,nm}$. (a)–(b) In the ferromagnetic case, we use $g(B_\perp) = g_0$ with $g_0 = 9\,\mathrm{meV}$. (c)–(d) In the paramagnetic case, we use $g(B_\perp) = g_0 B_\perp$ with $g_0 = 9\,\mathrm{meV/\,T}$. For this specific set of parameters, the paramagnetic magnetization matches the ferromagnetic one at $B_\perp = 1\,\mathrm{T}$. The blue regime marks the Dirac mass gap, i.e., the QAH regime. Chern numbers are indicated. Reprinted from Ref. [P6].

we see that this is the case if

$$\left(M + g(B_\perp) - B/l_{B_\perp}^2\right)\left(M - g(B_\perp) - B/l_{B_\perp}^2\right) < 0\,. \tag{2.104}$$

In comparison to Ref. [21], this generalizes the condition for the QAH effect to finite external magnetic fields. Equation (2.104) is fulfilled for $|B_\perp| > B_{\perp,QAH}$, where

$$B_{\perp,QAH} = \min\left[B_{\perp,triv,\uparrow}, B_{\perp,triv,\downarrow}\right] \tag{2.105}$$

$$= \min\left[\frac{M}{\mathrm{sgn}\,(eB_\perp)\,Be/\hbar \mp g_0}\right]\,. \tag{2.106}$$

In this regime, the Hall conductivity is given by $\sigma_{xy}^I = \mathrm{sgn}\,(g_0)\,\mathrm{sgn}\,(eB_\perp)\,e^2/h$, assuming a constant chemical potential within the Dirac mass gap. The $\mathrm{sgn}\,(eB_\perp)$ dependence results from the fact that, depending on the magnetic field direction, either $\sigma_{xy,\uparrow}^I$ or $\sigma_{xy,\downarrow}^I$ is nonzero. Paramagnetic TI do not violate therefore the Onsager relation even though each spin block can exhibit the parity anomaly. We can understand this effect also in

terms of band structure calculations. As an example, we show in Fig. 2.16(c) and (d) the band structures for $B_\perp = 1\,\mathrm{T}$ and $-1\,\mathrm{T}$, respectively. Depending on $\mathrm{sgn}\,(eB_\perp)$, the QAH edge states of either the spin up (orange) or down (green) block traverse the Dirac mass gap. Recall that their chirality is determined by their intrinsic Chern number and not by the magnetic field. Although the Onsager relation is therefore not violated, the survival of the QAH edge states in the Dirac mass gap is still apparent.

Ultimately, when the magnetic field is increased further, the system becomes a trivial insulator when the Dirac mass gap of the remaining, second spin block is closed at [cf. Eq. (2.101)]

$$B_{\perp,triv} = \max\left[B_{\perp,triv,\uparrow}, B_{\perp,triv,\downarrow}\right] \tag{2.107}$$

$$= \max\left(\frac{M}{\mathrm{sgn}\,(eB_\perp)\,Be/\hbar \mp g_0}\right). \tag{2.108}$$

Above this threshold, the Hall conductivity drops to zero [a]. As sketched in Fig. 2.15(b), the Hall conductivity (at constant μ) evolves therefore from 0 to $\pm e^2/h$, and again to 0 with increasing $|B_\perp|$. This so-called reentrant behavior of σ_{xy} [143] is hence encoded in the spectral asymmetry and can be interpreted as a representative of the parity anomaly.

2.8. Summary

In this chapter, we showed that the QAH effect persists in magnetic fields and can be differentiated from a conventional QH effect due to a peculiar topological quantity, the spectral asymmetry, given by Eq. (2.31). The latter is a consequence of the parity anomaly. We demonstrated that the spectral asymmetry consists of two separate contributions: The first one is connected to the $n = 0$ LL, which is the only LL that lacks a partner [b]. The second contribution stems from the asymmetry of all other LLs. Combined, the spectral asymmetry acts as if there is effectively an additional LL in magnetic fields. In Secs. 2.3 and 2.4, we showed that this 'effective LL' comprises the information of the QAH effect and, in particular, of the QAH edge states in magnetic fields. Interestingly, we were able to connect the coexistence of the QH and the QAH effect to the appearance of counterpropagating QH and QAH edge states. In comparison to helical edge states that characterize the QSH phase, these quasi-helical edge states are not protected by symmetry.

In the remainder of this chapter, we analyzed the properties of these counterpropagating QH and QAH edge states in magnetic fields in detail. In Sec. 2.5, it was shown that,

[a] The statement holds provided that the non-relativistic mass in Eq. (2.107) dominates in the large $B_\perp$-limit, $|B/l_{B_\perp}^2| > |g_0|$.

[b] The statement is made with respect to a single, topologically nontrivial Chern insulator.

if the total charge of the system is kept constant, the survival of the QAH edge states is connected to a unique type of charge pumping (via anomaly cancellation) from the QAH edge states into all valence band LLs. This effect highlighted once more that QAH edge states are indeed connected to the asymmetry of the entire spectrum and not to a single LL. Based on this result, we additionally predicted that, as a function of the magnetic field, a length dependent transition should occur from the charge pumping regime to a regime which is dominated by quasi-helical edge states. In Sec. 2.6.3, a toy model was presented to examine the transport signatures within this regime. Finally, in Sec. 2.7, we discussed signatures of the spectral asymmetry and, hence, of the parity anomaly in para- and ferromagnetic TIs which are described by the BHZ model.

3.

Emergent QH Effect in 2D Topological Insulators

Contents

3.1. Narrow gap or inverted gap semiconductors - The Kane model 100
3.1.1. The 8-band Kane model 100
3.1.2. Bulk inversion asymmetry 103
3.1.3. Pikus-Bir-Hamiltonian 103
3.2. Finite-difference-method 104
3.2.1. BenDaniel–Duke boundary condition 108
3.3. External magnetic field and magnetization in the Kane model 109
3.3.1. Orbital effect of out-of-plane magnetic field 110
3.3.2. Zeeman interaction 111
3.3.3. Exchange interaction 113
3.3.4. Bulk inversion asymmetry 115
3.4. Band structure of (Hg,Mn)Te 116
3.4.1. Experimental characterization of (Hg,Mn)Te quantum wells . 118
3.5. Emergent QH effect in the bulk p-regime 121
3.5.1. Toy model 121
3.5.2. Direct gap topological insulators 122
3.5.3. Indirect gap topological insulators 128
3.6. Emergent QH effect in QSH regime 129
3.7. Summary and Discussion 131

In the previous chapter, we have investigated the fate of 2D topological states of matter in the presence of external magnetic fields by means of the BHZ model. The advantage of using this low energy model is that it allows us to study topological effects analytically. However, its scope regarding the actual band structure of TIs is limited to small energies and small momenta. This means in particular that the BHZ model cannot account for additional extrema in the valence band at large momenta (known as 'camelback'), which typically arise as a consequence of hybridization between the subbands in an inverted band structure [75, 81, 143]. To investigate these features, one has to work instead with higher-energy models such as the 14×14 or the 8×8 Kane model [144]. The latter is conveniently used to describe narrow-gap or inverted band structure semiconductors in the vicinity of the Γ-point [a] [45, 145].

In this chapter, we use the 8×8 Kane model to explore the band structure of HgTe quantum wells alloyed with a few percent of Mn-atoms. The incorporation of Mn in the crystal structure has thereby two important consequences: Firstly, the localized d-electrons of Mn give rise to a paramagnetic exchange interaction [45, 91]. As discussed in the previous chapter, this effect is of particular interest as it can drive a topological material from the QSH into the QAH phase when Mn is magnetized [21]. Here however, we will mainly focus on small magnetic fields where the (Hg,Mn)Te quantum wells are still in the 'QSH phase'. The second effect of incorporating Mn is that it renormalizes the bulk band gap [91, 146]. As we will show in this chapter, this shifts the topological transition point to larger quantum well thicknesses d_{QW} with increasing Mn-concentration. In addition, it alters the height of the camelback maxima with respect to the energy of the valence band edge. The latter has important consequences when small magnetic fields are applied to the quantum well.

More specifically, we show that the interplay between the exchange interaction of the Mn-atoms and the camelback, which is associated to a Van-Hove-like singularity [very large density of states (DOS)], leads to rich LL structures. In direct gap TIs, when the chemical potential is in the bulk p-regime, the camelback pins the chemical potential below the valence band edge and, thereby, induces an onset to a series of QH plateaus with $\nu = -3, -2, -1$ at ultra-low magnetic fields (tens of mT). In contrast, in indirect gap TIs, the camelback pins the chemical potential above the valence band edge preventing an onset to QH plateaus up to large magnetic fields (a few tesla). In addition, in direct gap TIs, the pinning mechanism enables us to shift the onset fields of QH plateaus to even smaller magnetic fields by applying an in-plane magnetic field.

This chapter is divided into two main parts. The first part discusses the implementation of the 8×8 Kane model in the numerics. In this regard, Sec. 3.1 introduces the Kane

[a] The BHZ model is derived from the 8×8 Kane model using perturbation theory [15]. Extensions of the BHZ model have been also discussed in the literature [81]. A simple extension which includes the H2 band is presented in App. B.

model, while Sec. 3.2 outlines how the Kane model can be implemented in the numerics in the absence of an external magnetic field. Subsequently in Sec. 3.3, we extend the numerics to account for external out-of-plane and in-plane magnetic fields, including explicitly the effect of Zeeman and exchange coupling terms. In the second part of this chapter, we employ our numerics to characterize the band structure of (Hg,Mn)Te quantum wells focusing in particular on the role of the camelback. In Sec. 3.4, the phase space of (Hg,Mn)Te quantum wells is presented and, in Sec. 3.5, transport signatures of direct and indirect gap TIs are discussed in magnetic fields, when the chemical potential is in the p-doped regime. Thereby, we consider explicitly the role of an in-plane magnetic field, as well as of bulk inversion asymmetry (BIA) terms. In Sec. 3.6, we describe for completeness a different type of emergent QH effect that occurs also in (Hg,Mn)Te quantum wells, when the chemical potential is located in the bulk gap regime. In Sec. 3.7, we conclude this chapter and present an outlook.

Our theoretical model has been motivated by experiments on (Hg,Mn)Te quantum wells which were performed by Saquib Shamim with the help of A. Budewitz and P. Shekhar. Both the experimental results, as well as the theoretical results, which will be presented in this chapter, have been published in Ref. [P7] [a]. This chapter contains in parts a revised version of this manuscript, including the associated supplementary materials.

[a] S. Shamim, W. Beugeling, and I contributed equally to this work. I developed the numerical code for confining the 8×8 Kane Hamiltonian in the z-direction, which was used to compute the band structure and the LL fans of (Hg,Mn)Te quantum wells. Wouter Beugeling extended this code to allow for confinement in two directions (project name: *kdotpy*). His results are presented in Ref. [P7] and are briefly summarized in Sec. 3.6. W. Beugeling and I discussed and developed the implementation of Mn-atoms, as well as the introduction of an in-plane magnetic field in close collaboration. S. Shamim performed all measurements, which motivated this theoretical work, and analyzed the experimental data (with help of A. Budewitz and P. Shekhar). His results are summarized in Sec. 3.4.1. All authors contributed equally to the interpretation of the results.

3.1. Narrow gap or inverted gap semiconductors - The Kane model

Bulk semiconductors with a small band gap or an inverted band structure are described in the vicinity of the Γ-point by the 8×8 Kane model. This includes compound semiconductors like (Hg,Cd)Te, or (Hg,Mn)Te which are considered in this thesis. These materials crystallize in the zincblende structure, whose symmetry is described by the point group T_d. In comparison to the diamond structure (point group O_h), which typically describes elemental semiconductors from the 4th main group, the zincblende structure lacks inversion symmetry [147], i.e., $O_h = T_d \otimes I$, where I denotes inversion symmetry [144].

The Kane model, which includes bands from the conduction and valence band, is derived based on the $\mathbf{k} \cdot \mathbf{p}$-method using quasi-degenerate perturbation theory [145, 147]. In the absence of an external magnetic field, we can distinguish three terms in the full Kane model:

$$H = H_K(k_x, k_y, k_z) + H_B(k_x, k_y, k_z) + H_S \,. \tag{3.1}$$

Here, H_K is the part of the Kane model which preserves inversion symmetry. H_B is the BIA Hamiltonian which includes all bulk terms that break inversion symmetry. And H_S is the so-called Pikus-Bir Hamiltonian that allows us to consider the effect of strain [148]. The Hamiltonians H_K, H_B, and H_S are reviewed and discussed in Secs. 3.1.1, 3.1.2, and 3.1.3, respectively.

3.1.1. The 8-band Kane model

The 8×8 Kane model is typically written in the basis of the following set of Bloch functions [145]:

$$\begin{aligned}
|\Gamma_6, +\frac{1}{2}\rangle &= |\mathrm{S}, \uparrow\rangle \ , \\
|\Gamma_6, -\frac{1}{2}\rangle &= |\mathrm{S}, \downarrow\rangle \ , \\
|\Gamma_8, +\frac{3}{2}\rangle &= |\mathrm{HH}, \uparrow\rangle = \frac{1}{\sqrt{2}} |\mathrm{X} + \mathrm{iY}, \uparrow\rangle \ , \\
|\Gamma_8, +\frac{1}{2}\rangle &= |\mathrm{LH}, \uparrow\rangle = \frac{1}{\sqrt{6}} \left(|\mathrm{X} + \mathrm{iY}, \downarrow\rangle - 2\,|\mathrm{Z}, \uparrow\rangle\right) \ , \\
|\Gamma_8, -\frac{1}{2}\rangle &= |\mathrm{LH}, \downarrow\rangle = -\frac{1}{\sqrt{6}} \left(|\mathrm{X} - \mathrm{iY}, \uparrow\rangle + 2\,|\mathrm{Z}, \downarrow\rangle\right) \ , \\
|\Gamma_8, -\frac{3}{2}\rangle &= |\mathrm{HH}, \downarrow\rangle = -\frac{1}{\sqrt{2}} |\mathrm{X} - \mathrm{iY}, \downarrow\rangle \ , \\
|\Gamma_7, +\frac{1}{2}\rangle &= |\mathrm{SO}, \uparrow\rangle = \frac{1}{\sqrt{3}} \left(|\mathrm{X} + \mathrm{iY}, \downarrow\rangle + |\mathrm{Z}, \uparrow\rangle\right) \ ,
\end{aligned}$$

$$|\Gamma_7, -\frac{1}{2}\rangle = |\mathrm{SO}, \downarrow\rangle = \frac{1}{\sqrt{3}} \left(|\mathrm{X} - \mathrm{iY}, \uparrow\rangle - |\mathrm{Z}, \downarrow\rangle \right) . \tag{3.2}$$

In the case of a topologically nontrivial narrow-gap semiconductor, the two $|\Gamma_6, \pm 1/2\rangle$ bands form the s-like conduction band, while the $|\Gamma_8, \pm 3/2\rangle$, $|\Gamma_8, \pm 1/2\rangle$, and $|\Gamma_7, \pm 1/2\rangle$ bands, which respectively denote the p-like heavy-hole, light-hole, and split-off band, form the valence band. This is different from inverted semiconductors like HgTe, where the Γ_8 bands are above the Γ_6 bands [cf. Fig. 1.6]. Written in this basis, the (inversion symmetric) Kane Hamiltonian reads [45, 145, 147]

$$H_K = \begin{pmatrix}
T & 0 & -\frac{1}{\sqrt{2}}Pk_+ & \sqrt{\frac{2}{3}}Pk_z & \frac{1}{\sqrt{6}}Pk_- & 0 & -\frac{1}{\sqrt{3}}Pk_z & -\frac{1}{\sqrt{3}}Pk_- \\
0 & T & 0 & -\frac{1}{\sqrt{6}}Pk_+ & \sqrt{\frac{2}{3}}Pk_z & \frac{1}{\sqrt{2}}Pk_- & -\frac{1}{\sqrt{3}}Pk_+ & \frac{1}{\sqrt{3}}Pk_z \\
-\frac{1}{\sqrt{2}}k_-P & 0 & U+V & -\bar{S}_- & R & 0 & \frac{1}{\sqrt{2}}\bar{S}_- & -\sqrt{2}R \\
\sqrt{\frac{2}{3}}k_zP & -\frac{1}{\sqrt{6}}k_-P & -\bar{S}_-^\dagger & U-V & C & R & \sqrt{2}V & -\sqrt{\frac{3}{2}}\tilde{S}_- \\
\frac{1}{\sqrt{6}}k_+P & \sqrt{\frac{2}{3}}k_zP & R^\dagger & C^\dagger & U-V & \bar{S}_+^\dagger & -\sqrt{\frac{3}{2}}\tilde{S}_+ & -\sqrt{2}V \\
0 & \frac{1}{\sqrt{2}}k_+P & 0 & R^\dagger & \bar{S}_+ & U+V & \sqrt{2}R^\dagger & \frac{1}{\sqrt{2}}\bar{S}_+ \\
-\frac{1}{\sqrt{3}}k_zP & -\frac{1}{\sqrt{3}}k_-P & \frac{1}{\sqrt{2}}\bar{S}_-^\dagger & \sqrt{2}V & -\sqrt{\frac{3}{2}}\tilde{S}_+^\dagger & \sqrt{2}R & U-\Delta & C \\
-\frac{1}{\sqrt{3}}k_+P & \frac{1}{\sqrt{3}}k_zP & -\sqrt{2}R^\dagger & -\sqrt{\frac{3}{2}}\tilde{S}_-^\dagger & -\sqrt{2}V & \frac{1}{\sqrt{2}}\bar{S}_+^\dagger & C^\dagger & U-\Delta
\end{pmatrix} , \tag{3.3}$$

where

$$\begin{aligned}
k_\parallel^2 &= k_x^2 + k_y^2 \quad , \quad k_\pm = k_x \pm \mathrm{i}k_y, \\
T &= E_c + \frac{\hbar^2}{2m_0}\left[(2F+1)\, k_\parallel^2 + k_z\, (2F+1)\, k_z \right], \\
U &= E_v - \frac{\hbar^2}{2m_0}\left(\gamma_1 k_\parallel^2 + k_z \gamma_1 k_z \right), \\
V &= -\frac{\hbar^2}{2m_0}\left(\gamma_2 k_\parallel^2 - 2k_z \gamma_2 k_z \right), \\
R &= -\frac{\hbar^2}{2m_0}\sqrt{3}\left(\mu k_+^2 - \bar{\gamma} k_-^2 \right), \\
\bar{S}_\pm &= -\frac{\hbar^2}{2m_0}\sqrt{3} k_\pm \left(\{\gamma_3, k_z\} + [\kappa, k_z] \right), \\
\tilde{S}_\pm &= -\frac{\hbar^2}{2m_0}\sqrt{3} k_\pm \left(\{\gamma_3, k_z\} - \frac{1}{3}[\kappa, k_z] \right), \\
C &= \frac{\hbar^2}{m_0} k_- [\kappa, k_z] .
\end{aligned} \tag{3.4}$$

Here, E_c and E_v denote the conduction and valence band edge energies, respectively, Δ is the energy offset of the Γ_7 split-off bands, and we introduced the abbreviations $\mu = (\gamma_3 - \gamma_2)/2$ and $\bar{\gamma} = (\gamma_3 + \gamma_2)/2$. The Kane parameters F, $\gamma_{1,2,3}$, and κ are material specific parameters that are related to the effective masses of each band. We present an overview of these parameters for (Hg,Mn)Te and (Hg,Cd)Te in App. A. Throughout this chapter, we focus on (Hg,Mn)Te / (Hg,Cd)Te quantum well geometries

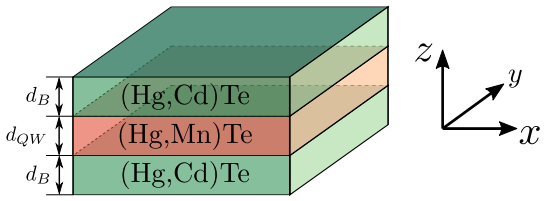

Figure 3.1.: Schematic layer stack of (Hg,Mn)Te/(Hg,Cd)Te quantum wells. In typical experimental setups, $Hg_{0.32}Cd_{0.68}Te$ is used as the barrier material. The well and the barrier thickness d_{QW} and d_B are indicated, respectively. The growth direction points in the z-direction.

as shown in Fig. 3.1 with growth direction [001] (z-axis). The band edge energies and the Kane parameters depend therefore exclusively on the growth direction z of the quantum well geometry. Their functional dependence can be described by the following expression:

$$\gamma(z) = \gamma_W \left[\theta\left(z + \frac{d_{QW}}{2}\right) - \theta\left(z - \frac{d_{QW}}{2}\right)\right] + \gamma_B \left[\theta\left(-\frac{d_{QW}}{2} - z\right) + \theta\left(z - \frac{d_{QW}}{2}\right)\right] , \tag{3.5}$$

where Θ is the Heaviside step function, $\gamma(z)$ is a representative of an arbitrary Kane parameter (or band edge energy), γ_W is the parameter in the well, γ_B is the parameter in the barrier, and d_{QW} is the width of the well material in z-direction.

The Kane Hamiltonian H_K exhibits a spherical symmetry if we would set $\mu = 0$ [144, 149]. However, since μ is typically quite small, it can be considered as a perturbation. In the so-called axial approximation, we set $\mu = 0$ which reestablishes a full in-plane rotational (cylindrical) symmetry [150], i.e., the bulk spectrum is fully symmetric in the k_x–k_y–plane, $E(k_x, k_y, k_z) \to E(k_\parallel, k_z)$.

Hermiticity: It is worth noting that the operator ordering in Eq. (3.3) is not accidental. It is mandatory to ensure hermiticity of the Kane Hamiltonian due to the z-dependence of the effective masses (γ_1, γ_2, ...). To understand the basic principle, let us consider the following two operators, $H_1 = k_z\gamma(z)k_z$ and $H_2 = \gamma(z)k_z^2$. As can be easily verified, H_1 describes a hermitian Hamiltonian,

$$\begin{aligned} \langle\phi_2|H_1\phi_1\rangle &= -\langle\phi_2|\partial_z\gamma(z)\partial_z\phi_1\rangle = \langle\gamma(z)\partial_z\phi_2|\partial_z\phi_1\rangle \\ &= -\langle\partial_z\gamma(z)\partial_z\phi_2|\phi_1\rangle = \langle H_1\phi_2|\phi_1\rangle , \end{aligned} \tag{3.6}$$

where $|\phi_1\rangle$ and $|\phi_2\rangle$ denote two arbitrary test states. In contrast, the operator H_2 is clearly not hermitian:

$$\langle\phi_2|H_2\phi_1\rangle = -\langle\gamma(z)\phi_2|\partial_z^2|\phi_1\rangle = \langle k_z^2\gamma(z)\phi_2|\phi_1\rangle \neq \langle H_2\phi_2|\phi_1\rangle . \tag{3.7}$$

3.1.2. Bulk inversion asymmetry

In a semiconductor with inversion symmetry (point group O_h), that is also invariant under TR, all bands are double degenerate (consequence of TR and inversion symmetry [a]) [144]. Since the point group T_d lacks inversion symmetry, the double degeneracy is lifted in all materials which crystallize in the zincblende structure. The BIA Hamiltonian, which describes this effect, is given by (up to linear order in momentum) [144, 147]

$$H_B = C \begin{pmatrix} 0 & 0 & 0 & 0 & 0 & 0 & 0 & 0 \\ 0 & 0 & 0 & 0 & 0 & 0 & 0 & 0 \\ 0 & 0 & 0 & \frac{-1}{2}k_+ & k_z & \frac{-\sqrt{3}}{2}k_- & \frac{1}{2\sqrt{2}}k_+ & \frac{1}{\sqrt{2}}k_z \\ 0 & 0 & \frac{-1}{2}k_- & 0 & \frac{\sqrt{3}}{2}k_+ & -k_z & 0 & \frac{-\sqrt{3}}{2\sqrt{2}}k_+ \\ 0 & 0 & k_z & \frac{\sqrt{3}}{2}k_- & 0 & \frac{-1}{2}k_+ & \frac{\sqrt{3}}{2\sqrt{2}}k_- & 0 \\ 0 & 0 & \frac{-\sqrt{3}}{2}k_+ & -k_z & \frac{-1}{2}k_- & 0 & \frac{k_z}{\sqrt{2}} & \frac{-1}{2\sqrt{2}}k_- \\ 0 & 0 & \frac{1}{2\sqrt{2}}k_- & 0 & \frac{\sqrt{3}}{2\sqrt{2}}k_+ & \frac{k_z}{\sqrt{2}} & 0 & 0 \\ 0 & 0 & \frac{1}{\sqrt{2}}k_z & \frac{-\sqrt{3}}{2\sqrt{2}}k_- & 0 & \frac{-1}{2\sqrt{2}}k_+ & 0 & 0 \end{pmatrix}, \tag{3.8}$$

where C is a material specific parameter [151]. As BIA is typically quite small in HgTe, we will neglect its effect in most calculations (error is $\sim 1\,\mathrm{meV}$). Nonetheless, we will briefly comment on its explicit role in Secs. 3.5.2.

3.1.3. Pikus-Bir-Hamiltonian

In a typical experiment, the quantum well geometry that is shown in Fig. 3.1 is pseudomorphically grown on a substrate, like (Hg,Cd)Te or (Cd,Zn)Te [80] (see also App. A). This means that the crystal structure of the well material gets strained, since it must adopt to the equilibrium lattice constant of the substrate. The strength of the strain is determined by the following ratio:

$$\epsilon_S = \frac{a_{Sub} - a_W}{a_W}\,, \tag{3.9}$$

where a_{Sub} is the equilibrium lattice constant of the substrate and a_W is the equilibrium lattice constant of the well material. The effect of strain can be included via the Pikus-

[a] The inversion symmetry operator ($\mathbf{x} \to -\mathbf{x}$) reads

$$I = \mathrm{Diag}\begin{pmatrix} 1 & 1 & -1 & -1 & -1 & -1 & -1 & -1 \end{pmatrix}.$$

The (block diagonal) TR symmetry operators reads

$$T = \mathrm{i}\,\mathrm{Diag}\begin{pmatrix} \sigma_y & \sigma_x \otimes \sigma_y & \sigma_y \end{pmatrix} K\,,$$

where K denotes the operator of complex conjugation.

Bir Hamiltonian [148, 152]

$$H_S = \begin{pmatrix} T_\epsilon & 0 & 0 & 0 & 0 & 0 & 0 & 0 \\ 0 & T_\epsilon & 0 & 0 & 0 & 0 & 0 & 0 \\ 0 & 0 & U_\epsilon + V_\epsilon & S_\epsilon & R_\epsilon & 0 & -\frac{1}{\sqrt{2}} S_\epsilon & -\sqrt{2} R_\epsilon \\ 0 & 0 & S_\epsilon^\dagger & U_\epsilon - V_\epsilon & 0 & R_\epsilon & \sqrt{2} V_\epsilon & \sqrt{\frac{3}{2}} S_\epsilon \\ 0 & 0 & R_\epsilon^\dagger & 0 & U_\epsilon - V_\epsilon & -S_\epsilon & \sqrt{\frac{3}{2}} S_\epsilon^\dagger & -\sqrt{2} V_\epsilon \\ 0 & 0 & 0 & R_\epsilon^\dagger & -S_\epsilon^\dagger & U_\epsilon + V_\epsilon & \sqrt{2} R_\epsilon^\dagger & -\frac{1}{\sqrt{2}} S_\epsilon^\dagger \\ 0 & 0 & -\frac{1}{\sqrt{2}} S_\epsilon^\dagger & \sqrt{2} V_\epsilon & \sqrt{\frac{3}{2}} S_\epsilon & \sqrt{2} R_\epsilon & U_\epsilon & 0 \\ 0 & 0 & -\sqrt{2} R_\epsilon^\dagger & \sqrt{\frac{3}{2}} S_\epsilon^\dagger & -\sqrt{2} V_\epsilon & -\frac{1}{\sqrt{2}} S_\epsilon & 0 & U_\epsilon \end{pmatrix}, \tag{3.10}$$

where $T_\epsilon = C\,(\epsilon_{xx} + \epsilon_{yy} + \epsilon_{zz})$, $U_\epsilon = a_S\,(\epsilon_{xx} + \epsilon_{yy} + \epsilon_{zz})$, $V_\epsilon = \frac{1}{2} b\,(\epsilon_{xx} + \epsilon_{yy} - 2\epsilon_{zz})$, $S_\epsilon = -d\,(\epsilon_{xz} - \mathrm{i}\epsilon_{yz})$, and $R_\epsilon = -\frac{\sqrt{3}}{2} b\,(\epsilon_{xx} - \epsilon_{yy}) + \mathrm{i}\,d\epsilon_{xy}$. The strain parameters C, a_S, b, and d are material parameters. An overview of some specific values for the compound materials, that are considered here, are listed in App. A. The rank-2 tensor ϵ describes the deformation of the coordinates due to strain:

$$\mathbf{x}_i = \sum_j (\delta_{ij} + \epsilon_{ij})\,\mathbf{x}_j\,. \tag{3.11}$$

If the quantum well is grown on a [001]-oriented substrate, this causes a biaxial strain in the x–y–plane that relaxes in the z-direction. According to Ref. [152], the strain tensor is in this specific case given by:

$$\epsilon_{xx} = \epsilon_{yy} = \epsilon_S \qquad , \qquad \epsilon_{zz} = -\frac{2C_{12}}{C_{11}} \epsilon_S$$
$$\epsilon_{ij} = 0 \quad \text{for} \quad i \neq j\,, \tag{3.12}$$

where ϵ_S is given by Eq. (3.9), and the material parameters C_{12} and C_{11} are given in App. A.

3.2. Finite-difference-method

To compute the band structure of a quantum well geometry, shown schematically in Fig. 3.1, we impose periodic boundary conditions in the x- and y-direction, and hard wall boundary conditions in the z-direction:

$$\psi(x, y, z) = \psi(x + L_x, y, z) = \psi(x, y + L_y, z)\,,$$
$$\psi(x, y, -L_z/2) = \psi(x, y, L_z/2) = 0\,, \tag{3.13}$$

where L_x and L_y is the width of the quantum well in x- and y-direction, respectively, $L_z = d_{QW} + 2d_B$ is the width of the quantum well in the z-direction. Here, d_{QW} and d_B are the thickness of the well, and the barrier layers, respectively. Note that the requirement of hard wall boundary conditions in the z-direction is natural, as the wave functions in the well decay exponentially in the insulating barrier layers. Using the ansatz,

$$\psi(\mathbf{x}) = \mathrm{e}^{\mathrm{i}(k_x x + k_y y)}\phi(z)\,, \tag{3.14}$$

where $\phi(z)$ is an eight component spinor, we can employ the FDM to solve the corresponding Schrödinger equation. Due to the translational symmetry in the x- and y-direction, we can replace all spatial derivatives of the form ∂_i or ∂_i^2 with $i = x, y$ according to Eqs. (1.28) and (1.29). We are therefore left with mapping the Kane Hamiltonian onto a lattice in the z-direction:

$$\begin{aligned} \phi(z) \quad &\rightarrow \quad \phi(z = ja) \equiv \phi_j\,, \\ \gamma(z) \quad &\rightarrow \quad \gamma(z = ja) \equiv \gamma_j\,, \end{aligned} \tag{3.15}$$

where a is the lattice constant, j labels the jth lattice site, and γ is representative for an arbitrary Kane parameter or a band edge energy. Furthermore, we replace in the numerics the Heaviside functions in $\gamma(z)$ by their corresponding analytic approximations [cf. Eq. (3.5)]:

$$\theta(z) \rightarrow \theta_\delta(z = ja) = \frac{1}{2}\left[1 + \tanh\left(\frac{ja}{\delta}\right)\right]\,, \tag{3.16}$$

where $\theta(z) = \lim_{\delta\rightarrow 0^+}\theta_\delta(z)$ [a]. The discretized Kane Hamiltonian is then given by a $8N \times 8N$-dimensional matrix, where $L_z = (N-1)a$ and N is the number of lattice sites.

In comparison to Sec. 1.1.3, where we employed the FDM to compute the spectrum of a Chern insulator, we deal in the present case with z-dependent effective masses. In particular, there are three types of terms in Eq. (3.3), that require further considerations regarding their numerical implementation:

$$1.\ k_z\gamma(z)k_z \qquad 2.\ \{\gamma(z), k_z\} \qquad 3.\ [\gamma(z), k_z]\,. \tag{3.17}$$

We will now discuss the FDM for these three terms in detail. To simplify the notation, we consider only a one-component Hamiltonian. A generalization to the full Kane model is straightforward.

1. Diagonal term - quadratic in momentum: The first type of terms appear

[a] We must choose δ sufficiently small to ensure convergence of the numerical results.

exclusively on the diagonal of Eq. (3.3). Suppose we would perform the product rule for this term, before we apply the finite-difference-method. This would yield the discretized expression

$$\begin{aligned} k_z\gamma(z)k_z\phi(z) &= -\partial_z\gamma(z)\partial_z\phi(z) \\ &= -\left[\partial_z\gamma(z)\right]\partial_z\phi(z) - \gamma(z)\partial_z^2\phi(z) \\ &\overset{\text{FDM}}{\to} -\frac{1}{4a^2}\left(\gamma_{j+1}-\gamma_{j-1}\right)\left(\phi_{j+1}-\phi_{j-1}\right) - \frac{1}{a^2}\gamma_j\left(\phi_{j+1}+\phi_{j-1}-2\phi_j\right) \\ &\equiv \sum_j H_{ji}\phi_i\,, \end{aligned} \tag{3.18}$$

where, in the third line, we replaced the continuum functions and their derivatives according to Eqs. (1.26), (1.27), and (3.15). We have,

$$\begin{aligned} H_{ji} &= \frac{2}{a^2}\gamma_j && \text{for} \quad i=j\,, \\ H_{ji} &= -\frac{1}{a^2}\left(\frac{\gamma_{j+1}-\gamma_{j-1}}{4}+\gamma_j\right) && \text{for} \quad i=j+1\,, \\ H_{ji} &= \frac{1}{a^2}\left(\frac{\gamma_{j+1}-\gamma_{j-1}}{4}-\gamma_j\right) && \text{for} \quad i=j-1\,. \end{aligned} \tag{3.19}$$

All other elements of H_{ji} are zero. Unfortunately, the resulting matrix is clearly not Hermitian. This means by naively applying the FDM in this manner, one could generate eigenvalues that contain an imaginary part.

To resolve this issue, there is a simple fix how to discretize such operators correctly [153]. Instead of employing first the product rule in Eq. (3.18), we directly replace the outer derivative by the FDM. This yields:

$$\begin{aligned} -\partial_z\gamma(z)\partial_z\phi(z) &\overset{\text{FDM}}{\to} -\frac{1}{2a}\left[\gamma(z+a)\,\partial_z\phi(z)|_{z+a} - \gamma(z-a)\,\partial_z\phi(z)|_{z-a}\right] \\ &= -\frac{1}{4a^2}\left[\gamma_{j+1}\left(\phi_{j+2}-\phi_j\right) - \gamma_{j-1}\left(\phi_j-\phi_{j-2}\right)\right] \\ &\overset{2a\to a}{\to} -\frac{1}{a^2}\left[\gamma_{j+\frac{1}{2}}\left(\phi_{j+1}-\phi_j\right) - \gamma_{j-\frac{1}{2}}\left(\phi_j-\phi_{j-1}\right)\right] \\ &\equiv \sum_j H_{ji}\phi_i\,, \end{aligned} \tag{3.20}$$

where the only nonzero matrix elements are

$$\begin{aligned} H_{ji} &= \frac{1}{a^2}\left(\gamma_{j+\frac{1}{2}}+\gamma_{j-\frac{1}{2}}\right) && \text{for} \quad i=j\,, \\ H_{ji} &= -\frac{1}{a^2}\gamma_{j+\frac{1}{2}} && \text{for} \quad i=j+1\,, \\ H_{ji} &= -\frac{1}{a^2}\gamma_{j-\frac{1}{2}} && \text{for} \quad i=j-1\,. \end{aligned} \tag{3.21}$$

This alternative discretization procedure yields an Hermitian matrix H_{ij} and, therefore,

real eigenvalues. Equation (3.20) is hence the proper way to discretize terms of the form $k_z\gamma(z)k_z$ in the Kane Hamiltonian.

2. Anticommutator - linear in momentum: This type of terms appear in the Kane Hamiltonian on the off-diagonal (matrix elements: $\bar{S}_\pm$ and $\tilde{S}_\pm$). To derive an Hermitian lattice representation, one has to follow the following steps:

$$\begin{aligned}\{\gamma(z), -\mathrm{i}\partial_z\}\,\phi(z) &= -\mathrm{i}\gamma(z)\,[\partial_z\phi(z)] - \mathrm{i}\partial_z\,[\gamma(z)\phi(z)] \\ &\overset{\text{FDM}}{\to} -\mathrm{i}\gamma_j\frac{\phi_{j+1}-\phi_{j-1}}{2a} - \mathrm{i}\frac{\gamma_{j+1}\phi_{j+1}-\gamma_{j-1}\phi_{j-1}}{2a} \\ &= \frac{-\mathrm{i}}{2a}\left[(\gamma_j+\gamma_{j+1})\,\phi_{j+1} - (\gamma_j+\gamma_{j-1})\,\phi_{j-1}\right] \\ &\equiv \sum_i H_{ji}\phi_i\,, \end{aligned} \tag{3.22}$$

where the only nonzero matrix elements are

$$\begin{aligned} H_{ji} &= 0 && \text{for} \quad i = j\,, \\ H_{ji} &= \frac{-\mathrm{i}}{2a}\,(\gamma_j+\gamma_{j+1}) && \text{for} \quad i = j+1\,, \\ H_{ji} &= \frac{\mathrm{i}}{2a}\,(\gamma_j+\gamma_{j-1}) && \text{for} \quad i = j-1\,. \end{aligned} \tag{3.23}$$

Note that in the second line of Eq. (3.22), we have replaced the second term directly by the FDM before evaluating the product rule. Like the terms of type 1, this is crucial to ensure hermiticity of the lattice Hamiltonian. If instead we would have first evaluated the product rule, the resulting lattice Hamiltonian would not have been Hermitian.

3. Commutator - linear in momentum: The last type of terms, which we have to consider, appear on the off-diagonal of the Kane Hamiltonian (matrix elements: $\bar{S}_\pm$, $\tilde{S}_\pm$, and C). For this type of term, we can safely perform the product rule directly:

$$\begin{aligned}[\gamma(z), k_z]\,\phi(z) &= \mathrm{i}\,[\partial_z\gamma(z)]\,\phi(z) \\ &\to \frac{\mathrm{i}}{2a}\,(\gamma_{j+1}-\gamma_{j-1})\,\phi_j \\ &\equiv \sum_i H_{ji}\phi_i\,, \end{aligned} \tag{3.24}$$

where the only nonzero matrix elements are given by

$$\begin{aligned} H_{ji} &= \frac{\mathrm{i}}{2a}\,(\gamma_{j+1}-\gamma_{j-1}) && \text{for} \quad i = j\,, \\ H_{ji} &= 0 && \text{for} \quad i = j+1\,, \\ H_{ji} &= 0 && \text{for} \quad i = j-1\,. \end{aligned} \tag{3.25}$$

The resulting matrix is anti-Hermitian. This is because the considered operator, $[\gamma(z), k_z]$, is also anti-Hermitian. In the full Kane Hamiltonian, terms of this type appear always off-diagonally in conjugate pairs, like

$$\begin{pmatrix} 0 & [\kappa, k_z] \\ [\kappa, k_z]^\dagger & 0 \end{pmatrix} . \tag{3.26}$$

This observation establishes the hermiticity of the full Kane Hamiltonian.

3.2.1. BenDaniel–Duke boundary condition

The careful reader might have noticed that we have bypassed an explicit discussion of the boundary conditions at the interfaces between the well and the barrier layers. This is because these boundary conditions are actually hard-coded in the FDM. Let us explain why this is the case.

Usually, if the Schrödinger equation is solved for a step potential, the continuity of the wave function and its first derivative must be required at the interface. However, this is no longer the case when a Hamiltonian with a z-dependent mass is considered:

$$H = k_z \gamma(z) k_z \,, \tag{3.27}$$

where $\gamma(z) = \gamma_0 \Theta(z)$. While the wave function must be still continuous at the boundary, $\phi(z = 0^+) = \phi(z = 0^-)$, it can be shown that this no longer applies for its first derivative:

$$\begin{aligned} &\lim_{\epsilon \to 0^+} \int_{-\epsilon}^{+\epsilon} dz \, [\partial_z \gamma(z) \partial_z \phi(z) + E\phi(z)] \stackrel{!}{=} 0 \\ \rightarrow \quad &\gamma(0^-) \, \partial_z \phi(z)|_{z=0^-} = \gamma(0^+) \, \partial_z \phi(z)|_{z=0^+} \,, \end{aligned} \tag{3.28}$$

where contributions from the second term, $E\phi(z)$, have vanished in the limit $\epsilon \to 0^+$ because of the required continuity of the wave function. Equation 3.28 shows that the derivative of the wave function changes proportional to the ratio of the effective masses at the two sides of the interface. This is known as BenDaniel - Duke boundary condition [154].

Let us now show that this boundary condition is naturally fulfilled by applying the FDM. Employing Eq. (3.20) yields the following discretized Schrödinger equation:

$$-\frac{1}{a^2} \left[\gamma_{j+\frac{1}{2}} \left(\phi_{j+1} - \phi_j \right) - \gamma_{j-\frac{1}{2}} \left(\phi_j - \phi_{j-1} \right) \right] = E\phi_j \,. \tag{3.29}$$

If this equation is multiplied by a and all terms $\mathcal{O}(a)$ are dropped, the Schrödinger

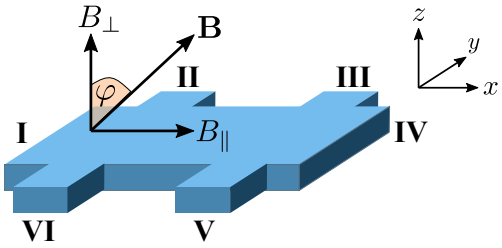

Figure 3.2.: Schematics of six terminal Hall bar that lies in the x–y–plane. The total magnetic field **B** is applied within the x–z–plane. The angle φ marks the angle between the z-axis and **B**.

equation at the interface $j = 0$ takes the form

$$\gamma_{\frac{1}{2}} \frac{\phi_1 - \phi_0}{a} = \gamma_{-\frac{1}{2}} \frac{\phi_0 - \phi_{-1}}{a} \,. \tag{3.30}$$

This is the discretized version of the BenDaniel - Duke boundary conditions, Eq. (3.28) [153]. We have therefore shown that the FDM fulfills the correct boundary conditions at the interface between well and barrier.

3.3. External magnetic field and magnetization in the Kane model

In this section, we discuss the implementation of an external magnetic field in the 8-band Kane model. The external magnetic field configuration, that we will consider throughout this chapter, is given by

$$\mathbf{B} = \begin{pmatrix} B_\parallel & 0 & B_\perp \end{pmatrix}^T = B_{tot} \begin{pmatrix} \sin\varphi & 0 & \cos\varphi \end{pmatrix}^T \,, \tag{3.31}$$

which is depicted schematically in Fig. 3.2. The effect of an out-of-plane magnetic field $B_\perp$ is twofold. Firstly, it gives rise to the formation of LLs due to the orbital effect (Peierls substitution), and, secondly, it induces a nonzero Zeeman and a paramagnetic exchange interaction term. The latter arises from the localized magnetic moments of the Mn-atoms [45, 91]. With respect to the in-plane magnetic field, we assume that it only induces a Zeeman and an exchange interaction term, while the orbital effect of $B_\parallel$ is neglected. This assumption is based on the fact that the magnetic length in-plane is much larger than the quantum well width for the considered range of magnetic field values, i.e., $l_{B_\parallel} \gg d_{QW}$, where $l_{B_\parallel} = \sqrt{\hbar / \left| eB_\parallel \right|}$ [a].

This section is organized as follows: In Sec. 3.3.1, we discuss how to implement the orbital effect of the magnetic field in the (inversion symmetric) Kane Hamiltonian,

[a] We consider typically quantum wells with $d_{QW} \sim 10\,\text{nm}$ and $l_{B_\parallel} > 25\,\text{nm}$, so that $l_{B_\parallel} \gg d_{QW}$. This is certainly not true for the out-of-plane magnetic field since $L_x, L_y \gg d_{QW}$.

H_K. The implementation of Zeeman and exchange interaction terms is discussed in Secs. 3.3.2 and 3.3.3, respectively. Finally in Sec. 3.3.4, we incorporate BIA terms into our model.

3.3.1. Orbital effect of out-of-plane magnetic field

The orbital effect of the external out-of-plane magnetic field gives rise to the formation of LLs and is incorporated into the Kane model via the Peierls substitution, given by Eq. (1.40), in the Landau gauge $\mathbf{A} = -yB_\perp \mathbf{e}_x$. Since the vector potential does not affect the explicit form of the wave functions in the z-direction, the bulk LL spectrum can be computed analogously to the discussion in Secs. 1.3.1 and 2.1. This means the canonical momentum operators in the x- and y-direction are replaced by magnetic ladder operators according to Eq. (1.51).

Working in the axial, approximation, the matrix structure of the (inversion symmetric) Kane Hamiltonian, $H_K(a, a^\dagger, k_z)$, yields the following set of LL spinors [45]

$$|\phi_n(z)\rangle = \Big(\; f_1^{(n)} |n\rangle \quad f_2^{(n)} |n+1\rangle \quad f_3^{(n)} |n-1\rangle \quad f_4^{(n)} |n\rangle \\ f_5^{(n)} |n+1\rangle \quad f_6^{(n)} |n+2\rangle \quad f_7^{(n)} |n\rangle \quad f_8^{(n)} |n+1\rangle \; \Big)^T \,, \tag{3.32}$$

for $n \geq 1$, and three distinct LL spinors for $n \leq 0$, given by:

$$|\phi_n(z)\rangle = \begin{cases} \Big(f_1^{(0)} |0\rangle \; f_2^{(0)} |1\rangle \; 0 \; f_4^{(0)} |0\rangle \; f_5^{(0)} |1\rangle \; f_6^{(0)} |2\rangle \; f_7^{(0)} |0\rangle \; f_8^{(0)} |1\rangle \Big)^T & \text{for } n = 0 \\ \Big(0 \; f_2^{(-1)} |0\rangle \; 0 \; 0 \; f_5^{(-1)} |0\rangle \; f_6^{(-1)} |1\rangle \; 0 \; f_8^{(-1)} |0\rangle \Big)^T & \text{for } n = -1 \\ \Big(0 \; 0 \; 0 \; 0 \; 0 \; f_6^{(-2)} |0\rangle \; 0 \; 0 \Big)^T & \text{for } n = -2 \,, \end{cases} \tag{3.33}$$

where $f_i^{(n)}$ is the z-dependent wave function of the nth LL with orbital component $i = 1, \ldots, 8$, enumerating the eight basis functions of the Kane model [cf. Eq. (3.2)].

To check whether the inversion symmetric Kane Hamiltonian $H = H_K + H_S$ is indeed diagonal in the basis formed by Eqs. (3.32) and (3.33), let us recast a general wave function as

$$|\phi_n(z)\rangle = A(n) F(z) \,, \tag{3.34}$$

where

$$A(n) = \mathrm{Diag}\Big(|n\rangle \quad |n+1\rangle \quad |n-1\rangle \quad |n\rangle \quad |n+1\rangle \quad |n+2\rangle \quad |n\rangle \quad |n+1\rangle \Big) \,, \tag{3.35}$$

$$F(z) = \Big(f_1^{(n)} \quad f_2^{(n)} \quad f_3^{(n)} \quad f_4^{(n)} \quad f_5^{(n)} \quad f_6^{(n)} \quad f_7^{(n)} \quad f_8^{(n)} \Big)^T \,. \tag{3.36}$$

Acting from the left on the Schrödinger equation with $A^\dagger(m)$, we arrive at

$$\begin{aligned} & A^\dagger(m)\left[H_K\left(a,a^\dagger,k_z\right)+H_S\right]|\phi_n(z)\rangle && = EA^\dagger(m)\,|\phi_n(z)\rangle \\ \rightarrow\quad & A^\dagger(m)\left[H_K\left(a,a^\dagger,k_z\right)+H_S\right]A(n)F(z) && = EA^\dagger(m)A(n)F(z) \\ \rightarrow\quad & \left[H_K(n,k_z)+H_S\right]\delta_{m,n}F(z) && = E\delta_{m,n}F(z)\,, \end{aligned} \tag{3.37}$$

which shows that the Hamiltonian is diagonal in the LL basis.

Implementation: Solving the Schrödinger equation in the presence of $B_\perp$ boils therefore down to mapping the Hamiltonian $H_K(n,k_z)+H_S$ via the FDM on a lattice in the z-direction. The LL spectrum can be computed by numerically diagonalizing for each LL index n an $8N\times 8N$ dimensional matrix. It is worth noting that we work here in the axial approximation because it enables us to treat the LL index n as a good quantum number. This is because terms that break the axial symmetry couple pairs of LLs with the LL indices n and $n+4$ [45]. Thus, working in the axial approximation reduces the numerical effort substantially, while the approximation error remains typically quite small ($\approx 1\,\mathrm{meV}$).

3.3.2. Zeeman interaction

A Zeeman interaction consists of an orbital angular momentum and a spin contribution. In total, the Zeeman Hamiltonian reads [144]

$$H_S=\mu_B\left(\kappa'(z)\mathbf{L}+\frac{g_S}{2}\boldsymbol{\sigma}\right)\mathbf{B}\,, \tag{3.38}$$

where $\mathbf{L}=(L_x,L_y,L_z)$ is the orbital angular momentum operator, $\boldsymbol{\sigma}=(\sigma_x,\sigma_y,\sigma_z)$ is the spin operator, $g_S\approx 2$ is the gyromagnetic ratio, and $\kappa'(z)$ is a material specific coupling constant, that depends on the growth direction z of the quantum well.

The appropriate Zeeman Hamiltonian in the Kane model is derived projecting Eq. (3.38) into the eight dimensional basis given by Eq. (3.2). As an example, let us calculate two components of the Zeeman Hamiltonian explicitly:

$$(H_z)_{11}=\langle \mathrm{S}\uparrow|H_S|\mathrm{S}\uparrow\rangle=\mu_B B_\perp\langle \mathrm{S}\uparrow|\sigma_z|\mathrm{S}\uparrow\rangle=\mu_B B_\perp\,, \tag{3.39}$$

$$\begin{aligned}(H_z)_{44}&=\langle \mathrm{LH}\uparrow|H_S|\mathrm{LH}\uparrow\rangle=\mu_B B_\perp\langle \mathrm{LH}\uparrow|\kappa' L_z+\sigma_z|\mathrm{LH}\uparrow\rangle\\ &=\mu_B B_\perp\frac{1}{3}\left(\kappa'+1\right)\,,\end{aligned} \tag{3.40}$$

where we used that $|\mathrm{S},\uparrow\rangle=|0,\frac{1}{2}\rangle$ and $|\mathrm{LH},\uparrow\rangle=\sqrt{\frac{2}{3}}\,|0,\frac{1}{2}\rangle+\sqrt{\frac{1}{3}}\,|1,-\frac{1}{2}\rangle$ [a]. All other components follow analogously, resulting in the following Hamiltonian [144]:

[a] The two components of $|m_l,m_s\rangle$ denote the eigenvalues of L_z and S_z, respectively.

$$H_z(B_\parallel, B_\perp) = \mu_B \begin{pmatrix} B_\perp & B_\parallel & 0 & 0 \\ B_\parallel & -B_\perp & 0 & 0 \\ 0 & 0 & -3\kappa B_\perp & -\sqrt{3}\kappa B_\parallel \\ 0 & 0 & -\sqrt{3}\kappa B_\parallel & -\kappa B_\perp \\ 0 & 0 & 0 & -2\kappa B_\parallel \\ 0 & 0 & 0 & 0 \\ 0 & 0 & \sqrt{\frac{3}{2}}(1+\kappa)B_\parallel & -\sqrt{2}(1+\kappa)B_\perp \\ 0 & 0 & 0 & \frac{1+\kappa}{\sqrt{2}}B_\parallel \end{pmatrix}$$
$$\begin{pmatrix} 0 & 0 & 0 & 0 \\ 0 & 0 & 0 & 0 \\ 0 & 0 & \sqrt{\frac{3}{2}}(1+\kappa)B_\parallel & 0 \\ -2\kappa B_\parallel & 0 & -\sqrt{2}(1+\kappa)B_\perp & \frac{1+\kappa}{\sqrt{2}}B_\parallel \\ \kappa B_\perp & -\sqrt{3}\kappa B_\parallel & -\frac{1+\kappa}{\sqrt{2}}B_\parallel & -\sqrt{2}(1+\kappa)B_\perp \\ -\sqrt{3}\kappa B_\parallel & 3\kappa B_\perp & 0 & -\sqrt{\frac{3}{2}}(1+\kappa)B_\parallel \\ -\frac{1+\kappa}{\sqrt{2}}B_\parallel & 0 & -(1+2\kappa)B_\perp & -(1+2\kappa)B_\parallel \\ -\sqrt{2}(\kappa+1)B_\perp & -\sqrt{\frac{3}{2}}(1+\kappa)B_\parallel & -(1+2\kappa)B_\parallel & (1+2\kappa)B_\perp \end{pmatrix}, \quad (3.41)$$

where $\kappa = -(\kappa' + 1)/3$.

This Hamiltonian is only diagonal in the LL basis and, therefore, compatible with the axial approximation, if $B_\parallel = 0$. This can be easily verified by projecting the Hamiltonian H_z into the basis formed by Eqs. (3.32) and (3.33):

$$\begin{aligned} H_z^{mn}(B_\parallel, B_\perp) &\equiv A^\dagger(m) H_z(B_\parallel, B_\perp) A(n) \\ &= H_z(0, B_\perp)\delta_{mn} + \mu_B B_\parallel \left(h_z \delta_{m,n+1} + h_z^\dagger \delta_{m+1,n} \right), \end{aligned} \quad (3.42)$$

where, for $n \geq 1$,

$$h_z = \begin{pmatrix} 0 & 1 & 0 & 0 & 0 & 0 & 0 & 0 \\ 0 & 0 & 0 & 0 & 0 & 0 & 0 & 0 \\ 0 & 0 & 0 & -\sqrt{3}\kappa & 0 & 0 & \sqrt{\frac{3}{2}}(1+\kappa) & 0 \\ 0 & 0 & 0 & 0 & -2\kappa & 0 & 0 & \frac{1+\kappa}{\sqrt{2}} \\ 0 & 0 & 0 & 0 & 0 & -\sqrt{3}\kappa & 0 & 0 \\ 0 & 0 & 0 & 0 & 0 & 0 & 0 & 0 \\ 0 & 0 & 0 & 0 & -\frac{1+\kappa}{\sqrt{2}} & 0 & 0 & -(1+2\kappa) \\ 0 & 0 & 0 & 0 & 0 & -\sqrt{\frac{3}{2}}(1+\kappa) & 0 & 0 \end{pmatrix}. \quad (3.43)$$

The corresponding matrix h_z for $n, m \leq 0$ is the same except that some of the matrix entries must be set to zero. This is because in these cases some of the components of the LL spinors are zero, cf. Eq. (3.33). For instance, let us consider the case $m = 1$

and $n = 0$. In this case, all matrix entries of Eq. (3.43) in the 3rd column must be set to zero because the $|\mathrm{HH}, \uparrow\rangle$-component in the LL spinor $|\phi_0(z)\rangle$ is zero. The other special cases follow analogously.

Implementation: If $B_\parallel = 0$, the Zeeman Hamiltonian can be easily incorporated in our lattice approach since the LL index n is still a good quantum number. However, given that $B_\parallel \neq 0$, determining the LL spectrum implies that an $8N_{max} \times 8N_{max}$–dimensional matrix must be mapped onto the lattice in the z-direction, where N_{max} is the maximal number of LLs that shall be considered in the numerics. Determining the spectrum implies therefore that in total an $8N_{max}N \times 8N_{max}N$–dimensional matrix must be diagonalized. The resulting wave function is a superposition of all LL spinors

$$|\Psi(z)\rangle = \sum_{n=-2}^{N_{max}} a_n \, |\phi_n(z)\rangle \ , \tag{3.44}$$

where a_n is the expansion coefficient which is determined by diagonalizing the matrix. Calculating the LL spectrum with a nonzero in-plane magnetic field costs therefore much more computational power compared to the case that $\mathbf{B}$ points solely in the z-direction.

3.3.3. Exchange interaction

The exchange interaction between the s- and p-band electrons and the localized $3d^5$ electrons of the Mn-atoms [a] is described by a Heisenberg-type interaction[91]:

$$H_{ex} = -\sum_{\mathbf{R}_i} J_{sp-d}\left(\mathbf{x} - \mathbf{R}_i\right) \boldsymbol{\sigma} \mathbf{S}_i \, , \tag{3.45}$$

where $J_{sp-d}\left(\mathbf{x} - \mathbf{R}_i\right)$ is the coupling constant between the magnetic moments of the band electrons at position $\mathbf{x}$ and the localized magnetic moments of the ith Mn-atom at position $\mathbf{R}_i$. $\mathbf{S}_i$ stands for the spin operator of the ith Mn-atom and $\boldsymbol{\sigma}$ is the spin operator of the band electrons. According to Ref. [45, 91], we employ in the following the mean-field approximation, as well as the virtual crystal approximation in order to simplify Eq. (3.45). We apply these approximations as we could otherwise only solve a system with a few grid points.

In the mean-field approximation, the spin operator $\boldsymbol{S}_i$ is replaced by the averaged spin operator $\langle \mathbf{S} \rangle$, given by

$$\langle \mathbf{S} \rangle = -S_0 B_{\frac{5}{2}}\left[\frac{5 g_{Mn} \mu_B B_{tot}}{2 k_B \left(T + T_0\right)}\right] \frac{\mathbf{B}}{|\mathbf{B}|} \, , \tag{3.46}$$

[a] The electron configuration of Mn-atom is $[\mathrm{Ar}]3d^5 4s^2$, i.e., it has a half-filled d-shell.

where $g_{Mn} = 2$ is the g-factor of Mn, $S_0 = 5/2$ is the total spin quantum number of a Mn-atom, $T_0 = 2.6\,\mathrm{K}$ accounts for a small antiferromagnetic coupling between the Mn-atoms, and $B_{\frac{5}{2}}$ is a Brillouin-function, that is defined by:

$$B_{\frac{5}{2}}(x) = \frac{6}{5}\coth\left(\frac{6}{5}x\right) - \frac{1}{5}\coth\left(\frac{1}{5}x\right) . \tag{3.47}$$

In the virtual crystal approximation, we make use of the fact that a band electron (Bloch wave function) is an extended state and 'sees' as such a large number of Mn-atoms. This allows us to replace $J_{sp-d}(\mathbf{x} - \mathbf{R}_i)$ by $yJ_{sp-d}(\mathbf{x} - \mathbf{R})$, where $\mathbf{R}$ labels the lattice sites of the crystal structure and y denotes the Mn-concentration.

After applying the mean-field and the virtual-crystal approximation, the Heisenberg-type interaction becomes

$$H_{ex} = -y\boldsymbol{\sigma}\langle\mathbf{S}\rangle \sum_{\mathbf{R}} J_{sp-d}(\mathbf{x} - \mathbf{R}) , \tag{3.48}$$

where the sum runs now over all lattice sites. To finally derive the mean-field exchange interaction Hamiltonian for the Kane model, Eq. (3.48) must be projected into the eight dimensional basis given by Eq. (3.2) [45, 144]:

$$H_{ex}(B_\parallel, B_\perp) = \begin{pmatrix} 3\alpha A_z & 3\alpha A_x & 0 & 0 \\ 3\alpha A_x & -3\alpha A_z & 0 & 0 \\ 0 & 0 & 3\beta A_z & \sqrt{3}\beta A_x \\ 0 & 0 & \sqrt{3}\beta A_x & \beta A_z \\ 0 & 0 & 0 & 2\beta A_x \\ 0 & 0 & 0 & 0 \\ 0 & 0 & \sqrt{6}\beta A_x & -2\sqrt{2}\beta A_z \\ 0 & 0 & 0 & \sqrt{2}\beta A_x \end{pmatrix}$$
$$\begin{pmatrix} 0 & 0 & 0 & 0 \\ 0 & 0 & 0 & 0 \\ 0 & 0 & \sqrt{6}\beta A_x & 0 \\ 2\beta A_x & 0 & -2\sqrt{2}\beta A_z & \sqrt{2}\beta A_x \\ -\beta A_z & \sqrt{3}\beta A_x & -\sqrt{2}\beta A_x & -2\sqrt{2}\beta A_z \\ \sqrt{3}\beta A_x & -3\beta A_z & 0 & -\sqrt{6}\beta A_x \\ -\sqrt{2}\beta A_x & 0 & -\beta A_z & -\beta A_x \\ -2\sqrt{2}\beta A_z & -\sqrt{6}\beta A_x & -\beta A_x & \beta A_z \end{pmatrix} , \tag{3.49}$$

where $A_i = -y\langle S_i\rangle/6$ with $i = x, y$, $\alpha = \langle \mathrm{S}|\sum_{\mathbf{R}} J_{sp-d}(\mathbf{x} - \mathbf{R})|\mathrm{S}\rangle$ is the exchange integral between s- and d-electrons, and $\beta = \langle \mathrm{X}|\sum_{\mathbf{R}} J_{sp-d}(\mathbf{x} - \mathbf{R})|\mathrm{X}\rangle$ is the exchange integral between p- and d-electrons. The material specific values for the exchange

integrals α and β are taken from literature, $\alpha = 0.4\,\mathrm{eV}$ and $\beta = -0.6\,\mathrm{eV}$ [21].

Like the Zeeman term, the exchange interaction Hamiltonian is only diagonal in the axial symmetric basis, given by Eqs. (3.32) and (3.33), if $B_\parallel = 0$. To be precise, projecting the exchange Hamiltonian in the LL basis gives

$$\begin{aligned} H_{ex}^{mn}(B_\parallel, B_\perp) &= A^\dagger(m) H_{ex}(B_\parallel, B_\perp) A(n) \\ &= H_{ex}(0, B_\perp)\delta_{mn} + A_x \left(h_{ex}\delta_{m,n+1} + h_{ex}^\dagger \delta_{m+1,n} \right) , \end{aligned} \tag{3.50}$$

where, for $n, m \geq 1$,

$$h_{ex,\parallel} = \begin{pmatrix} 0 & 3\alpha & 0 & 0 & 0 & 0 & 0 & 0 \\ 0 & 0 & 0 & 0 & 0 & 0 & 0 & 0 \\ 0 & 0 & 0 & \sqrt{3}\beta & 0 & 0 & \sqrt{6}\beta & 0 \\ 0 & 0 & 0 & 0 & 2\beta & 0 & 0 & \sqrt{2}\beta \\ 0 & 0 & 0 & 0 & 0 & \sqrt{3}\beta & 0 & 0 \\ 0 & 0 & 0 & 0 & 0 & 0 & 0 & 0 \\ 0 & 0 & 0 & 0 & -\sqrt{2}\beta & 0 & 0 & -\beta \\ 0 & 0 & 0 & 0 & 0 & -\sqrt{6}\beta & 0 & 0 \end{pmatrix} . \tag{3.51}$$

The special cases for which $n, m \leq 0$ follow analogously to the discussion below Eq. (3.43). Its implementation in the numerics is also analogous to the implementation of a Zeeman Hamiltonian (see Sec. 3.3.2).

3.3.4. Bulk inversion asymmetry

Incorporating the BIA Hamiltonian, given by Eq. (3.8), breaks the axial symmetry already at $B_{tot} = 0$. To study the consequences in the presence of LLs, let us project the BIA Hamiltonian into the LL basis

$$\begin{aligned} H_B^{mn}(B_\perp) &= A^\dagger(m) H_B(a, a^\dagger, k_z) A(n) \\ &= h_B(n, k_z)\delta_{m+2,n} + h_B^\dagger(n, k_z)\delta_{m-2,n} , \end{aligned} \tag{3.52}$$

where the ladder operators were introduced according to Eq. (1.51). For $n \geq 1$,

$$h_B(n,k_z) = C \begin{pmatrix} 0 & 0 & 0 & 0 & 0 & 0 & 0 & 0 \\ 0 & 0 & 0 & 0 & 0 & 0 & 0 & 0 \\ 0 & 0 & 0 & 0 & 0 & 0 & 0 & 0 \\ 0 & 0 & -\frac{\sqrt{2(n-1)}}{l_{B_\perp}} & 0 & 0 & 0 & 0 & 0 \\ 0 & 0 & k_z & \frac{\sqrt{3n}}{\sqrt{2}l_{B_\perp}} & 0 & 0 & \frac{\sqrt{3n}}{2l_{B_\perp}} & 0 \\ 0 & 0 & -\frac{\sqrt{3n}}{\sqrt{2}l_{B_\perp}} & -k_z & -\frac{\sqrt{n+1}}{\sqrt{2}l_{B_\perp}} & 0 & \frac{k_z}{\sqrt{2}} & -\frac{\sqrt{n+1}}{2l_{B_\perp}} \\ 0 & 0 & \frac{\sqrt{n-1}}{2l_{B_\perp}} & 0 & 0 & 0 & 0 & 0 \\ 0 & 0 & \frac{k_z}{\sqrt{2}} & -\frac{\sqrt{3n}}{2l_{B_\perp}} & 0 & 0 & 0 & 0 \end{pmatrix} . \tag{3.53}$$

The matrix $h_{BIA}(n)$ for $n \leq 0$ is the same as Eq. (3.53) except that all matrix elements, which depend on the LL index n, must be set to zero if the corresponding radicals would become imaginary numbers.

Equation (3.52) shows that a BIA Hamiltonian couples states $|\phi_n(z)\rangle$ with n and $n \pm 2$. Thus, in the presence of BIA, a linear combination of LL spinors is an appropriate ansatz for the Kane Hamiltonian in magnetic fields:

$$|\Psi^E(z)\rangle = \sum_{n=-1}^{N_{max}} a_{2n} \, |\phi_{2n}(z)\rangle \ , \tag{3.54}$$

$$|\Psi^O(z)\rangle = \sum_{n=-1}^{N_{max}} a_{2n+1} \, |\phi_{2n+1}(z)\rangle \ . \tag{3.55}$$

As a result, $|\Psi(z)\rangle$ decomposes into an even and odd subspace labeled by E and O, respectively, since there is no coupling between LLs with even and odd LL indices n. This allows us to compute the LL spectrum in the even and odd subspace separately.

3.4. Band structure of (Hg,Mn)Te

We are now in the position to explore the landscape of 2D $Hg_{1-y}Mn_yTe/Hg_{0.68}Cd_{0.32}Te$ quantum wells varying the quantum well thickness d_{QW} and the Mn-concentration using the discretized 8×8 Kane model [a]. Here, we take $Cd_{0.96}Zn_{0.04}Te$ as the substrate material which is included according to Sec. 3.1.3. To this end, we performed a large number of band structure calculations with different quantum well thicknesses, $5 < d_{QW}\,[\mathrm{nm}] < 13$, and Mn-concentrations, $0 < y\,[\%] < 4$. An overview of the topological landscape is presented in Fig. 3.3(a). The band structure of (Hg,Mn)Te quantum wells can be classified by two characteristic features: (i) the band ordering at the Γ-point

[a] Here, we do not make use of the axial approximation but neglect BIA terms. All band structures are shown along the line $k_x = \pm k_y$, where the camelback maxima occur.

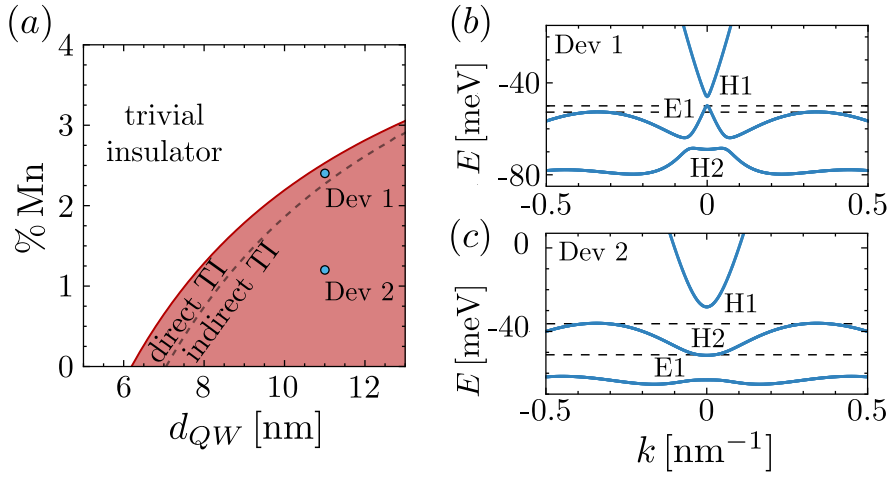

Figure 3.3.: Evolution of band structure for (Hg,Mn)Te quantum wells with various Mn concentrations and thicknesses d_{QW}. (a) Phase space obtained from 8×8 Kane model. The solid red line indicates the transition from trivial (white) to topologically nontrivial (red) regime. Along this line, the E1 (electron-like) and the H1 (heavy-hole-like) subbands get inverted. The dotted line indicates the direct- to indirect-gap transition. In (b) and (c), the band structure of (Hg,Mn)Te quantum wells are explicitly shown for two sample configurations: (Dev 1, direct gap) 11 nm and 2.4% Mn and (Dev 2, indirect gap) 11 nm with 1.2%, where H2 marks the second heavy-hole-like subband. Dashed lines mark band structure maxima. Reprinted from Ref. [P7].

and (*ii*) the energetic difference between the additional maxima in the band structure at large momenta (camelback maxima) and the valence band edge.

The first feature, the band ordering at Γ, determines the topology of the quantum well. As already discussed in Sec. 1.3.2, the compound semiconductor HgTe is topologically trivial for $d_{QW} < 6.3$ nm and enters the topologically nontrivial regime for $d_{QW} > 6.3$ nm, for which the E1 subbands lie energetically below the H1 subbands [16, 17]. When Mn-atoms are additionally incorporated in the crystal structure, we find that an increase of the Mn-concentration shifts the topological transition to larger quantum well thicknesses, as inferred from Fig. 3.3(a). This effect is caused by the renormalization of the band edge energies due to the Mn-atoms [cf. App. A]. For even larger d_{QW}, the E1subbands [a], also cross higher-order subbands like the H2 and $H3$ subbands. For clarity, these crossings are not indicated in the landscape since they do not change the topology of the semiconductor.

The second feature, the energetic difference between the camelback maxima and the valence band edge, marked in Fig. 3.3(b) and (c), determines whether the system is a direct or an indirect gap TI. The transition between these two regimes is indicated by the dashed line in Fig. 3.3(a). The camelback derives its significance from the fact that it is associated to a Van-Hove-like singularity. By this, we mean that the DOS is extremely

[a] The subband naming is explained in Sec. 1.3.2.

large at the camelback due to its large effective mass. In typical experiments, where the carrier density in the quantum well is controlled by an external gate voltage, this Van-Hove-like singularity pins the chemical potential and makes it difficult to shift the chemical potential into the valence band. In direct gap TIs, the chemical potential gets therefore pinned below the valence band edge, such that, additional to the carriers at the camelback maxima, mobile carriers close to the Γ-point can contribute to transport ($p \approx 2\times10^9\,\mathrm{cm}^{-2}$). In contrast, in indirect gap TIs, the chemical potential gets pinned above the valence band edge which means that only carriers close to the camelback maximum (with a large effective mass) contribute to transport. This essential difference between direct and indirect gap TIs will have important consequences for magnetotransport experiments as we will demonstrate in Sec. 3.5.

In the further course of this chapter, we focus on two specific, topologically nontrivial quantum well devices, labeled by Dev 1 and Dev 2. Dev 1 is a direct gap TI with $d_{QW} = 11.0\,\mathrm{nm}$ and $y = 2.4\%$ Mn, while Dev 2 is an indirect gap TI with the same thickness but with $y = 1.2\%$ Mn. Their respective band structures are shown in Fig. 3.3(b) and (c). Note that we consider confinement only in the z-direction, so that we do not see traces of helical edge states in the bulk gap in the theoretical analysis [a].

3.4.1. Experimental characterization of (Hg,Mn)Te quantum wells

The two devices Dev 1 and Dev 2 (Hall bars) have been experimentally characterized by S. Shamim (with help of A. Budewitz and P. Shekhar) for various magnetic field configurations and carrier densities. The latter can be tuned by applying a gate voltage $V_g^\star$ to the quantum well. Here, we will briefly summarize their main experimental findings [P7], as they motivated our theoretical model which will be presented in the following.

Dev 1: Let us at first focus on the direct gap TI Dev 1, which exhibits the QSH phase at $B_{tot} = 0$. Its longitudinal resistance $R_{xx}(V_g^\star)$, which is shown in Fig. 3.4(a), exhibits a maximal resistance when the chemical potential is placed in the bulk gap. Note that the resistance peak is much higher than the characteristic QSH value of $R_{xx} = h/2e^2$ due to the large dimensions of the device, $l = 600\,\mu\mathrm{m}$ and $w = 200\,\mu\mathrm{m}$ (cf. to discussion in Sec. 1.3.2) [85, 88, 155]. The chemical potential reaches the bulk p-regime for $V_g^\star \lesssim -0.5\,\mathrm{V}$ (valence band) and the bulk n-regime for $V_g^\star \gtrsim 0.5\,\mathrm{V}$ (conduction band). From an Arrhenius plot of conductance as a function of temperature, the bulk gap of Dev 1 was experimentally estimated to be $\approx 4.6\,\mathrm{meV}$, which is in very good agreement with the

[a] To observe edges states, hard wall boundary conditions would need to be imposed in the x- or y-direction. The latter calculation has been performed by W. Beugeling. His results can be found in Ref. [P7] and are summarized in Sec. 3.6.

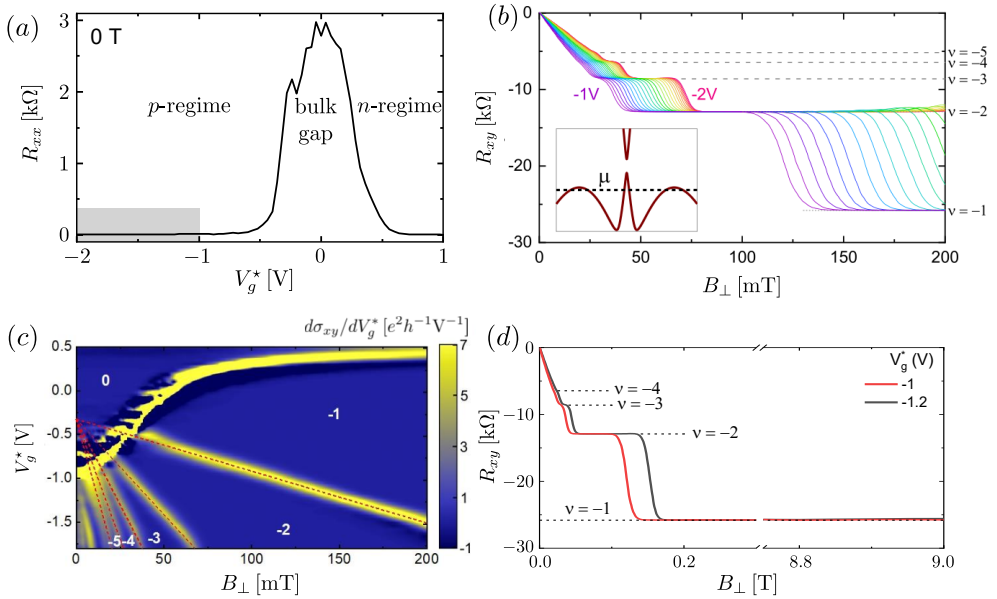

Figure 3.4.: Experimental characterization of Dev 1 (d_{QW} =11 nm, 2.4% Mn). (a) Longitudinal resistance R_{xx} as function of $V_g^\star$. (b) Magnetic field dependence of R_{xy} for various $V_g^\star$ highlighted in (a) by gray shaded area. Inset schematically shows band structure of Dev 1 and position of chemical potential μ. (c) LL fan shows differential conductivity $d\sigma_{xy}/dV_g^\star$, where blue marks QH plateaus and yellow indicates transitions between adjacent plateaus. The corresponding QH filling factors ν are highlighted by white numbers. (d) The $\nu = -1$ plateau extends up to very large $B_\perp$. Figures show experimental data and are reprinted from Ref. [P7].

theoretical value of 4 meV, cf. Fig. 3.3(b). This agreement demonstrates the accuracy of the employed 8×8 Kane model.

To further characterize the device in the presence of magnetic fields, we focus now on the case for which the chemical potential is placed in the bulk p-regime [a]. Here, the main experimental findings are:

1. An onset to a series of QH plateaus ranging from $\nu = -5$ to -1 is observed at ultra-low magnetic fields of 20–30 mT for a wide range of gate voltages $V_g^\star$ [Figs. 3.4(b) and (c)].

2. These 'emergent' QH plateaus show a strong in-plane magnetic field dependence. The larger $B_\parallel$, the smaller is the onset field $B_\perp$ to the QH plateaus [Fig. 3.5].

3. The $\nu = -1$ plateau extends up to exceptionally large magnetic fields (a few tesla) [Fig. 3.4(d)].

The emergence of QH plateaus at such ultra-low magnetic fields is usually not expected. This is because typical high-mobility 2D systems exhibit a metal to insulator transitions below a critical density of $\sim 1 - 2 \times 10^{10}\,\mathrm{cm}^{-2}$ [156] preventing an observation of QH

[a] The n-regime behaves like a conventional 2D electron gas and is thus not of particular interest.

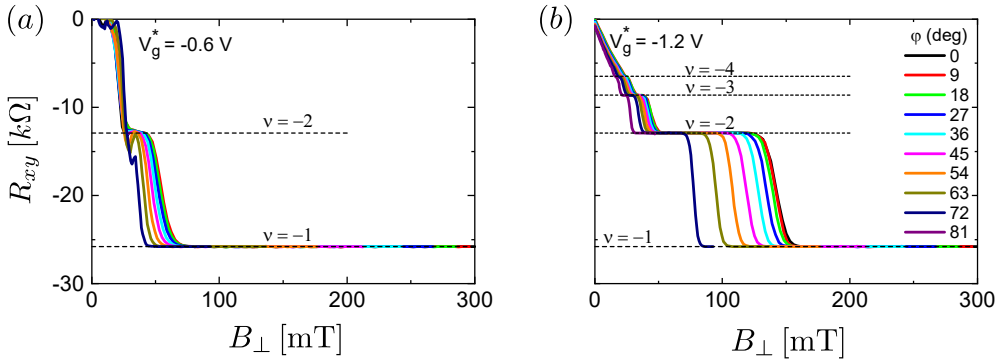

Figure 3.5.: Effect of in-plane magnetic field on QH plateaus for Dev 1. In both plots, transverse resistance R_{xy} is shown as a function of the out-of-plane component of the magnetic field $B_\perp$ for various in-plane magnetic field values, $B_\parallel = B_{tot}\sin(\varphi)$ at (a) $V_g^\star = -0.6\,\mathrm{V}$ and (b) $-1.2\,\mathrm{V}$. The associated experimental setup is schematically depicted in Fig. 3.2. Figures show experimental data and are reprinted from Ref. [P7].

plateaus at such low magnetic fields. In addition, the onset fields of conventional LLs do not depend on the in-plane magnetic field $B_\parallel$, since the QH filling factor $\nu = n/n_{B_\perp}$ [see also Eq. (1.56)] depends only on the carrier density n and the out-of-plane component of the magnetic field $B_\perp$.

Finally, note that a magnetic field of a few tens of mT, corresponding to a spin polarization $\langle S_z\rangle \sim 0.1$ [cf. Eq. (3.46)], can only close a gap of $\approx 1\,\mathrm{meV}$ [a]. Since the topological bulk gap is a factor of ~ 5 larger than this theoretical estimate, it is unlikely that the magnetic field is sufficient to drive the (Hg,Mn)Te quantum wells into the QAH phase. In comparison to the previous chapter, we therefore do not expect to find signatures of coexistent QH and QAH states at such low magnetic fields.

Dev 2: In comparison, magnetotransport experiments on Dev 2 do not show an early onset of QH plateaus (see supplementary material of Ref. [P7]). Instead, QH plateaus are in this case only observed for $B_\perp \gtrsim 4\,\mathrm{T}$, when the chemical potential is placed in the bulk p-regime. In general, the experiment shows an early onset to QH plateaus in the bulk p-regime only for direct gap TIs, i.e., left of the direct-to-indirect transition (dashed line) in Fig. 3.3(a).

Bulk gap regime: We have focused so far on the experimental characterization of (Hg,Mn)Te quantum wells in the bulk p-regime [cf. Fig. 3.4(a)]. The bulk gap regime has been also analyzed experimentally by S. Shamim and has been theoretically described by W. Beugeling. In a nutshell, the bulk gap regime exhibits, similar to the p-regime, an early onset to a $\nu = -1$ QH plateau ($\sim 50\,\mathrm{mT}$). But, in contrast to the p-regime, its onset value is independent of the in-plane magnetic field. In addition, QH plateaus with filling factor $\nu = -2, -3, \ldots$ are not observed. Further details of this

[a] This approximation is based on Eq. (2.104) and takes the combined effect of exchange interaction, Zeeman effect, and an additional orbital contribution into account.

particular regime are discussed in Ref. [P7] and the theoretical findings of W. Beugeling are briefly summarized in Sec. 3.6. Note that the emphasis of this chapter lies however on the bulk p-regime.

3.5. Emergent QH effect in the bulk p-regime

In this section, we compute the bulk LL spectrum of (Hg,Mn)Te quantum wells using the 8×8 Kane model for various magnetic field configurations. Our goal is to compare signatures of direct and indirect gap TIs in the bulk p-regime in magnetic fields to derive an interpretation for the peculiar experimental findings, that we have described in Sec. 3.4.1. In that regard, we will shed light on the important role of the camelback when LLs form.

To gain a simplistic understanding of the LL physics associated to the camelback, we start in Sec. 3.5.1 studying a toy Hamiltonian that mimics the camelback dispersion. Results for Dev 1 and Dev 2, that are based on the full 8×8 Kane model, are presented in Secs. 3.5.2 and 3.5.3, respectively.

3.5.1. Toy model

To develop a simplistic understanding of the formation of LLs in the valence band of (Hg,Mn)Te quantum wells, let us consider the following toy model Hamiltonian (no spin degree of freedom):

$$H(k) = \alpha k^2 + \beta k^4 + \gamma k^6 \,, \tag{3.56}$$

where $k^2 = k_x^2 + k_y^2$ and α, β, and γ are parameters that can be tuned to implement different types of camelback. In particular, we are interested in the two cases, where the camelback maximum is either slightly below or above the valence band edge, as exemplary shown in Fig. 3.6(a) and (c), respectively. Therein, the dashed lines indicate the various extrema of the bulk band structure.

The LL spectrum of Eq. (3.56) can be easily calculated by replacing all momentum operators by ladder operators according to:

$$k^{2j} \to \left(\frac{2}{l_{B_\perp}^2}\right)^j \left(a^\dagger a + \frac{1}{2}\right)^j \,, \tag{3.57}$$

where $j = 1, 2, 3 \ldots$, and a is a conventional magnetic ladder operator. Making use of

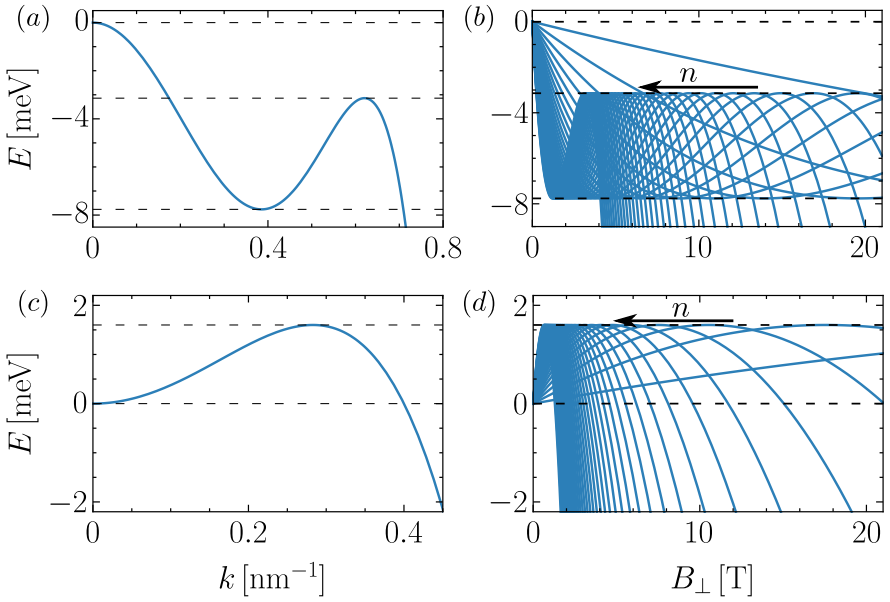

Figure 3.6.: Formation of LLs for simple toy Hamiltonian, given by Eq. (3.56), for different shapes of the camelback. In (a) and (b), the band structure and the corresponding LL fan are shown for a direct gapped semiconductor with a pronounced camelback. The parameters are $\alpha = -120\,\mathrm{meV\,nm^2}$, $\beta = 560\,\mathrm{meV\,nm^4}$, and $\gamma = -700\,\mathrm{meV\,nm^6}$. In (c) and (d), the band structure and the LL fan are depicted for an indirect gapped semiconductor with $\alpha = 40\,\mathrm{meV\,nm^2}$, $\beta = -250\,\mathrm{meV\,nm^4}$, and $\gamma = 0$. The arrows point in the direction of increasing n. The dashed lines mark all extrema of the band structures.

Eq. (1.52), we derive the following expression for the LL spectrum

$$E_n(B_\perp) = \frac{2}{l_{B_\perp}^2}\left(n+\frac{1}{2}\right)\left[\alpha + \frac{2\beta}{l_{B_\perp}^2}\left(n+\frac{1}{2}\right) + \frac{4\gamma}{l_{B_\perp}^4}\left(n+\frac{1}{2}\right)^2\right]. \tag{3.58}$$

In Figs. 3.6(b) and (d), the LL spectra are explicitly shown corresponding to the band structures in Figs. 3.6(a) and (c), respectively. It is apparent that there is a one-to-one correspondence between the band structure at $B_\perp = 0$ and the evolution of LLs in magnetic fields. Each LL describes the same curve shape (as a function of $B_\perp$) as the band structure at $B_\perp = 0$ (with the same extrema), except that the slope of each curve increases with increasing LL index n. This means the larger n, the smaller is the magnetic field at which a LL exhibits its maxima. With this basic rule in mind, it will be straightforward to understand the formation of LLs in (Hg,Mn)Te quantum wells in the following.

3.5.2. Direct gap topological insulators

Employing the discretized Kane model in the axial approximation and neglecting BIA terms (cf. Sec. 3.3.1), we have computed the LL spectrum of Dev 1 as a function of the external out-of-plane magnetic field $B_\perp$ (i.e., $B_\parallel = 0$) at temperature $T = 0\,\mathrm{K}$. The

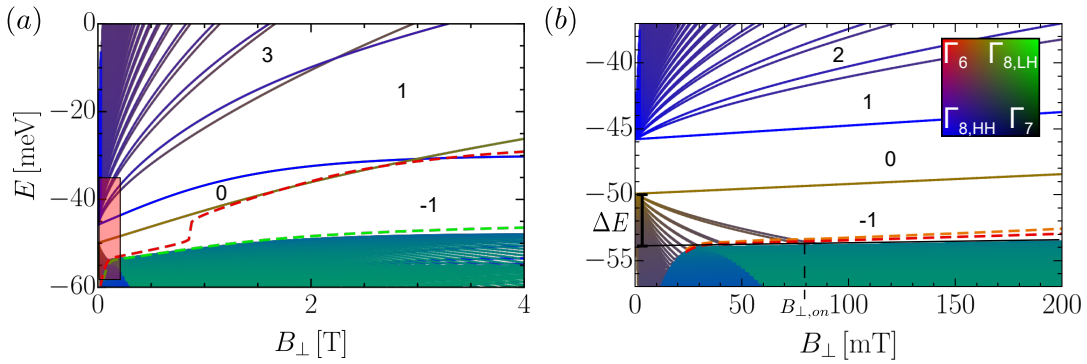

Figure 3.7.: Evolution of bulk LL energies as function of magnetic field $B_\perp$ for Dev 1 (direct band gap) for a maximal $B_\perp$ of (a) 4 T, and (b) 200 mT [red shaded area in (a)]. Color code indicates orbital character. Corresponding plot legend is shown in (b). Dashed lines depict evolution of chemical potential as function of $B_\perp$ at constant hole densities: $p = 0.05 \times 10^{11}\,\mathrm{cm}^{-2}$ (orange), $p = 0.2 \times 10^{11}\,\mathrm{cm}^{-2}$ (red), and $p = 2 \times 10^{11}\,\mathrm{cm}^{-2}$ (green). Numbers indicate the QH filling factors ν. In (b), the black solid line extrapolates height of camelback to $B_\perp = 0$; ΔE is the energetic difference between the valence band edge and the camelback. Reprinted from Ref. [P7].

effect of Zeeman and exchange coupling is taken into account according to Secs. 3.3.2 and 3.3.3. The corresponding LL fan is shown for a magnetic field range of 0 to 4 T in Fig. 3.7(a). To highlight the regime at which emergent QH plateaus are observed in the experiment, Fig. 3.7(b) shows an excerpt of the same LL fan in a magnetic field range from 0 to 200 mT [a]. For clarity, the QH filling factor ν, which is related to the Hall conductivity via $\sigma_{xy} = \nu e^2/h$, is indicated in the LL fan. The latter can be computed by means of Streda's relation, Eq. (1.59).

In Fig. 3.7, the color code, which represents the orbital character of the respective wave functions, clearly shows that Dev 1 exhibits an inverted band structure. The E1subband, which consists of a mixture of S- and LH-character (brown color, $E \approx -50\,\mathrm{meV}$), lies at $B_\perp = 0$ energetically below the HH-like H1 subband (blue, $E \approx -45\,\mathrm{meV}$). The characteristic LL crossing of an inverted band structure [17, 61] occurs for this specific sample at $B_\perp \approx 3\,\mathrm{T}$. Whereas the conduction band looks quite conventional, the appearance of the valence band is dominated by a very dense collection of LLs. Based on our experience from the toy model [see Fig. 3.6(b)], it is apparent that these LLs can be attributed to the camelback. In particular, we see in Fig. 3.7(b) that the upper edge of the camelback extrapolates against $E \approx -54\,\mathrm{meV}$ for $B_\perp = 0$ (black line), which agrees with the camelback maximum of the corresponding band structure at $B_\perp = 0$, cf. Fig. 3.3(b). It is worth noting that below $B_\perp < 70\,\mathrm{mT}$, LLs with small LL indices ($n = -2, -1, \ldots$), resulting from highly mobile carriers at small k, can coexist at the same energy with higher LLs ($n \sim 500$–1000), stemming from the

[a] While for calculating Fig. 3.7(a) only the first 300 LLs were considered, Fig. 3.7(b) is based on the first 1000 LLs.

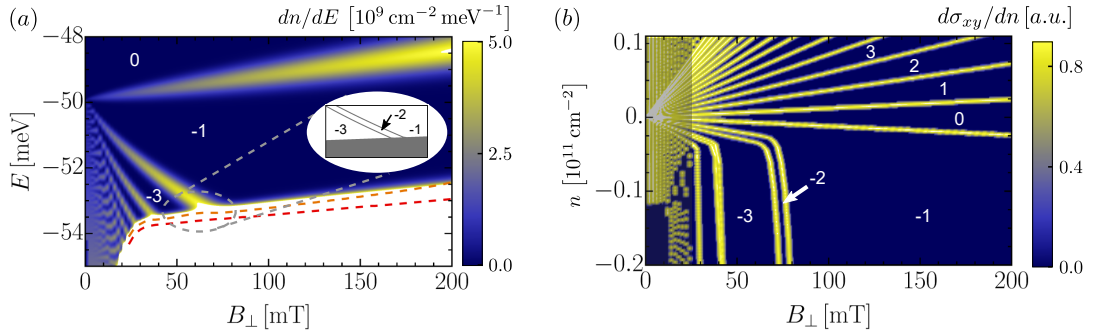

Figure 3.8.: Analogously to Fig. 3.7(b), bulk LL energies are shown for Dev 1 employing different types of representations including LL broadening. (a) Energy as function of $B_\perp$ plot, where color code indicates DOS, dn/dE. White implies that the DOS is out-of-scale. The orange and red curves correspond to a chemical potential with densities $p = 5 \times 10^9\,\mathrm{cm}^{-2}$ and $2 \times 10^{10}\,\mathrm{cm}^{-2}$, respectively. The inset shows a zoom of the lowest LLs without broadening. (b) Different representation of the same LL fan: y-axis shows carrier density and color code highlights $d\sigma_{xy}/dn$. The shaded area at low magnetic fields marks a regime below the computation limit. In both plots, numbers indicate the QH filling factors ν. Reprinted from Ref. [P7].

camelback.

LL broadening: So far, we have not yet included disorder in our model which should give rise to LL broadening [64, 69]. To account for this effect, we assume in the following that the DOS $D(E)$ of each LL is broadened to a Gaussian shape [45]:

$$D\left(E\right) = \frac{1}{2\pi l_{B_\perp}^2} \sum_{n=-2}^{N_{max}} \frac{1}{\sqrt{2\pi\sigma^2}} \exp\left(-\frac{(E-E_n)^2}{2\sigma^2}\right), \tag{3.59}$$

where the summation runs over all LLs with energy E_n, N_{max} is the maximal number of LLs which we consider in the numerics, and σ determines the width of the LL broadening. Here, we take $\sigma = \sigma_0\sqrt{B_\perp/B_0}$ with $\sigma_0 = 0.85\,\mathrm{meV}$ and $B_0 = 1\,\mathrm{T}$ [45].

Low-magnetic-field features: In Fig. 3.8(a), we show the same LL fan as in Fig. 3.7(b) except that LL broadening is explicitly taken into account, and that only the regime in the vicinity of the camelback is shown (bulk p-regime). The color code represents the DOS, i.e., blue indicates the absence of states, yellow indicates a LL (or two LLs which are close to each other), and white implies that the DOS is out-of-scale. To be more precise, the white area below $E < -52\,\mathrm{meV}$ in Fig. 3.8(a) implies that the DOS is ~ 400 times larger than in a single LL, i.e., the dense collection of LLs stemming from the camelback is associated to a Van-Hove-like singularity in the valence band.

An important consequence of the Van-Hove-like singularity is the pinning of the chemical potential μ to the edge of the camelback in the bulk p-regime. This is because any small decrease of the chemical potential would result in a large increase of the p-density if the chemical potential is at the edge of the camelback. To highlight this fact, the

evolution of μ as a function of $B_\perp$ is shown for two exemplary cases in Figs. 3.7(b) and 3.8(a) at constant p-density. As a result of this pinning mechanism, the chemical potential crosses LLs with small LL indices, originating from states close to the valence band edge, already at very small $B_\perp$ (tens of mT). This differentiates (Hg,Mn)Te quantum wells from a conventional 2D electron gas, where μ crosses LLs with small LL indices only at much larger magnetic fields. For instance at $p = 2 \times 10^{10}\,\mathrm{cm}^{-2}$, an onset to the $\nu = -1$ QH plateau is usually expected to occur not before $B_\perp \approx 1\,\mathrm{T}$ [estimate is based on Eq. (1.56)].

To investigate the evolution of the Hall conductivity $\sigma_{xy}(B_\perp)$ at constant carrier density, we show in Fig. 3.8(b) the same LL fan as in Fig. 3.8(a) with the only difference that the carrier density is taken as the y-axis and that the color code represents $d\sigma_{xy}/dn$, where n is the carrier density. Here, it is assumed that only extended states, located in the center of each broadened LL, can give rise to a change in σ_{xy} [a]. Since $n \sim V_g^\star$, this form of depicting a LL fan is analogous to the experimental results presented in Fig. 3.4(c). Figure 3.8(b) reveals that the Van-Hove-like singularity stemming from the camelback is responsible for an early onset of QH plateaus with $\nu = -3, -2, -1$ for a large range of p-densities. This means we can attribute the experimentally observed early onsets of QH plateaus in the bulk p-regime, shown in Fig. 3.4(c), to pinning of the chemical potential to the camelback.

Another consequence of the pinning mechanism is that all observed QH plateaus in the p-regime are very sensitive to the energetic difference ΔE of the valence band edge and the maximum of the camelback at $B_\perp = 0$ [marked in Fig. 3.7(b)]: The onset fields of the QH plateaus decreases as ΔE decreases. This results from the fact that the upper edge of the camelback in magnetic fields extrapolates to the camelback at $B_\perp = 0$. Consequently, we expect that any (Hg,Mn)Te TI with a direct gap and close to the direct-indirect-gap transition [dashed line in Fig. 3.3(a)] exhibits a similar characteristic behavior in the p-regime.

Finally, note that despite the macroscopic occupation of bulk states near the camelback, the bulk conduction should remain suppressed at low temperatures, because bulk carriers are localized by disorder. Indeed, the higher Landau plateaus are well resolved in experiments at 20 mK, but they are not robust against increased temperatures, see supplementary material in Ref. [P7]. This finding is further supported by the fact that the theoretically calculated density of the highly mobile carriers lying above the camelback in Fig. 3.3(b) ($p \approx 2 \times 10^9\ \mathrm{cm}^{-2}$) agrees well with the experimentally determined mobile p-carrier density of ~ 2–$3 \times 10^9\,\mathrm{cm}^{-2}$ for the entire range of $V_g^\star$ [b].

[a] Recall that extended states exist exclusively in the center of each broadened LL, while states in the tails of the Gaussian-shaped DOS are localized. A QH transition is observed whenever the chemical potential crosses extended states [69].

[b] In the experiment, the p-carrier density has been extracted from a Drude fit at low fields $B_\perp < 20\,\mathrm{mT}$.

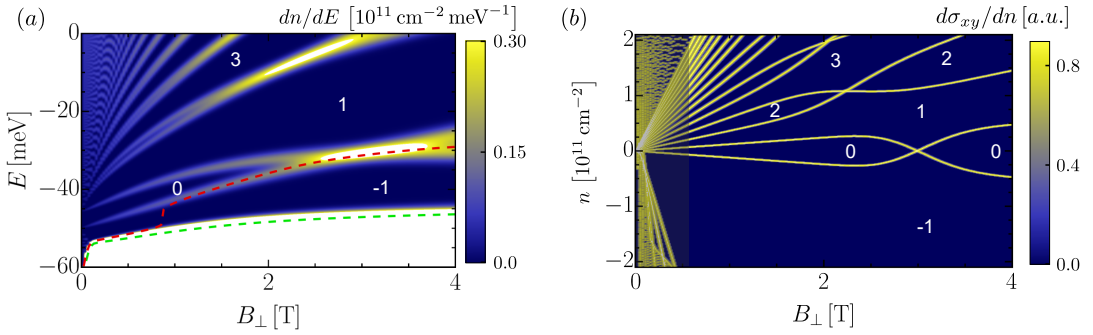

Figure 3.9.: Analogously to Fig. 3.8, bulk LL energies are shown for Dev 1 employing different types of representations including LL broadening (same color code). However, in comparison to Fig. 3.8, this figure focuses on the large $B_\perp$ behavior. Red and green curves correspond to a chemical potential with hole densities $p = 2 \times 10^{10}\,\mathrm{cm}^{-2}$ and $2 \times 10^{11}\,\mathrm{cm}^{-2}$, respectively. Reprinted from Ref. [P7].

High-magnetic-field features: To study also the high-field features of Dev 1, we show further results in Fig. 3.9. Due to pinning of the chemical potential to the camelback, we find that the $\nu = -1$ QH plateau in the bulk p-regime can extend up to very large $B_\perp$. This is in good agreement with the observation of an exceptional long $\nu = -1$ QH plateau in the experiment, shown in Fig. 3.4(d). Moreover, it is apparent that the camelback manifests itself as a large asymmetry between n- and p-densities. The latter is also typically observed in the experiment.

Role of in-plane magnetic field: While the onset fields of QH plateaus in a conventional 2D electron gas depend only on the out-of-plane component of the magnetic field $B_\perp$, the experiment shows that QH plateaus in the p-regime of direct gap TIs are very sensitive to the applied in-plane magnetic field $B_\parallel$ (cf. Fig. 3.5). To explain this dependency, we include now the effect of an in-plane magnetic field in our band structure calculations according to Secs. 3.3.2 and 3.3.3.

Let us at first consider the effect of an in-plane magnetic field at constant $B_\perp$ on the band structure, neglecting the orbital effect of $B_\perp$ (i.e., without Peierls substitution). The resulting spectrum is shown in Fig. 3.10(a). We find that an in-plane magnetic field does not alter the band structure close to $k = 0$ significantly, while the height of the camelback is very sensitive to $B_\parallel$ and increases for larger φ [defined in Eq. (3.31)]. Assuming that the chemical potential is pinned to the camelback, the resulting decrease of ΔE entails lower onset fields for the QH plateaus in the bulk p-regime. This can be especially seen from comparing the onset field $B_{\perp,on}$ to the $\nu = -1$ plateau in Figs. 3.7 and 3.10(b). Thus, the observed in-plane field dependence in the experiment can be attributed to pinning of the chemical potential to the camelback.

Note that the difference between the $k = 0$ and the camelback regime is connected to the interplay between the exchange coupling and the variation in orbital character of

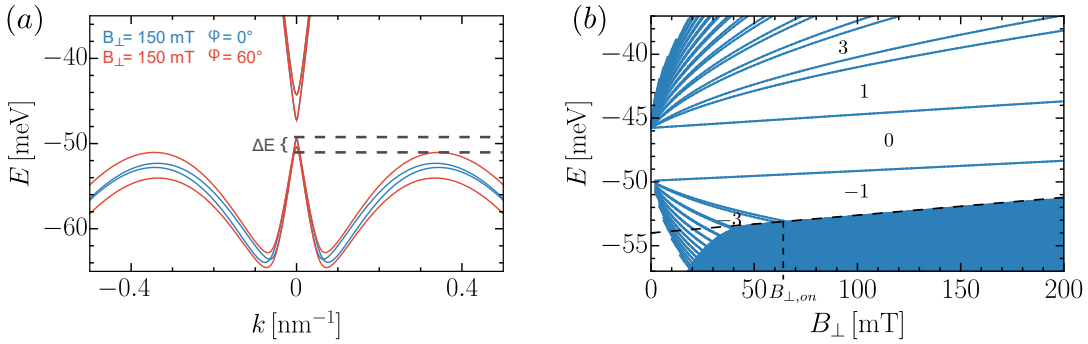

Figure 3.10.: Study of the role of in-plane magnetic field $B_\parallel$. (a) At constant $B_\perp = 150\,\mathrm{mT}$, effect of $B_\parallel$ on the band structure is shown neglecting orbital effect of $B_\perp$. Blue and orange lines depict band structure with $\varphi = 0°$ and $60°$ [angle is defined in Eq. (3.31)], respectively. ΔE decreases with increasing φ. (b) Landau level fan for $\varphi = 60°$, i.e., including the effect of $B_\parallel$. QH filling factors ν are indicated by numbers. Dashed line extrapolates edge of camelback against $B_\perp = 0$. $B_{\perp,on}$ marks critical field at which onset to $\nu = -1$ plateau can be observed. (a) Reprinted from Ref. [P7].

the band structure as a function of momentum. A strong in-plane field dependence of the camelback can therefore only exist in Mn-doped samples [a].

Role of bulk inversion asymmetry: Although our theoretical pinning model agrees qualitatively well with the experiment for p-densities, there is a minor difference between theory and experiment on the quantitative level. In particular, the theory points to a broad $\nu = -3$ and a very narrow $\nu = -2$ QH plateau at low magnetic fields, whereas, in the experiment, $\nu = -2$ is the most visible QH plateau, cf. Figs. 3.4(c) and 3.8. In the numerics, the even-odd difference arises since all valence band LLs with small n come in almost-degenerate (small gap) pairs suggesting that only odd plateaus with $\nu = -1, -3, -5$ should be nicely visible. Each of these pairs is linked to two different LLs with LL indices n and $n + 2$.

This discrepancy may be resolved by considering a perturbation that couples and, therefore, splits these LL pairs, thus leading to an increased width of all even plateaus ($\nu = -2, -4$). Bulk inversion asymmetry, which has been neglected so far, is a possible candidate: In linear approximation, the BIA Hamiltonian couples states with n to $n+2$, as we have shown in Sec. 3.1.2 [b] . Let us therefore include now the effect of BIA in our LL calculations, explicitly.

Figure 3.11(a) shows that the energetic distance ΔE between the valence band edge and the camelback maximum is reduced by including BIA. This is because BIA lifts the degeneracy of the bands for large momenta, while the energy of the valence band

[a] The effect of Zeeman terms is in this magnetic field range more than order of magnitude smaller than the effect of exchange coupling and can be therefore neglected.

[b] Removing the axial approximation, which we employed to calculate the LL fan, would result in a coupling between LLs with n and $n + 4$, cf. Sec. 3.3.1. This means neglecting terms that break the axial symmetry cannot be the source for the discrepancy between theory and experiment.

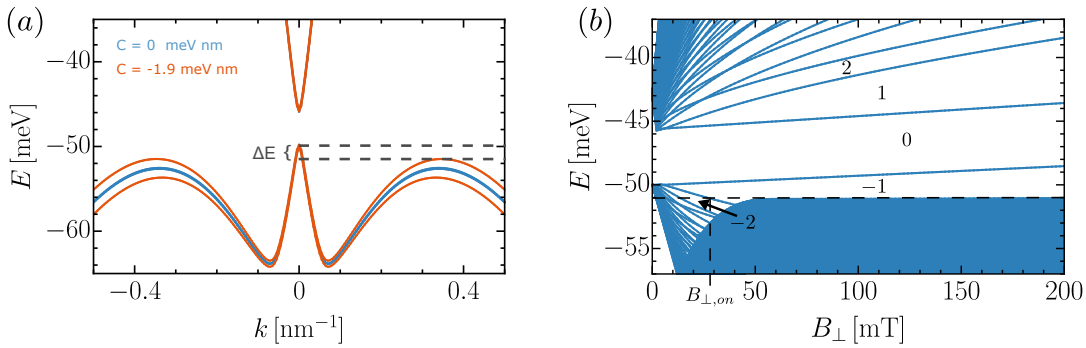

Figure 3.11.: Role of BIA for Dev 1. (a) Including BIA lifts the degeneracy already at $B_\perp = 0$, causing a decrease of ΔE. Blue and orange lines correspond to BIA parameters $C = 0$ and $-1.9\,\mathrm{meV\,nm}$, respectively [cf. Eq. (3.8)]. (b) LL fan is shown for the case with BIA, where numbers indicate QH filling factors ν. The camelback crosses LLs with small LL indices at even smaller magnetic fields. $B_{\perp,on}$ marks the critical field at which onset to $\nu = -1$ plateau can be observed. Dashed line extrapolates camelback against $B_\perp = 0$. Note that the $\nu = -2$ QH plateau is well resolved. Reprinted from Ref. [P7].

at $k_x = k_y = 0$ is hardly affected. The decrease of ΔE is also reflected by the LL fan shown in Fig. 3.11(b), i.e., the camelback maximum crosses LLs with small LL indices even at smaller magnetic fields compared to the case without BIA, shown in Fig. 3.7. Moreover, since BIA couples LL with n and $n + 2$, we find that the $\nu = -2$ plateau becomes clearly visible.

The presented results can only serve as a proof of principle that BIA explains the small discrepancy between theory and experiment. This is because we do not know exact BIA parameters for (Hg,Mn)Te quantum wells. For a better quantitative estimate, an in-depth investigation into BIA in (Hg,Mn)Te would be necessary, which substantially goes beyond the scope of this work. For the presented results in Fig. 3.11, we have assumed BIA parameters that are similar to the ones of bulk HgTe [151].

3.5.3. Indirect gap topological insulators

Further evidence in favor of the pinning mechanism can be gained by comparing theory and experiment for other device configurations. For Dev 2, which is an indirect gap TI unlike Dev 1, the experiment shows an onset to QH plateaus in the p-regime only for $B_\perp \gtrsim 4\,\mathrm{T}$.

To study pinning to the camelback also for this device configuration, we provide LL fans for Dev 2 in Fig. 3.12. Because of the indirect gap, the camelback penetrates into the QSH regime which is enclosed by the two characteristic LLs of an inverted band structure which cross at about 6.5 T. Thus, LLs with small LL indices n are covered completely by the camelback, preventing the early onset of the $\nu = -1$ plateau.

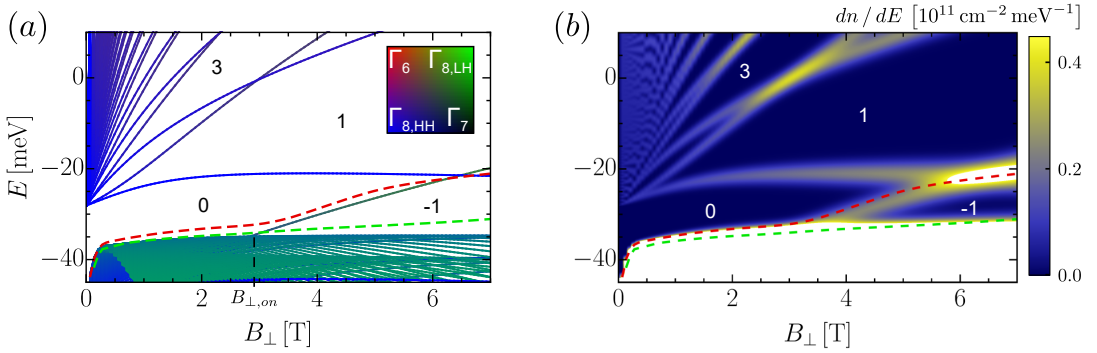

Figure 3.12.: Evolution of bulk LL energies as function of $B_\perp$ for Dev 2 (indirect TI). (a) LL fan without LL broadening. Color code indicates orbital character (see plot legend). $B_{\perp,on}$ marks the critical field at which onset to $\nu = -1$ plateau can be observed. It is instructive to compare this figure to Fig. 3.6(d). (b) Analogous figure including LL broadening. Color code indicates DOS, dn/dE. In both figures, numbers indicate QH filling factors ν. The red and green curves correspond to a chemical potential with hole densities $p = 2 \times 10^{10}\,\mathrm{cm}^{-2}$ and $2 \times 10^{11}\,\mathrm{cm}^{-2}$, respectively. For p-densities, the chemical potential remains pinned to the $\nu = 0$ QH plateaus up to large magnetic fields. Reprinted from Ref. [P7].

The numerics demonstrate that the chemical potential is instead pinned to the $\nu = 0$ plateau. From these theoretical results, an onset to the $\nu = -1$ QH plateau is expected to emerge at about 3–4 T, where the camelback separates from the QSH regime [a]. This number shows good agreement with the experimental value, highlighting once again the accuracy of the pinning model.

Since Dev 2 has an indirect gap, we can conclude that an onset to QH plateaus at ultra-low magnetic fields is a hallmark of direct gap TIs close to the direct-indirect transition line, cf. dashed line in Fig. 3.3(a). This also highlights the crucial role of Mn in tuning the band structure and in realizing the emergent QH phenomena, since the two devices have the same thickness and differ only in Mn concentration.

3.6. Emergent QH effect in QSH regime

So far, we have focused on describing the early onset of QH plateaus in the bulk p-regime. When the chemical potential is instead in the bulk gap regime (for direct gap TIs), another type of emergent QH effect at ultra-low magnetic fields ($\approx 50\,\mathrm{mT}$) with $\nu = -1$ has been observed in the experiment on (Hg,Mn)Te quantum wells (cf. Sec. 3.4.1) [P7]. In contrast to the bulk p-regime, this emergent QH effect is independent of the in-plane magnetic field and, thus, does not arise due to pinning of the chemical potential to the camelback. To analyze this regime, W. Beugeling extended the implementation of the 8×8 Kane model, described in Sec. 3.2, to account not

[a] We therefore do not show in detail the low-field regime ($B_\perp < 200\,\mathrm{mT}$) for Dev 2.

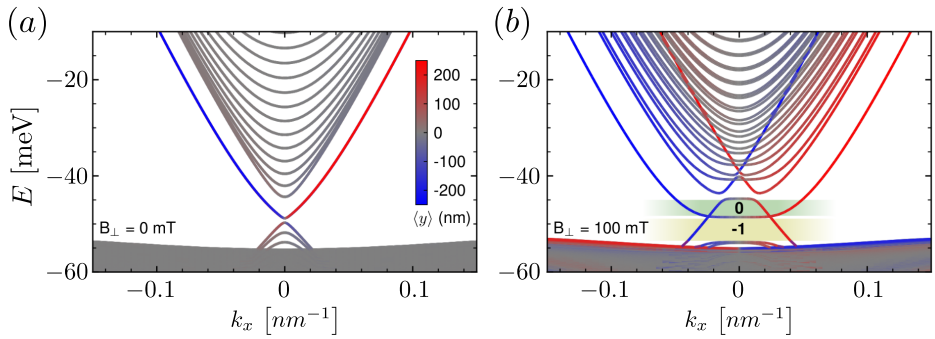

Figure 3.13.: Band structure of Dev 1 calculated for confinement in y- and z-direction for (a) $B_\perp = 0$ and (b) 100 mT. The width of the device in y-direction is $L_y = 500$ nm. Color code indicates wave function localization in the y-direction, as depicted by plot legend in (a). Numbers in (b) indicate QH filling factors ν. Computation was performed by W. Beugeling employing the *kdotpy* program. Reprinted from Ref. [P7].

only for confinement in the z-direction, but also for confinement in the y-direction. For completeness, we will here briefly summarize his main findings.

Similar to our calculations for the BHZ model in Ch. 2, imposing additionally hard wall boundary conditions in the y-direction within the 8×8 Kane model allows to study the topological edge channels. However, as the typical size of the $n \times n$ dimensional lattice matrix reaches already for samples with a width of $L_y = 500$ nm values of almost $n \approx 2 \times 10^6$, the numerical computation becomes quite heavy.

Figures 3.13(a) and (b) show the band structure of Dev 1 for $B_\perp = 0$ and 100 mT, respectively. The color code depicts the wave localization in the y-direction. At $B_\perp = 0$, where the system is in the QSH phase, it is apparent that QSH edge states traverse the bulk band gap (red and blue states; double degenerate). With increasing magnetic fields, the QSH edge states split: One of the QSH edge states moves up, while the other one moves down in energy. Figure 3.13(b) reveals that only the QSH edge states which are pushed into the conduction bands remain clearly visible, since they are protected from hybridizing with bulk bands due to a different wave function localization. In comparison, the second pair of QSH edge states which are pushed into the valence band hybridize strongly with the bulk bands and, thus, disappear. The presented results are very similar to our findings in Ch. 2, with the difference that, in the 8×8 Kane model, only the QSH edge states with spin-down character remain clearly visible. In contrast, within the BHZ model, we found that the QSH edge states of the spin-up block are protected from hybridizing with bulk bands. While the quantitative picture is therefore slightly different, the general observation described in Ch. 2 is still valid. This means topological edge channels survive in the presence of an external magnetic field, as they are protected from hybridizing with bulk bands. We believe that the discrepancy between the two models is connected to the occurrence of spurious solutions [138, 139], as mentioned in Sec. 2.6.2. Nonetheless, we are still working on understanding this

point in more detail.

Below the QSH regime in Fig. 3.13(b) (green shaded area), which is characterized by counterpropagating QSH edge channels such that $\nu = 0$, the presence of a single chiral edge channel per edge points to a $\nu = -1$ QH regime (yellow shaded area). As stated in Sec. 3.4.1, this regime is not related to the QAH effect as the magnetization is not yet sufficient to close the Dirac mass gap [cf. Eq. (2.104)]. Since this edge state is however directly connected to the QSH edge states, the emergence of this $\nu = -1$ plateau at such low magnetic fields is related to the preexistence of the QSH phase. Furthermore in Ref. [P7], it is shown that this peculiar regime is not affected by an in-plane magnetic field. The latter confirms that the yellow shaded area in Fig. 3.13(b) is related to the observed $\nu = -1$ QH plateau in the experiment on (Hg,Mn)Te quantum wells. The respective results are discussed in more detail in Ref. [P7].

3.7. Summary and Discussion

In this chapter, we have demonstrated that the experimentally observed, emergent QH effect in (Hg,Mn)Te quantum wells at ultra-low magnetic fields ($\sim$20–30 mT) in the bulk p-regime can be attributed to the camelback in direct gap TIs. The latter causes pinning of the chemical potential when the carrier density is tuned into the bulk p-regime. Moreover, we have shown that the camelback prevents the emergence of QH plateaus for indirect gap TIs, where the chemical potential remains pinned to the $\nu = 0$ plateau up to large magnetic fields (a few tesla). Further support for this pinning picture was gained by exploring the influence of an in-plane magnetic field on the camelback in direct gap TIs. Here, we found in agreement with the experiment that increasing the in-plane magnetic field reduces the onset fields at which QH plateaus can emerge in the bulk p-regime.

To the best of our knowledge, QH plateaus have never been reported to occur at such low magnetic fields. This makes a direct gap (Hg,Mn)Te quantum well an ideal candidate to realize chiral Majorana fermions. The latter have been proposed to exist in chiral topological superconductors which can be realized by proximitzing a chiral edge channel with an s-wave superconductor [157]. In comparison, in typical QAH insulators, like Cr-doped Bi-compounds, the large magnetization (on the order of a few tesla) makes it difficult to induce superconductivity. Furthermore, as the occurrence of the camelback is a byproduct of the band inversion, we expect that our findings could apply likewise to other 2D topological materials, such as WTe_2 or InAs/GaSb quantum wells.

With respect to our previous chapter, it is natural ask whether signatures of the QAH effect have been observed in (Hg,Mn)Te quantum wells. While we have focused here

on transport signatures in the bulk p-regime for small magnetic fields, for which the QAH effect does not occur, recent experiments by S. Shamim et al. seem to show signatures of counterpropagating QH and QAH edges states at larger magnetic fields. As we have explained in Ch. 2, the observation of such quasi-helical edge states would be an indication for the coexistence of QH and QAH phases in magnetic fields. Our research on this subject is however still ongoing.

4.

Manipulating surface states of 3D topological insulators

Contents

4.1. 2D to 3D crossover 135
4.2. Manipulating topological surface states 138
4.2.1. HH–LH coupling at interfaces 138
4.2.2. Gating of topological surface states 140
4.3. Summary 142

Band structure engineering gives the opportunity to access various topological phases selectively by modifying different material properties, such as the layer thickness (confinement), the strain, or the material composition. The 8×8 Kane model, whose numerical implementation was discussed in the previous chapter, allows us to study all these effects within a single model. In particular, it enables us to study the crossover from 2D to 3D by continuously increasing the quantum well thickness d_{QW}. In this respect, a particularly interesting material is HgTe, as it can be experimentally produced with a very high crystal quality [17, 28]. In the thin-film (2D) limit, HgTe exhibits the QSH phase when $d_{QW} > 6.3\,\mathrm{nm}$ [15, 17]. For larger quantum well thicknesses, a crossover emerges to the 3D regime where (unstrained) HgTe is a semimetal. To be precise, at charge neutrality, the Fermi level lies in this case at the fourfold degenerate touching point between the four Γ_8-bands (see Fig. 1.6). The latter is protected by the lattice symmetries of the zincblende structure [19].

To drive HgTe into the 3D TI phase [19, 28], this fourfold degeneracy must be lifted by imposing uniaxial (tensile) strain to the crystal lattice, which opens a bulk gap at the Γ-point [148, 158]. The 3D TI phase is characterized by metallic 2D topological surface states (TSS), which are localized at the interfaces to topologically trivial materials (this includes vacuum) [159]. Although it seems to be well-established that in HgTe the Dirac points of the TSS are buried in the HH-like valence band, various values for their precise energetic position have been reported in the literature [28, 35, 160–162].

In this chapter, we investigate the 2D to 3D crossover in HgTe quantum wells and analyze various properties of their TSS. We show that the 2D to 3D crossover occurs continuously without exhibiting any oscillations between topologically trivial and nontrivial regimes which are predicted to occur in Bi-based TIs [163, 164]. In the 3D limit, we demonstrate that the positions of the Dirac points can be manipulated by including an additional surface term at the interface between the quantum well and the barrier layers. The latter arises due to a lowering of the crystal symmetry at the interface [165]. By adjusting the value of this interface term, we demonstrate that the Dirac points can be shifted closer to the valence band edge such that their energetic position can be matched with ab-initio calculations [35, 160, 161] and angle-resolved photoemission spectroscopy (ARPES) measurements [28, 166]. Furthermore, in the spirit of Ref. [P2], we make use of effective Hartree potentials to account for electrostatic charging of the TSS due to an externally applied gate voltage. By means of these effective Hartree potentials, we show that the Dirac points can be shifted into the bulk band gap, so that it becomes feasible to probe also the hole-part of the 2D Dirac cones. The latter is usually not easily accessible due to the buried Dirac points of HgTe. Finally, we determine the cyclotron frequency of surface electrons, and reveal a strong electron-hole asymmetry in the effective masses of the TSS. The latter may explain the observed large electron-hole asymmetry in the experiments by Jost et al.

which is observed in the thermopower between surface electrons and holes [P4].

This chapter is structured as follows: In Sec. 4.1, we analyze the crossover from 2D to 3D in HgTe quantum wells. In Sec. 4.2, we discuss various ways to manipulate the position of the Dirac points and determine the effective masses of surface electrons and holes. Based on these calculations, we determine the cyclotron frequency of surface electrons and compare them with experimental measurements on strained HgTe. In Sec. 4.3, we summarize our findings.

The results in Sec. 4.2 have been published in Refs. [P4] and [P3] [a], which are copyrighted by the PNAS and Nature Publishing Group, respectively. The following chapter focuses on the band structure calculations which I have performed in order to understand some of the experimental signatures. This chapter contains small excerpts of these manuscripts.

4.1. 2D to 3D crossover

So far, in Ch. 3, we have focused on 2D materials for which quantum confinement causes a large level spacing between adjacent subbands. To study the 2D to 3D crossover, we have computed the band structure for a large number of quantum well devices with quantum well thicknesses ranging from $d_{QW} = 4$ to 30 nm (step size: $\Delta d_{QW} = 0.1$ nm) using the 8×8 Kane model (for the numerical implementation, see Secs. 3.1 and 3.2). In the following, we focus in particular on HgTe/$Hg_{0.7}Cd_{0.3}$Te quantum wells with a $Cd_{0.96}Zn_{0.04}$Te substrate. The latter introduces a small strain in the crystal structure of HgTe which removes the fourfold degeneracy of the Γ_8 bands at Γ [b]. For this setup, we show in Fig. 4.1(b) the evolution of the band edge energies of the quantum well subbands, where the color code indicates the orbital character. This figure is similar to Fig. 1.7 with the difference that, in order to investigate the crossover to the 3D regime, we consider here quantum wells with a well thickness of up to 30 nm.

Let us start the discussion in the 2D regime. As we have pointed out previously, HgTe enters the 2D QSH regime after the crossing of the E1 and H1 subbands, i.e., for $d_{QW} > d_c = 6.3$ nm [15, 17]. For clarity, we have highlighted the QSH regime in Fig. 4.1(b) by a gray shading and indicated the evolution of the charge neutrality point by a dashed line. Since with a further increase of d_{QW} no other quantum well subbands cross the Fermi level [dashed line in Fig. 4.1(b)], the system remains in the QSH phase as long as the bulk gap between the H1 and H2 subbands remains open. As the bulk gap decreases with increasing d_{QW}, the QSH phase is destroyed for $d_{QW} \gtrsim 25$ nm.

[a] I am a co-author of both publications. I provided band structure calculations and helped in analyzing some of the experimental results.

[b] The lattice mismatch between HgTe and $Cd_{0.96}Zn_{0.04}$Te amounts to $\epsilon_S \approx 0.0007$ [see Eq. (3.9) and App. A] causing the opening of a bulk gap of $\Delta E \approx 5$ meV at Γ [cf. Eqs. (3.3) and (3.10)].

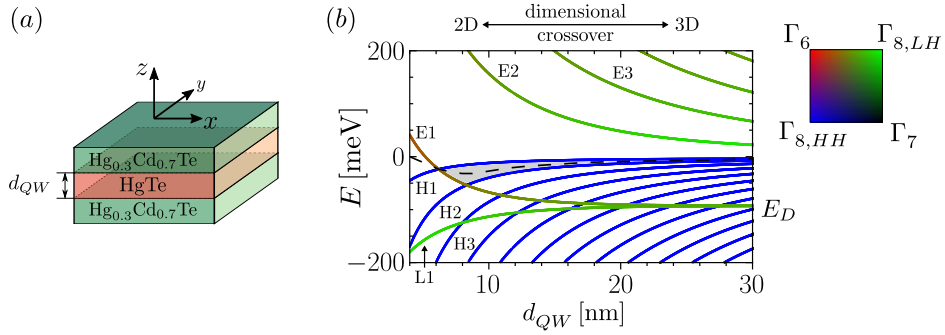

Figure 4.1.: 2D to 3D crossover as function of quantum well thickness d_{QW}. (a) Schematic layer stack of $HgTe/Hg_{0.3}Cd_{0.7}Te$ quantum well with well thickness d_{QW}. (b) Evolution of band edge energies of quantum well subbands as function of d_{QW}. QSH regime is marked by a grading shading. Dashed line indicates evolution of chemical potential at charge neutrality. E_D marks the Dirac points which are buried deep in the valence band. Color code indicates the orbital character as depicted in the plot legend.

Figure 4.1 in particular demonstrates that the 2D to 3D crossover in HgTe quantum wells occurs continuously without exhibiting oscillations between topologically trivial and nontrivial regimes, which are predicted for Bi-based TIs [163, 164]. The latter would require multiple crossings between the E1 and H1 subbands.

Another important observation in Fig. 4.1(b) is that the E1 and L1 subbands behave differently compared to all other E($n > 1$) and L($n > 1$) subbands in the large system limit. The E($n > 1$) subbands, which constitute the LH-like conduction band, converge against $E = E_v + U_\epsilon - V_\epsilon \approx 2.5\,\text{meV}$. The L($n > 1$) subbands, which constitute the S-like valence band, converge against $E = E_c + T_\epsilon \approx -305\,\text{meV}$ (out of plot range). Here, the conduction band edge energy E_c and the valence band edge energy E_v are defined below Eq. (3.3), and the strain related parameters T_ϵ, U_ϵ, and V_ϵ are defined in Eq. (3.10) [see also App. A]. In comparison, the E1 and L1 subbands converge against an energy of $E_D \approx -95\,\text{meV}$ for large d_{QW}. To understand the exceptional behavior of these subbands, we can study their wave function localization in the z-direction. In this respect, we find that their wave functions are strongly localized at the interfaces between HgTe and $Hg_{0.7}Cd_{0.3}Te$ (decay length $\approx 3\,\text{nm}$). As a result, we can identify the E1 and L1 states as TSS which form due to the band inversion of the Γ_6 and Γ_8 bands in HgTe [cf. Fig. 4.2(b); note however that in this figure a CdTe substrate was used]. The increase of the gap between the E1 and L1 subbands with decreasing d_{QW} can be therefore understood as a consequence of hybridization between the top and bottom TSS [a]. Thus, the energy E_D marks the Dirac points which are in the present case buried deep in the HH-like valence band. It is worth noting that the formation of these surface states is independent on whether HgTe is a bulk insulator (strained) or a semimetal (unstrained), since they originate from the band inversion and exist

[a] For a discussion of hybridization between TSS in the thin film limit see Ref. [12].

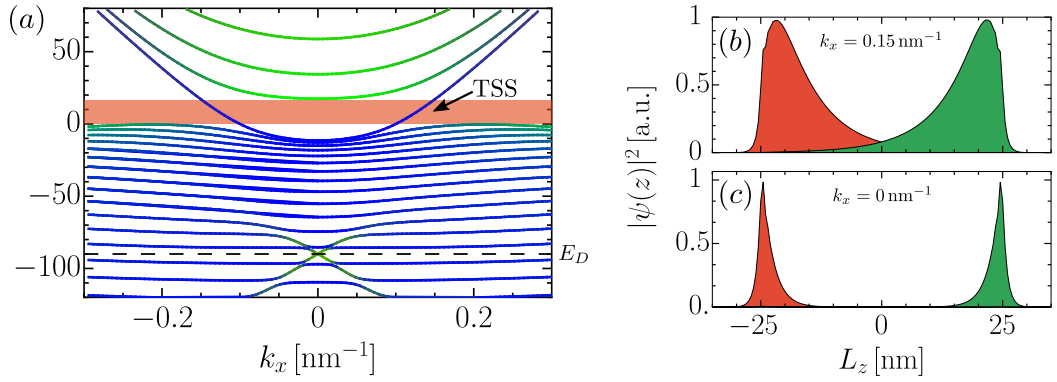

Figure 4.2.: (a) Band structure of 3D TI ($HgTe/Hg_{0.7}Cd_{0.3}Te$ quantum well with a CdTe substrate) for a quantum well thickness of $d_{QW} = 50\,\mathrm{nm}$. The color code depicts the orbital character [legend, see Fig. 4.1(b)]. Topological surface states (TSS) cross the bulk band gap which is indicated by the red shaded area. The Dirac points E_D are highlighted by a dashed line. Probability distribution of top and bottom TSS at (b) $k_x = 0$ and $E = E_D$, as well as (c) $k_x = 0.15\,\mathrm{nm}^{-1}$ and $E = 17\,\mathrm{meV}$.

therefore independent of the strain. Signatures of the TSS have been therefore also observed in the Dirac semimetal phase (requires compressive strain), even though the system is not a 3D TI [35] [a].

Band structure of 3D TI: For completeness, we show in Fig. 4.2(a) the band structure of a $d_{QW} = 50\,\mathrm{nm}$ thick HgTe quantum well, where we chose CdTe as the substrate material. Due to the larger lattice mismatch between HgTe and CdTe compared to a $Cd_{0.96}Zn_{0.04}Te$ substrate (i.e., $\epsilon_S = 0.003$), this amounts to a strain induced band gap of $E_g \approx 22\,\mathrm{meV}$ [b]. For clarity, we highlighted the bulk gap by a red shading and marked the position of the Dirac points E_D by a dashed line. Although we cannot continuously trace the evolution of the TSS in the valence band due to hybridization with the HH-like subbands (see also Ref. [162]), we see that the TSS reappear in the bulk band gap, as required by topology. The wave functions of the TSS at the Dirac points and in the bulk gap for finite k_x are shown in Fig. 4.2(b) and (c), respectively. Note that the decay length of the TSS in the bulk gap at finite k_x is much larger than at the Γ-point due to the strong hybridization with the HH subbands (decay length $\approx$ 15–20 nm). In the experiment, signatures of the two decoupled top and bottom TSS are therefore only observed for quantum well devices with $d_{QW} > 40\,\mathrm{nm}$ [28, 80].

[a] The difference between the TSS in the 3D TI phase and the 'TSS' in the Dirac semimetal phase is that only in the former case TSS can be probed without any additional residual bulk conductance.
[b] The gap in Fig. 4.2(a) is slightly larger due to additional contributions which result from the quantum confinement at a well thickness of $d_{QW} = 50\,\mathrm{nm}$.

4.2. Manipulating topological surface states

Since TSS are strongly localized at the interfaces between HgTe and $Hg_{0.7}Cd_{0.3}Te$, the position of the Dirac points E_D is strongly affected by the local environment at their interfaces. For instance, if we replace the barrier materials (here, $Hg_{0.7}Cd_{0.3}Te$) by vacuum, it is found that the energy of the Dirac points decreases by more than 150 meV [162]. However, although our presented band structure calculations take the barriers explicitly into account, we find that the Dirac points E_D are located much deeper in energy as suggested by ARPES measurements [28, 166] and ab-initio calculations [35, 160, 161]. We will show in this section that this discrepancy may be explained by a reduced point group symmetry at the interfaces between HgTe and (Hg,Cd)Te [165], which we have yet to account for in our model.

In Sec. 4.2.1, we incorporate an additional surface term in our Kane model that results from the reduced point group symmetry at the interface, and study its affect on the position of the Dirac points. For the presented system, we determine the cyclotron frequency of the surface electrons and compare our findings with experimental measurements. In Sec. 4.2.2, we show how the Dirac points can be further modified by applying an external gate voltage due to charging of the TSS. Note that the presented results are based on an earlier version of our $\mathbf{k}\cdot\mathbf{p}$ code, in which we have neglected the contributions of the Γ_7 bands (this means we work with the 6×6 Kane model). In the 3D limit, this approximation is justified as the orbital contribution of the Γ_7 bands in the vicinity of the bulk band gap is typically less than 5% [150].

4.2.1. HH–LH coupling at interfaces

Bulk HgTe and CdTe crystallize both in the zincblende structure and are therefore described by the point group T_D. The latter consists of 24 group elements. However, if two different zincblende semiconductors, like HgTe and $Hg_{0.7}Cd_{0.3}Te$, are brought into contact, Ivchenko et al. [165] showed that the lattice symmetry reduces at their interface to the point group C_{2v} [a]. In comparison to the point group T_d, C_{2v} consists only of four group elements: the identity, a twofold rotational symmetry C_2, and two-mirror planes (110) and $(1\bar{1}0)$. Since a Hamiltonian which describes this heterostructure must be invariant under all symmetry operations of the point group, the symmetry reduction at the interface gives rise to an additional (local) term in the Kane Hamiltonian (we focus on the valence band part of the Kane Hamiltonian, i.e., Γ_8 [b]) [165] :

$$H_{sur} = \sum_{j=1}^{2} C_{\Gamma_8}\delta(z-z_j)\left\{J_x, J_y\right\} , \tag{4.1}$$

[a] This statement holds provided that HgTe and $Hg_{0.7}Cd_{0.3}Te$ share a common Te-atom at the interface.
[b] The symmetry reduction allows also to couple S- and HH-bands, but this hybridization does not affect the energetic position of the Dirac points strongly.

where C_{Γ_8} is a material specific parameter, δ is the Dirac delta function, as well as z_1 and z_2 denote the positions of the top and bottom interfaces between the barrier and well materials, respectively, i.e., $\pm d_{QW}/2$. J_x and J_y are the total angular momentum matrices of spin 3/2, which are given by

$$J_x = \frac{1}{2}\begin{pmatrix} 0 & \sqrt{3} & 0 & 0 \\ \sqrt{3} & 0 & 2 & 0 \\ 0 & 2 & 0 & \sqrt{3} \\ 0 & 0 & \sqrt{3} & 0 \end{pmatrix} \quad , \quad J_y = \frac{\mathrm{i}}{2}\begin{pmatrix} 0 & -\sqrt{3} & 0 & 0 \\ \sqrt{3} & 0 & -2 & 0 \\ 0 & 2 & 0 & -\sqrt{3} \\ 0 & 0 & \sqrt{3} & 0 \end{pmatrix} . \tag{4.2}$$

Note that Eq. (4.1) couples HH and LH bands even if $k_x = k_y = 0$.

We can easily show that this Hamiltonian is allowed by symmetry by determining the matrix representations of all four group elements of C_{2v}, which should commute with H_{sur}. As a mirror symmetry can be constructed by a rotation followed by an inversion, we find for the Γ_8 representation that

$$\begin{aligned} E &= I_4 \,, & C_2 &= \mathrm{e}^{-\mathrm{i}J_z\pi} \,, \\ R_1 &= -\mathrm{e}^{-\mathrm{i}J_z\frac{\pi}{2}}\mathrm{e}^{-\mathrm{i}J_x\pi} \,, & R_2 &= -\mathrm{e}^{-\mathrm{i}J_z\frac{\pi}{2}}\mathrm{e}^{-\mathrm{i}J_y\pi} \,, \end{aligned} \tag{4.3}$$

where J_z is a total angular momentum matrix of spin 3/2

$$J_z = \frac{1}{2}\,\mathrm{Diag}\begin{pmatrix} 3 & 1 & -1 & -3 \end{pmatrix} . \tag{4.4}$$

Here, E, C_2, R_1, and R_2 denote the identity (I_4 is the four dimensional identity matrix), the twofold rotational symmetry, and the two mirror symmetries, respectively. The minus sign in R_1 and R_2 originates from spatial inversion, cf. Sec. 3.1. All four unitary matrices commute with H_{sur}, which verifies that the latter is allowed by symmetry.

We can now adjust the value of C_{Γ_8} in Eq. (4.1) to study its effect on the band structure. In that regard, Fig. 4.3 shows that we can shift the Dirac points E_D much closer to the valence band edge [cf. to Fig. 4.2(a)], so that the position of the Dirac points E_D becomes comparable to the one of ab-initio calculations [35, 160, 161] and ARPES measurements [28, 166].

Cyclotron frequency: Analyzing the cyclotron frequency provides an inside into the band structure of semiconductors. Assuming that the chemical potential μ is located in the bulk band gap, as indicated by the green line in Fig. 4.3(a), we can determine the cyclotron frequency Ω_c of the 2D surface electrons by the following relation [68]:

$$\Omega_c / B_\perp = \frac{2\pi e}{\hbar^2}\frac{\partial E(k_x)}{\partial A} \,, \tag{4.5}$$

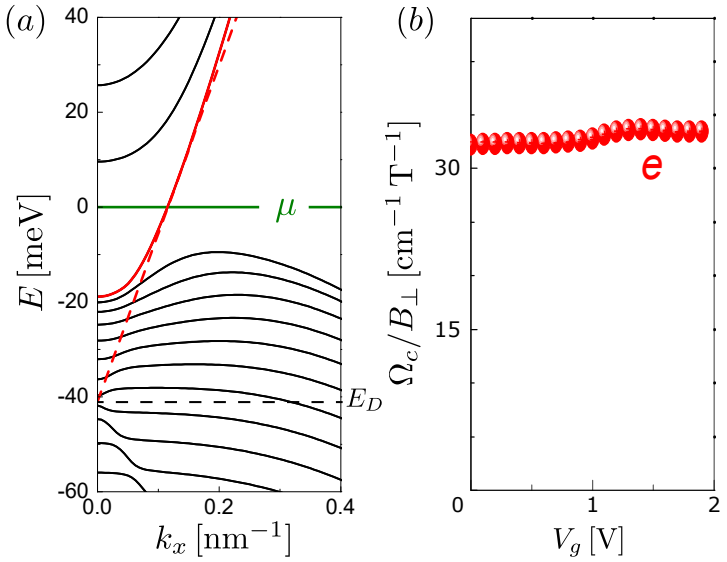

Figure 4.3.: (a) Band structure of 58 nm thick HgTe/$Hg_{0.3}Cd_{0.7}$Te 3D TI is calculated using 6×6 Kane model (CdTe substrate). The HH-LH coupling, given by Eq. (4.1), is adjusted to $C_{\Gamma_8} = -1.7\,\text{eV}$. TSS are highlighted by red (double degenerate); dashed line sketches evolution of TSS neglecting hybridization to heavy-hole bands. Dirac points lie at $E_D \approx -40\,\text{meV}$ (dashed line). Chemical potential μ is indicated by green line. (b) Cyclotron frequency $\Omega_c/B_\perp$ as function of external gate voltage (experimental data). From Ref. [P3]. Reprinted with permission from the Nature Publishing Group.

where $B_\perp$ is the external out-of-plane magnetic field, $E(k_x)$ denotes the energy dispersion, and A is the area that is enclosed by the wave vector k_x. We calculate for the TSS a cyclotron frequency of $\Omega_c/B_\perp \approx 35\,\text{cm}^{-1}/\,\text{T}$. The latter agrees extremely well with the experimentally determined value for surface electrons, shown in Fig. 4.3(b). Note that the latter is almost independent on the applied gate voltage V_g as long as the Dirac points remain buried in the valence band.

4.2.2. Gating of topological surface states

Transport measurements on the 3D TI HgTe have unambiguously demonstrated surface dominated transport for a large range of gate voltages [28, P2, P4]. The latter can be adjusted to modify the carrier densities on the top and bottom TSS. In particular, it has been shown in Ref. [P4] that tuning the gate voltage allows to alter the Dirac points E_D such that also the surface holes can be probed in magnetotransport experiments, i.e., the Dirac point can be shifted into the conduction band (or at least into the bulk band gap).

To model the effect of the external gate voltage in our 6×6 Kane model, we employ effective Hartree potentials that are constructed in the spirit of the Dirac screening

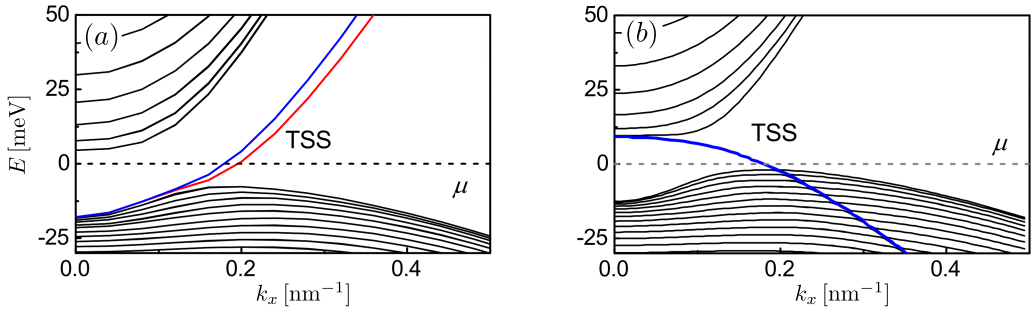

Figure 4.4.: Band structure of 104 nm thick strained HgTe quantum well sandwiched in between $Hg_{0.3}Cd_{0.7}Te$ barrier layers based on 6×6 Kane model for two different carrier densities (CdTe substrate). Top (bottom) TSS are highlighted in red (blue). Chemical potential μ is indicated by dashed line. (a) Dirac point is buried in the valence band. (b) Dirac point is buried in the conduction band. From Ref. [P4]. Reprinted with permission from the PNAS.

model, which has been proposed in Ref. [162, P2] [a]. This phenomenological approach is motivated by the disagreement between self-consistent Hartree calculations [P1] and the experimentally observed surface dominated QHE for a large range of gate voltages [P2]. Effective Hartree potentials exhibit peaks at the interfaces, whereas they decay quickly into the bulk [cf. Fig. 4(d) in Ref. [P2]]. For that reason, they allow us to primarily dope the Dirac surface states from the n- to the p-regime, while the structure of the bulk bands remains only weakly affected.

In Fig. 4.4, we show the band structure for two effective Hartree potentials, where the TSS are highlighted by color. As in Sec. 4.2.1, we have here likewise included the local HH-LH coupling term in the Kane model which stems from the reduced point group symmetry at the interfaces, Eq. (4.1) [b]. In Fig. 4.4(a), the effective Hartree potential is chosen such that the Dirac point is buried in the valence bands. The carrier density on the top and bottom TSS is given by $n_1 = 3.33 \times 10^{11}\,\mathrm{cm}^{-2}$ and $n_2 = 2.65 \times 10^{11}\,\mathrm{cm}^{-2}$, respectively, which corresponds to a gate voltage of $V_g = +1\,\mathrm{V}$ in the experiments by Jost et al. [P4]. In comparison, in Fig. 4.4(b), the effective Hartree potential is chosen such that the Dirac point is buried in the conduction band. The hole carrier density on the top and bottom TSS is given by $p_1 = p_2 = 2.58 \times 10^{11}\,\mathrm{cm}^{-2}$, corresponding to a gate voltage of $V_g = -3\,\mathrm{V}$. Analyzing the curvature of the TSS in the bulk band gap, we find that their dispersion relations deviate strongly from an ordinary linear behavior which is typically observed in Bi-based 3D TIs [12, 167]. We attribute these deviations to a strong coupling between the TSS and the HH subbands. From the dispersion relations in Fig. 4.4(a) and (b), we obtain an effective mass of $m_e \approx 0.02\,m_0$ for surface electrons

[a] The effective Hartree potentials are constructed assuming different dielectric constants for the bulk and the surfaces of the 3D TI.

[b] Note that without this interface term, additional massive Volkov-Pankratov states [35], that arise from the Hartree potential, would cross the bulk band gap before the Dirac points E_D can reach this regime.

and $m_h \approx 0.11\, m_0$ for surface holes, where m_0 is the free electron mass. Thus, we find that the dispersion relation of the 2D Dirac cone is strongly asymmetric for electrons and holes due to hybridization of the TSS with the HH subbands. This observation was used in Ref. [P4] to explain the salient asymmetry in the measured thermopower S_{xx}, also known as the Seebeck effect (the voltage difference that arises when a thermal gradient is applied along the sample).

4.3. Summary

Based on the 8×8 Kane model, whose numerical implementation was discussed in Ch. 3, we have analyzed in this chapter for HgTe the transition from a 2D QSH insulator to a 3D TI by changing the quantum well thickness d_{QW}. In addition, we discussed two possible ways to manipulate the position of the Dirac points E_D. We demonstrated that the 2D to 3D crossover occurs smoothly without exhibiting oscillations between topologically trivial and nontrivial regimes which are predicted for Bi-based TIs [163, 164]. We showed that an additional surface term in the Kane model, which couples HH and LH bands due to a reduced point group symmetry at the interface between the well (HgTe) and the barrier material ($Hg_{0.3}Cd_{0.7}Te$), modifies the position of the Dirac points. Intriguingly, it is thus possible to adjust the position of the Dirac points such that they become comparable with the one of ab-initio calculations [35, 160, 161] and ARPES measurements [28, 166]. Considering additional surface potentials (effective Hartree potentials) that arise from the electrostatic charging of the TSS (gating), we furthermore showed that the Dirac points can be shifted into the conduction band. This allowed us to reveal a strong electron-hole asymmetry in the dispersion relation between surface electrons and holes. The latter are usually not easily accessible due to the buried Dirac point in HgTe [28].

In collaboration with Dziom et al. [P3] and Jost et al. [P4], we have compared these theoretical findings to actual experiments on HgTe. In this respect, we have found an excellent agreement for the cyclotron frequency of surface electrons and attributed the observed asymmetry in the thermopower between surface electrons and holes in the experiment to the asymmetry in their effective masses.

5.

Conclusion and Outlook

The last 15 years have been characterized by tremendous progress in predicting and realizing novel topological phases of matter in solid state systems. While it was common belief that topology is something rather exotic, we now know that a quarter of all materials in nature are topological [18]. This rapid progress has heavily profited from topological classification schemes, which classify topological states of matter based on discrete symmetries [11]. Furthermore, low-energy models, like the Bernevig-Hughes-Zhang (BHZ) model, have proven to be a powerful tool to investigate topological properties analytically. This thesis contributes to the vast field of topology by exploring the fate of topological states of matter in the presence of external magnetic fields and investigating their relation to quantum anomalies. In addition, we developed a numerical implementation of the 8×8 Kane model to study the landscape of (Hg,Mn)Te quantum wells by varying the quantum well thickness, the material composition, as well as the strain. By avoiding the use of low-energy models, we were able to reveal some unexpected signatures of topological materials in magnetic fields which are connected to their characteristic band dispersion at large momenta.

In Ch. 2, we investigated the effect of an external out-of-plane magnetic field on the quantum anomalous Hall (QAH) phase. Similar to the quantum Hall (QH) phase which can be induced by a magnetic field, the QAH phase is described by a $\mathbb{Z}$ topological invariant. But in contrast to the QH phase, the QAH phase derives its nontrivial topology from an inverted band structure without Landau levels (LLs) and is as such a condensed matter analog of the parity anomaly. Although the topological classification suggests that these two topological states of matter cannot be distinguished, as they are both described by a $\mathbb{Z}$ topological invariant, we showed that QH and QAH phases can coexist and can be disentangled by virtue of the parity anomaly. In this respect, we demonstrated that the QAH topology remains encoded in a peculiar topological quantity, the spectral asymmetry η. Deriving the effective action of a QAH insulator, we demonstrated that while each QH edge state is related to a single LL, the QAH edge

state is encoded in the asymmetry of the entire LL spectrum (i.e., η). The latter acts effectively as if there is an additional 'LL' in magnetic fields (mathematically speaking, the QAH edge state is related to a peculiar Chern-Simons term in the effective action). As a result of the survival of the QAH phase, we revealed that counterpropagating QH and QAH edge states can emerge in QAH insulators. We analyzed the behavior of these quasi-helical edge states [a] and found some exotic magnetotransport signatures: First, we demonstrated a peculiar type of charge pumping from the QAH edge states into all valence band LLs with increasing magnetic field. Second, we studied a toy model to show that, when quasi-helical edge states are coupled to a small residual bulk conductivity, which can for example arise due to a large charge puddle density, exotic values can emerge for the longitudinal and transverse resistance. The latter is possible due to the different band character and the different localization length of the two counterpropagating edge states. We closed this chapter by exploring in more detail signatures of the parity anomaly (spectral asymmetry) in para- and ferromagnetic topological insulators (TIs). For ferromagnetic TIs, we showed that the key signature of the QAH phase in magnetic fields (at constant chemical potential) is a hysteresis-like behavior of the Hall conductivity. While this feature has been already confirmed experimentally [24], we showed that it is limited to a regime where the magnetization of the ferromagnet dominates over the external (orbital) field. When the orbital part of the magnetic field starts to dominate, we predicted a sudden drop of σ_{xy} to zero. The experimental observation of this prediction is so far outstanding. In the case of paramagnetic TIs, we demonstrated that the Hall conductivity follows a reentrant like behavior. This means a transition with increasing magnetic fields from 0 to $\pm e^2/h$ back to 0. We showed that both signatures are encoded in the spectral asymmetry and are as such a representative of the parity anomaly.

In the presented calculations, we have assumed so far that the temperature $T = 0\,\mathrm{K}$. In a future study, it would be thus very instructive to extend the spectral asymmetry calculation to finite temperatures. My collaborator C. Tutschku is already proceeding in that direction. Another assumption, that we have made to keep the derivation of the spectral asymmetry analytically manageable, is that we have neglected Rashba spin-orbit interaction [168] and bulk inversion asymmetry terms [17]. As both terms cannot cause a topological transition [b], I do not expect that these terms should contribute to the spectral asymmetry. Nonetheless, a rigorous proof of this statement is still outstanding. Regarding the QAH edge state, it is interesting to study the effect of the boundary conditions in more detail. So far, we have assumed hard-wall boundary conditions in one of the spatial directions. But recently, it was argued that these boundary conditions can result in spurious solutions which can affect the energetic

[a] By quasi-helical, we mean that the edge states are counterpropagating but not protected by time-reversal symmetry.

[b] They do not break time-reversal symmetry.

position of the QAH edge states [138, 139]. In this regard, it will be interesting in a future study to play with the boundary conditions and investigate their influence on the coexistence of QH and QAH edge states.

Motivated by the experimental observation of emergent QH plateaus in (Hg,Mn)Te quantum wells at magnetic fields as low as 20–30 mT, we developed in Ch. 3 a numerical implementation of the 8×8 Kane model. The latter allowed us to investigate (Hg,Mn)Te/(Hg,Cd)Te quantum wells for a large range of quantum well thicknesses and Mn-concentrations. The advantage of using the 8×8 Kane model instead of the BHZ model is that it captures the additional maxima in the valence band dispersion at large momenta (the 'camelback'). These maxima arise from an inverted band structure and are as such a byproduct of the nontrivial band structure topology. We demonstrated that these maxima, which represent a Van-Hove-like-singularity, pin the chemical potential and lead to rich LL structures in magnetic fields. In general, it is found that the landscape of topologically nontrivial TIs can be further subdivided into direct and indirect gap TIs. In direct gap TIs, pinning of the chemical potential to the camelback can cause an onset to QH plateaus at exceptionally small magnetic fields (tens of mT). In comparison, in indirect gap TIs, the camelback prevents the observation of QH plateaus up to large magnetic fields (a few tesla). Furthermore, we showed that the paramagnetic exchange interaction, resulting from the localized d-electrons of the Mn atoms, offer the possibility to further reduce the onset fields by applying an in-plane magnetic field. All in all, our theoretical results allowed us to attribute the experimentally observed onset of QH plateaus at exceptionally small magnetic fields to the camelback.

An onset of QH plateaus in the mT-regime clearly opens the door for a wide range of possible applications: For instance, it has been proposed that a chiral edge channel proximitized with an s-wave superconductor is a possible setup to realize chiral Majorana fermions [157]. Since a small magnetization is crucial to induce superconductivity, an onset in the mT-regime is clearly desired. In contrast, in typical QAH insulators like Cr doped Bi-compounds, the large magnetization (a few tesla) poses a challenge for superconductivity. Another direction for future works involves an extension of our analysis to other 2D TIs, such as InAs/GaSb [75] quantum wells or WTe_2 [76]. Finally, let us comment on the relation between the results of Ch. 2 and 3. Clearly, (Hg,Mn)Te quantum wells are a prototype paramagnetic TI for which we expect to find signatures of quasi-helical QH and QAH edge states. The experiments, which have been presented in Ch. 3, focus however on carrier densities in the bulk p-regime and at ultra-low magnetic fields, for which the QAH effect cannot be induced. More recent experiments (in the group of Laurens W. Molenkamp) on (Hg,Mn)Te quantum wells at larger magnetic fields seem to confirm our prediction of quasi-helical edge transport. However, as the research on this subject is currently ongoing, it might be too early to draw any final

conclusions.

In Ch. 4, we extended our work from Ch. 3 studying the 2D to 3D crossover in HgTe quantum wells by increasing the quantum well thickness. We found that the crossover occurs thereby without exhibiting oscillations between topologically trivial and non-trivial regimes, which are predicted to occur in Bi-based TIs [163]. In the large system limit, we showed that the Dirac point is buried deep in the heavy hole like valence band and is formed by the E1 and L1 subbands. By considering additional terms in the Kane Hamiltonian that result from a reduced point group symmetry at the interface between well and barrier material, we showed that the Dirac point can be shifted closer to the valence band edge in agreement with ab-initio calculations [35, 160, 161] and ARPES measurements [28, 166]. In addition, we modeled the electrostatic charging of the topological surface states by effective Hartree potentials to shift the Dirac point from the valence into the conduction band. The cyclotron frequency was determined for the surface electrons, which showed an excellent agreement with the experiment. The latter confirms the accuracy of our $k \cdot p$ approach.

In the presented model, we tried to estimate the strength of the additional surface terms by comparing our results from the Kane model with ab-initio calculations and ARPES measurements. At the present stage, it is however not clear whether other terms exist in the Kane model which would additionally modify the position of the Dirac point. In the future, it would be interesting to perform an exhaustive symmetry analysis to identify all terms that manipulate the position of the Dirac point and perform detailed calculations of the electrostatics in these materials.

Appendices

A.

Kane parameters for various compound semiconductors

The bulk band structure parameters of HgTe, CdTe, and MnTe, employed in Ch. 3, are listed in Tab. A.1. Since MnTe does not crystallize in the zincblende structure [91], parameters for MnTe are obtained by extrapolating data for $Hg_{1-x}Mn_xTe$, which are known for $x < 0.2$ [146], against $x = 1$. This approximation is justified since we consider only cases for which $x \leq 0.04$. According to Ref. [91, 146], incorporating small fractions of Mn-atoms alters mainly the band gap E_g and the lattice constant a of HgTe, while all other parameters remain almost unaffected [b]. We therefore take the same parameters for MnTe as for HgTe, except for a and E_g, cf. Tab. A.1.

	a [nm]	E_g [eV]	Δ [eV]	P [eVnm]	F	γ_1	γ_2	γ_3	κ
HgTe	0.6462	−0.303	1.08	0.846	0	4.1	0.5	1.3	−0.4
CdTe	0.6482	1.606	0.91	0.846	−0.09	1.47	−0.28	0.03	−1.31
MnTe	0.6349	4.423	1.08	0.846	0	4.1	0.5	1.3	−0.4

Table A.1.: List of bulk band structure parameters [Kane parameters, cf. Eq. (3.3)] for various compound semiconductors. Parameters for HgTe and CdTe are taken from Ref. [150], parameters for MnTe are adapted from Refs. [91, 146].

A.1. Kane parameters for (Hg,Cd)Te

Let us first focus on the compound semiconductor $Hg_{1-x}Cd_xTe$, for which x can be continuously tuned from $x = 0$ to 1, since the materials crystallize in the zincblende structure for all x. The discussion follows along the lines of Ref. [150]. The valence band offset (see Fig. 1.7) between bulk HgTe and bulk CdTe is given by $E_{vo} =$

[b] W. Beugeling performed the data interpolation.

$E_v(\mathrm{HgTe}) - E_v(CdTe) = 0.57\,\mathrm{eV}$ [169]. We assume that the valence band edge energy E_v of $\mathrm{Hg}_{1-x}\mathrm{Cd}_x\mathrm{Te}$ interpolates linearly with x

$$E_v(x) = -E_{vo}\,x\,, \tag{A.1}$$

i.e., we fix the energy reference with respect to $E_v(0) = E_v(HgTe) \equiv 0\,\mathrm{meV}$. The band gap evolves according to [170]

$$E_g(x) = E_g^{\mathrm{HgTe}}\,(1-x) + E_g^{\mathrm{CdTe}}\,x - 0.132x(1-x)\,\mathrm{eV}\,, \tag{A.2}$$

where E_g^{HgTe} and E_g^{CdTe} denote the bulk band gap of HgTe and CdTe, respectively (see Tab. A.1). For the remaining Kane parameters, except for the lattice constant, we assume that they linearly interpolate with the Cd-concentration x. The lattice constant of $\mathrm{Hg}_{1-x}\mathrm{Cd}_x\mathrm{Te}$ is modeled according to Ref. [171]:

$$a_{\mathrm{HgCdTe}}(x) = a_{\mathrm{HgTe}} + \left(0.0009\,x + 0.0017\,x^2 - 0.0006\,x^3\right)\,\mathrm{nm}\,, \tag{A.3}$$

where a_{HgTe} and a_{CdTe} is the equilibrium lattice constant of bulk HgTe and CdTe, respectively (see Tab. A.1).

A.2. Kane parameters for (Hg,Mn)Te

For small fractions of Mn, $\mathrm{Hg}_{1-x}\mathrm{Mn}_x\mathrm{Te}$ crystallizes in the zincblende structure [172]. We assume that the bulk band gap interpolates linearly with the Mn-concentration:

$$E_g^{HgMnTe} = E_g^{\mathrm{HgTe}} + \left(E_g^{\mathrm{MnTe}} - E_g^{\mathrm{HgTe}}\right)\,x\,. \tag{A.4}$$

For the valence band edge energy E_v and the conduction band edge energy E_c, we model the influence of Mn-atoms as:

$$E_v^{HgMnTe}(x) = -\alpha E_{vo}\,x\,, \tag{A.5}$$

$$E_c^{HgMnTe}(x) = E_g^{HgMnTe}(x) + E_v^{HgMnTe}(x)\,, \tag{A.6}$$

where $\alpha = (E_g^{\mathrm{MnTe}} - E_g^{\mathrm{HgTe}})/(E_g^{\mathrm{CdTe}} - E_g^{\mathrm{HgTe}})$. The lattice constant of $\mathrm{Hg}_{1-x}\mathrm{Mn}_x\mathrm{Te}$ is given by [91]:

$$a_{HgMnTe}(x) = a_{\mathrm{HgTe}} - 0.01131x\,\mathrm{nm}\,. \tag{A.7}$$

A.3. Strain parameters

In the experiment, (Hg,Mn)Te / (Hg,Cd)Te quantum wells are pseudomorphically grown on different substrate materials. This yields a lattice mismatch for the well material, which is given by [see also Eq. (3.9)]

$$\epsilon_S = \frac{a_{Sub} - a_W}{a_W}\,, \tag{A.8}$$

where a_{Sub} is the equilibrium lattice constant of the substrate and a_W is the equilibrium lattice constant of the well material. For the well material, we focus on (Hg,Mn)Te whose lattice constant is given by Eq. (A.7). For the substrate, we consider either (Hg,Cd)Te, for which the lattice constant is given by Eq. (A.3), or $\mathrm{Cd}_(1-x)\mathrm{Zn}_x\mathrm{Te}$ for which the lattice constant is given by [173]:

$$a_{CdZnTe}(x) = a_{\mathrm{CdTe}} - 0.0378x\,\mathrm{nm}\,, \tag{A.9}$$

where a_{CdTe} is the lattice constant of bulk CdTe. Adjusting the Zn-concentration to $x \approx 0.04$ allows to lattice match the substrate to bulk HgTe. As explained in Sec. 3.1.3, strain is included in the Kane model via the Pikus-Bir Hamiltonian, Eq. (3.10). The associated bulk parameters are listed in Tab. A.2.

	C [eV]	a_S [eV]	b [eV]	d [eV]	C_{11} [GPa]	C_{12} [GPa]
HgTe	−3.83	0	−1.50	−2.08	53.6	36.6
CdTe	−4.06	−0.7	−1.17	−3.20	53.6	37.0

Table A.2.: Pikus-Bir strain parameters, Eq. (3.10), taken from Ref. [150]. For (Hg,Mn)Te, we assume the same parameters as for bulk HgTe.

B.

Limitations and extensions of Bernevig-Hughes-Zhang model

The BHZ model is derived from the 8×8 Kane model based on quasi-degenerate perturbation theory (also known as Löwdin perturbation theory) [15]. The latter subdivides the space of all quantum well subbands into two weakly coupled classes: Class A contains only those states for which the interaction is supposed to be computed exactly, while states in class B are taken into account perturbatively up to the desired order [144, 152]. For instance, in the case of the BHZ model, class A consists of the four basis states $|\mathrm{E1},\uparrow\rangle$, $|\mathrm{H1},\uparrow\rangle$, $|\mathrm{E1},\downarrow\rangle$, and $|\mathrm{H1},\downarrow\rangle$ (cf. Sec. 1.3.2).

As a perturbative model, the scope of the BHZ model is limited to small energies and small momenta. In particular, it does not account for the camelback at large momenta [cf. Ch. 3]. Its scope can be however improved by including more quantum well subbands within the class A. The most simple extension of the BHZ model contains therefore additionally to the usual BHZ basis states the two H2 subbands. The Hamiltonian of this extended BHZ model is given by [81]:

$$H_{6\times6}(\mathbf{k}) = \begin{pmatrix} h_{3\times3}(\mathbf{k}) & 0 \\ 0 & h^{\star}_{3\times3}(-\mathbf{k}) \end{pmatrix}, \tag{B.1}$$

where

$$h_{3\times3}(\mathbf{k}) = CI_3 + \begin{pmatrix} M-(B+D)k^2 & Ak_+ & Rk_-^2 \\ Ak_- & -M+(B-D)k^2 & 0 \\ Rk_+^2 & 0 & \Delta - B_{H2}k^2 \end{pmatrix}. \tag{B.2}$$

Equation (B.1) is thereby written in the basis $|\mathrm{E1},\uparrow\rangle$, $|\mathrm{H1},\uparrow\rangle$, $|\mathrm{H2},\uparrow\rangle$, $|\mathrm{E1},\downarrow\rangle$, $|\mathrm{H1},\downarrow\rangle$, and $|\mathrm{H2},\downarrow\rangle$; Δ denotes the energetic position of the H2-subband, B_{H2} describes its effective mass, R describes the coupling between the H2 and E1 subbands, and C denotes an energetic offset (I_3 is the three dimensional identity matrix).

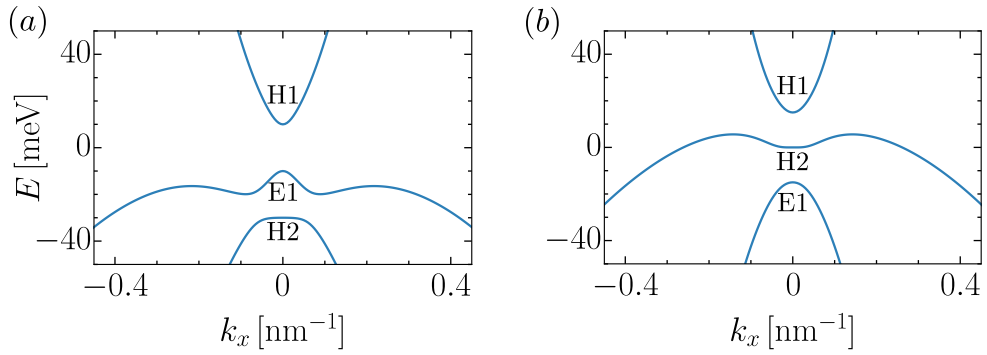

Figure B.1.: Bulk band structure of extended BHZ model for a (a) direct and (b) an indirect semiconductor. The parameters in (a) are given by $M = -10\,\text{meV}$, $B = -1000\,\text{meV nm}^2$, $D = -800\,\text{meV nm}^2$, $A = 365\,\text{meV nm}$, $\Delta = -30\,\text{meV}$, $B_{H2} = -100\,\text{meV nm}^2$, $R = 1500\,\text{meV nm}^2$, and $C = 0\,\text{meV}$. The parameters in (b) are given by $M = -15\,\text{meV}$, $B = -1000\,\text{meV nm}^2$, $D = -800\,\text{meV nm}^2$, $A = 365\,\text{meV nm}$, $\Delta = 0\,\text{meV}$, $B_{H2} = -100\,\text{meV nm}^2$, $R = 3000\,\text{meV nm}^2$, and $C = 0\,\text{meV}$. The band ordering of the $E1$, $H1$, and $H2$ subbands are indicated.

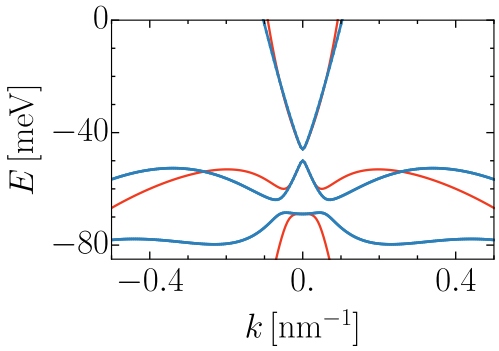

Figure B.2.: Comparison between 8×8 Kane model (blue line) for a $Hg_{0.976}Mn_{0.024}Te$ quantum well with $d_{QW} = 11\,\text{nm}$ (compare Ch. 3) and extended BHZ model (red line) with $M = -2\,\text{meV}$, $B = -640\,\text{meV nm}^2$, $D = -560\,\text{meV nm}^2$, $A = 365\,\text{meV nm}$, $\Delta = -21\,\text{meV}$, $B_{H2} = -100\,\text{meV nm}^2$, $R = 4000\,\text{meV nm}^2$, and $C = -48\,\text{meV}$. The extended BHZ parameters are optimized with respect to the height of all extrema of the 8×8 Kane model.

The advantage of using this extended BHZ model is that it allows us to describe the band structure of direct and indirect gap semiconductors as shown in Fig. B.1. Nonetheless, deviations from the full 8×8 Kane model are expected due to the perturbative nature of this model. For completeness, we compare therefore in Fig. B.2 the dispersion of the full Kane model with the extended BHZ model. While the extended BHZ model does clearly a better job than the conventional (four-band) BHZ model in describing the camelback, there are still strong deviations with respect to the position of the extrema and the curvature of the valence bands (parameters are optimized with respect to the height of the extrema). Despite being computationally more heavy, it is therefore sometimes advisable to work with the full 8×8 Kane model, when very accurate results are desired.

Bibliography

[1] M. M. Waldrop, The chips are down for Moore's law, Nature **530**, 144 (2016).

[2] J. Yang, P. Hu, and G. Yu, Perspective of graphene-based electronic devices: Graphene synthesis and diverse applications, APL Mat. **7**, 020901 (2019).

[3] B. S. Jessen, L. Gammelgaard, M. R. Thomsen, D. M. A. Mackenzie, J. D. Thomsen, J. M. Caridad, E. Duegaard, K. Watanabe, T. Taniguchi, T. J. Booth, T. G. Pedersen, A.-P. Jauho, and P. Bøggild, Lithographic band structure engineering of graphene, Nat. Nanotechnol. **14**, 340 (2019).

[4] D. R. Nelson and J. M. Kosterlitz, Universal jump in the superfluid density of two-dimensional superfluids, Phys. Rev. Lett. **39**, 1201 (1977).

[5] D. J. Thouless, M. Kohmoto, M. P. Nightingale, and M. den Nijs, Quantized Hall conductance in a two-dimensional periodic potential, Phys. Rev. Lett. **49**, 405 (1982).

[6] F. D. M. Haldane, Nonlinear field theory of large-spin Heisenberg antiferromagnets: Semiclassically quantized solitons of the one-dimensional easy-axis néel state, Phys. Rev. Lett. **50**, 1153 (1983).

[7] Q. Niu, D. J. Thouless, and Y.-S. Wu, Quantized Hall conductance as a topological invariant, Phys. Rev. B **31**, 3372 (1985).

[8] F. D. M. Haldane, Model for a quantum Hall effect without Landau levels: condesed-matter realization of the "parity anomaly", Phys. Rev. Lett. **61**, 2015 (1988).

[9] K. von Klitzing, G. Dorda, and M. Pepper, New method for high-accuracy determination of the fine-structure constant based on quantized Hall resistance, Phys. Rev. Lett. **45**, 494 (1980).

[10] A. P. Schnyder, S. Ryu, A. Furusaki, and A. W. W. Ludwig, Classification of topological insulators and superconductors in three spatial dimensions, Phys. Rev. B **78**, 195125 (2008).

[11] C.-K. Chiu, J. C. Y. Teo, A. P. Schnyder, and S. Ryu, Classification of topological quantum matter with symmetries, Rev. Mod. Phys. **88**, 035005 (2016).

[12] X.-L. Qi and S.-C. Zhang, Topological insulators and superconductors, Rev. Mod. Phys. **83**, 1057 (2011).

[13] C. L. Kane and E. J. Mele, Quantum spin Hall effect in graphene, Phys. Rev. Lett. **95**, 226801 (2005).

[14] C. L. Kane and E. J. Mele, Z_2 topological order and the quantum spin Hall effect, Phys. Rev. Lett. **95**, 146802 (2005).

[15] B. A. Bernevig, T. L. Hughes, and S.-C. Zhang, Quantum spin Hall effect and topological phase transition in HgTe quantum wells, Science **314**, 1757 (2006).

[16] M. König, S. Wiedmann, C. Brüne, A. Roth, H. Buhmann, L. W. Molenkamp, X.-L. Qi, and S.-C. Zhang, Quantum spin Hall insulator state in HgTe quantum wells, Science **318**, 766 (2007).

[17] M. König, H. Buhmann, L. W. Molenkamp, T. L. Hughes, C.-X. Liu, X.-L. Qi, and S.-C. Zhang, The quantum spin Hall effect: Theory and experiment, J. Phys. Soc. Jpn. **77**, 031007 (2008).

[18] M. G. Vergniory, L. Elcoro, C. Felser, N. Regnault, B. A. Bernevig, and Z. Wang, A complete catalogue of high-quality topological materials, Nature **566**, 480 (2019).

[19] L. Fu and C. L. Kane, Topological insulators with inversion symmetry, Phys. Rev. B **76**, 045302 (2007).

[20] C. Liu, T. L. Hughes, X.-L. Qi, K. Wang, and S.-C. Zhang, Quantum spin Hall effect in inverted type-II semiconductors, Phys. Rev. Lett. **100**, 236601 (2008).

[21] C.-X. Liu, X.-L. Qi, X. Dai, Z. Fang, and S.-C. Zhang, Quantum anomalous Hall effect in $Hg_{1-y}Mn_yTe$ quantum wells, Phys. Rev. Lett. **101**, 146802 (2008).

[22] R. Yu, W. Zhang, H.-J. Zhang, S.-C. Zhang, X. Dai, and Z. Fang, Quantized anomalous Hall effect in magnetic topological insulators, Science **329**, 61 (2010).

[23] C.-Z. Chang, J. Zhang, X. Feng, J. Shen, Z. Zhang, M. Guo, K. Li, Y. Ou, P. Wei, L.-L. Wang, Z.-Q. Ji, Y. Feng, S. Ji, X. Chen, J. Jia, X. Dai, Z. Fang, S.-C. Zhang, K. He, Y. Wang, L. Lu, X.-C. Ma, and Q.-K. Xue, Experimental observation of the quantum anomalous Hall effect in a magnetic topological insulator, Science **340**, 167 (2013).

[24] C.-Z. Chang, W. Zhao, D. Y. Kim, P. Wei, J. K. Jain, C. Liu, M. H. W. Chan, and J. S. Moodera, Zero-field dissipationless chiral edge transport and the nature of dissipation in the quantum anomalous Hall state, Phys. Rev. Lett. **115**, 057206 (2015).

[25] J. G. Checkelsky, R. Yoshimi, A. Tsukazaki, K. S. Takahashi, Y. Kozuka, J. Falson, M. Kawasaki, and Y. Tokura, Trajectory of the anomalous Hall effect towards the quantized state in a ferromagnetic topological insulator, Nat. Phys. **10**, 731 (2014).

[26] D. Hsieh, D. Qian, L. Wray, Y. Xia, Y. S. Hor, R. J. Cava, and M. Z. Hasan, A topological Dirac insulator in a quantum spin Hall phase, Nature **452**, 970 (2008).

[27] Y. Xia, D. Qian, D. Hsieh, L. Wray, A. Pal, H. Lin, A. Bansil, D. Grauer, Y. S. Hor, R. J. Cava, *et al.*, Observation of a large-gap topological-insulator class with a single Dirac cone on the surface, Nat. Phys. **5**, 398 (2009).

[28] C. Brüne, C. X. Liu, E. G. Novik, E. M. Hankiewicz, H. Buhmann, Y. L. Chen, X. L. Qi, Z. X. Shen, S. C. Zhang, and L. W. Molenkamp, Quantum Hall effect from the topological surface states of strained bulk HgTe, Phys. Rev. Lett. **106**, 126803 (2011).

[29] A. Barfuss, L. Dudy, M. R. Scholz, H. Roth, P. Höpfner, C. Blumenstein, G. Landolt, J. H. Dil, N. C. Plumb, M. Radovic, A. Bostwick, E. Rotenberg, A. Fleszar, G. Bihlmayer, D. Wortmann, G. Li, W. Hanke, R. Claessen, and J. Schäfer, Elemental topological insulator with tunable Fermi level: Strained α-Sn on InSb(001), Phys. Rev. Lett. **111**, 157205 (2013).

[30] N. P. Armitage, E. J. Mele, and A. Vishwanath, Weyl and Dirac semimetals in three-dimensional solids, Rev. Mod. Phys. **90**, 015001 (2018).

[31] X. Huang, L. Zhao, Y. Long, P. Wang, D. Chen, Z. Yang, H. Liang, M. Xue, H. Weng, Z. Fang, X. Dai, and G. Chen, Observation of the chiral-anomaly-induced negative magnetoresistance in 3D Weyl semimetal TaAs, Phys. Rev. X **5**, 031023 (2015).

[32] S.-M. Huang, S.-Y. Xu, I. Belopolski, C.-C. Lee, G. Chang, B. Wang, N. Alidoust, G. Bian, M. Neupane, C. Zhang, S. Jia, A. Bansil, H. Lin, and M. Z. Hasan, A Weyl fermion semimetal with surface Fermi arcs in the transition metal monopnictide TaAs class, Nat. Commun. **6**, 7373 (2015).

[33] Z. Wang, Y. Sun, X.-Q. Chen, C. Franchini, G. Xu, H. Weng, X. Dai, and Z. Fang, Dirac semimetal and topological phase transitions in A_3Bi (A = Na, K, Rb), Phys. Rev. B **85**, 195320 (2012).

[34] Z. K. Liu, B. Zhou, Y. Zhang, Z. J. Wang, H. M. Weng, D. Prabhakaran, S.-K. Mo, Z. X. Shen, Z. Fang, X. Dai, Z. Hussain, and Y. L. Chen, Discovery of a three-dimensional topological Dirac semimetal, Na_3Bi, Science **343**, 864 (2014).

[35] D. M. Mahler, J.-B. Mayer, P. Leubner, L. Lunczer, D. Di Sante, G. Sangiovanni, R. Thomale, E. M. Hankiewicz, H. Buhmann, C. Gould, and L. W. Molenkamp, Interplay of Dirac nodes and Volkov-Pankratov surface states in compressively strained HgTe, Phys. Rev. X **9**, 031034 (2019).

[36] M. Sato and Y. Ando, Topological superconductors: a review, Rep. Prog. Phys. **80**, 076501 (2017).

[37] G. W. Semenoff, Condensed-matter simulation of a three-dimensional anomaly, Phys. Rev. Lett. **53**, 2449 (1984).

[38] Q. Li, D. E. Kharzeev, C. Zhang, Y. Huang, I. Pletikosic, A. V. Fedorov, R. D. Zhong, J. A. Schneeloch, G. D. Gu, and T. Valla, Chiral magnetic effect in $ZrTe_5$, Nat. Phys. **12**, 550 (2016).

[39] C.-L. Zhang, S.-Y. Xu, I. Belopolski, Z. Yuan, Z. Lin, B. Tong, G. Bian, N. Alidoust, C.-C. Lee, S.-M. Huang, T.-R. Chang, G. Chang, C.-H. Hsu, H.-T. Jeng, M. Neupane, D. S. Sanchez, H. Zheng, J. Wang, H. Lin, C. Zhang, H.-Z. Lu, S.-Q. Shen, T. Neupert, M. Z. Hasan, and S. Jia, Signatures of the Adler–Bell–Jackiw chiral anomaly in a Weyl fermion semimetal, Nat. Commun. **7**, 10735 (2016).

[40] B. Yan and C. Felser, Topological materials: Weyl semimetals, Annu. Rev. Condens. Matter Phys. **8**, 337 (2017).

[41] J. Gooth, A. C. Niemann, T. Meng, A. G. Grushin, K. Landsteiner, B. Gotsmann, F. Menges, M. Schmidt, C. Shekhar, V. Süß, R. Hühne, B. Rellinghaus, C. Felser, B. Yan, and K. Nielsch, Experimental signatures of the mixed axial–gravitational anomaly in the Weyl semimetal NbP, Nature **547**, 324 (2017).

[42] X. G. Wen, Gapless boundary excitations in the quantum Hall states and in the chiral spin states, Phys. Rev. B **43**, 11025 (1991).

[43] H. B. Nielsen and M. Ninomiya, Absence of neutrinos on a lattice: (I). Proof by homotopy theory, Nucl. Phys. B **185**, 20 (1981).

[44] H. B. Nielsen and M. Ninomiya, Absence of neutrinos on a lattice: (II). Intuitive topological proof, Nucl. Phys. B **193**, 173 (1981).

[45] E. G. Novik, A. Pfeuffer-Jeschke, T. Jungwirth, V. Latussek, C. R. Becker, G. Landwehr, H. Buhmann, and L. W. Molenkamp, Band structure of semimagnetic $Hg_{1-y}Mn_yTe$ quantum wells, Phys. Rev. B **72**, 035321 (2005).

[46] M. Z. Hasan and C. L. Kane, Colloquium: Topological insulators, Rev. Mod. Phys. **82**, 3045 (2010).

[47] Y. Ando, Topological insulator materials, J. Phys. Soc. Jpn. **82**, 102001 (2013).

[48] A. B. Bernevig and T. L. Hughes, *Topological insulators and topological superconductors* (Princeton University Press, Princeton and Oxford, 2013).

[49] R. A. Bertlmann, *Anomalies in quantum field theory* (Oxford University Press, New York, 1996).

[50] G. V. Dunne, Aspects of Chern-Simons theory, arXiv:hep-th/9902115 (1999).

[51] M. Nakahara, *Geometry, topology and physics*, edited by T. Spicer (Institute of Physics Publishing, Bristol and Philadelphia, 2003).

[52] X.-L. Qi, T. L. Hughes, and S.-C. Zhang, Topological field theory of time-reversal invariant insulators, Phys. Rev. B **78**, 195424 (2008).

[53] D. Tong, The quantum Hall effect (2016), accessed: 27-11-2019.

[54] M. R. Zirnbauer, Riemannian symmetric superspaces and their origin in random matrix theory, J. Math. Phys. **37**, 4986 (1996).

[55] A. Altland and M. R. Zirnbauer, Nonstandard symmetry classes in mesoscopic normal-superconducting hybrid structures, Phys. Rev. B **55**, 1142 (1997).

[56] A. Kitaev, Periodic table for topological insulators and superconductors, AIP Conf. Proc. **1134**, 22 (2009).

[57] J. J. Sakurai, *Modern quantum mechanics*, edited by S. F. Tuan (Addison-Wesley Publishing Company, 1994).

[58] X.-L. Qi, Y.-S. Wu, and S.-C. Zhang, Topological quantization of the spin Hall effect in two-dimensional paramagnetic semiconductors, Phys. Rev. B **74**, 085308 (2006).

[59] H.-Z. Lu, W.-Y. Shan, W. Yao, Q. Niu, and S.-Q. Shen, Massive Dirac fermions and spin physics in an ultrathin film of topological insulator, Phys. Rev. B **81**, 115407 (2010).

[60] R. Stacey, Eliminating lattice fermion doubling, Phys. Rev. D **26**, 468 (1982).

[61] B. Scharf, A. Matos-Abiague, and J. Fabian, Magnetic properties of HgTe quantum wells, Phys. Rev. B **86**, 075418 (2012).

[62] S. Deser, R. Jackiw, and S. Templeton, Topologically massive gauge theories, Ann. Phys. **140**, 372 (1982).

[63] M. Büttiker, Absence of backscattering in the quantum Hall effect in multiprobe conductors, Phys. Rev. B **38**, 9375 (1988).

[64] B. I. Halperin, Quantized Hall conductance, current-carrying edge states, and the existence of extended states in a two-dimensional disordered potential, Phys. Rev. B **25**, 2185 (1982).

[65] J.-C. Chen, J. Wang, and Q.-F. Sun, Effect of magnetic field on electron transport in HgTe/CdTe quantum wells: Numerical analysis, Phys. Rev. B **85**, 125401 (2012).

[66] A. Roth, C. Brüne, H. Buhmann, L. W. Molenkamp, J. Maciejko, X.-L. Qi, and S.-C. Zhang, Nonlocal transport in the quantum spin Hall state, Science **325**, 294 (2009).

[67] M. Kohmoto, Topological invariant and the quantization of the Hall conductance, Ann. Phys. (N. Y.) **160**, 343 (1985).

[68] N. W. Ashcroft and N. D. Mermin, *Solid state physics*, edited by D. G. Crane (Cornell University, 1976).

[69] M. O. Goerbig, Quantum Hall effects, arXiv:0909.1998 (2009).

[70] J. E. Avron, R. Seiler, and B. Simon, Homotopy and quantization in condensed matter physics, Phys. Rev. Lett. **51**, 51 (1983).

[71] P. Streda, Theory of quantised Hall conductivity in two dimensions, J. Phys. C: Solid State Phys. **15**, L717 (1982).

[72] L. Onsager, Reciprocal relations in irreversible processes. II., Phys. Rev. **38**, 2265 (1931).

[73] M. Büttiker, Symmetry of electrical conduction, IBM J. Res. Develop. **32**, 317 (1988).

[74] H. Min, J. E. Hill, N. A. Sinitsyn, B. R. Sahu, L. Kleinman, and A. H. MacDonald, Intrinsic and rashba spin-orbit interactions in graphene sheets, Phys. Rev. B **74**, 165310 (2006).

[75] L. Du, I. Knez, G. Sullivan, and R.-R. Du, Robust helical edge transport in gated InAs/GaSb bilayers, Phys. Rev. Lett. **114**, 096802 (2015).

[76] S. Wu, V. Fatemi, Q. D. Gibson, K. Watanabe, T. Taniguchi, R. J. Cava, and P. Jarillo-Herrero, Observation of the quantum spin Hall effect up to 100 kelvin in a monolayer crystal, Science **359**, 76 (2018).

[77] F. Reis, G. Li, L. Dudy, M. Bauernfeind, S. Glass, W. Hanke, R. Thomale, J. Schäfer, and R. Claessen, Bismuthene on a sic substrate: A candidate for a high-temperature quantum spin Hall material, Science **357**, 287 (2017).

[78] F. Herman, C. D. Kuglin, K. F. Cuff, and R. L. Kortum, Relativistic corrections to the band structure of tetrahedrally bonded semiconductors, Phys. Rev. Lett. **11**, 541 (1963).

[79] J. W. Nicklas and J. W. Wilkins, Accurate electronic properties for (Hg,Cd)Te systems using hybrid density functional theory, Phys. Rev. B **84**, 121308 (2011).

[80] P. Leubner, L. Lunczer, C. Brüne, H. Buhmann, and L. W. Molenkamp, Strain engineering of the band gap of HgTe quantum wells using superlattice virtual substrates, Phys. Rev. Lett. **117**, 086403 (2016).

[81] S. S. Krishtopenko and F. Teppe, Realistic picture of helical edge states in HgTe quantum wells, Phys. Rev. B **97**, 165408 (2018).

[82] G. Tkachov and E. M. Hankiewicz, Spin-helical transport in normal and superconducting topological insulators, Phys. Status Solidi (B) **250**, 215 (2013).

[83] C. Brüne, A. Roth, H. Buhmann, E. M. Hankiewicz, L. W. Molenkamp, J. Maciejko, X.-L. Qi, and S.-C. Zhang, Spin polarization of the quantum spin Hall edge states, Nat. Phys. **8**, 486 (2012).

[84] S. Datta, *Electronic transport in mesoscopic systems*, edited by H. Ahmed, M. Pepper, and A. Broers (Cambridge University Press, 2003).

[85] K. Bendias, S. Shamim, O. Herrmann, A. Budewitz, P. Shekhar, P. Leubner, J. Kleinlein, E. Bocquillon, H. Buhmann, and L. W. Molenkamp, High mobility HgTe microstructures for quantum spin Hall studies, Nano Lett. **18**, 4831 (2018).

[86] L. Lunczer, P. Leubner, M. Endres, V. L. Müller, C. Brüne, H. Buhmann, and L. W. Molenkamp, Approaching quantization in macroscopic quantum spin Hall devices through gate training, Phys. Rev. Lett. **123**, 047701 (2019).

[87] J. I. Väyrynen, M. Goldstein, and L. I. Glazman, Helical edge resistance introduced by charge puddles, Phys. Rev. Lett. **110**, 216402 (2013).

[88] J. I. Väyrynen, M. Goldstein, Y. Gefen, and L. I. Glazman, Resistance of helical edges formed in a semiconductor heterostructure, Phys. Rev. B **90**, 115309 (2014).

[89] G. Jotzu, M. Messer, R. Desbuquois, M. Lebrat, T. Uehlinger, D. Greif, and T. Esslinger, Experimental realization of the topological Haldane model with ultracold fermions, Nature **515**, 237 (2014).

[90] C.-X. Liu, S.-C. Zhang, and X.-L. Qi, The quantum anomalous Hall effect: Theory and experiment, Annu. Rev. Condens. Matter Phys. **7**, 301 (2016).

[91] J. K. Furdyna, Diluted magnetic semiconductors, J. Appl. Phys. **64**, R29 (1988).

[92] J. Wang, Q. Zhou, B. Lian, and S.-C. Zhang, Chiral topological superconductor and half-integer conductance plateau from quantum anomalous Hall plateau transition, Phys. Rev. B **92**, 064520 (2015).

[93] A. J. Bestwick, E. J. Fox, X. Kou, L. Pan, K. L. Wang, and D. Goldhaber-Gordon, Precise quantization of the anomalous Hall effect near zero magnetic field, Phys. Rev. Lett. **114**, 187201 (2015).

[94] E. J. Fox, I. T. Rosen, Y. Yang, G. R. Jones, R. E. Elmquist, X. Kou, L. Pan, K. L. Wang, and D. Goldhaber-Gordon, Part-per-million quantization and current-induced breakdown of the quantum anomalous Hall effect, Phys. Rev. B **98**, 075145 (2018).

[95] M. Götz, K. M. Fijalkowski, E. Pesel, M. Hartl, S. Schreyeck, M. Winnerlein, S. Grauer, H. Scherer, K. Brunner, C. Gould, F. J. Ahlers, and L. W. Molenkamp, Precision measurement of the quantized anomalous Hall resistance at zero magnetic field, Appl. Phys. Lett. **112**, 072102 (2018).

[96] S. Grauer, S. Schreyeck, M. Winnerlein, K. Brunner, C. Gould, and L. W. Molenkamp, Coincidence of superparamagnetism and perfect quantization in the quantum anomalous hall state, Phys. Rev. B **92**, 201304 (2015).

[97] T. R. F. Peixoto, H. Bentmann, S. Schreyeck, M. Winnerlein, C. Seibel, H. Maaß, M. Al-Baidhani, K. Treiber, S. Schatz, S. Grauer, C. Gould, K. Brunner, A. Ernst, L. W. Molenkamp, and F. Reinert, Impurity states in the magnetic topological insulator V : $(Bi, Sb)_2Te_3$, Phys. Rev. B **94**, 195140 (2016).

[98] M. E. Peskin and D. V. Schroeder, *An introduction to quantum field theory* (Perseus Books Publishing, 1995).

[99] M. Shifman, *Advanced topics in quantum field theory* (Cambridge University Press (N.Y.), 2012).

[100] A. J. Niemi and G. W. Semenoff, Fermion number fractionization in quantum field theory, Phys. Rep. **135**, 99 (1986).

[101] I. V. Krive and A. S. Rozhavskiĭ, Fractional charge in quantum field theory and solid-state physics, Sov. Phys. Usp. **30**, 370 (1987).

[102] R. Rajaraman, Fractional charge, arXiv:cond-mat/0103366 (2001).

[103] E. Witten, Fermion path integrals and topological phases, Rev. Mod. Phys. **88**, 035001 (2016).

[104] K. Fujikawa, Path-integral measure for gauge-invariant fermion theories, Phys. Rev. Lett. **42**, 1195 (1979).

[105] K. Fujikawa, Path integral for gauge theories with fermions, Phys. Rev. D **21**, 2848 (1980).

[106] C. G. Callan and J. A. Harvey, Anomalies and fermion zero modes on strings and domain walls, Nucl. Phys. **B250**, 427 (1985).

[107] J. Collins, *Renormalization* (Cambridge University Press, 1984).

[108] A. J. Niemi and G. W. Semenoff, Spectral asymmetry on an open space, Phys. Rev. D **30**, 809 (1984).

[109] R. Jackiw and C. Rebbi, Solitons with fermion number 1/2, Phys. Rev. D **13**, 3398 (1976).

[110] R. MacKenzie and F. Wilczek, Illustrations of vacuum polarization by solitons, Phys. Rev. D **30**, 2194 (1984).

[111] R. Jackiw and J. R. Schrieffer, Solitons with fermion number 1/2 in condensed matter and relativistic field theories, Nucl. Phys. B **190**, 253 (1981).

[112] R. Jackiw and G. Semenoff, Continuum quantum field theory for a linearly conjugated diatomic polymer with fermion fractionization, Phys. Rev. Lett. **50**, 439 (1983).

[113] J. Goldstone and F. Wilczek, Fractional quantum numbers on solitons, Phys. Rev. Lett. **47**, 986 (1981).

[114] R. Rajaraman and J. S. Bell, On solitons with half integral charge, Phys. Lett. B **116**, 151 (1982).

[115] J. Froehlich, Chiral anomaly, topological field theory, and novel states of matter, arXiv:1802.01385 (2018).

[116] X.-G. Wen, Theory of the edge states in fractional quantum Hall effects, Int. J. Mod. Phys. B **06**, 1711 (1992).

[117] J. Fröhlich and A. Zee, Large scale physics of the quantum Hall fluid, Nucl. Phys. B **364**, 517 (1991).

[118] J. Fröhlich and T. Kerler, Universality in quantum Hall systems, Nucl. Phys. B **354**, 369 (1991).

[119] S. C. Zhang, The Chern-Simons-Landau-Ginzburg theory of the fractional quantum Hall effect, Int. J. Mod. Phys. B **06**, 25 (1992).

[120] N. Maeda, Chiral anomaly and effective field theory for the quantum Hall liquid with edges, Phys. Lett. B **376**, 142 (1996).

[121] R. B. Laughlin, Quantized Hall conductivity in two dimensions, Phys. Rev. B **23**, 5632 (1981).

[122] A. N. Redlich, Parity violation and gauge noninvariance of the effective gauge field action in three dimensions, Phys. Rev. D **29**, 2366 (1984).

[123] A. N. Redlich, Gauge noninvariance and parity nonconservation of three-dimensional fermions, Phys. Rev. Lett. **52**, 18 (1984).

[124] R. Narayanan and J. Nishimura, Parity-invariant lattice regularization of a three-dimensional gauge-fermion system, Nucl. Phys. B **508**, 371 (1997).

[125] M. Mulligan and F. J. Burnell, Topological insulators avoid the parity anomaly, Phys. Rev. B **88**, 085104 (2013).

[126] A. J. Niemi and G. W. Semenoff, Axial-anomaly-induced fermion fractionization and effective gauge-theory actions in odd-dimensional space-times, Phys. Rev. Lett. **51**, 2077 (1983).

[127] M. F. Atiyah, V. K. Patodi, and I. M. Singer, Spectral asymmetry and Riemannian geometry. I, Math. Proc. Camb. Phil. Soc. **77**, 43 (1975).

[128] D. Boyanovsky, R. Blankenbecler, and R. Yahalom, Physical origin of topological mass in 2+1 dimensions, Nucl. Phys. **B270**, 483 (1986).

[129] J. Wang, B. Lian, H. Zhang, and S.-C. Zhang, Anomalous edge transport in the quantum anomalous Hall state, Phys. Rev. Lett. **111**, 086803 (2013).

[130] R. Jackiw, Fractional charge and zero modes for planar systems in a magnetic field, Phys. Rev. D **29**, 2375 (1984).

[131] M. F. Atiyah and I. M. Singer, The index of elliptic operators: I, Ann. Math. **87**, 484 (1968).

[132] R. Blankenbecler and D. Boyanovsky, Induced quantum numbers in (2+1)-dimensional QED, Phys. Rev. D **34**, 612 (1986).

[133] B. Zhou, H.-Z. Lu, R.-L. Chu, S.-Q. Shen, and Q. Niu, Finite size effects on helical edge states in a quantum spin-Hall system, Phys. Rev. Lett. **101**, 246807 (2008).

[134] A. J. Niemi, Topological solitons in a hot and dense Fermi gas, Nucl. Phys. **B251**, 155 (1985).

[135] A. Abouelsaood, Relation between the chiral anomaly and the quantized Hall effect, Phys. Rev. Lett. **54**, 1973 (1985).

[136] J. B. Kogut, The lattice gauge theory approach to quantum chromodynamics, Rev. Mod. Phys. **55**, 775 (1983).

[137] R. Skolasinski, D. I. Pikulin, J. Alicea, and M. Wimmer, Robust helical edge transport in quantum spin Hall quantum wells, Phys. Rev. B **98**, 201404 (2018).

[138] P. C. Klipstein, A k·p treatment of edge states in narrow 2D topological insulators, with standard boundary conditions for the wave function and its derivative, J. Phys. Condens. Materie **30**, 275302 (2018).

[139] L. Gioia, M. G. Christie, U. Zülicke, M. Governale, and A. J. Sneyd, Spherical topological insulator nanoparticles: Quantum size effects and optical transitions, Phys. Rev. B **100**, 205417 (2019).

[140] D. R. Candido, M. Kharitonov, J. C. Egues, and E. M. Hankiewicz, Paradoxical extension of the edge states across the topological phase transition due to emergent approximate chiral symmetry in a quantum anomalous Hall system, Phys. Rev. B **98**, 161111 (2018).

[141] M. Büttiker, Role of quantum coherence in series resistors, Phys. Rev. B **33**, 3020 (1986).

[142] G. Tkachov and E. M. Hankiewicz, Ballistic quantum spin Hall state and enhanced edge backscattering in strong magnetic fields, Phys. Rev. Lett. **104**, 166803 (2010).

[143] W. Beugeling, C. X. Liu, E. G. Novik, L. W. Molenkamp, and C. Morais Smith, Reentrant topological phases in Mn-doped HgTe quantum wells, Phys. Rev. B **85**, 195304 (2012).

[144] R. Winkler, *Spin orbit coupling effects in two-dimensional electron and hole systems* (Springer, 2003).

[145] E. O. Kane, Band structure of indium antimonide, J. Phys. Chem. Solids **1**, 249 (1957).

[146] M. Dobrowolska and W. Dobrowolski, Temperature study of interband magnetoabsorption in $Hg_{1-x}Mn_xTe$ mixed crystals, J. Phys. C: Solid State Phys. **14**, 5689 (1981).

[147] H. R. Trebin, U. Rössler, and R. Ranvaud, Quantum resonances in the valence bands of zinc-blende semiconductors. I. Theoretical aspects, Phys. Rev. B **20**, 686 (1979).

[148] G. L. Bir and G. E. Pikus, *Symmetry and strain-induced effects in semiconductors* (John Wiley and Sons, Inc. (NY), 1974).

[149] N. O. Lipari and A. Baldereschi, Angular momentum theory and localized states in solids. Investigation of shallow acceptor states in semiconductors, Phys. Rev. Lett. **25**, 1660 (1970).

[150] A. Pfeuffer-Jeschke, *Bandstruktur und Landau-Niveaus quecksilberhaltiger II-VI-Heterostrukturen*, Ph.D. thesis, Würzburg University, Würzburg, Germany (2000).

[151] M. Cardona, N. E. Christensen, and G. Fasol, Terms linear in k in the band structure of zinc-blende-type semiconductors, Phys. Rev. Lett. **56**, 2831 (1986).

[152] S. L. Chuang, *Physics of optoelectronic devices* (John Wiley and Sons, Inc. (NY), 1995).

[153] P. Harrison, *Quantum wells, wires and dots*, second edition ed. (Wiley-Interscience, John Wiley and Sons, LTD, 2005).

[154] D. J. BenDaniel and C. B. Duke, Space-charge effects on electron tunneling, Phys. Rev. **152**, 683 (1966).

[155] T. L. Schmidt, S. Rachel, F. von Oppen, and L. I. Glazman, Inelastic electron backscattering in a generic helical edge channel, Phys. Rev. Lett. **108**, 156402 (2012).

[156] Y. Hanein, U. Meirav, D. Shahar, C. C. Li, D. C. Tsui, and H. Shtrikman, The metalliclike conductivity of a two-dimensional hole system, Phys. Rev. Lett. **80**, 1288 (1998).

[157] X.-L. Qi, T. L. Hughes, and S.-C. Zhang, Chiral topological superconductor from the quantum Hall state, Phys. Rev. B **82**, 184516 (2010).

[158] B. J. Roman and A. W. Ewald, Stress-induced band gap and related phenomena in gray tin, Phys. Rev. B **5**, 3914 (1972).

[159] L. Fu, C. L. Kane, and E. J. Mele, Topological insulators in three dimensions, Phys. Rev. Lett. **98**, 106803 (2007).

[160] S.-C. Wu, B. Yan, and C. Felser, Ab initio study of topological surface states of strained HgTe, EPL **107**, 57006 (2014).

[161] C. Liu, G. Bian, T.-R. Chang, K. Wang, S.-Y. Xu, I. Belopolski, I. Miotkowski, H. Cao, K. Miyamoto, C. Xu, C. E. Matt, T. Schmitt, N. Alidoust, M. Neupane, H.-T. Jeng, H. Lin, A. Bansil, V. N. Strocov, M. Bissen, A. V. Fedorov, X. Xiao, T. Okuda, Y. P. Chen, and M. Z. Hasan, Tunable spin helical Dirac quasiparticles on the surface of three-dimensional HgTe, Phys. Rev. B **92**, 115436 (2015).

[162] J. Böttcher, *Anomalous Dirac surface screening versus self-consistent Hartree band structure calculations for the 3D TI HgTe*, Master's thesis, Julius-Maximilians-Universität Würzburg (2014).

[163] C.-X. Liu, H. Zhang, B. Yan, X.-L. Qi, T. Frauenheim, X. Dai, Z. Fang, and S.-C. Zhang, Oscillatory crossover from two-dimensional to three-dimensional topological insulators, Phys. Rev. B **81**, 041307 (2010).

[164] Y. Zhang, K. He, C.-Z. Chang, C.-L. Song, L.-L. Wang, X. Chen, J.-F. Jia, Z. Fang, X. Dai, W.-Y. Shan, S.-Q. Shen, Q. Niu, X.-L. Qi, S.-C. Zhang, X.-C. Ma, and Q.-K. Xue, Crossover of the three-dimensional topological insulator Bi_2Se_3 to the two-dimensional limit, Nat. Phys. **6**, 584 (2010).

[165] E. L. Ivchenko, A. Y. Kaminski, and U. Rössler, Heavy-light hole mixing at zinc-blende (001) interfaces under normal incidence, Phys. Rev. B **54**, 5852 (1996).

[166] O. Crauste, Y. Ohtsubo, P. Ballet, P. A. L. Deplace, D. Carpentier, C. Bouvier, T. Meunier, A. Taleb-Ibrahimi, and L. Levy, Topological surface states of strained mercury-telluride probed by ARPES, arXiv:1307.2008 (2013).

[167] H. Zhang, C.-X. Liu, X.-L. Qi, X. Dai, Z. Fang, and S.-C. Zhang, Topological insulators in Bi_2Se_3, Bi_2Te_3 and Sb_2Te_3 with a single Dirac cone on the surface, Nat. Phys. **5**, 438 (2009).

[168] D. G. Rothe, R. W. Reinthaler, C. X. Liu, L. W. Molenkamp, S.-C. Zhang, and E. M. Hankiewicz, Fingerprint of different spin-orbit terms for spin transport in HgTe quantum wells, New J. Phys. **12**, 065012 (2010).

[169] C. R. Becker, V. Latussek, A. Pfeuffer-Jeschke, G. Landwehr, and L. W. Molenkamp, Band structure and its temperature dependence for type-III $HgTe/Hg_{1-x}Cd_xTe$ superlattices and their semimetal constituent, Phys. Rev. B **62**, 10353 (2000).

[170] J. P. Laurenti, J. Camassel, A. Bouhemadou, B. Toulouse, R. Legros, and A. Lusson, Temperature dependence of the fundamental absorption edge of mercury cadmium telluride, J. Appl. Phys. **67**, 6454 (1990).

[171] A. Christopher, *Molecular beam epitaxy of 2D and 3D HgTe, a topological insulator*, Ph.D. thesis, Julius-Maximilians-Universität Würzburg (2015).

[172] R. T. Delves and B. Lewis, Zinc blende type HgTe–MnTe solid solutions–I, J. Phys. Chem. Solids **24**, 549 (1963).

[173] H. Landolt and R. Börnstein, *Semiconductors*, B: II-VI and I-VII compounds; semimagnetic compounds ed., edited by U. Rössler (Springer-Verlag Berlin Heidelberg, 1999).

Publications

[P1] Y. Baum, **J. Böttcher**, C. Brüne, C. Thienel, L. W. Molenkamp, A. Stern, and E. M. Hankiewicz. *Self-consistent $k \cdot p$ calculations for gated thin layers of three-dimensional topological insulators.* Phys. Rev. B **89**, 245136 (2014).

[P2] C. Brüne, C. Thienel, M. Stuiber, **J. Böttcher**, H. Buhmann, E. G. Novik, C.-X. Liu, E. M. Hankiewicz, and L. W. Molenkamp. *Dirac-screening stabilized surface-state transport in a topological insulator.* Phys. Rev. X **4**, 041045 (2014).

[P3] V. Dziom, A. Shuvaev, G. V. Astakhov, C. Ames, K. Bendias, **J. Böttcher**, G. Tkachov, E. M. Hankiewicz, C. Brüne, H. Buhmann, and L. W. Molenkamp. *Observation of the universal magnetoelectric effect in a 3D topological insulator.* Nat. Commun. **8**, 15197 (2017).

[P4] A. Jost, M. Bendias, **J. Böttcher**, E. M. Hankiewicz, C. Brüne, H. Buhmann, L. W. Molenkamp, J. C. Maan, U. Zeitler, N. Hussey, and S. Wiedmann. *Electron–hole asymmetry of the topological surface states in strained HgTe.* PNAS **114**, 3381 (2017).

[P5] **J. Böttcher***, C. Tutschku*, L. W. Molenkamp, and E. M. Hankiewicz. *Survival of the quantum anomalous Hall effect in orbital magnetic fields as a consequence of the parity anomaly.* Phys. Rev. Lett. **123**, 226602 (2019).

[P6] **J. Böttcher**, C. Tutschku, and E. M. Hankiewicz. *Fate of quantum anomalous Hall effect in external magnetic fields in the presence of particle-hole asymmetry.* arXiv:2002.01443. Send to Phys. Rev. B (2020).

[P7] S. Shamim*, W. Beugeling*, **J. Böttcher***, P. Shekhar, A. Budewitz, P. Leubner, L. Lunczer, E. M. Hankiewicz, H. Buhmann, and L. W. Molenkamp. *Emergent quantum Hall effects below 50 mT in a two-dimensional topological insulator.* arXiv:2004.00091. Send to Sci. Adv. (2020).

[P8] C. Tutschku, **J. Böttcher**, R. Meyer, and E. M. Hankiewicz. *Momentum-dependent mass and AC Hall conductivity of quantum anomalous Hall insulators and their relation to the parity anomaly.* arXiv:2003.03146v1. Send to Phys. Rev. Res. (2020).

* These authors contributed equally to this work.

Acknowledgements

During the last five years of my PhD, I had the pleasure of collaborating with a variety of friends and colleagues. Without them, this work would not have been possible in this form. First and foremost, I would like to thank my supervisor Ewelina M. Hankiewicz for giving me the opportunity to work on this intriguing research project. I am very thankful to her that she gave me the opportunity to attend a variety of conferences and to bring me into contact with many well-respected experts in our research field. Furthermore, I am indebted to Björn Trauzettel, who always made time for me whenever I needed further guidance and help.

Although some years have already past by, I would still like to thank my former colleagues R. Reinthaler, D. Rothe, and S. Jürgens who welcomed me with open arms at the beginning of my time at the TP4. Generally speaking, I am thankful to all my colleagues at the TP4 with whom I shared so many fruitful discussions over the years. In this respect, I am especially indebted to my office mate C. Tutschku. I find it difficult to quantify the countless hours we discussed about life and physics. I would also like to thank my friends and colleagues at the EP3: W. Beugeling, S. Shamim, and D. Mahler. With W. Beugeling, I have had the pleasure to work on the Kane model, while, with S. Shamim and D. Mahler, I have had countless fruitful discussions about their experimental findings. I am also particularly grateful to Laurens W. Molenkamp and Hartmut Buhmann who supported me with their lifelong experience in condensed matter physics. Last but not least, I am very grateful to J. Hofmann for helping me with his knowledge of symmetries, R. Meyer for supporting me in understanding quantum field theory, and B. Scharf for sharing with me his expertise in electron transport. My special thanks goes to C. Tutschku, D. Mahler, and W. Beugeling for being so kind to proof-read and, therefore, improve this thesis.

Finally, I would like to express my appreciation and special thanks to my friends and family. I am extremely indebted to my parents for their emotional support, and I have to thank my girlfriend Nora who accompanied me through all the ups and downs of my PhD.